

MICROSTRUCTURAL EFFECTS ON FRACTURE BEHAVIOR OF PARTICULATE
COMPOSITES: INVESTIGATION OF TOUGHENING MECHANISMS
USING OPTICAL AND BOUNDARY ELEMENT METHODS

Except where reference is made to the work of others, the work described in this is my own or was done in collaboration with my advisory committee. This does not include proprietary or classified information.

Rajesh Kitey

Certificate of Approval:

Jeffrey C. Suhling
Quina Distinguished Professor
Mechanical Engineering

Hareesh V. Tippur, Chair
Alumni Professor
Mechanical Engineering

Winfred A. Foster
Professor
Aerospace Engineering

Ruel A. Overfelt
Philpott-Westpoint Stevens Professor
Materials Engineering

Anh -Vu Phan
Assistant Professor
Mechanical Engineering
University of South Alabama, Mobile,
AL

Stephen L. McFarland
Acting Dean
Graduate School

MICROSTRUCTURAL EFFECTS ON FRACTURE BEHAVIOR OF PARTICULATE
COMPOSITES: INVESTIGATION OF TOUGHENING MECHANISMS
USING OPTICAL AND BOUNDARY ELEMENT METHODS

Rajesh Kitey

A Dissertation
Submitted to
the Graduate Faculty of
Auburn University
in Partial Fulfillment of the
Requirements for the
Degree of
Doctor of Philosophy

Auburn, Alabama

August 07, 2006

MICROSTRUCTURAL EFFECTS ON FRACTURE BEHAVIOR OF PARTICULATE
COMPOSITES: INVESTIGATION OF TOUGHENING MECHANISMS
USING OPTICAL AND BOUNDARY ELEMENT METHODS

Rajesh Kitey

Permission is granted to Auburn University to make copies of this dissertation at its discretion, upon the request of individuals or institutions and at their expense. The author reserves all publication rights.

Signature of Author

Date of Graduation

VITA

Rajesh Kitey was born on October 21, 1972 in Bhilai, India. He graduated with a Bachelor of Engineering degree in Mechanical Engineering from Maulana Azad National Institute of Technology (REC), Bhopal in 1994. Subsequently, he worked for three years as a Maintenance Engineer in Kedia Castle Delleon Industries Limited, Bhilai. Simultaneously, he earned his Post Graduate Diploma in Computer Science from Kalyan College, Bhilai in 1995. In 1997, he joined Indian Institute of Technology, Kanpur, IITK, for a Master's degree in Aerospace Structures. He was awarded Master of Technology degree in 1998 with his thesis entitled "Finite element analysis of laminated composite plates based on hierarchic modeling and p-extensions." Following graduation, he joined Tata Consultancy Services, Secunderabad, India, in 1999 where he worked for Unigraphics Solutions for two years. He joined Auburn University in Fall 2001 as a Ph.D. candidate in Mechanical Engineering where he conducted research on fracture behavior of particulate composites using experimental and numerical techniques.

DISSERTATION ABSTRACT

MICROSTRUCTURAL EFFECTS ON FRACTURE BEHAVIOR OF PARTICULATE
COMPOSITES: INVESTIGATION OF TOUGHENING MECHANISMS
USING OPTICAL AND BOUNDARY ELEMENT METHODS

Rajesh Kitey

Doctor of Philosophy, August 07, 2006
(M.Tech., Indian Institute of Technology, Kanpur, India, 1999)
(B.E., National Institute of Technology, Bhopal, India, 1994)

219 Typed Pages

Directed by Hareesh V. Tippur

Particulate polymer composites are used in a variety of engineering applications. These are generally two phase materials with polymeric phase reinforced by a filler phase to improve overall mechanical, thermal and/or dielectric functionalities. From a mechanical perspective, polymers when filled with stiffer particulates generally show enhanced elastic properties and creep resistance. Achieving similar improvement in failure characteristics has not been consistent due to a lack of thorough understanding of microstructural and loading rate effects. This dissertation addresses a few of these issues by studying effects of filler particle size, filler size distribution and filler-matrix adhesion strength on fracture behavior under quasi-static and dynamic loading conditions.

Glass-filled epoxy composites consisting of solid spherical particles are studied in this research. Spherical particles of mean dia. (D) $7\ \mu m$ to $200\ \mu m$ are used to reinforce epoxy matrix at a constant volume fraction ($V_f = 10\%$) and two different filler-matrix

strengths, weak and strong. Optical interferometry in conjunction with high-speed photography is used to quantify crack growth and deformation histories during impact loading. Although elastic characteristics remain unaffected by microstructural variations, significant differences in fracture behaviors are seen. Both weakly and strongly bonded particles in the matrix show higher values of steady-state dynamic fracture toughness, $K_{I_{ss}}$, relative to unfilled material. Filler particle size affects $K_{I_{ss}}$ significantly when particles are weakly bonded to the matrix but not when bonded strongly. Weakly bonded fillers result in consistently higher $K_{I_{ss}}$ values compared to strongly bonded counterparts. A particle size of 35 μm appears to be the optimum at the chosen V_f . The $K_{I_{ss}}$ of two inter-mixed particle sizes (each of 5% V_f) is bounded by the $K_{I_{ss}}$ values of the composite with corresponding single particle size. Fracture surface micromerements show that fracture toughness cannot be correlated with average fracture surface roughness Ra as in neat polymers. Therefore, a model for calculating fracture induced roughness, Ra_f , a component of Ra representative of the fracture process, is proposed. A linear relationship between macroscopically measured fracture toughness $K_{I_{ss}}$ and microstructure dependent quantity Ra_f/\sqrt{D} is demonstrated.

Crack front deflection, attraction, twisting and blunting are some of the micromechanisms responsible for the observed fracture characteristics in particle reinforced composites. To gain fundamental insight into the problem, optical and boundary element studies on how a growing crack front interacts with an isolated inclusion or an inclusion-cluster are carried out. A symmetric Galerkin boundary element method is implemented in conjunction with quarter-point crack tip element and maximum tangential stress fracture criteria for simulating crack growth. Both experiments and computations support

the observation that weakly bonded inclusions in the matrix attract a propagating crack front while strongly bonded inclusions repel the same. The former increases the crack path tortuosity and hence increases dynamic fracture toughness.

ACKNOWLEDGMENTS

I would like to thank my research advisor Dr. Hareesh V. Tippur for rendering constant guidance and motivation throughout my PhD program. I also thank him for showing complete trust in my abilities to work in an experimental environment. I am immensely grateful to him for introducing me to the exciting fields of optical methods and fracture mechanics and for giving me an opportunity to teach an undergraduate course. I would also like to express my gratitude to Dr. Anh -Vu Phan for helping me in the numerical field of boundary element method. His timely guidance and valuable inputs helped me immensely in the research. Special thanks to Dr. Jeffrey C. Suhling for teaching the courses which greatly helped me in understanding my research problem. I thank Dr. Ruel A. Overfelt and Dr. Winfred A. Foster for serving on my committee. Dr. Bart Prorok's input to the dissertation as an external reader is also appreciated. Financial support from National Science Foundation (CMS-9912066) and Army Research Office (W911NF-04-1-0257) which enabled this research is gratefully acknowledged.

I would like to acknowledge my friends in Auburn with whom I spent exciting and memorable years. Particularly, Kashyap's support and encouragement made my stay at Auburn pleasant and enthusiastic. The lively lab environment in the presence of Madhu, Mike, Piyush and Taylor made working in late hours an enjoyable experience. Finally, I would like to acknowledge the love and inspiration of my parents, brother and sister which has always boosted my morale. And last, but not the least, it is the love and patience of my wife Gouri which enabled me to reach to this joyous end. I dedicate this work to her.

TABLE OF CONTENTS

LIST OF FIGURES		xii
LIST OF TABLES		xix
1	INTRODUCTION	1
1.1	Motivation and Literature Review	9
1.2	Objectives	17
1.3	Organization of Dissertation	18
2	EXPERIMENTAL AND NUMERICAL METHODS USED	21
2.1	Experimental method: Coherent Gradient Sensing	21
2.1.1	Experimental set-up: CGS	22
2.1.2	Working principle and governing equation of CGS	25
2.1.3	Crack velocity and stress intensity factor evaluation	30
2.2	Numerical Methods: Symmetric-Galerkin BEM	33
2.2.1	Boundary Element Method: Formulation	36
2.2.2	Symmetric Galerkin Boundary Element Method (SGBEM)	40
3	MATERIAL PREPARATION AND CHARACTERIZATION	48
3.1	Material preparation	48
3.2	Specimen surface preparation	50
3.3	Material Characterization	52
3.3.1	Quantitative microscopy	52
3.4	Material properties: Quasi-static loading	55
3.5	Material properties: pulse-echo measurements	59
4	DYNAMIC FRACTURE OF PARTICULATE COMPOSITES	62
4.1	Experimental Details	62
4.1.1	Weakly bonded particles	63
4.1.2	strongly bonded particles	65
4.1.3	Mixed weakly bonded particles	66
4.2	Experimental repeatability	67
4.3	Particle size effect	70
4.3.1	Weakly bonded (uncoated) particles	70
4.3.2	Strongly bonded (silane treated) particles	76
4.4	Filler-matrix adhesion strength effect	79
4.5	Particle size (bimodality) distribution effect	81

4.6	Comparison between static and dynamic fracture toughness	85
4.7	Potential difference in toughening mechanisms	90
5	MICROMEASUREMENTS	92
5.1	Fracture surface micrographs: Qualitative observation	92
5.2	Quantitative investigation of fractured surfaces	97
5.2.1	Particle size and filler-matrix adhesion effect	100
5.2.2	Potential toughening mechanisms and surface roughness	103
5.3	Linking macro- and micro-measurements	108
5.3.1	Particle related roughness	109
5.3.2	Fracture toughness - Surface roughness relation excluding particle-size effect	113
5.3.3	Fracture toughness - Surface roughness correlation	115
6	EXPERIMENTAL INVESTIGATION OF CRACK-PARTICLE INTERACTIONS	120
6.1	Material preparation and specimen geometry	120
6.2	Fringe analysis	123
6.2.1	Weakly bonded inclusion ($e = 0$)	123
6.2.2	Strongly bonded inclusion ($e = 0$)	129
6.2.3	Weakly and strongly bonded inclusions ($e = d/2$)	132
6.3	Effect of crack-inclusion interaction on crack velocity	133
6.3.1	Effect of inclusion eccentricity	134
6.3.2	Effect of inclusion-matrix adhesion strength	136
6.4	Effect of crack-inclusion interaction on SIF histories	139
6.4.1	Effect of inclusion eccentricity	140
6.4.2	Effect of inclusion-matrix adhesion strength	142
7	CRACK-PARTICLE INTERACTION STUDY USING BEM	145
7.1	Model geometry	145
7.2	Benchmarking and mesh convergence	146
7.3	Effect of inclusion-matrix adhesion on crack growth	150
7.4	Effect of delamination on fracture parameters	152
7.5	Parametric study of strongly bonded inclusion and inclusion clusters	154
7.5.1	Crack tip shielding	156
7.5.2	Particle eccentricity effect	158
7.5.3	Particle size effect	162
7.5.4	Crack propagation through particle clusters	165
8	CONCLUSIONS	173
	BIBLIOGRAPHY	181
	APPENDICES	189

A LEAST-SQUARES ANALYSIS OF OPTICAL DATA	189
B SGBEM INPUT DATA FILE: DETAILS	196

LIST OF FIGURES

1.1	Application of particle filled polymers: underfill material in electronic packaging.	2
1.2	Applications of particle filled polymer: microballoons-filled epoxy in naval applications: offshore platforms, buoys, recreation boats etc.	3
1.3	Application of particle filled polymers in bio-medical engineering: Tooth fillings and implants.	4
1.4	Application of particle filled polymers: Self-healing material.	5
1.5	Functionally graded material showing variation in volume fraction, elastic properties and failure characteristics across the width of the sheet.	5
2.1	Schematic representing the experimental set-up for reflection Coherent Gradient Sensing method.	22
2.2	Experimental set-up for Coherent Gradient Sensing shearing interferometry.	23
2.3	Diffraction of a collimated beam through two parallel high density Ronchi gratings.	25
2.4	CGS interferogram recorded during dynamic experiment; t represents post impact time duration, Fringe orders N are identified in the interferogram.	31
2.5	Reciprocal nature of elastic solid; Two systems in equilibrium (real and complementary) under different loading.	36
2.6	A unit point force at P , represented by a Dirac delta function is considered as a complementary body force.	38
2.7	Unit point force applied on source point P to represent Kelvin's fundamental solution at field point Q	39
2.8	An elastic body containing crack.	40
2.9	Applying BIE and HBIE on domain boundaries.	42

2.10	1-D element: (a) standard mid-node element, (b) quarter-point element.	43
2.11	Shape functions used in SGBEM formulation. Dotted lines and solid line plots show the shape functions correspond to standard quarter-point element and modified quarter point element (MQP).	44
2.12	Deformed and undeformed crack, (a) crack-tip element showing crack opening displacement, (b) tangential stress near the crack-tip.	45
3.1	Material Preparation, (a) filler-matrix mixture pouring into the mold, (b) 10% V_f particle filled matrix monolithic specimen, (c) two different particle sizes (each of 5% V_f) filled epoxy specimen. ($S = 152$ mm, $W = 42$ mm, $B = 8$ mm, $a = 10$ mm)	51
3.2	Optical micrographs of polished surfaces: (a)-(i) 35 μm uncoated particles, (ii) 35 μm coated particles, (iii) 11 μm uncoated particles, (ii) 11 μm coated particles, (b) Schematic for quantitative analysis of micrographs shown in (a) using lineal method.	53
3.3	Stress-strain behavior under quasi-static loading condition in spherical glass particle filled epoxy, $V_f = 0.1$, (a) uncoated particles (b) silane treated particles.	56
3.4	Particle size and filler-matrix adhesion effect on failure properties of particle filled epoxy under quasi-static loading condition, $V_f = 0.1$, (a) Failure stress variation with particle size (b) Failure strain variation with particle size.	58
4.1	Selected fringe pattern representing surface slope contours of $\delta w / \delta x$ for glass-filled epoxy specimens with weakly bonded filler, (a) 11 μm particles, (b) 35 μm particles and (c) 203 μm . Indicated time corresponds to the instants after impact.	64
4.2	Selected fringe pattern representing surface slope contours of $\delta w / \delta x$ for glass-filled epoxy specimens with strongly bonded fillers, (a) 11 μm particles, (b) 35 μm particles and (c) 203 μm . Indicated time corresponds to the instants after impact.	65
4.3	Selected fringe patterns representing surface slope contours of $\delta w / \delta x$ for glass-filled epoxy specimens with (a) 35+203 μm fillers and (b) 11+203 μm fillers. Two different particle sizes are mixed in 5% V_f each. Legends correspond to the time instants after impact.	67

4.4	Crack velocity history (a), and stress intensity factor histories for two identical specimens with $35\ \mu\text{m}$ uncoated filler particles demonstrating repeatability of experimental measurements.	69
4.5	Crack velocity histories (a), and stress intensity factor histories (b) for different glass-filled epoxy specimens with weakly bonded (uncoated) particles.	72
4.6	Stress intensity factor history for neat epoxy.	73
4.7	Particle size effect on steady state fracture toughness of glass-filled epoxy.	75
4.8	Variation in steady state velocity and fracture toughness with particle size in glass-filled epoxy with weakly bonded fillers.	76
4.9	Crack velocity histories (a), and stress intensity factor histories (b) for different glass-filled epoxy specimens with strongly bonded (silane treated) particles.	78
4.10	Filler-matrix adhesion effect on fracture behavior; Crack velocity history (a), and stress intensity factor histories (b) for $35\ \mu\text{m}$ and $11\ \mu\text{m}$ (coated and uncoated) particles filled epoxy, $V_f = 0.1$	80
4.11	Crack velocity history (a), and stress intensity factor histories (b) in specimen with $35 + 203\ \mu\text{m}$ mixed fillers (total $V_f = 10\%$. For comparison corresponding histories in specimens with single particle size are also shown.	83
4.12	Steady-state fracture toughness and steady-state velocity variation with constituent filler percentage in 10% glass-filled epoxy specimens.	84
4.13	Quasi-statically loaded Single edge notch bend specimen ($S = 90\ \text{mm}$, $W = 30\ \text{mm}$, $B = 8\ \text{mm}$).	85
4.14	Particle size effect on fracture toughness; (a) Variation in quasi-static crack initiation toughness with particle size, (b) Effect of loading rate (quasi-static and dynamic) on fracture toughness.	88
5.1	Schematic representing a growing crack in composite and steady-state region where micromasurements are performed.	93
5.2	SEM micrographs: (a) $203\ \mu\text{m}$ uncoated particles, (b) $203\ \mu\text{m}$ coated particles, (c) $35\ \mu\text{m}$ uncoated particles, (d) $35\ \mu\text{m}$ coated particles, (e) $11\ \mu\text{m}$ uncoated particles, (f) $203\ \mu\text{m}$ coated particles. Solid arrow shows crack propagation direction and broken arrow shows "Tail lines".	94

5.3	SEM micrographs of fractured surfaces, (a) shows 35 + 203 μm diffuse interface, (b) and (c) show fractured surfaces of 203 μm and 35 μm monolithic materials, respectively.	96
5.4	Representative fracture surface profiles for different glass-filled epoxy specimens. (a) particle size effect and (b) filler-matrix adhesion effect.	98
5.5	Steady-state fracture toughness variation as a function of overall surface roughness for different particle sizes.	101
5.6	Schematic showing potential crack growth pattern: (a) weakly bonded particles and (b) strongly bonded particles.	104
5.7	Schematic showing different crack front twisting mechanisms in case of: (a) weakly bonded particles and (b) strongly bonded particles. Formation of tail-lines from weakly bonded particles and particle foot-prints (a) and from the matrix in the vicinity of strongly bonded particles (b) are shown in micrographs of 203 μm particles filled epoxy.	106
5.8	Schematic representation of the effect of embedded particle/particle foot-prints on fracture surface morphology: (a) fracture surface profile excluding embedded particles/particle foot prints, (b) isolated surface profile due to embedded particles/particle foot-prints and (c) fracture surface profile in the presence of embedded particles/particle foot-prints.	109
5.9	Schematic representation of fracture surface: (a) in the presence of particle foot-prints, (b) in the presence of particles, (c) in the presence of particles and particle foot-prints.	110
5.10	Fracture toughness-surface roughness dependence excluding particle size effect.	114
5.11	Steady-state fracture toughness variation with fracture induced roughness and particle size of glass-filled epoxy composite.	115
6.1	Epoxy specimen preparation with cylindrical glass inclusion located in front of initial crack-tip. Inclusion location is defined by p , the initial distance of the inclusion center from the specimen edge which contains the crack and the eccentricity e , the distance between the inclusion center and the line-of-symmetry. $p = 20 mm$, $d = 4 mm$, $S = 140 mm$, $W = 42 mm$, $B = 8 mm$, $a = 5 mm$	121
6.2	Sharp crack tip created by forcing a razor blade into the notch root. . . .	122

6.3	Selected fringe pattern representing surface slope contours ($\delta w/\delta x$) for epoxy specimen with weakly bonded inclusion located symmetrically ($e = 0$) with respect to the initial crack-tip. (Distance between the crack and the vertical line is 10 <i>mm</i> .)	124
6.4	Stress waves due to crack-inclusion interaction when the inclusion is weakly bonded. Trace of kinks in fringes suggest arrest and reinitiation waves. . .	125
6.5	Images of fractured specimens showing differences in crack-inclusion interaction: (a) symmetrically located ($e = 0$) weakly bonded inclusion, (b) symmetrically located ($e = 0$) strongly bonded inclusion, (c) tangentially located ($e = d/2$) weakly bonded inclusion, (d) tangentially located ($e = d/2$) strongly bonded inclusion. (Arrow indicates crack growth direction.)	127
6.6	Selected fringe pattern representing surface slope contours ($\delta w/\delta x$) for specimen with strongly bonded inclusion located symmetrically ($e = 0$) with respect to the initial crack-tip. (Vertical line is at 10 <i>mm</i> from the crack line.)	130
6.7	Stress waves due to crack-inclusion interaction when the inclusion is strongly bonded. Trace of kinks in fringes suggest arrest and reinitiation waves. . .	131
6.8	Selected fringe pattern representing surface slope contours of $\delta w/\delta x$ for specimen with tangentially located inclusion with respect to initial crack orientation ($e = d/2$). Images show crack-inclusion interaction for the specimen with, (a) Weakly and (b) Strongly bonded inclusion.	132
6.9	Crack velocity histories in specimens embedded with (a) weakly bonded and (b) strongly bonded cylindrical inclusions.	135
6.10	Crack velocity histories in epoxy specimen embedded with inclusions, (a) symmetrically located ($e = 0$) in front of crack-tip, (b) tangentially located ($e = d/2$) to initial crack orientation.	137
6.11	Stress intensity factor histories in specimen embedded with (a) weakly bonded and (b) strongly bonded cylindrical inclusions.	141
6.12	Stress intensity factor histories in specimen embedded with cylindrical inclusions, (a) symmetrically located ($e = 0$) in front of the crack-tip, (b) tangentially located ($e = d/2$) to initial crack orientation.	143

7.1	(a) Comparison between analytical results and SGBEM results for various boundary element lengths, (b) Crack propagation for mixed-mode loading; crack trajectory from BEM is superimposed on experimentally obtained crack path for an eccentrically applied load at the distance $L/4$ from the line-of-symmetry.	147
7.2	Validation of ERR calculation from SGBEM in the presence of secondary phase filler, (a) Problem geometry and loading configuration, (b) Variation of nondimensional ERR for various $E_p/E_m, \nu_p = 0.17, \nu_m = 0.33$	149
7.3	Modeling role of interfacial strength on Crack-particle interaction, (a) Specimen configuration, (b) The angle, α , represents the part of inclusion delaminated from matrix, (c) Crack paths for weakly and strongly bonded inclusions: Crack attracted towards delaminated inclusion-matrix interface ($\alpha = 180^\circ$), and deflected away from inclusion when it is strongly bonded to matrix.	151
7.4	Effects of inclusion-matrix delamination on (a) Energy release rate (b) Mode-mixity.	153
7.5	Crack tip shielding by a rigid inclusion in front of a mode-I crack, (a) Loading configuration, (b) Comparison between SIF variations in the presence and absence of inclusion.	155
7.6	Crack tip shielding and amplification effects due to a pair of symmetrically situated inclusions in the crack path.	157
7.7	The effect of eccentrically situated rigid inclusions relative to the initial crack on crack deflection and energy release rate (ERR), (a) Crack deflection with varying inclusion eccentricity; the inclusion location is shown with respect to initial crack orientation, (b) Variation of maximum crack deflection from the line-of-symmetry with inclusion eccentricity for inclusion diameter $d = W/10$, (c) Variation in nondimensional ERR with a/W , (d) Crack propagation around a rigid inclusion from SGBEM simulation.	159
7.8	Variation of G/G_0 with a/W in the presence of eccentrically located pair of inclusions showing the combined effect of shielding and inclusion eccentricity (Note: Eccentricity of the inclusion-pair is defined for the nearest inclusion center relative to the crack).	161

7.9 Role of particle size on crack deflection and ERR: (a) Crack deflection in the presence of inclusions of various diameters for a fixed eccentricity $e = d/2$, (b) Variation of maximum crack deflection from the line-of-symmetry with inclusion diameter, (c) Variation in nondimensional ERR with a/W 163

7.10 Interaction between a crack and a particle cluster with a pentagonal arrangement. Cluster orientation is defined in terms of θ . Crack path in the presence of particle cluster is shown. 165

7.11 Crack growth through a particle cluster is, (a) Crack deflection in the presence of particle cluster of various orientations, (b) Variation of ERR with a/W showing the effect of cluster orientation. 167

7.12 Interaction of a crack with a particle cluster to study the effect of volume fraction, (a) Crack deflection for various volume ratios; volume ratio is changed by expanding the cluster radius R shown in Fig. 7.10, (b) Variation of energy release rate with crack growth. 170

B.1 A cracked geometry with an inclusion. Node numbers are assigned to run the crack growth simulation using SGBEM. Outer boundary is meshed counter-clockwise whereas the meshing on inclusion-matrix interface is clockwise. Quarter point element is defined at the crack-tip. Crack leg is modeled with triple node. Specimen corners contain double nodes. 198

LIST OF TABLES

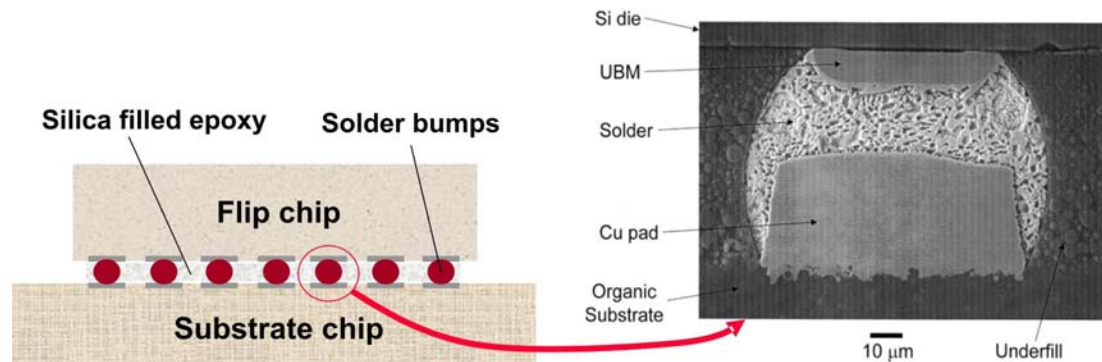
3.1	Quantitative image analysis on polished surface	55
3.2	Elastic and failure properties (quasi-static) of glass-filled epoxy particulate composite (weakly and strongly bonded particles at $V_f = 0.1$).	59
3.3	Material properties (dynamic) of weakly bonded (uncoated) and strongly bonded (silane coated) glass fillers in epoxy matrix, $V_f = 0.1$ (* uncoated particles, ** silane treated particles, + mixture of two different particle sizes).	60
4.1	Crack growth parameters for glass-filled epoxy with weakly bonded filler ($V_f=0.1$)	71
4.2	Crack growth parameters for glass-filled epoxy with strongly bonded filler ($V_f=0.1$)	77
4.3	Crack growth parameters for glass-filled epoxy with single size filler particles and bimaterial mixtures with diffuse interface ($V_f=0.1$)	82
4.4	Crack growth parameters for uncoated (weakly bonded) glass-filled epoxy ($V_f=0.1$) showing loading rate dependence as well as particle size effect on fracture parameters	86
4.5	Crack growth parameters for strongly bonded (silane treated) glass-filled epoxy ($V_f=0.1$) showing loading rate dependence as well as particle size effect on fracture parameters	87
5.1	Roughness parameters for weakly and strongly bonded glass fillers in epoxy matrix, $V_f = 0.1$. * denotes strongly bonded particles.	100
5.2	Fracture and Roughness parameters for different particle sizes and filler-matrix strengths at $V_f = 0.1$. (subscript <i>ss</i> denotes “steady state”), * denotes data from Ref.[1]	102

CHAPTER 1

INTRODUCTION

Polymer based particulate composites are mixtures of two or more constituent phases. They are known to offer many desirable thermo-mechanical properties at a relatively low cost and are hence used in a variety of engineering applications - as light-weight structural composites, as electrically conducting adhesives, as underfill materials in electronic packages, as syntactic foams for civilian and marine structures, as surface coats/paints for thermal insulation, as self-healing materials, to name a few. The macroscopic isotropy of particulate composites, unlike conventional fiber reinforced or woven composites, often adds to simplicity of mechanical design. From the perspective of mechanical and/or structural applications, the addition of stiff filler particles to the polymer matrix generally increases the overall stiffness of the composite while improving creep resistance. The accompanying reduction in the coefficient of thermal expansion, depending upon the type of the filler used, could be an added advantage also. The properties of constituent phases, filler volume fraction, filler particle size and shape, particle size distribution, and filler-matrix interfacial strength, are some of the important factors which influence macroscopic properties in general and failure properties such as tensile strength and fracture toughness in particular. Hence, a systematic study of the interplay between these factors is essential for understanding the mechanics of particulate composites.

In the following, a brief description of the aforementioned applications is given. As mentioned earlier, particle filled polymers are widely used in the electronic industry as



Ref: Darrel R. Frear, 51(3), 1999, JOM.

Figure 1.1: Application of particle filled polymers: underfill material in electronic packaging.

underfill materials. The procedure involves dispensing a controlled amount of silica-filled anhydride resin polymer (epoxy) into the space between a flip-chip and its substrate (see, Fig. 1.1) to help interlock the chip to the substrate [1]. The fillers provide the required stiffness and strength to the polymer mixture whereas the resin bonds with the die and the substrate. The underfill material decreases the thermal expansion and hence, stress gradients between the chip and the substrate. This in turn decreases the possibility of mechanical failure of solder interconnects.

Another application of particulate composites is electrically conducting polymeric adhesives where metallic particles are used as fillers. Depending upon the filler concentration these composites can be used as insulating materials or conductors having linear or nonlinear electrical behavior[2]. At low filler volume fractions the composite acts as an insulator. At an intermediate filler concentration, the electrons jump across the conductive particles located in the close proximity. This gives a nonlinear relationship between voltage and current. On the other hand a linear voltage-current relation is achieved at higher filler volume fractions when the particles are in contact with each other.

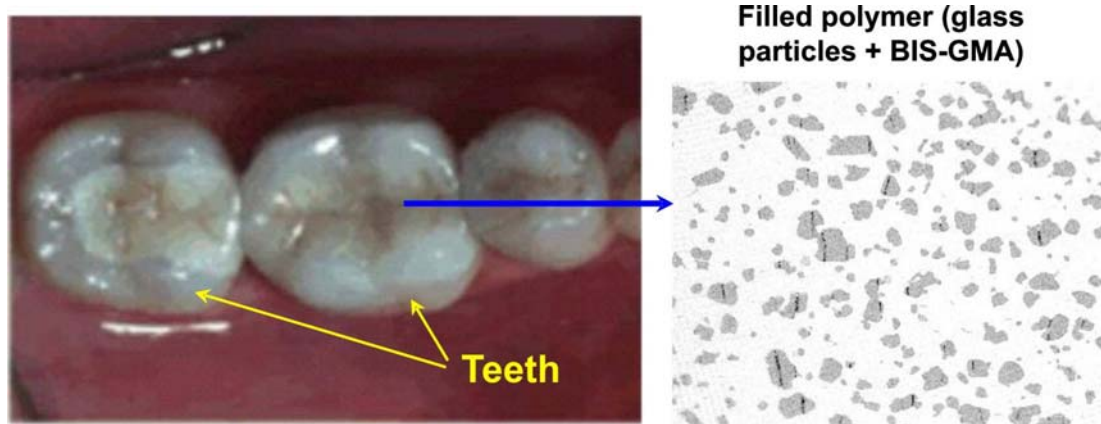


Ref: http://www.naval-technology.com/contractors/advanced_materials/syntech.

Figure 1.2: Applications of particle filled polymer: microballoons-filled epoxy in naval applications: offshore platforms, buoys, recreation boats etc.

The suspended fine particles in surface coats and paints is another well known application of particulate composites. Structural surface coating is used for enhancing abrasion, corrosion and erosion resistance. For example, nano fillers are used in the automotive industry to improve chemical and scratch resistance of surface coating[3]. The suspended nanoparticles are also helpful for producing extremely thin coats and promote better adherence to surfaces resulting in reduced cracking, chipping and scratching.

The filled polymers containing thin walled hallow microballons, commonly referred to as syntactic foams, belong to another widely used class of particulate composites. These have many applications in aerospace and marine applications due to their light-weight characteristics[4, 5, 6]. Syntactic foams with carbon microballoons are useful in aerospace applications as heat shields while the ones containing glass microballoons are used in boats, marine platforms and buoys (see Fig.1.2). Due to their ability to absorb impact energy, syntactic foams have other military applications as well.

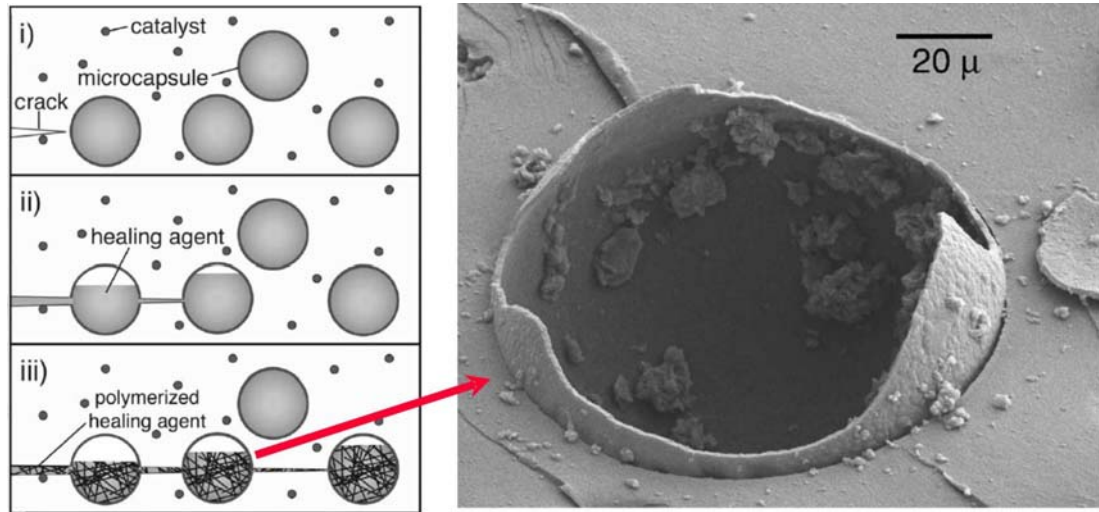


Ref: http://www.doctorspiller.com/dental_materials.htm.

Figure 1.3: Application of particle filled polymers in bio-medical engineering: Tooth fillings and implants.

Biomedical industries widely utilize particulate composites also. Dental implants, artificial bones and bone cements are among the applications of particle filled polymers in biomedical engineering[7]. The BIS-GMA (Bisphenol A Diglycidyl Methacrylate), a derivative of methylmethacrylate or urethane dimethacrylate resin, is used as a cavity-filler matrix material in dental implants (see Fig.1.3). The matrix is embedded with 20 nm to $60\text{ }\mu\text{m}$ sized filler particles in 70 – 80% volume fraction. Usually, crystalline quartz and/or lithium glass ceramics, calcium silicate, glass beads and calcium fluoride are used as filler particles. Similarly, hydroxyapatite particles of $0.5\text{ – }20\text{ }\mu\text{m}$ in size are used to reinforce polyethylene matrix to develop biocompatible artificial bone cement. Depending upon the nature of the bone being replaced and the physiological loading, filler volume fraction is chosen to achieve desirable stiffness, tensile strength and fracture toughness.

Recently, there is a great deal of interest in the development of self-healing materials. These are inspired by biological systems which initiate healing process following



Ref: Kessler et. al., 34 (2003), Composites Part-A.

Figure 1.4: Application of particle filled polymers: Self-healing material.

damage. The self-healing response is typically produced by dispersing resin encapsulated microballoons into a matrix containing a catalyst that promotes polymerization[8]. When a propagating crack ruptures a thin walled microcapsule, the released healing agent flows into the crack by capillary action (see Fig.1.4). Subsequently, self-healing agent reacts chemically with the catalyst present in the matrix and bonds the crack faces. Upto $\sim 90\%$ strength recovery in the healed polymer relative to the virgin material has been reported[9].

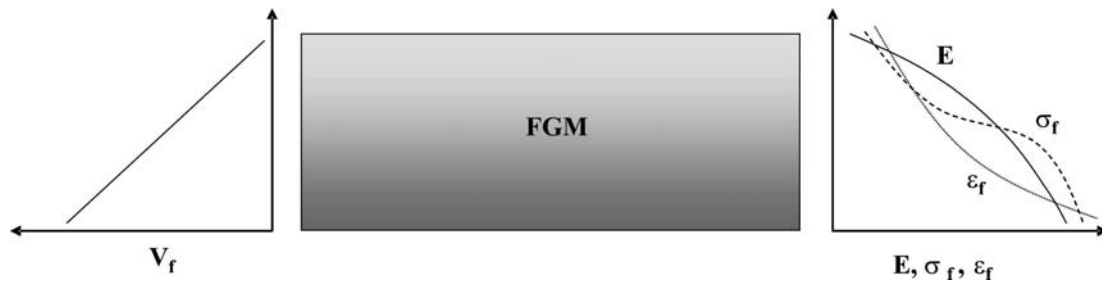


Figure 1.5: Functionally graded material showing variation in volume fraction, elastic properties and failure characteristics across the width of the sheet.

Conventional composites and layered materials suffer from the development of large stresses in thermo-mechanical loading environments due to material property jumps across discrete interfaces. Resulting microscopic or macroscopic interfacial failure due to design, manufacturing and/or service related issues are inherent drawbacks of these material systems. To overcome these problems in critical loading environments a new class of materials called *functionally graded materials* (FGM) having a gradual variation of material properties is proposed (see Fig.1.5). In these, spatial variations of properties are generally achieved by varying composition and/or microstructure in a controlled fashion using filler particles. In the past few years, such material systems have been produced using a variety of techniques such as selective UV irradiation, spin and gravity casting, differential sedimentation, extrusion, etc. Using the technique of gravity casting, glass-filled epoxy as well as epoxy based syntactic foams having monotonic and bilinear variations of volume fractions have been successfully produced at Auburn[10, 11, 12].

In all the above applications of particulate polymer composites in engineering, prominent issues from the perspective of mechanical reliability are stiffness and failure characteristics. Fracture mechanics is widely used to characterize failure behavior of engineering materials in the presence of cracks and defects. In this approach fracture toughness is defined as a measure of material resistance to growth of a pre-existing crack/ flaw. In a homogeneous material, fracture characteristics vary with physical and mechanical properties of the material as well as with loading pattern. There are additional parameters which play vital role in the fracture behavior of a heterogeneous material besides properties of its constituent phases. The improved failure characteristics of a multiphase material results from a complex interplay of various toughening

mechanisms due to microscopic material discontinuities. Second phase inhomogeneities dispersed in a brittle matrix act as obstacles by impeding a moving crack front thereby increasing fracture toughness either by increasing the length of the crack front and/or by blunting. Crack deflection, bowing, and crack blunting are common phenomena in the presence of second phase material in the vicinity of a propagating crack front causing reduction in stress intensity. Filler particle size, size distribution, shape and volume fraction, as well as properties of constituent phases, crack-particle interaction and filler-matrix interface strength are some of the parameters influencing toughening mechanisms and hence fracture properties.

Investigation of the failure behavior of materials using post-mortem analysis of fractured surfaces is quite common in engineering. It is recognized that fracture parameters leave an imprint of various failure mechanisms when fracture surfaces are created. Thus, fracture surface morphology can be used to decipher mechanics of fracture by performing micromerements. In conventional homogeneous materials it is seen that crack velocity and stress intensity factors have considerable effect on microscopic features such as surface roughness, average slope of the surface profile, etc. It is also widely recognized that the increase in crack velocity or fracture toughness increases surface roughness in conventional monolithic materials. However, an understanding of surface parameters becomes complicated when secondary phases of various size, shape and volume fraction come into the picture in heterogeneous materials. Mechanisms such as crack deflection, twisting, microcracking, bridging or crack tip blunting, dominate failure processes in heterogeneous materials and have an immense effect on energy dissipation and hence

fracture surface morphology. An investigation into macro and micro scale fracture responses using controlled experimental and analytical/numerical approaches would be needed to shed light on the fracture process in heterogeneous materials.

Performing analytical and experimental investigation of each of the previously mentioned phenomena is rather complicated. The need to understand and link failures at vastly different scales makes the task even more challenging. Numerical investigations alone may not be feasible due to several undefined parameters such as material characteristics at filler-matrix interface besides all the aforementioned difficulties. Finite element analyses utilizing fracture theories, spring-release methods along with remeshing and cohesive element strategies are relatively common in simulating fracture behavior. Alternatively, Boundary Element Methods (BEM) can be used to simulate crack growth since the method needs only boundaries to be discretized. However, this simplicity is accompanied by a relatively complex formulation involving singular integrals. This method is still at a developing stage, especially for performing simulations under dynamic loading conditions and for simulating nonlinear material behavior.

As can be seen from the above description, the choice of particle size, shape, size distribution and volume fraction depends upon the application on hand. A chosen microstructure can enhance the required material property, but may affect adversely other functionalities. In the following, a literature review of the role of microstructure on mechanical behavior of particle-filled polymers is provided.

1.1 Motivation and Literature Review

The effects of particle size and filler-matrix adhesion strength on failure characteristics, mostly for the case of static loading, have been addressed in previous studies. Spanoudakis and Young[13, 14] have shown that critical stress intensity factor (K_{Ic}) decreases with an increase in particle size at lower volume fractions, while the critical energy release rate (G_{Ic}) drops with increasing particle size to a minimum value at 47 μm particle diameter. They suggested that crack pinning followed by particle-matrix interface failure and crack tip blunting due to the break down of particle-matrix interfaces are the primary toughening mechanisms. They have also concluded that the values of K_{Ic} are not strongly dependent on the strength of adhesion but poor bonding causes an increase in energy release rate due to the reduction of Young's modulus. Moloney *et al.*[15] have investigated 40% volume fraction silica-filled epoxy with particle size in the range of 60 μm to 300 μm . Negligible effect of particle size is observed on fracture toughness. However, they have noticed that weaker matrix-filler interface results in higher fracture toughness due to possible crack tip blunting. Nakamura *et al.*[16] investigated particle size effect on fracture properties for 35% volume fraction for 2 μm to 30 μm spherical silica-filled epoxy. The decrease in K_{Ic} with a decrease in particle size was noticed, and was attributed to crack deflection, interfacial debonding and particle fracture. They have also noticed that there is no effect of bonding strength on K_{Ic} . In a similar investigation[17] on silica-filled epoxy with particle size range of 2 μm to 42 μm (55% and 64% weight fraction), both fracture toughness and energy released rate is reported to have increased with increase in particle size. Static fracture tests based on

3-point bend specimens show higher toughness when compared to double torsion and impact fracture tests.

Previous attempts on quantifying microstructural effects on failure characteristics have generally been made under quasi-static loading conditions and dynamic responses are largely unknown at the moment. Further, none of the available dynamic results provide complete pre- and post- crack initiation behaviors. Also, conclusions drawn contain significant differences. While some have reported an increase in K_{Ic} as particle size decreases, others report either a decreasing trend or no effect at all. Similar differences can be noticed in case of filler-matrix adhesion effect when some investigators have noticed no effect on K_{Ic} while others have reported decreasing K_{Ic} with increasing filler-matrix adhesion strength. Hence, it is necessary to investigate particle size and filler-matrix adhesion effect on fracture toughness, particularly over a relatively large range of particle sizes.

Layered material systems which occur in a wide range of applications from microelectronics to aircraft engines, could benefit from tailoring material microstructure. In general interfaces in layered materials are discrete and are susceptible to interfacial failure. Among the various failure scenarios, two situations are widely recognized under dominant tensile loading conditions. First, when the interface is strong relative to the individual components of the layered system, cracks tend to kink into the weaker material and grow nearly parallel to the interface[18]. In this situation fracture properties of the weaker material becomes the limiting value for deciding overall fracture toughness of the material system. The second situation corresponds to a relatively weaker interface wherein crack initiation and propagation occurs along the interface. Here, the interfacial

characteristics control overall fracture parameters. Most works to date in these categories deal with elastically dissimilar interfaces characterized by an oscillatory inverse of \sqrt{r} singularity [19]. Graded interfaces can aid in mitigating deficiencies of discrete interfaces where a sudden jump in material characteristics are often at the root of the problem[10, 11, 20]. Diffuse bimaterial interfaces can be considered as a subset of layered material systems with nonhomogeneous interfacial regions within which material characteristics transition from that of one constituent to the other in a predetermined fashion. In practice, such diffuse or graded interfacial regions are realized by microstructurally varying the relative proportions of the two constituents in the interfacial region. Plasma spraying, screw extrusion, differential sedimentation, sintering, gravity and centrifugal castings, etc. are some of the common methods used for producing graded materials and interfaces[21, 22, 23]. The microstructural variations influence not only elastic characteristics but failure behavior as well. However, focus in the past has been either on elastic mismatch or combinations of elastic and failure mismatches[11] and the role of microstructure in governing the fracture behavior of bimaterials has not been fully investigated, which is also among the motivations of conducting this research.

Understanding fracture mechanics of discrete and diffuse interfaces is relevant in other situations as well. Filler sizes often show variations in cementitious materials when constituents from multiple sources are used or curing conditions are varied during construction. This is a common occurrence in this class of materials since the aggregate sizes are not tightly controlled and vary over a range[24, 25, 26]. Another situation where microstructurally dissimilar interfaces occur include heat affected zones having grain size/shape variations. Geological formations across fault lines correspond to a

large scale example of interfaces with microstructural variations. Lastly, there exists a strong interest towards functionalizing interfaces with nanophases to enhance failure characteristics. Fracture mechanics modeling of any of these scenarios requires an understanding of the role microstructure plays at an interface of a discrete or diffuse variety. Particularly, questions relevant to (a) whether particle size bimodality would enhance or diminish interfacial fracture toughness and (b) crack path selection in discrete interfaces, must be explored.

It is widely recognized that variation in fracture behavior due to microstructural changes is manifested on fracture surface morphology. Therefore, microscopic observation of fracture surfaces can give an insight into toughening mechanisms involved during fracture process. The effects of crack velocity and/or stress intensity factor on surface roughness has been studied in the past in monolithic materials. Cottrell's [27] work on PMMA (poly methyl methacrylate) has shown that surface roughness increases with crack velocity. Ravi-chandar and Knauss[28] have also shown consistent increase in surface roughness with stress intensity factor for Homilite-100. Arakawa *et al.*[29, 30] have studied the effects of dynamic stress intensity factor on various roughness parameters for PMMA, Homilite-100 and Epoxy (Araldite-B). They have reported an increase in surface roughness with crack velocity. However, they have found that crack velocities to be not uniquely related to surface roughness due to differences stemming from crack accelerations and decelerations. They have identified that surface roughness correlates better with $R^*\dot{a}$ (\dot{a} being crack velocity, $R^*\dot{a}$ being the specific crack extension resistance) than other fracture parameters. Furthermore, they have also shown a qualitative relation between *RMS* roughness value with crack velocity and dynamic stress intensity

factor with some discrepancies. Sharon *et al.*[31] have measured energy flux into the tip of a dynamically moving crack and the total surface area created due to microbranching in PMMA. They have demonstrated that the total surface area, resulting from the generation of microbranches above the critical crack velocity, increases linearly with energy flux. Among the studies on heterogeneous materials, a significant body of literature exists on cementitious materials. Tandon and Faber[24] have studied the effect of loading rate on fracture behavior of cement paste, mortar and concrete. They show a qualitative relationship between fracture toughness and surface roughness by noting that with an increase in loading rate both fracture toughness and surface roughness increase. Using fractal dimensions to correlate fracture and surface roughness parameters in concrete has been suggested by Issa *et al.*[25]. They have used aggregates of different maximum sizes varying from 10 *mm* to 70 *mm* in their study. They have been able to show that *modified* fracture energy and fractal dimension could be fitted with similar logarithmic functions. Further a linear relation between fractal dimension and modified fracture energy has been suggested. However, this relation is found to depend on specimen geometry because the fractal dimension and the modified fracture energy depend on specimen size. Abell and Lange[26] have taken a different approach to relate fracture and roughness parameters. They have used confocal laser microscopy and video density technique to characterize surface geometry of cementitious material. They have calculated toughening ratio in the presence of aggregates by using crack deflection model proposed by Faber and Evans[32, 33]. A relationship between toughening ratio and roughness number has

been shown by fitting data for linear elastic materials. They report that fracture behavior of cementitious materials increasingly deviates from linear elastic behavior as surface roughness increases.

Among the few works on non-cementitious materials with microsize fillers, Davidson[34] has reported experimental results of fracture toughness and roughness parameters for silicon carbide reinforced aluminum alloy particulate composite ($V_f = 15\%$ and 25%). He has analyzed various fracture parameters like surface roughness ratio coefficient, profile roughness factor coefficient and fractal dimensions from fractured surfaces. None of these parameters have been found to correlate with fracture toughness satisfactorily. He has attributed this to very little work being expended in the formation of new surfaces compared to plastic dissipation in the matrix.

As can be seen in the above literature review, correlation of micro- and macro-fracture parameters is yet to be achieved satisfactorily, particularly for heterogeneous materials. This is attributed to the fact that micromasurements are relatively complex in heterogeneous material systems due to the presence of secondary phases. Furthermore, most of the studies with secondary phase material has been performed with relatively uncontrolled filler sizes and shapes and mostly in cementitious materials with relatively large fillers. Also there is no unique roughness parameter that has been shown to correlate well with fracture toughness. These provide additional motivation to systematically study the effect of macro-measured fracture parameters on micro-measured surface features in heterogeneous material with identical size fillers.

Thus fracture behavior in heterogeneous material and the associated toughening mechanisms depend on various characteristics of the constituent phases, crack front

interactions, and the filler-matrix bonding strength. Various analytical models have been proposed to predict crack path perturbation in the presence of second phase material and crack tip blunting mechanism in case of failure of filler-matrix bonding. Analogous to dislocation pinning, Lange[35] has proposed a widely cited theory about *line tension* according to which the propagating crack front bows out between dispersed impenetrable second phase particles while remaining pinned at the locations where it interacts with the particles. This increases the length of the crack front depending upon inter-particle spacing. As a result, the total energy for fracture increases by an amount required to increase the length of the crack front rather than just the energy needed to form new surfaces as in the case of unfilled materials. Furthermore, Evans[36] has demonstrated that the ratio of the energy associated to the increased crack front geometry and the fracture energy is a function of both particle size and spacing. Moreover, the major contribution to the increase in strength is from crack extension stress, which is larger than stress needed to propagate an unbowed crack, depending on the ratio of particle size to the inter-particle spacing.

Other investigators have focussed on stress fields and stress intensification when cracks interact with inclusions. Atkinson [37] calculated the stress field around a crack tip for a symmetrically located crack in the presence of an inclusion. He concluded that inverse \sqrt{r} singularity exists for crack positions up to a distance very close to the inclusion until the crack is not touching the inclusion. In a similar investigation Erdogan *et al.*[38] calculated the generalized stress field around the crack tip and stress intensity factors (SIFs) using Green's functions for an arbitrarily oriented crack with respect to a circular inclusion. A model predicting an increase in fracture toughness due

to crack deflection and twisting around a secondary phase filler is proposed by Faber and Evans [39]. The tilt angle depends on the orientation and the position of the particle with respect to an advancing crack front and the presence of residual stresses developed between filler and matrix, causing reduction in stress intensity in mode I + mode II. The magnitude of crack twist depends upon the orientation of adjacent particles forcing the crack to tilt in opposite directions resulting in mode I + mode III conditions. Both the models and experimental results conclude the dependence of fracture toughness on the shape and the volume fraction of second phase material while being invariant of particle size. There have been several numerical studies on the topic in the recent past. Li and Chudnovsky[40] have numerically shown that when a crack approaches a rigid inclusion in a relatively compliant matrix, the crack tip is shielded from the far-field stresses. This decreases stress intensification at the crack tip and hence lowers the Energy Release Rate (ERR). They also show that generally, a crack tip gets shielded when the crack approaches an inclusion while stresses are amplified when the crack propagates away (recedes) from the particle. Bush[41] has investigated the effect of single inclusion and an inclusion cluster on crack trajectory and ERR. He considered two different types of inclusions in his simulations - ones with perfect bonding with the matrix and the others with partial separation from the matrix. He showed that pre-existing flaws on inclusion-matrix interface attract a propagating crack. The crack deflection around an inclusion is noticed when the crack tip is about one radius away from the inclusion. Knight *et al.*[42] have examined crack deflection/attraction mechanisms in a crack-particle interaction investigation by performing a series of parametric studies for different Young's modulus and Poisson's ratio mismatches. For inclusions with and without interphase regions

between filler and matrix, Poisson's ratio has been shown to significantly affect crack trajectories.

In all the above experimental, analytical and numerical studies, it is evident that accurately predicting the crack trajectory is particularly important for drawing conclusions regarding fracture behavior of particulate composites. A step in that direction is to study interaction of a crack with a particle cluster in a matrix. Analytical approaches have been developed for problems concerning cracks along an interface of various types of inclusions [43, 44, 45]. Numerical techniques, including finite element method [40, 46, 47, 48, 49] and boundary element method (BEM) [41, 42, 50], have also been employed to investigate fracture behavior under static loading conditions. Recently, the dynamic response of a crack interacting with an inclusion has been studied by Lei *et al.*[51] using time-domain BEM.

1.2 Objectives

The literature review of microstructural effects on fracture behavior of heterogeneous materials suggests that there is a strong need for a systematic study of failure behavior in general and dynamic fracture in particular. It appears that it is necessary to carry out such a study using a relatively large variation of filler particle sizes. Examination of the filler-matrix adhesion strength effects as well as particle size distribution such as bimodality would also be appropriate. More importantly, any attempt to link macroscopically measured fracture parameters with microscopic parameters would be valuable. Solid spherical glass fillers of different average sizes and surface treatments are readily available commercially. If these can be dispersed into a polymeric matrix uniformly and

consistently, one can examine and potentially model fracture behavior under laboratory conditions. Thus, the following are the primary objectives of the present research:

- Investigate dynamic fracture behavior of microstructurally heterogeneous material.
- Investigate the role of particle size and filler-matrix adhesion on effective fracture toughness under impact loading conditions.
- Investigate the role of particle size bimodality on dynamic crack growth in particulate composites.
- Investigate micro mechanisms affecting the fracture behavior in the presence of filler particles of various sizes and adhesion strengths.
- Model experimentally and numerically potential interactions of a propagating crack with isolated inclusions and inclusion-clusters to understand basic toughening mechanisms in particulate composites.

1.3 Organization of Dissertation

This dissertation is organized into eight chapters, including Introduction. The experimental technique and the numerical tool used for investigating fracture are briefly described in Chapter 2. The optical interferometric method of coherent gradient sensing, CGS, used to map crack tip deformation fields is discussed. The method is applied to evaluate fracture parameters of a particulate composite and to investigate the fracture behavior when a stiff inclusion is embedded in a compliant matrix. This Chapter also includes a brief description of symmetric Galerkin boundary element method (SGBEM)

employed to simulate crack propagation in the presence of an isolated inclusion and the cluster of inclusions.

Chapter 3 describes the material preparation of weakly and strongly bonded glass-filled epoxy particulate composites. The quasi-static and dynamic material property characterization as well as methods used for performing micro measurements are detailed in this Chapter.

In Chapter 4 the effects of microstructural variation on fracture behavior of particulate composites under impact loading conditions are described. The Chapter focuses on examining filler particle size, filler-matrix adhesion strength and particle size distribution effects on fracture parameters. The macro- measurements include analysis of interferograms obtained using CGS and high-speed photography. This Chapter also discusses quasi-static experiments performed to evaluate loading rate effects on fracture toughness of the composite.

The micro-measurements performed on fractured surfaces are discussed in Chapter 5. Based on qualitative observation of surface features using scanning electron microscopy potential toughening mechanisms in particulate composites having weakly and strongly bonded fillers are identified. Fractured surfaces are also analyzed quantitatively using surface profilometry to determine roughness parameters. A model is proposed to link optically measured fracture toughness and a component of surface roughness.

In Chapter 6 experimental investigations of dynamically growing crack interacting with inclusions is reported. In these initial results on the topic, primary focus is on a crack approaching an inclusion. The differences in toughening mechanisms when an

inclusion is strongly and weakly bonded to the matrix is explained and quantified by evaluating fracture parameters.

Chapter 7 details numerical investigations of crack-inclusion interaction. SGBEM is used to simulate the difference in crack growth behaviors when inclusions are weakly and strongly bonded to the matrix. The parametric studies are performed to investigate inclusion-matrix delamination effect in case of weakly bonded inclusion and particle-cluster orientation and volume fraction effects when the inclusions are strongly bonded.

Finally, major conclusions of the dissertation is summarized in Chapter 8 and potential topics for future research are proposed.

CHAPTER 2

EXPERIMENTAL AND NUMERICAL METHODS USED¹

In this chapter experimental and numerical techniques are used in the investigation of fracture behavior of heterogeneous materials are described. The optical method of Coherent Gradient Sensing, CGS, is used to study crack tip deformations in various particle filled composite specimens. This method is also applied to investigate interaction of a growing crack with an isolated glass inclusion in a matrix. CGS measures surface slopes when used in the study of opaque solids. The relative ease of implementation of CGS used in conjunction with a high-speed camera is attractive to study dynamic crack growth problems. The interaction of a crack with perfectly bonded stiff inclusions and inclusion-clusters in a brittle matrix is further investigated using numerical simulations. A symmetric-Galerkin boundary element method, SGBEM, is used as a crack-growth prediction tool. The SGBEM tool is accompanied with a modified quarter-point crack-tip element, the displacement correlation technique for evaluating SIFs, and the maximum tangential stress criterion for crack-growth direction prediction.

2.1 Experimental method: Coherent Gradient Sensing

Various optical methods have been used in the literature to measure elastic and plastic crack tip deformations under quasi-static and dynamic loading conditions. Among the commonly used techniques to map in-plane and out-of-plane deformations and stresses,

¹ *Parts of this chapter appear in Ref. [52]*

Photoelasticity[53, 54, 55], different interferometric methods[56]-[61] including holography and speckle methods[62, 63, 64], the method of caustics are predominant. In most of these methods adequate control over sensitivity of the measurement is crucial due to a wide range of deformation magnitudes near the crack tip. Due to simplicity of implementation and relative insensitivity to vibrations, wave front shearing interferometers have been applied to fracture studies in recent years. The method of CGS, being a lateral shearing interferometer, has successfully been applied to quasi-static and dynamic crack growth studies in both transparent and opaque solids[59, 60].

2.1.1 Experimental set-up: CGS

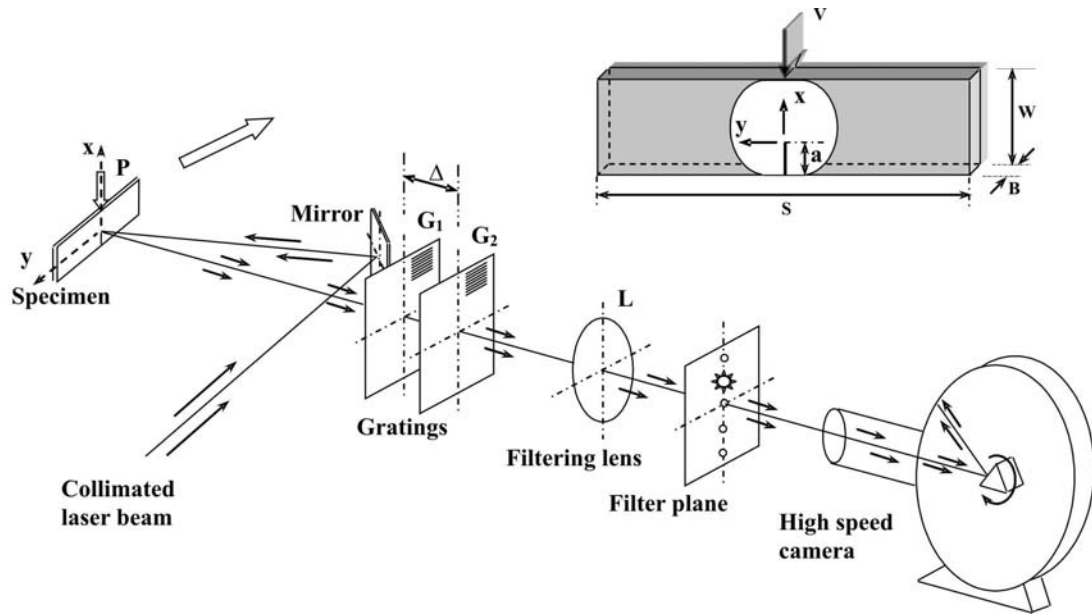


Figure 2.1: Schematic representing the experimental set-up for reflection Coherent Gradient Sensing method.

The schematic of experimental set-up for reflection CGS[65, 66] is shown in Fig. 2.1. A collimated beam of coherent laser light illuminates an opaque specimen with a

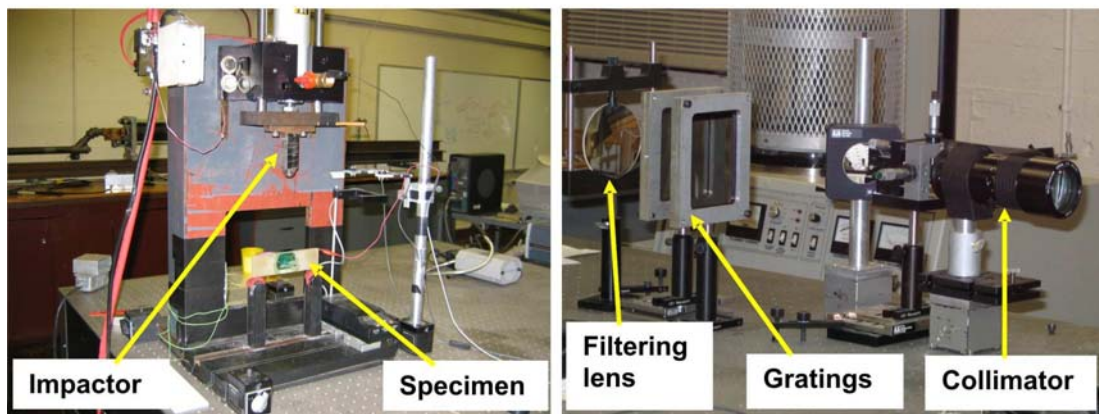
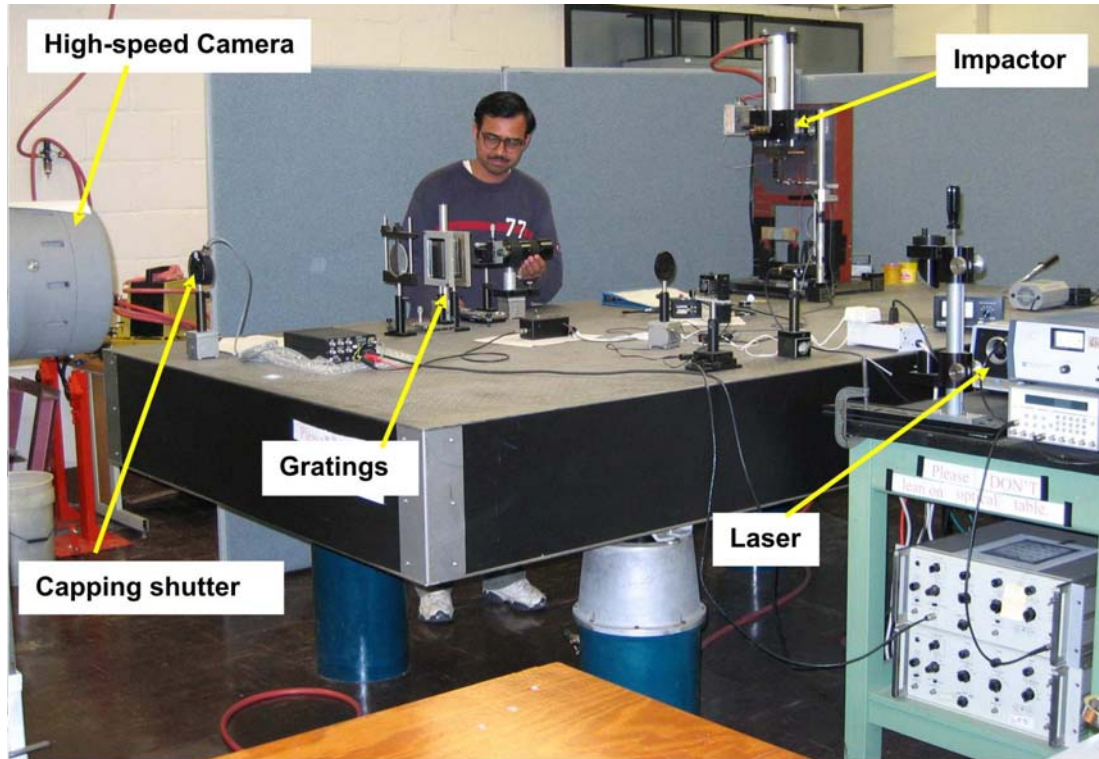


Figure 2.2: Experimental set-up for Coherent Gradient Sensing shearing interferometry.

specularly reflective surface. The reflected object wave front is incident on a pair of high-density Ronchi gratings G_1 and G_2 , spatially separated by a distance Δ , as shown. These parallel gratings diffract the object wave-front successively in several discrete directions. The filtering lens L collects the light field and displays its frequency content on its back focal plane as a series of diffraction spots, as shown. By locating a filtering aperture around ± 1 diffraction order, the information about surface slopes in the form of interference fringes is captured at the image plane. The optical set-up requires that the imaging system (lens+image plane) be focused on the object surface. An actual photograph of the set-up is shown in Fig. 2.2.

The experimental set-up includes an impactor, a pulse laser, CGS interferometer and a continuous access high-speed camera (see, Fig. 2.2). An Argon-ion laser beam (wave length $\lambda = 514 \text{ nm}$) is expanded and collimated into a 50 mm diameter beam. A pneumatically operated cylindrical steel hammer with hemispherical tip is used to impact (velocity 5.3 m/sec) the center of the specimen along the negative x -axis, as shown in Fig. 2.1. The specimen is initially rested on two blocks of soft-putty to simulate ‘free-free’ supports. Before the impactor contacts the specimen, a flag (of width $\sim 6.4 \text{ mm}$) is used to trigger a photo-detector which in turn opens a capping shutter in front of the camera lens. This allows the laser beam to expose a strip of Kodak TMAX-400 photographic film located in a circular track in the camera. As soon as the impactor touches an adhesive backed copper tape on the top edge of the specimen, an electric circuit initiates a gate pulse of $320 \text{ }\mu\text{sec}$ duration. Laser pulses of 50 ns width are repeated at $5 \text{ }\mu\text{sec}$ intervals (200,000 fps) during the gate period. With these settings, approximately 70 images are exposed onto the photographic film. The incident beam

reflecting from the deformed surface carries information about the local non-planarity of the surface near the crack tip and the impact point. The angular deflections of light rays relative to the optical axis are measured as interference fringes by filtering out all but ± 1 diffraction order. The fringe patterns representing contours of $\partial w / \partial x$ where w is the out-of-plane displacement and x is along the direction of crack orientation, are recorded in this study.

2.1.2 Working principle and governing equation of CGS[67]

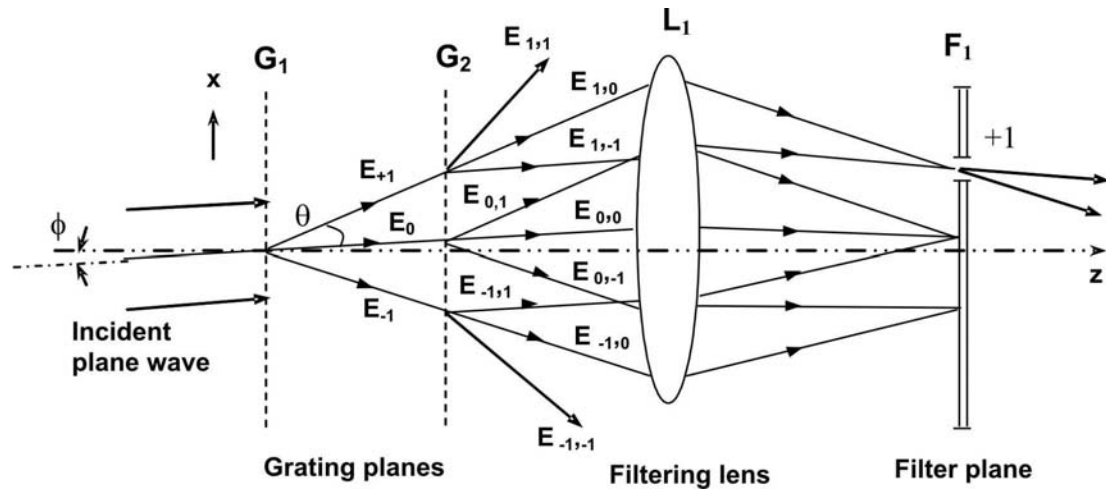


Figure 2.3: Diffraction of a collimated beam through two parallel high density Ronchi gratings.

Consider an object wave traveling in the $x - z$ plane such that it makes an angle ϕ with the optical z -axis and transmitted through Ronchi gratings G_1 and G_2 oriented with their principal grating axes along the x -direction. Let the gratings (of pitch p) be separated by a distance Δ as shown in Fig. 2.3. Upon incidence, the first grating G_1 diffracts light beam into several diffraction orders, $0, \pm 1, \pm 2 \dots$, and so on. The corresponding complex amplitude distribution of resulting diffracted waves are denoted by

$E_0, E_{\pm 1}, E_{\pm 2}, \dots$. For simplicity consider only three diffracted wave fronts E_0 and $E_{\pm 1}$. These waves which are propagating in discretely different directions are separated by an angle θ , also known as the diffraction angle given by $\theta = \sin^{-1}(\lambda/p)$ where λ is the wave length of incident light. For small angle of diffraction, $\theta \approx \lambda/p$. Each of these diffracted wave fronts are once again diffracted by the second grating G_2 . The resulting wavefronts propagating in discretely different directions after the second diffraction are denoted by $E_{i,j}$, where $i, j = 0, \pm 1, \pm 2, \dots$. The first and second subscripts correspond to the diffraction orders from the first and the second grating, respectively. Once again consider only three diffraction orders 0 and ± 1 for each incident light wave for consistency. These propagating waves traveling in discretely different directions are brought to focus on the image plane using a Fourier lens L_1 . From the figure it can be noticed that $E_{1,-1}, E_{0,0}$ and $E_{-1,1}$ are propagating parallel to each other and contribute to the zeroth diffraction spot on the focal plane. Similarly, the diffracted wave fronts $E_{\pm 1,0}$ and $E_{0,\pm 1}$ produce ± 1 diffraction spots. Using a filtering aperture placed at the focal plane of the lens as shown, the desired diffraction order, ± 1 diffraction spot in this case, is allowed to propagate further while blocking out the rest.

The laterally displaced wave fronts meeting at discretely different diffraction spots produce interference due to their optical path difference. The optical path lengths corresponding to E_0 and $E_{\pm 1}$ be denoted by l_0 and $l_{\pm 1}$, respectively. From the geometry as shown in Fig. 2.3,

$$l_0 = \frac{\Delta}{\cos \phi}, \quad l_{\pm 1} = \frac{\Delta}{\cos(\theta \pm \phi)}. \quad (2.1)$$

By expanding $\cos(\cdot)$ about $(\cdot) = 0$ and neglecting the terms of the order $(\cdot)^3$ and higher, for small angles we get,

$$l_0 = \frac{\Delta}{\left(1 - \frac{\phi^2}{2!} + \frac{\phi^4}{4!} - \dots\right)} \approx \frac{\Delta}{\left(1 - \frac{\phi^2}{2!}\right)},$$

$$l_{\pm 1} = \frac{\Delta}{\left(1 - \frac{(\theta \pm \phi)^2}{2!} + \frac{(\theta \pm \phi)^4}{4!} - \dots\right)} \approx \frac{\Delta}{\left(1 - \frac{(\theta \pm \phi)^2}{2!}\right)}. \quad (2.2)$$

Using binomial expansion on the above and neglecting cubic and higher order terms we get,

$$l_0 \approx \frac{\Delta}{\left(1 - \frac{\phi^2}{2!}\right)} \approx \Delta \left(1 + \frac{\phi^2}{2!}\right),$$

$$l_{\pm 1} \approx \frac{\Delta}{\left(1 - \frac{(\theta \pm \phi)^2}{2!}\right)} \approx \Delta \left(1 + \frac{(\theta \pm \phi)^2}{2!}\right). \quad (2.3)$$

The intensity of interference fringes can be evaluated from complex amplitudes of corresponding overlapped wave fronts. For the diffracted wave fronts from the first grating,

$$E_0 = A_0 e^{ikl_0},$$

$$E_{\pm 1} = A_{\pm 1} e^{ikl_{\pm 1}}, \quad (2.4)$$

where $A_0, A_{\pm 1}$ denote amplitudes. In the above the wave number k is given as $k = 2\pi/\lambda$ and $i = \sqrt{-1}$.

It can be noted from the figure that no additional path difference is introduced after the waves are transmitted out of the second grating. Consider a case when only +1 (or -1) diffraction order is allowed to pass through the filtering aperture. The intensity

distribution at the image plane is given by,

$$I = (E_{1,0} + E_{0,1})(E_{1,0} + E_{0,1})^* = A_0^2 + A_1^2 + 2A_0A_1 \cos k(l_0 - l_1), \quad (2.5)$$

where A_0 and A_1 are constant amplitudes associated to the diffracted wave fronts from the second grating and superscript ‘*’ denotes complex conjugate. Substituting Eq. (2.3) in the above, we get the intensity distribution,

$$I \approx A_0^2 + A_1^2 + 2A_0A_1 \cos \left[k\Delta \left(\frac{\theta^2}{2} + \theta\phi \right) \right]. \quad (2.6)$$

For constructive interference,

$$k\Delta \left(\frac{\theta^2}{2} + \theta\phi \right) = 2m\pi, \quad m = 0, \pm 1, \pm 2, \dots, \quad (2.7)$$

where m represents fringe order. The equation can be expressed in terms of wave length of incident light by using $k = 2\pi/\lambda$. That is,

$$\frac{\Delta}{\lambda} \left(\frac{\theta^2}{2} + \theta\phi \right) = m, \quad m = 0, \pm 1, \pm 2, \dots \quad (2.8)$$

The above equation represents the condition for a bright fringe at the image plane (constructive interference) when object waves are perturbed from the original path by an angular deflection ϕ due to out-of-plane deformation of the specimen surface.

Now, recognizing that when object waves are propagating parallel to the optical axis in case of an undeformed object, $\phi = 0$ in Eq. (2.7). That is, when the object is

undeformed, the condition for constructive interference is,

$$\frac{\Delta \theta^2}{\lambda} = n, \quad n = 0, \pm 1, \pm 2, \dots \quad (2.9)$$

Since, θ , λ and Δ are constants, a uniform fringe (infinite fringe spacing) of order n covers the entire region of interest on the specimen.

The magnitude of angular deflection in a deformed object can be evaluated by subtracting Eq. (2.7) from Eq. (2.9) and using $\theta \approx \lambda/p$ to get,

$$\phi = \frac{Np}{\Delta}, \quad (2.10)$$

where fringe order $N = m - n = 0, \pm 1, \pm 2, \dots$

As shown above, CGS measures angular deflections of light rays bouncing off of a specularly reflective surface in the principal direction of gratings. The angle ϕ can be related to surface slopes as,

$$\phi = 2 \frac{\partial w}{\partial x}, \quad (2.11)$$

where w is out-of-plane displacement. Therefore, surface deformations measured in terms of fringe order, grating pitch and grating separation distance from Eq. (2.10) and Eq. (2.11) is,

$$\frac{\partial w}{\partial x} = \frac{Np}{2\Delta}, \quad N = 0, \pm 1, \pm 2, \pm 3, \dots \quad (2.12)$$

This can further be expressed in terms of stress gradients for plane stress condition as,

$$\frac{\partial w}{\partial x} \approx -\frac{\nu B}{2E} \left[\frac{\partial(\sigma_x + \sigma_y)}{\partial x} \right] = \frac{Np}{2\Delta}, \quad (2.13)$$

where E is the elastic modulus, ν is the Poisson's ratio and B is the undeformed thickness of the planar specimen.

Figure 2.4 shows a representative interferogram recorded during a dynamic experiment using CGS and high-speed photography. The image is from post crack-initiation time instant. Fringe orders are identified near the impact point and the crack tip. The interferogram and evaluations of fringes are explained in detail in Chapter 4.

2.1.3 Crack velocity and stress intensity factor evaluation

Instantaneous crack length is measured by locating the crack tip from the digitized images. From the crack tip location histories, crack speeds (da/dt) are calculated using the central difference method :

$$v_i = \left(\frac{da}{dt} \right)_i = \frac{a_{i+1} - a_{i-1}}{t_{i+1} - t_{i-1}}, \quad (2.14)$$

where a_i and t_i denote instantaneous crack length and time instants, respectively.

Interferograms are also used to quantify instantaneous fracture parameters by digitizing optical information around the crack tip to obtain fringe location, (r, θ) , and fringe order, N , data (see Fig. 2.4).

Considering linear elastic asymptotic stress field in the vicinity of a steadily propagating mode-I crack[66],

$$\frac{\partial w}{\partial x} = -\frac{\nu B}{2E} f(v) \sum_{n=1}^{\infty} \left[A_n \left(\frac{n}{2} - 1 \right) r_l^{\left(\frac{n}{2} - 2 \right)} \cos \left(\frac{n}{2} - 2 \right) \theta_l \right] = \frac{Np}{2\Delta}, \quad (2.15)$$

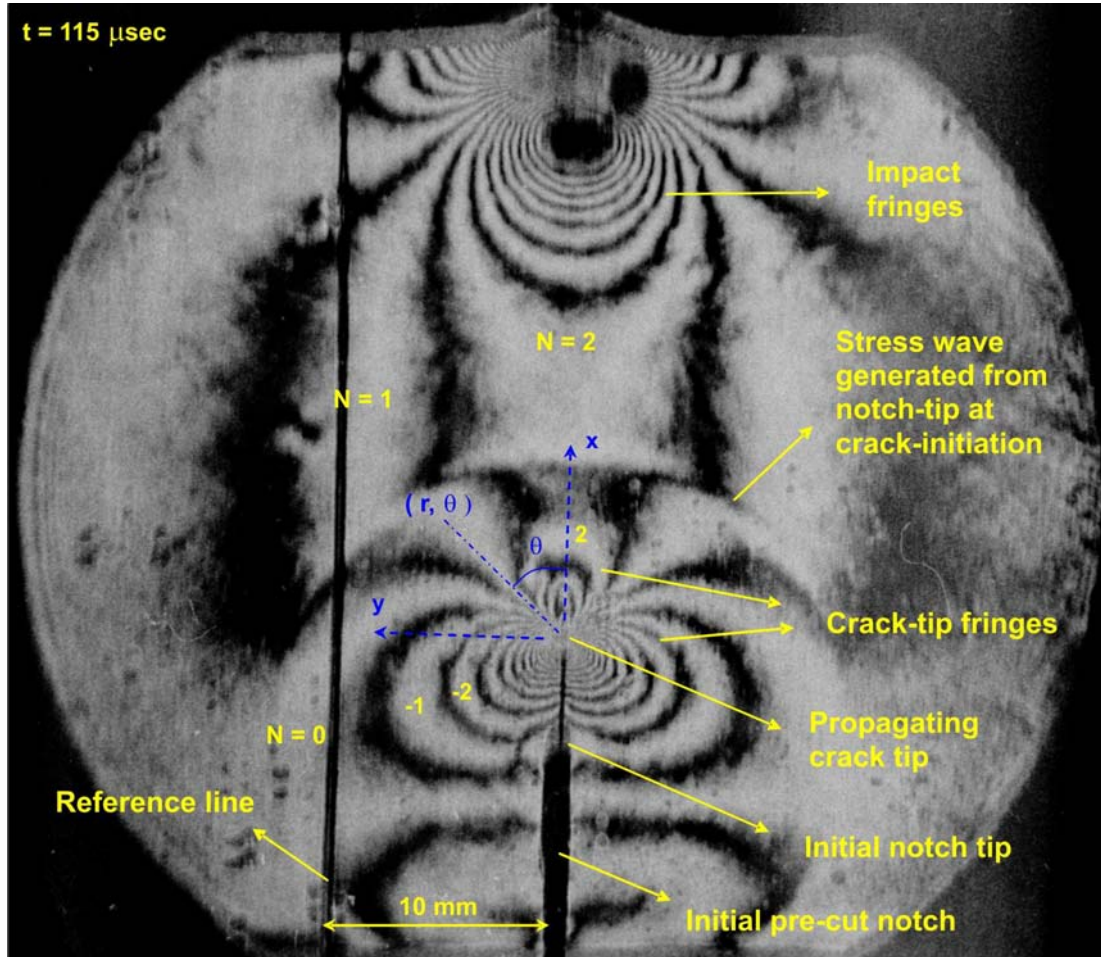


Figure 2.4: CGS interferogram recorded during dynamic experiment; t represents post impact time duration, Fringe orders N are identified in the interferogram.

where

$$\begin{aligned}
f(v) &= \frac{(1 + \alpha_s^2)(\alpha_l^2 - \alpha_s^2)}{4\alpha_l\alpha_s - (1 + \alpha_s^2)^2}, \\
\theta_l &= \tan^{-1}(\alpha_l \tan \theta), \\
r_l &= r \cos \theta (1 + \alpha_l \tan^2 \theta), \\
\alpha_{l:s} &= \sqrt{1 - (\dot{a}/C_{l:s})^2},
\end{aligned} \tag{2.16}$$

r and θ are the polar coordinates defined at the instantaneous crack tip. Equation (5) can also be used for analyzing pre-initiation interferograms as $f(v) \rightarrow 1$ as $v \rightarrow 0$, reducing the equation to the form of its quasi-static counterpart. Overdeterministic least-squares analysis² is performed using Eq.(2.15) and the resulting functional is minimized with respect to constants A_n . This results in a set of linear equations of the form,

$$[Q] \{A\} = \{Z\} . \tag{2.17}$$

In Eq.(2.17), $\{A\}$ is the vector of unknown constants A_n with $A_1 = K_I \sqrt{\frac{2}{\pi}}$, $[Q]$ is the matrix with its elements $Q_{ij} \equiv Q_{ij}(r, \theta, \dot{a}, C_l, C_s)$ and $\{Z\}$ is known vector of $Z_i \equiv Z_i(r, \theta, N, E, \nu, B, \dot{a}, C_l, C_s)$. The resulting set of linear equations can be solved to get A_n .

Using the least-squares analysis described above, mode-I dynamic stress intensity factors K_I are evaluated. The region of dominant 3-D effects in the vicinity of the crack tip ($r/B < 0.5$) is excluded from the analysis. Also, only the data behind the crack ($90^\circ < \theta < 150^\circ$) is considered since it has been demonstrated that triaxial effects are

²Overdeterministic least-squares analysis of CGS fringes is explained in Appendix A.

minimum in this region[65]. Since the measured data considered in the analysis comes from a region beyond $r/B = 0.5$, inclusion of non-singular terms in the least-squares analysis is necessary to account for far-field stresses. It has been found during this research that by including the first three terms of the asymptotic stress field, K_I can be evaluated accurately.

2.2 Numerical Methods: Symmetric-Galerkin BEM

Among the various numerical tools developed in past, Finite Element Method (FEM) and Boundary Element Method (BEM) have been widely used for solving fracture mechanics problems. FEM is particularly very popular as a crack-growth prediction tool because of its relatively simple formulation and availability of many commercial structural software packages. Cohesive zone modeling[68, 69], moving mesh technique[70], continual remeshing[71], element enrichment technique[72, 73] and mesh free method[74, 75] are among the approaches used in conjunction with finite element method to predict crack initiation and growth. In some of these methods a set of extra elements in the crack growth region is required in addition to regular finite elements in the domain. This increases the number of degrees of freedom of the problem significantly. On the other hand few other methods, which use continuously varying mesh and mesh geometry, are cumbersome and not so easy to implement with commercially available FEA routines. Also, in many of these methods, the use of sufficiently refined mesh is important to accurately predict crack path, which again increases the necessary degrees of freedom and hence the size of the system of equations to be solved. Boundary element method, in contrast, greatly decreases the number of unknowns due to its

inherent attribute of reducing the dimensionality of the problem. Comparatively easier meshing also facilitates modeling regions of high concentration more efficiently. Detailed reviews of development of BEM in fracture investigations are reported in Refs.[76, 77]. The early usage of BEM in fracture mechanics can be traced back to late 60s[78, 79]. To resolve the problem of degeneracy at crack faces various models have been proposed and implemented. Modeling crack tip as a notch[80], subdomain technique[81, 82], dual boundary element method (DBEM)[83], displacement discontinuity method[84], Green's function method[85], symmetric-Galerkin technique (SGBEM)[87] etc. are a few notable approaches.

The key feature of BEM is that only the boundary of the domain is to be discretized and only boundary quantities are determined. It is generally recognized that BEM is particularly well suited for linear elastic fracture mechanics. It is known to provide more accurate results for stress and there is no need for re-meshing the boundary during crack growth modeling. It should be noted that the BEM and the DBEM are collocation methods while the SGBEM employs a Galerkin approximation. The main disadvantage associated with the sub-domain BEM technique is the additional computational effort due to the use of an artificial interface along a crack, while the major drawback of the DBEM is that the relaxation of continuity requirements at element boundaries and junctions lead to stress field singularities in the vicinity of these points. Recently, SGBEM has been developed ([86, 87]) and has shown several key advantages in fracture applications: (a) SGBEM uses the displacement boundary integral equation (BIE) on the boundary where displacement is prescribed and traction BIE on the boundary where traction is known. As the name implies, this results in a symmetric coefficient matrix,

which remains true for fracture problems provided the unknowns on the crack faces are crack opening displacements (COD), (b) the presence of both displacement and traction BIE enables fracture problems to be solved without using artificial sub-domains, (c) unlike collocation techniques, there is no smoothness requirement on the displacement ([88, 89]) in order to evaluate the hypersingular integral; thus, standard *continuous* and quarter-point (QP) elements can be employed, and (d) the weighted averaging formulation of Galerkin, by avoiding direct collocation at corners and junction points, provides a smoother solution in the neighborhood of geometric discontinuities.

In both finite and boundary element fracture modeling, the standard approach consists of incorporating the \sqrt{r} displacement behavior at the crack tip by means of the QP element [90, 91], where r is the radial distance from the crack tip. Use of this QP element at the crack tip has improved the accuracy of SIF calculations ([92, 93]). Recently, Gray and Paulino [94] have proved that, for an arbitrary crack geometry, a constraint exists in the series expansion of the crack opening displacement at the tip. As discussed in [94], the QP element in general fails to satisfy this constraint, and has led to the development of an improved modified quarter-point (MQP) element [95]. It was demonstrated in [95] that the accuracy of the computed SIFs using the Displacement Correlation Technique (DCT) can be significantly improved by incorporating this MQP element into the SGBEM. This suggests that stress methods such as the maximum tangential stress (MTS) criteria[96] can effectively be used for crack-growth direction prediction when all these are symmetrically used. The next section presents the proposed crack-growth prediction tool by providing a brief review of the SGBEM fracture analysis, the MQP element, the DCT, and the MTS criteria.

2.2.1 Boundary Element Method: Formulation[97, 98]

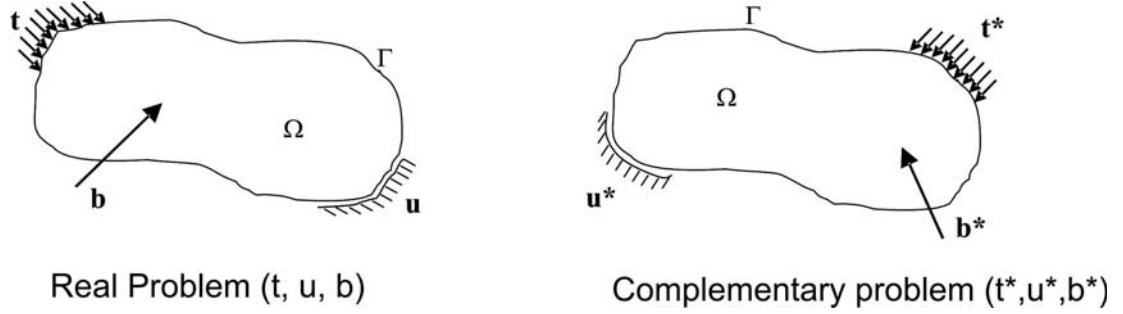


Figure 2.5: Reciprocal nature of elastic solid; Two systems in equilibrium (real and complementary) under different loading.

Boundary element method, based on the so-called Boundary Integral Equation (BIE), can be derived in several ways. The formulation given below starts from reciprocal theorem. Consider two equilibrium states of a domain Ω surrounded by the boundary Γ as shown in Fig. 2.5. From Betti's reciprocal work principle, the work done by stresses of the first equilibrium state on the strains of the second is equal to the work done by stresses of the second equilibrium state on strains of the first. Let stresses and strains for the two states be $(\sigma_{ji}, \epsilon_{ji})$ and $(\sigma_{ji}^*, \epsilon_{ji}^*)$, then from reciprocal theorem,

$$\int_{\Omega} \sigma_{ji}^* \epsilon_{ji} d\Omega = \int_{\Omega} \sigma_{ji} \epsilon_{ji}^* d\Omega, \quad (j = 1, 2, 3). \quad (2.18)$$

Here, summation over repeated indices are implied. Using strain-displacement relation,

$$\int_{\Omega} \sigma_{ji}^* u_{j,i} d\Omega = \int_{\Omega} \sigma_{ji} u_{j,i}^* d\Omega. \quad (2.19)$$

Here \mathbf{u} and \mathbf{u}^* are displacement fields in two different equilibrium states. Integrating the equation by parts and using Gauss theorem we get,

$$\int_{\Gamma} \sigma_{ji}^* u_j n_i d\Gamma - \int_{\Omega} u_j \sigma_{ji,i}^* d\Omega = \int_{\Gamma} \sigma_{ji} u_j^* n_i d\Gamma - \int_{\Omega} u_j^* \sigma_{ji,i} d\Omega . \quad (2.20)$$

Now, applying stress equilibrium equation ($\sigma_{ji,i} + b_j = 0$, where b_j denote body force components per unit volume in j th direction) and representing tractions in the form of Cauchy's stress tensor ($t_i = \sigma_{ji} n_i$) we get,

$$\int_{\Gamma} t_j^* u_j d\Gamma + \int_{\Omega} b_j^* u_j d\Omega = \int_{\Gamma} t_j u_j^* d\Gamma + \int_{\Omega} b_j u_j^* d\Omega , \quad (2.21)$$

where, t, t^* and b, b^* are surface traction and body force terms, respectively.

Now consider that quantities (t, \mathbf{u}, b) correspond to real problem in hand whereas quantities with '*' as the superscript (t^*, \mathbf{u}^*, b^*) are for a complementary problem or load case. For quasi-static loading conditions, body force $b_j = 0$, and the above equation reduces to,

$$\int_{\Gamma} t_j^* u_j d\Gamma + \int_{\Omega} b_j^* u_j d\Omega = \int_{\Gamma} t_j u_j^* d\Gamma . \quad (2.22)$$

The selection of complementary load case is completely arbitrary. This facilitates choosing (t^*, \mathbf{u}^*, b^*) such that the reciprocal equation can be simplified further for numerical calculations. Let us choose a complementary load case as unit point force acting at a point P as shown in Fig. 2.6. The unit concentrated force can be represented as a Dirac delta function $\delta(P)$ (see, figure). Therefore, the complementary body force integral term in Eq.(2.22) takes the form,

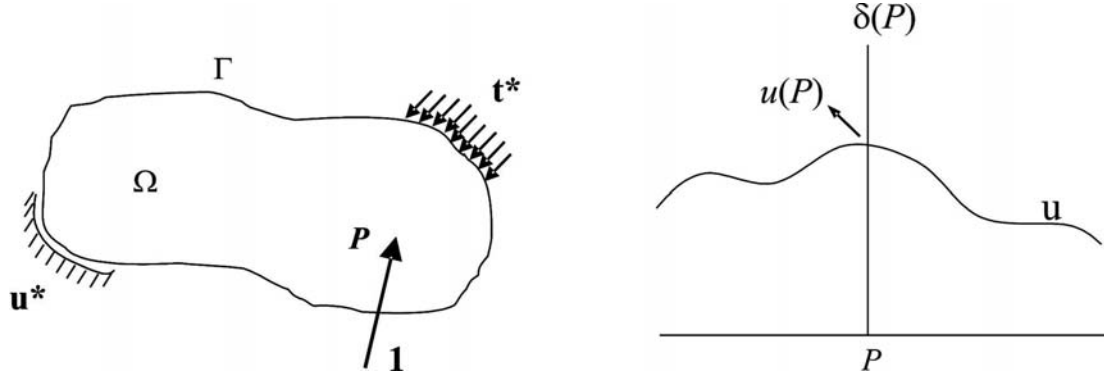


Figure 2.6: A unit point force at P , represented by a Dirac delta function is considered as a complementary body force.

$$\int_{\Omega} b_j^* u_j d\Omega = \int_{\Omega} \delta(P) \tilde{e}_j u_j d\Omega = \int_{\Omega} \delta(P) \delta_{ji} \tilde{e}_i u_j d\Omega = \int_{\Omega} \delta(P) \tilde{e}_i u_i d\Omega = \tilde{e}_i u_i(P) \quad (2.23)$$

where δ_{ji} is Kronecker delta ($\delta_{ij} = 0$ for $i \neq j$ and $\delta_{ij} = 1$ for $i = j$).

Another important step in boundary element formulation is applying the fundamental solution to Boundary Integral Equation. The solution to the Navier's equation of displacements for elastostatics due to a unit point force was given by Kelvin in 1948 and is referred to as Kelvin's Fundamental Solution. Navier's equation for displacement u_j can be written as,

$$\mu u_{j,kk}^* + \frac{\mu}{1-2\nu} u_{k,kj}^* + b_j^* = 0. \quad (2.24)$$

The solution to the above equation, in terms of displacements and tractions at the field point (Q) due to unit point force at source point (P), is given by,

$$\begin{aligned} u_j^* &= U_{ij}^* \tilde{e}_i \\ t_j^* &= T_{ij}^* \tilde{e}_i \end{aligned} \quad (2.25)$$

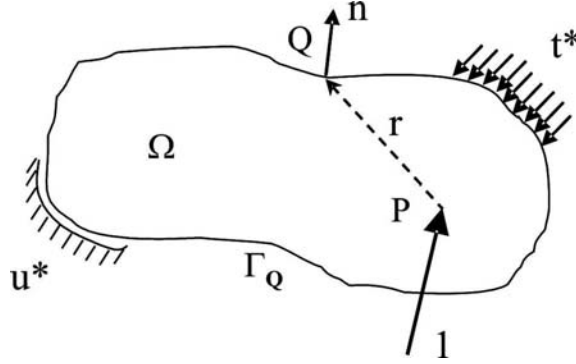


Figure 2.7: Unit point force applied on source point P to represent Kelvin's fundamental solution at field point Q .

where kernel tensor functions U_{ij}^* and T_{ij}^* for two dimensional elastic solid are given as,

$$U_{ij}^* = \frac{1}{8\pi\mu(1-\nu)} \left\{ (3-4\nu) \ln \frac{1}{r} \delta_{ij} + \frac{\partial r}{\partial x_j} \frac{\partial r}{\partial x_i} \right\},$$

$$T_{ij}^* = -\frac{1}{4\pi(1-\nu)r} \frac{1}{r} \frac{\partial r}{\partial n} \left\{ (1-2\nu) \delta_{ij} + 2 \frac{\partial r}{\partial x_j} \frac{\partial r}{\partial x_i} \right\}$$

$$+ \frac{1-2\nu}{4\pi(1-\nu)r} \left\{ \frac{\partial r}{\partial x_j} \frac{\partial x_i}{\partial n} - \frac{\partial r}{\partial x_i} \frac{\partial x_j}{\partial n} \right\}.$$

Here r and n represent distance between P and Q and unit outward normal at Q as shown in Fig.2.7. Now, by substituting fundamental solutions (Eq.(2.25)) and body force integral terms (Eq.(2.23)) in Eq.(2.22) we get,

$$\tilde{e}_i u_i(P) + \int_{\Gamma} T_{ij}^* \tilde{e}_i u_j d\Gamma_Q = \int_{\Gamma} U_{ij}^* \tilde{e}_i t_j d\Gamma_Q. \quad (2.26)$$

For each component of the unit vector \tilde{e}_i a separate equation results:

$$u_i(P) + \int_{\Gamma} T_{ij}^* u_j d\Gamma_Q = \int_{\Gamma} U_{ij}^* t_j d\Gamma_Q. \quad (2.27)$$

The above equation is known as the Boundary Integral Equation (BIE) for displacements. Similar to the displacement field, stress field in the domain can be derived by differentiating Eq.(2.27) with respect to spatial coordinates x_k and using Hooke's law to get,

$$\sigma_{ik}(P) + \int_{\Gamma} S_{ijk}^* u_i d\Gamma_Q = \int_{\Gamma} D_{ijk}^* t_i d\Gamma_Q, \quad (2.28)$$

where kernel functions S_{ijk}^* and D_{ijk}^* are,

$$D_{ijk}^* = \frac{1}{4\pi(1-\nu)} \frac{1}{r} \left\{ (1-2\nu) \left(\delta_{ij} \frac{\partial r}{\partial x_k} + \delta_{jk} \frac{\partial r}{\partial x_i} - \delta_{ik} \frac{\partial r}{\partial x_j} \right) + 2 \frac{\partial r}{\partial x_i} \frac{\partial r}{\partial x_j} \frac{\partial r}{\partial x_k} \right\}$$

$$S_{ijk}^* = \frac{\mu}{2\pi(1-\nu)} \frac{1}{r^2} \left[\begin{aligned} & 2 \frac{\partial r}{\partial n} \left\{ (1-2\nu) \delta_{ik} + 2 \frac{\partial r}{\partial x_j} + \nu \left(\delta_{ij} \frac{\partial r}{\partial x_k} + \delta_{jk} \frac{\partial r}{\partial x_i} \right) - 4 \frac{\partial r}{\partial x_j} \frac{\partial r}{\partial x_i} \frac{\partial r}{\partial x_k} \right\} \\ & + 2\nu \left(\frac{\partial x_i}{\partial r} \frac{\partial r}{\partial x_j} \frac{\partial r}{\partial x_k} + \frac{\partial x_k}{\partial n} \frac{\partial r}{\partial x_i} \frac{\partial r}{\partial x_j} \right) \\ & + (1-2\nu) \left(2 \frac{\partial x_j}{\partial n} \frac{\partial r}{\partial x_i} \frac{\partial r}{\partial x_k} + \delta_{ij} \frac{\partial r}{\partial x_k} + \delta_{ik} \frac{\partial r}{\partial x_j} \right) - (1-4\nu) \delta_{ik} \frac{\partial x_j}{\partial n} \end{aligned} \right] \quad (2.29)$$

The BIE for stresses (Eq.(2.28)) is also known as Hypersingular Boundary Integral Equation due to the presence of $1/r^2$ singularity in S_{ijk}^* .

2.2.2 Symmetric Galerkin Boundary Element Method (SGBEM)

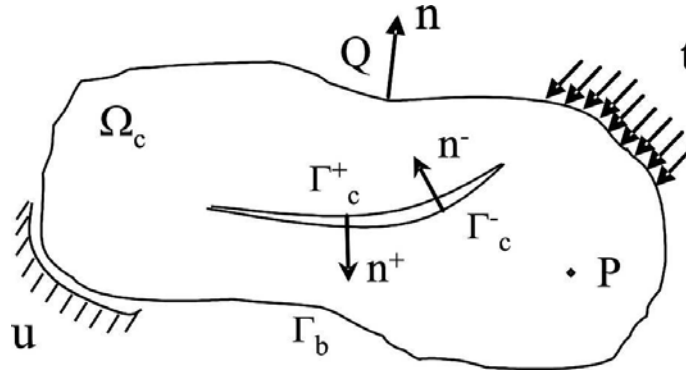


Figure 2.8: An elastic body containing crack.

Now, rewrite Eq.(2.27) in the form of functional $\mathcal{U}(P)$ as,

$$\mathcal{U}(P) = u_i(P) - \int_{\Gamma} \left[T_{ij}^* u_i - \int_{\Gamma_Q} U_{ij}^* t_i \right] d\Gamma_Q . \quad (2.30)$$

In a domain Ω_c containing a crack $\Gamma_c = \Gamma_c^+ + \Gamma_c^-$ on which only traction t_c is prescribed such that $t_c^+ = -t_c^-$ (see Fig. 2.8). Here Γ_b denotes the outer boundary of the domain. For a source point P interior to the domain, if the displacements u_c^+ and u_c^- on crack faces are replaced by the crack opening displacement (COD), $\Delta u_c = u_c^+ - u_c^-$ on Γ_c^+ , and note that $u_c^+ + u_c^- = 0$, then the BIE can be written as functional $\mathcal{U}(P)$,

$$\begin{aligned} \mathcal{U}(P) = u_i(P) - \int_{\Gamma_b} [(U_{ij}(P, Q) t_j(Q) - T_{ij}(P, Q) u_j(Q))] dQ_b \\ + \int_{\Gamma_c^+} T_{ij}(P, Q) \Delta u_j(Q) dQ_c = 0 \end{aligned} \quad (2.31)$$

It can be shown that the limit of the integral in Eq. (2.31) as P approaches the boundary exists. From now on, for $P \in \Gamma = \Gamma_b + \Gamma_c$, the BIE is understood in this limiting sense. Similar to the Eq.(2.31), hypersingular BIE (HBIE) in the form of functional $\mathcal{S}(P)$ can be written as,

$$\begin{aligned} \mathcal{S}(P) = \sigma_{ik}(P) - \int_{\Gamma_b} [D_{ijk}(P, Q) t_j(Q) - S_{ijk}(P, Q) u_j(Q)] dQ \\ + \int_{\Gamma_c^+} S_{ijk}(P, Q) \Delta u_j(Q) dQ = 0 . \end{aligned} \quad (2.32)$$

The Galerkin boundary integral formulation is obtained by taking shape functions ψ_m employed in approximating the boundary tractions and displacements as weighting functions for Eqs. (2.31) and (2.32). Thus,

$$\int_{\Gamma} \psi_m(P) \mathcal{U}(P) dP = 0 , \quad (2.33)$$

$$\int_{\Gamma} \psi_m(P) \mathcal{S}(P) dP = 0. \quad (2.34)$$

A symmetric coefficient matrix and hence a symmetric-Galerkin approximation, is ob-

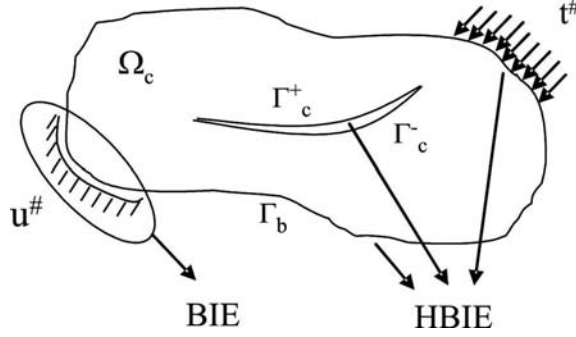


Figure 2.9: Applying BIE and HBIE on domain boundaries.

tained by employing Eq. (2.33) on the boundary Γ_u where displacements $u^\#$ are prescribed, and similarly Eq. (2.34) is employed on the boundary Γ_t with prescribed tractions $t^\#$, as shown in Fig.2.9. Note that $\Gamma = \Gamma_u + \Gamma_t$. The additional boundary integration is the key to obtain a symmetric coefficient matrix as this ensures that the source point P and field point Q are treated in the same manner.

2.2. Modified quarter-point element

The 2-D QP element is based on the three-equidistant-noded quadratic element. For $t \in [0, 1]$, the shape functions for this element are given by

$$\begin{aligned} \psi_1(t) &= (1-t)(1-2t), \\ \psi_2(t) &= 4t(1-t), \\ \psi_3(t) &= t(2t-1). \end{aligned} \quad (2.35)$$

Since, $\Delta \mathbf{u} = 0$ at the crack tip, which is assumed to be at $t = 0$ (Fig. 2.12), the

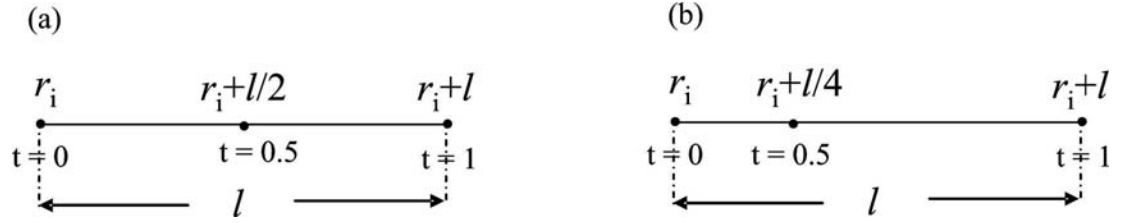


Figure 2.10: 1-D element: (a) standard mid-node element, (b) quarter-point element.

geometry and COD representations of the crack tip element are,

$$\Gamma(t) = \sum_{j=1}^3 \left(x_j \psi_j(t), y_j \psi_j(t) \right), \quad (2.36)$$

$$\Delta u_k(t) = \sum_{j=2}^3 \left(\Delta u_1^{(j)} \psi_j(t), \Delta u_2^{(j)} \psi_j(t) \right), \quad (2.37)$$

where (x_j, y_j) are the coordinates of the three nodes defining the crack tip element, and $\Delta u_k^{(j)}$ the nodal values of the COD. By moving the mid-node coordinates (x_2, y_2) three-fourths of the way towards the tip (see Fig. 2.10), the parameter t becomes $\sqrt{r/L}$ [90, 91]. As a consequence, the leading order term in $\Delta u_k^{(j)}$ at $t = 0$, is $\sim \sqrt{r}$. Note however, that the next term, which is t^2 , is r/L . According to Refs. [94, 99], this term should vanish, and the modification presented in Ref. [95] accomplishes the cancelation of this t^2 term. The resulting shape functions for the MQP element are

$$\begin{aligned} \hat{\psi}_2(t) &= -\frac{8}{3}(t^3 - t), \\ \hat{\psi}_3(t) &= \frac{1}{3}(4t^3 - t), \end{aligned} \quad (2.38)$$

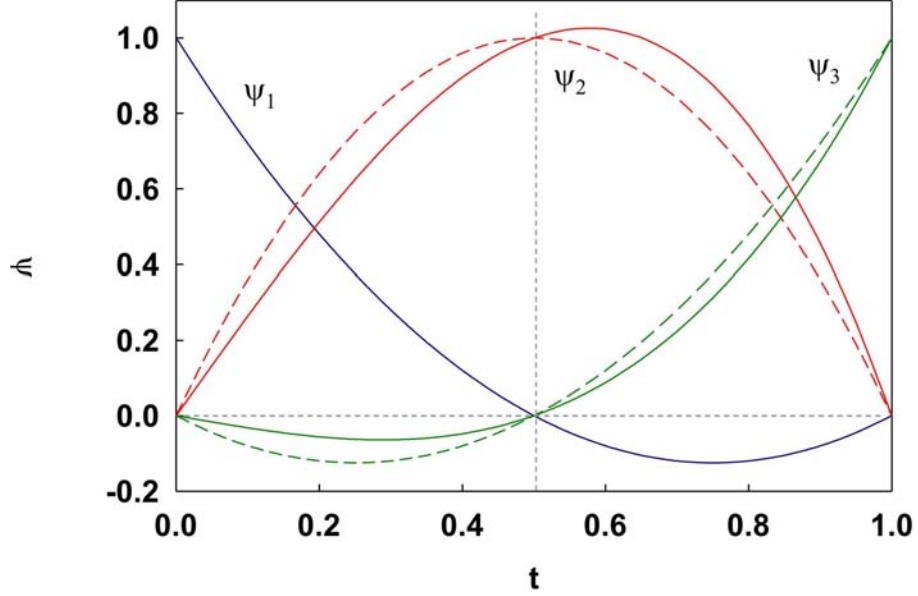


Figure 2.11: Shape functions used in SGBEM formulation. Dotted lines and solid line plots show the shape functions correspond to standard quarter-point element and modified quarter point element (MQP).

which should be used in Eq. (2.37) instead of $\psi_j(t)$. It can be observed that the modified shape functions (2.38) still satisfy the properties of a Kronecker delta $\hat{\psi}_i(t_j) = \delta_{ij}$ (see Fig.2.11). This new approximation is only applied to the COD keep the representation of the crack tip geometry as in Eq. (2.36). This ensures that the property $t \sim \sqrt{r}$ remains.

2.3. Stress Intensity Factors by the DCT

There are several approaches for evaluating SIFs numerically. Among these approaches, the displacement correlation technique (DCT) based on the COD in the crack

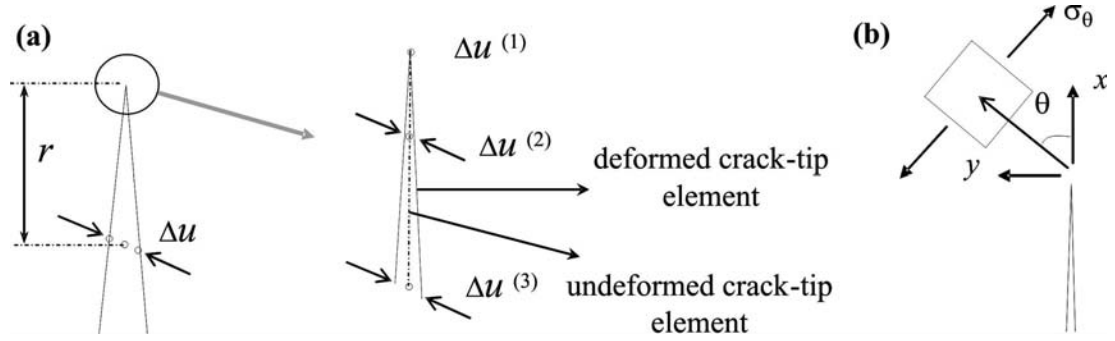


Figure 2.12: Deformed and undeformed crack, (a) crack-tip element showing crack opening displacement, (b) tangential stress near the crack-tip.

tip vicinity is a very simple method. In the case of using the MQP element, the expressions for SIFs by means of DCT are given by [95] (see Fig.2.12(a)).

$$\begin{aligned}
 K_I &= \frac{\mu}{3(\kappa + 1)} \sqrt{\frac{2\pi}{L}} \left(8\Delta u_2^{(2)} - \Delta u_2^{(3)} \right) , \\
 K_{II} &= \frac{\mu}{3(\kappa + 1)} \sqrt{\frac{2\pi}{L}} \left(8\Delta u_1^{(2)} - \Delta u_1^{(3)} \right) . ,
 \end{aligned} \tag{2.39}$$

where μ is the shear modulus, ν is Poisson's ratio, and

$$\kappa = 3 - 4\nu \quad (\text{plane strain}) , \quad \kappa = \frac{3 - \nu}{1 + \nu} \quad (\text{plane stress}) . \tag{2.40}$$

Since SIFs are directly given in terms of nodal values of COD at the crack tip element, the use of MQP element herein is highly beneficial as it would enhance the accuracy of nodal CODs and hence SIFs. Furthermore, energy release rate G is calculated using SIFs by,

$$G = \frac{\kappa + 1}{8\mu} (K_I^2 + K_{II}^2) . \tag{2.41}$$

2.4. Maximum tangential stress criterion (MTS)

There are several criteria for predicting crack growth direction[96, 100]. The MTS criteria proposed by Erdogan and Sih [96] is adopted herein. According to this criteria, the crack growth direction θ_c is perpendicular to that of the maximum tangential stress (see Fig.2.12(b)), and the crack will propagate when K_I exceeds the fracture toughness K_{Ic} of the material.

Since in the direction θ_c , $\sigma_{r\theta} = 0$, we get,

$$\sigma_{r\theta} = K_I \sin \theta_c + K_{II}(3 \cos \theta_c - 1) = 0 \quad (2.42)$$

and

$$\theta_c = 2 \tan^{-1} \left(\frac{K_I}{4K_{II}} \pm \frac{1}{4} \sqrt{\left(\frac{K_I}{K_{II}}\right)^2 + 8} \right). \quad (2.43)$$

A crack-growth prediction tool based upon the SGBEM, the MQP crack-tip element, the DCT and the MTS criteria is employed for the simulations conducted in the current work. By incorporating the MQP shape functions (Eq. (2.38)) into a SGBEM code, accurate CODs $\Delta \mathbf{u}$ at the mid and end nodes of a crack-tip element may be obtained (see Eqs. (2.31) and (2.32)). The SIFs at the crack tip of interest will then be evaluated by substituting the related CODs in the DCT formulas (2.39). If $K_I \geq K_{Ic}$, the crack-growth direction θ_c of the crack tip in question is determined by Eq. (2.43), and an infinitesimal crack increment is added in that direction during simulation. As a result, remeshing a propagating crack is straightforward. Only a new crack-tip element needs to be added in the crack-growth direction θ_c while the rest of discretization remains

unchanged. At issue is obviously the size of the new crack-tip element. Smaller sizes, although leading to more time-consuming simulations, are expected to result in more accurate results.

CHAPTER 3

MATERIAL PREPARATION AND CHARACTERIZATION¹

In this chapter details on materials preparation for experimental studies are provided. Preparation of homogeneous sheets with a constant volume fraction of the filler of various sizes, size distribution and filler-matrix adhesion strength are described. Details on how the filler segregation/settlement are prevented, how well-defined particle distributions are achieved, etc. are discussed.

3.1 Material preparation

From literature review it is clear that role of particle size and filler-matrix adhesion strength on dynamic fracture behavior are evident even at low volume fractions. Also the contradictory conclusions by various authors in this regard suggests the need to experiment with wide range of particle sizes and different filler matrix adhesion strengths. Hence 10% volume fraction (V_f) of soda-lime glass (A-glass) spheres² of bulk density 2500 kg/m^3 is chosen to prepare glass-filled epoxy, specimens throughout this study. The relatively low V_f could assist in avoiding agglomeration problems yet be high enough to influence fracture properties. Glass particles are readily available in various sizes. The availability of both uncoated and silane treated fillers facilitate development of both weak and strong filler-matrix interfaces. Also the material preparation using epoxy matrix is easy and feasible in standard laboratory conditions.

¹ *Parts of this chapter appear in Ref. [52]*

² Soda-Lime glass (Composition %: SiO₂ - 72.5, Na₂O - 13.7, CaO - 9.8, MgO - 3.3, Al₂O₃ - 0.4, FeO/Fe₂O₃ - 0.2, K₂O - 0.1), Spherglass, Potters Industries Inc.

Solid glass spheres of mean diameters $7\ \mu\text{m}$, $11\ \mu\text{m}$, $35\ \mu\text{m}$, $71\ \mu\text{m}$ and $203\ \mu\text{m}$ have been used to study particle size effects. To study filler-matrix adhesion effect, both weak and strong filler-matrix interfaces have been created by using uncoated and silane coated particles of the above mentioned sizes. Amino Silane, Γ -aminopropyltrimethoxysilane ($\text{H}_2\text{NC}_2\text{H}_4\text{NHC}_3\text{H}_6\text{Si}(\text{OCH}_3)_3$) of specific gravity 1.02 (at 25°C) is used as a binder between filler and matrix materials to provide strong filler-matrix interface. This is relatively inexpensive, readily available and commonly used in various engineering materials. Moreover, it is compatible with the Amine based hardener used for polymerizing epoxies. Low viscosity epoxy³, prepared by mixing Bisphenol-A resin and Amine based hardener of densities $1129.9\ \text{kg}/\text{m}^3$ and $961.2\ \text{kg}/\text{m}^3$ in the ratio of 100:36, is used as matrix material. Initial low viscosity of epoxy poses small resistance to dispersed filler particles movement which helps in mixing the filler particles evenly. Continuous stirring of the mixture as polymerization progresses gradually, increases the viscosity of the mixture. The increasing viscosity restricts the filler motion and helps in filler particle suspension. This is particularly important to avoid settlement of particles to the bottom of the mold due to gravity.

Epoxy and glass particles were mixed until the mixture partially gelled before transferring to a mold. Careful mixing for a proper duration is very important, particularly for large particles. Mixing the material for longer duration than the optimum can cause instant solidification even before the mixture is transferred into the mold. On the other hand, mixing for shorter durations can lead to settling of filler particles due to gravity. The approximate time to pour the mixture was arrived at by trial and error, by feeling

³Epo-Thin, Buehler Inc., USA (pre-2003 formulation)

the temperature of the mixture while being stirred continuously in a container. The mixture is then poured into the mold when the temperature rise due to exothermic reaction is to such an extent that the mixture cannot be held with bare hands. After the mixture is poured into the mold, it is cured at room temperature for approximately 72 hours. The room temperature curing reduces the residual stresses.

Furthermore, the particle size distribution effect on fracture behavior was studied by using two distinctly different filler sizes in epoxy matrix. Evenly mixed glass-fillers, each of 5% V_f , are dispersed in epoxy as described earlier for single size particles. The two different particle sizes used in the mixture were 203 μm and either of 35 μm and 11 μm in diameter. To avoid settling down of larger particles due to gravity, this mixture of total 10% V_f , is poured into the mold once it gains enough viscosity and partially gelled.

3.2 Specimen surface preparation

Cast sheets are machined into test samples of dimensions 152 mm x 42 mm x 8 mm . The surface is then roughened with 150 grit sand paper and cleaned. Subsequently, the surface is made optically flat and specular by transferring a thin (a few nm thick) Aluminum film using an optical flat and a layer of epoxy. The Aluminum film is first deposited on optically flat Borosilicate glass window of ≈ 50 mm diameter using vapor deposition technique. A vacuum of 2×10^{-5} $torr$ generated in DV-502A High Vacuum Evaporator (Denton Vacuum, Inc.) is used for metal vapor deposition. A layer of liquid epoxy is sandwiched between the roughened specimen and the face of the optical flat deposited with Aluminum. The reflective film gets transferred to the specimen upon curing of epoxy layer due to higher bond strength between epoxy and Aluminum when

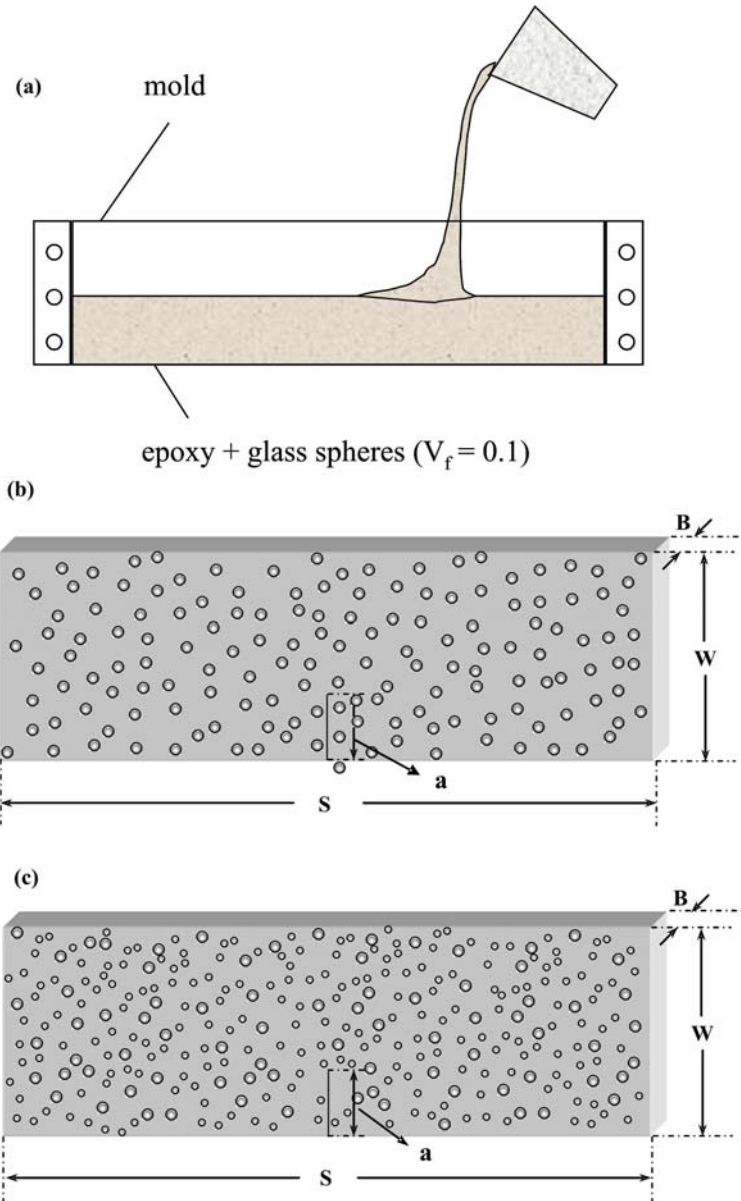


Figure 3.1: Material Preparation, (a) filler-matrix mixture pouring into the mold, (b) 10% V_f particle filled matrix monolithic specimen, (c) two different particle sizes (each of 5% V_f) filled epoxy specimen. ($S = 152$ mm, $W = 42$ mm, $B = 8$ mm, $a = 10$ mm)

compared to the bond strength between Aluminum and glass. An edge notch of root radius $150\ \mu\text{m}$ and nominal length of $10\ \text{mm}$ is cut into the sample using a high-speed diamond impregnated circular saw. The notched specimen is then used to perform fracture experiments.

3.3 Material Characterization

As discussed earlier, glass-filled epoxy particulate composite is prepared by manually mixing filler particles into the matrix material. Improper mixing can lead to the entrapment of air bubbles in the matrix and/or cause agglomeration of filler particles. Agglomeration can also occur due to high filler volume fraction or high filler surface areal density in case of sub-micron size particles. Moreover, the tendency of silane treated particles to agglomerate is higher and special care is taken to avoid this. The agglomerated particles act as larger particles with lesser surface area exposed to the matrix material. Clearly, particle agglomeration can greatly affect both particle size effect and filler-matrix adhesion strength effect on fracture behavior. Therefore, prior to preparing specimens from cured sheet, and performing experiments it is necessary to verify that particles are uniformly distributed in the matrix.

3.3.1 Quantitative microscopy

To ensure that agglomeration problem does not exist in cast materials, specimens were sliced and examined using an optical microscope. Samples with cross-sectional area of $25\ \text{mm} \times 8\ \text{mm}$ were cut from cast sheets. The samples were polished using 1000 and 2000 grit wet emery followed by $1\ \mu\text{m}$ diamond paste and $0.04\ \mu\text{m}$ alumina suspension.

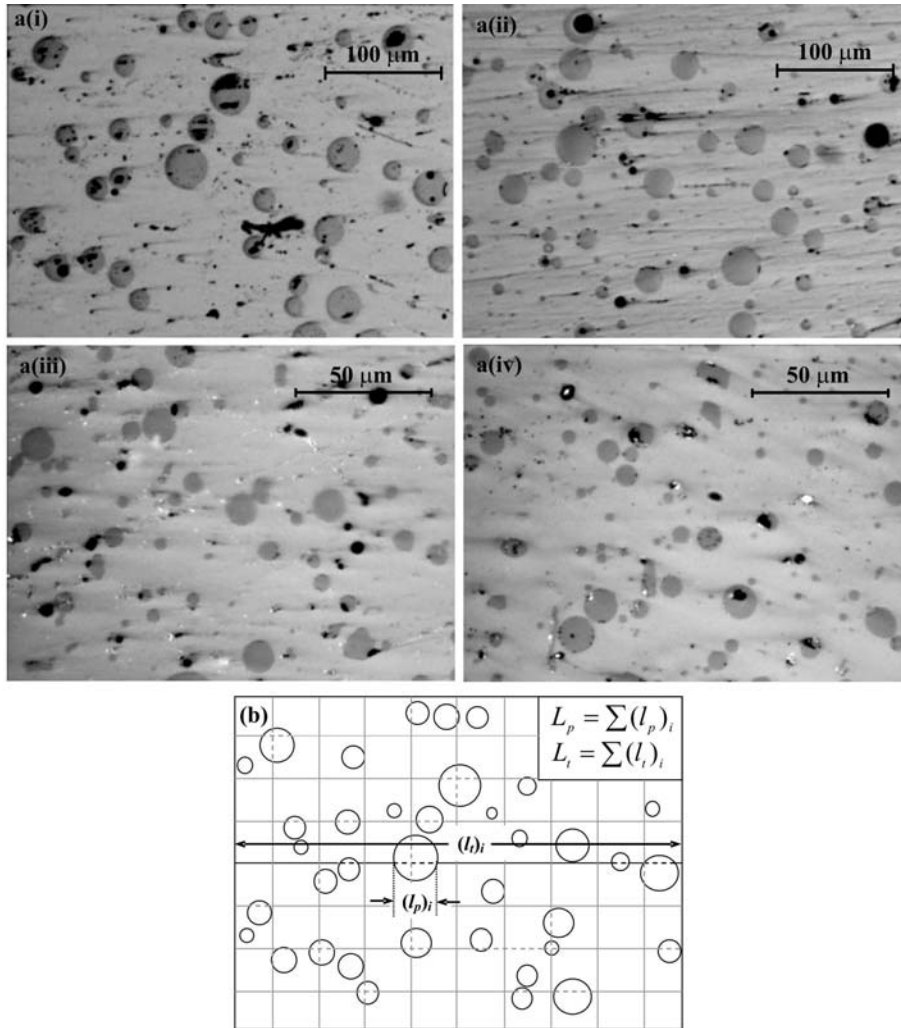


Figure 3.2: Optical micrographs of polished surfaces: (a)-(i) 35 μm uncoated particles, (ii) 35 μm coated particles, (iii) 11 μm uncoated particles, (iv) 11 μm coated particles, (b) Schematic for quantitative analysis of micrographs shown in (a) using lineal method.

Representative micrographs shown in Fig. 3.2 are for samples with $35\ \mu\text{m}$ and $11\ \mu\text{m}$ uncoated and silane coated particles, respectively. One can qualitatively assert that agglomeration is absent in all micrographs, suggesting neither size nor silane treatment induced agglomeration in the specimens. Dark spots in these micrographs are debris artifacts due to polishing. To confirm the consistency in particle dispersion at different particle sizes (coated and uncoated) three scanned images at random locations of the sample were digitized for each case and quantitative measurements were performed using the lineal method[101, 102]. The data was collected from $840\ \mu\text{m} \times 630\ \mu\text{m}$ scanned region for $35\ \mu\text{m}$ particles and $160\ \mu\text{m} \times 120\ \mu\text{m}$ area for $11\ \mu\text{m}$ particles. A square grid of density $D/8$ was used to calculate volume fraction V_f and inter-particle spacing (volume mean free path) l , where D is the mean particle diameter. The quantities V_f and l were retrieved from digitized images using,

$$V_f = \frac{L_p}{L_t} \qquad l = \frac{1 - V_f}{N_p}$$

where L_p is total transverse intercept length within particle phase and L_t is the total transverse length. In the above equation, N_p is the average number of particle hits per unit transverse length. In the calculations, summation of all horizontal and vertical lengths in the grid was taken as the total transverse length. Table 3.1 shows quantitative measurements of number of particles per unit area, inter-particle separation distance and volume fraction. Similar number of particles, volume fraction and inter-particle separation distances, when coated and uncoated cases are compared suggest that silane coating has not introduced any measurable agglomeration of particles. The same is true even in case of smaller particle sizes. Furthermore, the average inter-particle separation

Particle diameter (μm)	Average number of particles/area (mm^{-2})	Average inter- particle separation (μm)	Average particle Volume fraction
35(uncoated)	194 ± 4	218 ± 10	10.0 ± 0.1
35(coated)	192 ± 3	215 ± 12	9.9 ± 0.3
11(uncoated)	3246 ± 45	56 ± 5	9.7 ± 0.3
11(coated)	3122 ± 54	59 ± 3	9.5 ± 0.4

Table 3.1: Quantitative image analysis on polished surface

distance for spherical particles given by Fullman[103],

$$l = \frac{2D(1 - V_f)}{3V_f} \quad (3.1)$$

closely matches with the measured inter-particle spacings reported in the Table 3.1.

3.4 Material properties: Quasi-static loading

To measure the elastic and failure properties under quasi-static loading conditions, a uniaxial tension test was performed on standard dog-bone shaped specimens using an INSTRON 4465 testing machine. The specimen were loaded in displacement control mode with a cross-head speed of $0.06 \text{ mm}/\text{min}$ and the force-strain data were recorded until failure. An extensometer and Merlin/INSTRON software were used for load and strain data acquisition. The specimen had $10 \text{ mm} \times 6 \text{ mm}$ cross sectional dimensions within a gage length of 0.5 in . The acquired data was used to plot stress-strain response.

Figures 3.3(a) and (b) show stress-strain behavior of glass-filled epoxy with weakly and strongly bonded particles, respectively. The plots are used to determine elastic modulus (E), failure stress (σ_f) and failure strain (ϵ_f). In the figure, the stress-strain curves nearly overlap on each other for various particle sizes, however, failure properties,

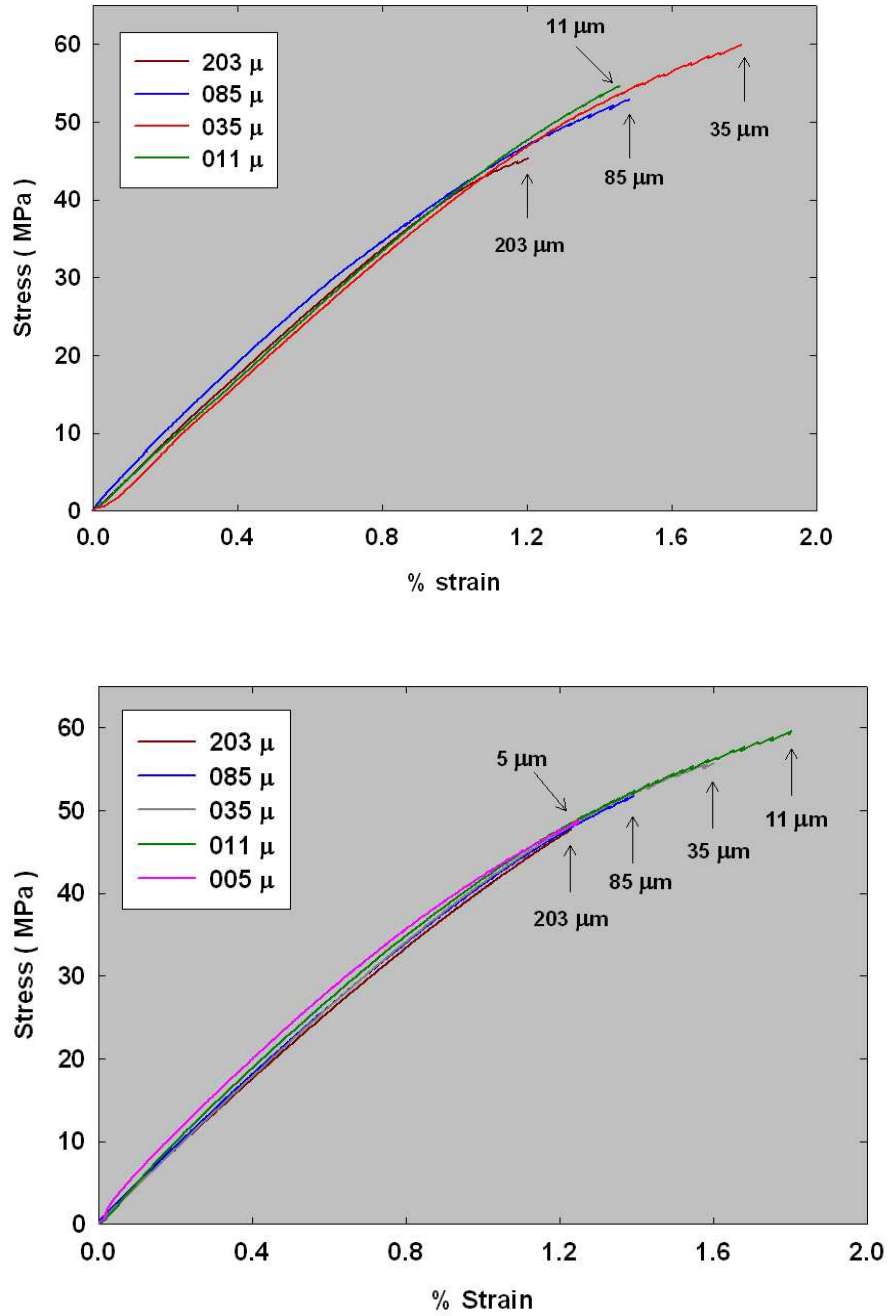


Figure 3.3: Stress-strain behavior under quasi-static loading condition in spherical glass particle filled epoxy, $V_f = 0.1$, (a) uncoated particles (b) silane treated particles.

σ_f and ϵ_f vary with particle sizes and filler-matrix adhesion strength. Identification of an initial linear stress-strain behavior is relatively difficult due to slack in the grips. Therefore, the data in the strain range from 0.0025 to 0.007 was chosen to define the elastic modulus. In this region the slope of a linear fit has been identified as elastic modulus values. Both elastic and failure properties are reported in Table 3.2. It can be noticed from the table that particle size or filler coating has a negligible effect on elastic modulus. For all particle sizes, coated and uncoated, elastic modulus ranges between 4.1 *GPa* and 4.2 *GPa*. The variation of failure stress and failure strain with particle size are plotted in Fig. 3.4(a) and (b), respectively. For both, failure properties vary non-monotonically with particle size and variations seem nonmonotonic. The coated particles show maximum σ_f and ϵ_f for 11 μm particle size. With a decrease or increase in particle size relative to this size, failure properties seem to decrease monotonically. Similar non-monotonic variation in σ_f and ϵ_f with particle size have been noticed for weakly bonded particles too, except that the optimum particle size for maximum failure stress and strain is now shifted to 35 μm .

For comparison purposes stress-strain behavior of neat epoxy ($E = 3.5 \text{ GPa}$, $\sigma_f = 68.21 \text{ MPa}$, $\epsilon_f = 2.24\%$) is shown in Figures 3.3(a) and (b). Both failure stress and strain show higher values when compared to the filled material. However, an average elastic modulus for filled composite (10% V_f) is 20% higher when compared to unfilled epoxy.

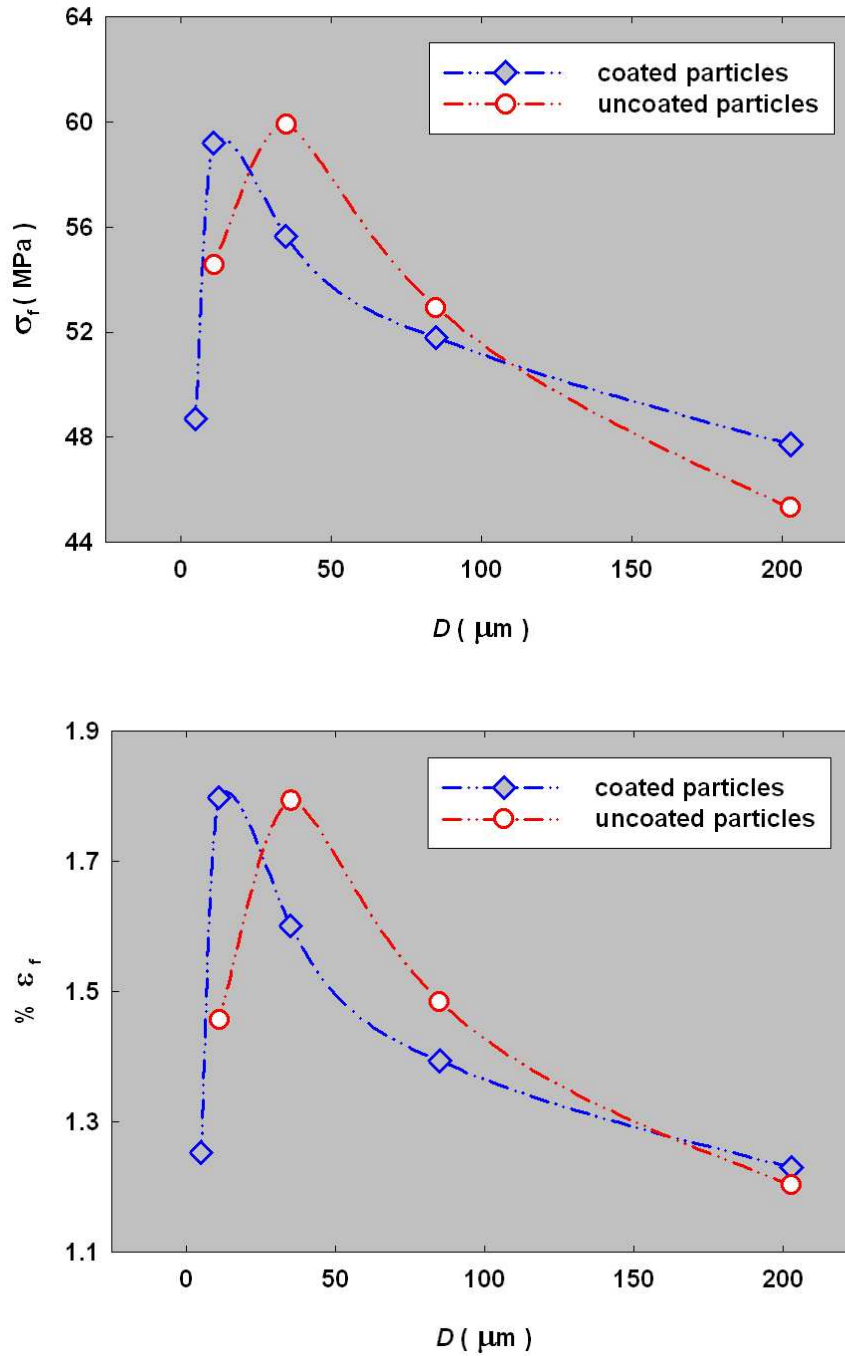


Figure 3.4: Particle size and filler-matrix adhesion effect on failure properties of particle filled epoxy under quasi-static loading condition, $V_f = 0.1$, (a) Failure stress variation with particle size (b) Failure strain variation with particle size.

Average particle size (μm)	weakly bonded particles			strongly bonded particles		
	Failure stress σ_f	% Failure strain ϵ_f	Elastic modulus E (MPa)	Failure stress σ_f	% Failure strain ϵ_f	Elastic modulus E (MPa)
203	45.31	1.20	4161	47.72	1.23	4075
85	52.93	1.48	4200	51.79	1.39	4133
35	59.89	1.79	4150	55.65	1.60	4204
11	54.56	1.46	4195	59.18	1.80	4177
5	–	–	–	48.71	1.25	4175

Table 3.2: Elastic and failure properties (quasi-static) of glass-filled epoxy particulate composite (weakly and strongly bonded particles at $V_f = 0.1$).

3.5 Material properties: pulse-echo measurements

Longitudinal and shear wave speeds (C_l and C_s) were measured in cast sheets by *pulse-echo technique* at discrete locations of the cured material. Transit time for the pulse to travel was twice the thickness of the sample measured with the help of a digital oscilloscope (Gould model 5052UA), a longitudinal wave transducer (Panametrics# V129RM; 10 MHz) and a shear wave transducer (Panametrics# V156RM; 5 MHz). The mass density of the material was also determined using conventional measurements. Subsequently, dynamic elastic modulus E_d and Poisson's ratio ν_d were calculated using,

$$C_l = \sqrt{\frac{E_d(1 - \nu_d)}{\rho(1 + \nu_d)(1 - 2\nu_d)}}, \quad C_s = \sqrt{\frac{E_d}{2\rho(1 + \nu_d)}}, \quad (3.2)$$

where ρ is the mass density of the composite. From the Table 3.3 it can be noticed that longitudinal and shear wave speeds for all the particle sizes (coated/uncoated) have been measured to be $2550 \pm 20 \text{ m/sec}$ and $1180 \pm 10 \text{ m/sec}$, respectively. Nearly the

Avg particle diameter D (μm)	Density ρ (kg/m^3)	Longitudinal wave speed C_l (m/sec)	Shear wave speed C_s (m/sec)	Elastic modulus E_d (GPa)	Poisson's ratio ν_d
203*	1279	2567	1174	4.83	0.368
71*	1282	2585	1182	4.90	0.368
35*	1296	2550	1172	4.87	0.366
11*	1291	2561	1188	4.97	0.363
7*	1298	2581	1183	4.97	0.367
203**	1286	2536	1181	4.89	0.361
35**	1285	2535	1172	4.82	0.364
11**	1278	2577	1190	4.94	0.365
203+35*	1292	2536	1173	4849	0.36
203+11*	1278	2558	1175	4822	0.37
epoxy	1132	2468	1109	3.82	0.374

Table 3.3: Material properties (dynamic) of weakly bonded (uncoated) and strongly bonded (silane coated) glass fillers in epoxy matrix, $V_f = 0.1$ (* uncoated particles, ** silane treated particles, + mixture of two different particle sizes).

same wave speeds and material densities lead to similar dynamic elastic modulus and Poisson's ratio. Average values of $E_d = 4.9 GPa$ and $\nu_d = 0.365$ have been obtained.

For studying particle size distribution effects, sheets with 5% V_f of 203 μm and 35 μm each and 203 μm and 11 μm each (all uncoated) were also characterized using pulse-echo measurements. These show nearly the same dynamic elastic properties, as noticed for materials with single particle size. Therefore, from the table it can be concluded that dynamic elastic properties remain unaffected by filler size variation.

For comparison purposes a cured unfilled epoxy specimen was also characterized in a similar manner and material density, wave speeds and dynamic elastic properties are listed in Table 3.3. The measured density of the unfilled epoxy is lower than the filled composite, which causes lower longitudinal and shear wave speeds. The average dynamic elastic modulus for filled material is about 30% higher when compared to the value of

3.82 *GPa* for neat epoxy. The ν_d for unfilled epoxy has been found to be marginally increased to 0.37 when compared to 10% V_f glass-filled composite.

CHAPTER 4

DYNAMIC FRACTURE OF PARTICULATE COMPOSITES¹

As discussed previously, microstructure plays a vital role on fracture behavior of particulate composites. At a constant volume fraction, microstructural variations can exist in filler shape and size, particle size bimodality, and filler-matrix adhesion strength. Few studies in this regard have been reported in the literature, particularly under dynamic loading conditions. In this chapter fracture behavior of particulate composite with different particle sizes, filler-matrix adhesion strengths and filler size bimodality is described.

4.1 Experimental Details

The fracture investigations were performed under dynamic loading conditions. The specimens were subjected to low-velocity impact ($\sim 5.3 \text{ m/sec}$). The full field shearing interferometric technique (CGS) was employed to observe the evolution of deformations during fracture. Fringe contours representing surface slopes in the direction of initial crack orientation are recorded using high-speed photography. Interference fringes are the outcome of stress waves due to impact which travel back and forth across the sample, loading the notch tip to crack initiation. The crack subsequently propagates dynamically, at speeds of up to 530 m/sec depending upon the type of the filler. The fringes were analyzed to determine to calculate instantaneous mode-I stress intensity factors during fracture.

¹ *Parts of this chapter appear in Ref. [52, 105]*

The qualitative analysis of interference fringes from dynamic experiments is reported next. Three different sets of experiments are described. First, the specimens with weakly bonded fillers are considered to study the particle size effect. Second, specimens with silane coated particles are tested to examine filler-matrix adhesion strength effect. And finally, the experiments are conducted on specimens with two different filler sizes (each of 5% V_f) to study particle size distribution (bimodality) effect.

4.1.1 Weakly bonded particles

Optical interference fringes obtained from CGS and high-speed photography are shown in Fig. 4.1. Highly discernible fringes on the specimen surface near the impact point and the crack tip are evident. The first set of four fringes in Fig. 4.1(a) are for 11 μm particles, next four in Fig. 4.1(b) for 35 μm and third set in Fig. 4.1(c) for 203 μm particles, all for weakly bonded fillers in the matrix. In each set, the first two images are for pre-crack initiation instants and the last two are from post-initiation time instants. Impact point fringes (at the top of every image) develop and accumulate soon after the impactor contacts the specimen, while the crack tip fringes start appearing about 35 – 40 μsec after initial impact. As stress waves reach the crack tip, tri-lobed fringes, symmetric with respect to the crack representing mode-I deformations, start evolving around the crack tip. The second image in each set is a fringe pattern acquired just before crack initiation. At initiation, sudden release of energy results in stress waves emanating from the crack tip seen as a circular discontinuity in an otherwise continuous fringe pattern centered at the initial notch tip (third image of each set). After initiation, nearly stable crack growth ensures for about 40 – 60 μsec . This is followed by a monotonic

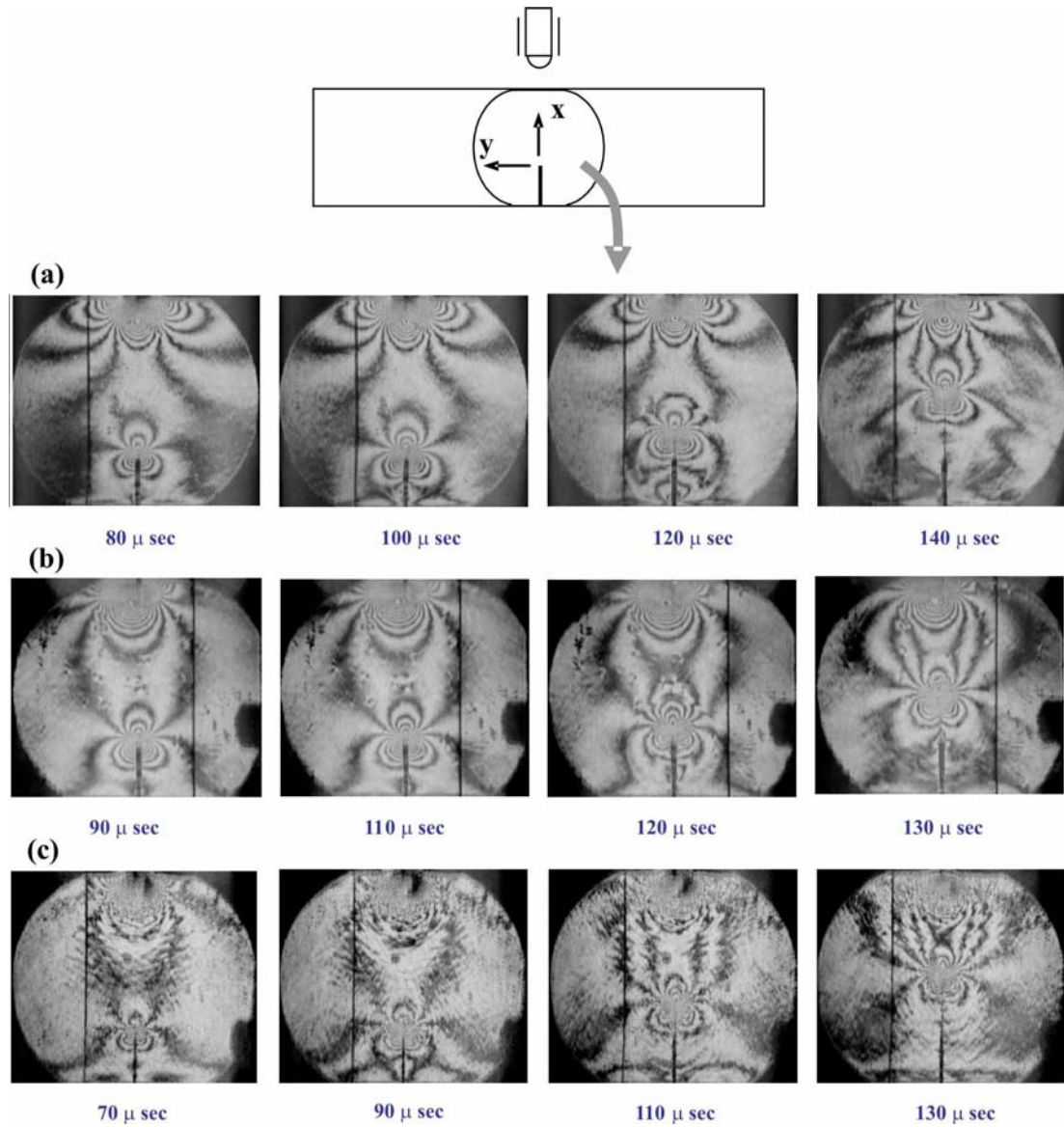


Figure 4.1: Selected fringe pattern representing surface slope contours of $\delta w / \delta x$ for glass-filled epoxy specimens with weakly bonded filler, (a) 11 μm particles, (b) 35 μm particles and (c) 203 μm . Indicated time corresponds to the instants after impact.

reduction in the size of fringe lobes. These fringes represent contours of $\partial w/\partial x$ where w is out-of-plane displacement. The resolution of the fringes is $\approx 0.015^0/fringe$. In the case of $203\ \mu m$ diameter fillers, fringes are relatively lower quality due to larger scale of heterogeneities.

4.1.2 strongly bonded particles

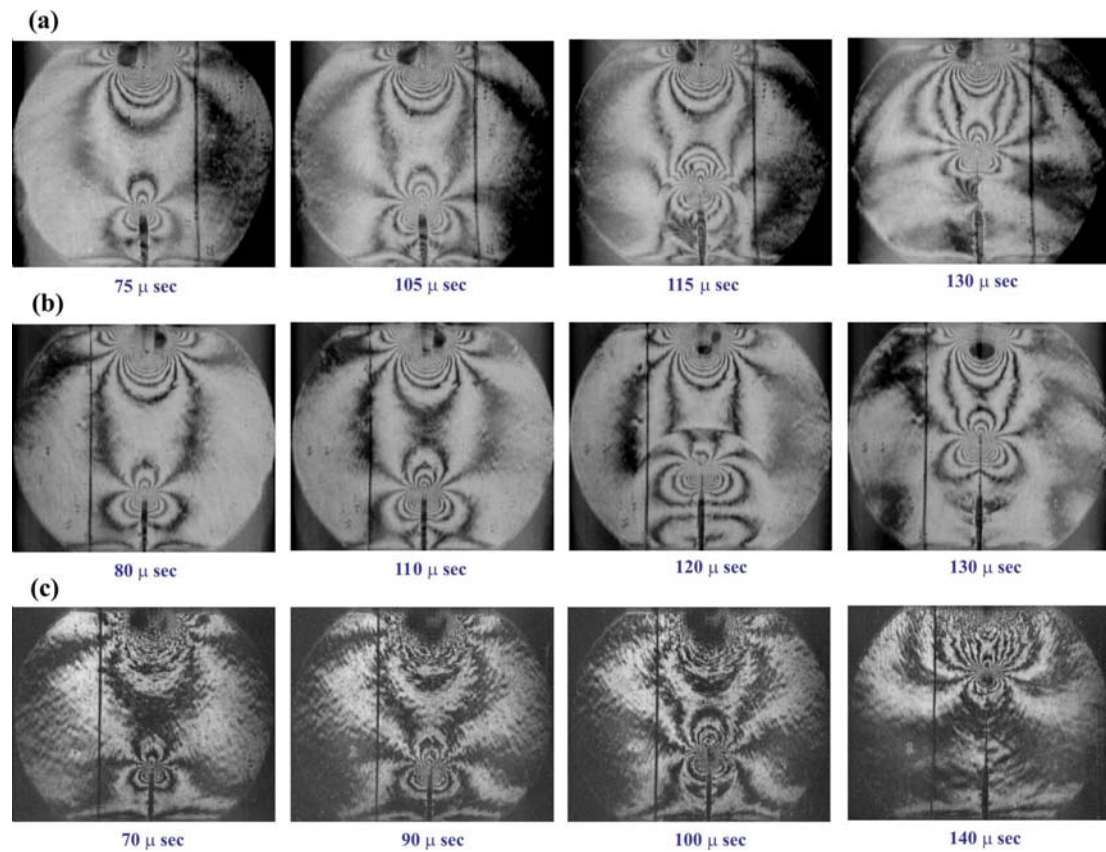


Figure 4.2: Selected fringe pattern representing surface slope contours of $\delta w/\delta x$ for glass-filled epoxy specimens with strongly bonded fillers, (a) $11\ \mu m$ particles, (b) $35\ \mu m$ particles and (c) $203\ \mu m$. Indicated time corresponds to the instants after impact.

Figure 4.2 shows representative interferograms from specimens with coated (strongly bonded) particles. Three different sets of fringes shown in the figure are for specimens

with $11\ \mu\text{m}$ (a), $35\ \mu\text{m}$ (b) and $203\ \mu\text{m}$ (c) particle sizes, respectively. Highly discernible impact point fringes and crack tip fringes for both pre- and post-crack initiation instants can be noticed. The time instants shown represent the time span after the impact takes place. The impact point and crack-tip fringes evolve monotonically until the crack initiates. Following crack initiation, crack-tip moves in a stable fashion for some time and then monotonically decrease in size. A third image in each set is for the time instant just after the crack initiation which shows an emerging stress wave from the initial notch tip as a circular discontinuity similar to the case of weakly bonded fillers. Once again the specimen with $203\ \mu\text{m}$ diameter fillers shows lower quality fringes due to larger scale of heterogeneities.

4.1.3 Mixed weakly bonded particles

It will be discussed in the following sections that fracture behavior is nearly unaffected by particle sizes for the case of strongly bonded fillers. Weakly bonded fillers, on the other hand, show discernible particle size effect with maximum and minimum fracture toughness correspond to $35\ \mu\text{m}$ and $203\ \mu\text{m}$ particles, respectively. Therefore, to examine the effect of bimodal particle size distribution on fracture parameters, these two (uncoated particle) sizes were chosen. Also, for comparison purposes specimens with bimodal distribution of $11\ \mu\text{m}$ and $203\ \mu\text{m}$ fillers were also tested.

Figure 4.3 shows interference fringes for specimens with $35+203\ \mu\text{m}$ and $11+203\ \mu\text{m}$ fillers. Note that the '+' sign represents mixed particles of two different sizes, each of $5\% V_f$ resulting in total filler volume fraction of 10% in the composition. In both sets first two images are from before crack initiation, while the next two are for the propagating

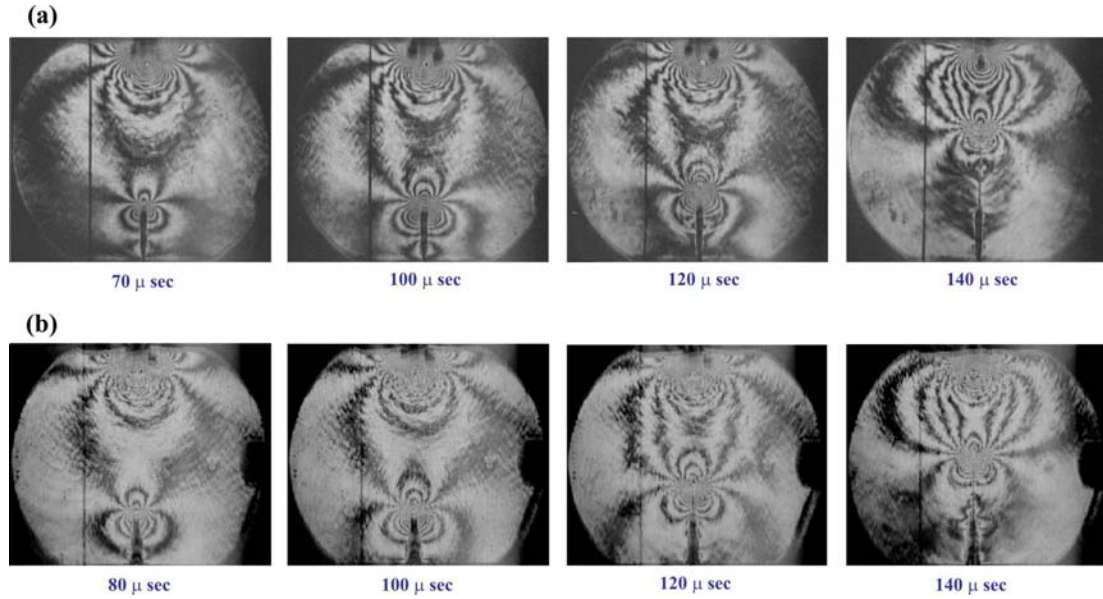


Figure 4.3: Selected fringe patterns representing surface slope contours of $\delta w/\delta x$ for glass-filled epoxy specimens with (a) $35 + 203 \mu m$ fillers and (b) $11 + 203 \mu m$ fillers. Two different particle sizes are mixed in $5\% V_f$ each. Legends correspond to the time instants after impact.

crack. Fringe patterns are quite similar to the ones seen in case of specimens with single particle size (see Figs.4.1 and 4.2). The smeared appearance in fringes results from the larger size fillers in the mixture. Emanating stress waves from the crack tip at initiation can be noticed as well.

4.2 Experimental repeatability

In this section results from experiments to demonstrate the repeatability and robustness of the experimental methodology adopted for macro scale optical measurements is presented. Figure 4.4(a) shows crack growth histories for two different specimens with $35 \mu m$ uncoated particles as the filler. Both sets of data show crack initiation at $105 \mu sec$ with an experimental accuracy of $5 \mu sec$. An instantaneous increase in velocities up to

about 400 m/sec can be noticed initially. The sudden release of energy from the initial notch results in such a rapid acceleration to about $4 \times 10^7 \text{ m/sec}^2$ (~ 4 million ‘g’s) and a maximum velocity (v_{max}) of about 30% of the Rayleigh wave speed for the material following crack initiation. The record shows a drop in velocity following this initial acceleration to a steady state value (v_{ss}) of approximately 300 m/sec . The steady state crack growth region is followed by a continuous drop in velocity as the free surface and impact points are encountered by the propagating crack tip. The specimen fracture is complete at $\sim 260 \mu \text{ sec}$ in both the specimens.

The stress intensity factor histories for the same two specimens with $35 \mu\text{m}$ uncoated filler particles are shown in Fig. 4.4(b). In each case the stress intensity factors increase monotonically upto crack initiation. As is evident from the figure, pre-initiation stress intensity factor histories for both specimens essentially coincide. The rate of increase of stress intensity factor (dK_I/dt) until crack initiation is $\sim 34 \times 10^3 \text{ MPa}\sqrt{\text{m}}/\text{sec}$. In both the experiments the crack has initiated at $\sim 105 \mu\text{sec}$ and crack initiation toughness $K_{Ii} \sim 2.5 \text{ MPa}\sqrt{\text{m}}$. Crack initiation is associated with a sudden drop in stress intensity factor which can be noticed in the figure. The maximum value of K_I just before the drop is identified as K_{Ii} . Further, instantaneous values of post-crack initiation stress intensity factors show an oscillatory behavior due to discrete wave reflections driving the crack forward during the failure event. Additionally, oscillations can also be attributed to the micro structural inhomogeneities (It should be noted that such oscillations occur even in monolithic materials such as neat epoxy, to be discussed later). Intermittent interactions with particles and continuously varying arrangement of particle clusters around the propagating crack also gives rise to different amounts of crack-tip shielding[41,

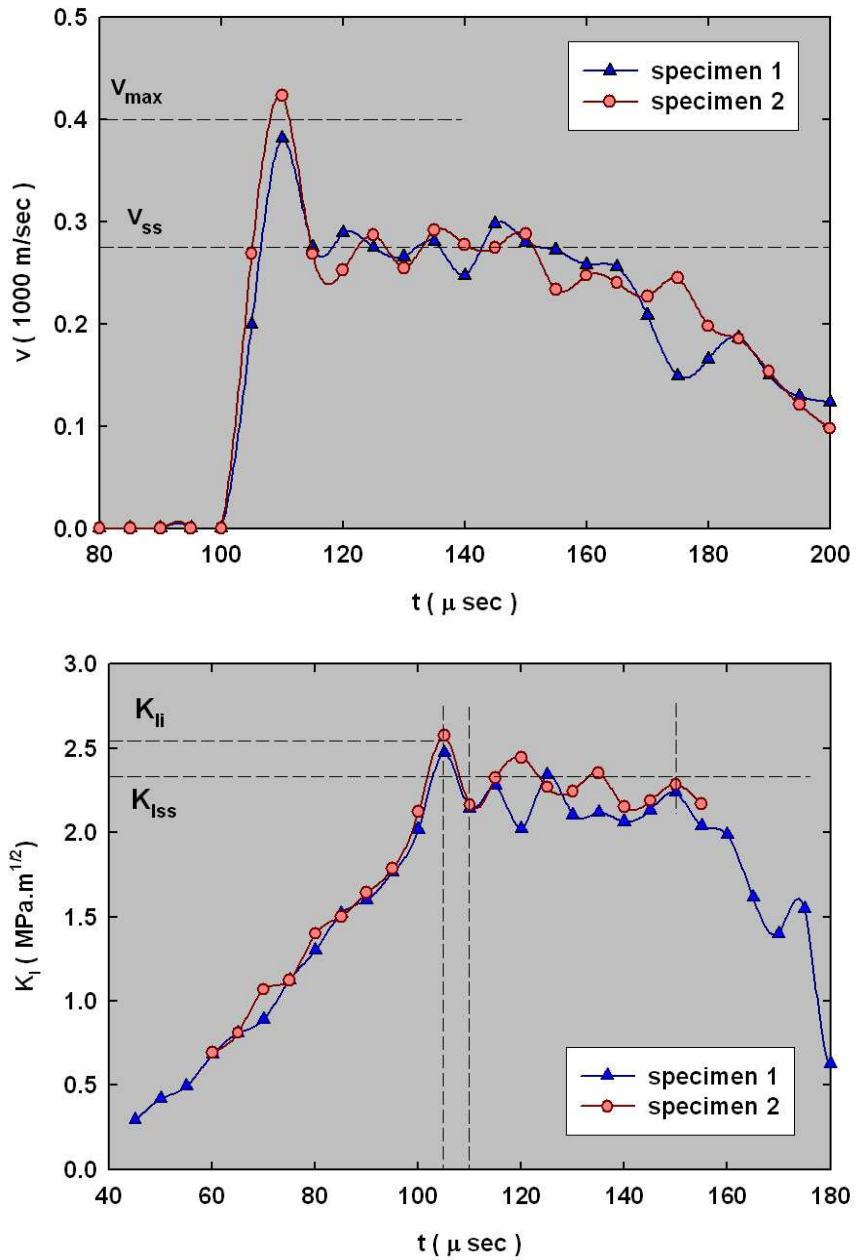


Figure 4.4: Crack velocity history (a), and stress intensity factor histories for two identical specimens with $35 \mu\text{m}$ uncoated filler particles demonstrating repeatability of experimental measurements.

42] and different failure mechanisms[32]. These in turn affect crack velocity as well as stress intensity factor histories. The post crack initiation oscillations continue for about $50 \mu\text{sec}$. The average value of stress intensity factor for this period is identified as steady state fracture toughness $K_{I_{ss}}$ values of the material. For both the specimens, their post-crack initiation steady state fracture behaviors are nearly similar, with a $K_{I_{ss}}$ of $\sim 2.35 \text{ MPa}\sqrt{\text{m}}$. The steady state behavior is followed by a monotonic drop in K_I until the specimen fractures completely. The accuracy of fringe analysis beyond $160 \mu\text{sec}$ is relatively low due to severe interaction between crack tip and impact point deformation fields which affect crack tip K-dominance.

Similarity of pre- and post-initiation behaviors for crack tip velocity and stress intensity factor histories in multiple specimens suggest the robustness and repeatability of the experiments and the method employed in this study. Similar repeatability tests have also been undertaken successfully for several other particle sizes and interfacial strengths and are not reported here.

4.3 Particle size effect

4.3.1 Weakly bonded (uncoated) particles

Crack velocity histories for specimens with weakly bonded fillers are shown in Fig. 4.5(a). Only the results for $11 \mu\text{m}$, $35 \mu\text{m}$ and $203 \mu\text{m}$ sizes are shown in order to avoid data clutter and consistent comparison with strongly bonded fillers to be presented in the next section. In each case crack velocity history shows rapid increase in velocity at crack initiation reaching a maximum value v_{max} , followed by a noticeable drop. Subsequently, crack velocity is oscillatory about an average value identified as steady state velocity,

Particle diameter D (μm)	Crack initiation time t_i (μsec)	Maximum crack velocity v_{max} (m/sec)	Steady state crack velocity v_{ss} (m/sec)	Steady state duration t_{ss} (μsec)	Crack initiation toughness K_{Ii} ($MPa\sqrt{m}$)	Steady state fracture toughness K_{Iss} ($MPa\sqrt{m}$)
203	95-100	325	310	55	1.89	1.67
71	100-105	341	300	50	2.19	1.92
35	105-110	382	285	45	2.48	2.31
11	100-105	464	345	35	2.25	1.96
7	110-115	493	370	25	1.97	1.87
epoxy	125-130	350	325	45	2.28	1.5

Table 4.1: Crack growth parameters for glass-filled epoxy with weakly bonded filler ($V_f=0.1$)

v_{ss} . Some of these observations about crack initiation and growth are quantified in Table 4.1. The maximum crack velocity and acceleration at crack initiation increases as the particle size decreases. In the current study the maximum velocity ranges between $\sim 325 m/sec$ for the largest particles to $\sim 500 m/sec$ for the smallest. The acceleration at crack initiation is of the order of $10^7 m/sec^2$. As the particle size decreases, duration of steady state crack growth, t_{ss} , decreases. That is, t_{ss} is the least for the smallest particle size and longest for the largest particle size. It is noticed in these experiments that specimen fracture is complete at nearly the same time, $\sim 260 \mu sec$, irrespective of the particle size. As the particle size decreases, maximum velocities increase. Since all specimens took same time to fail completely, the duration of steady state growth t_{ss} decreases for smaller particles at the cost of higher maximum velocities. Table 4.1 shows minimum steady state velocity in case of $35 \mu m$ particles. Further increase or decrease in particle size only results in an increase in steady state velocity. This interesting velocity trend, which can be related to steady state fracture toughness, will be discussed later on.

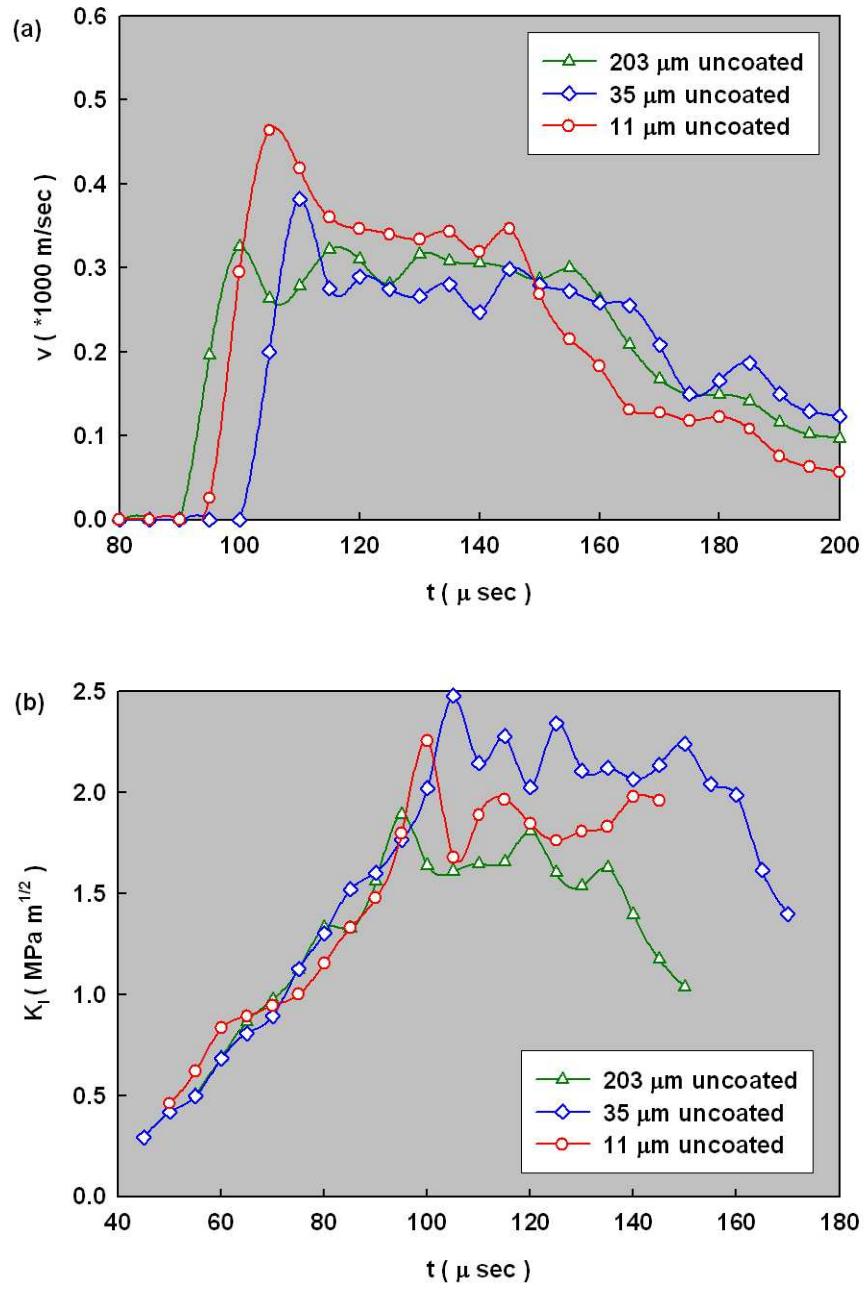


Figure 4.5: Crack velocity histories (a), and stress intensity factor histories (b) for different glass-filled epoxy specimens with weakly bonded (uncoated) particles.

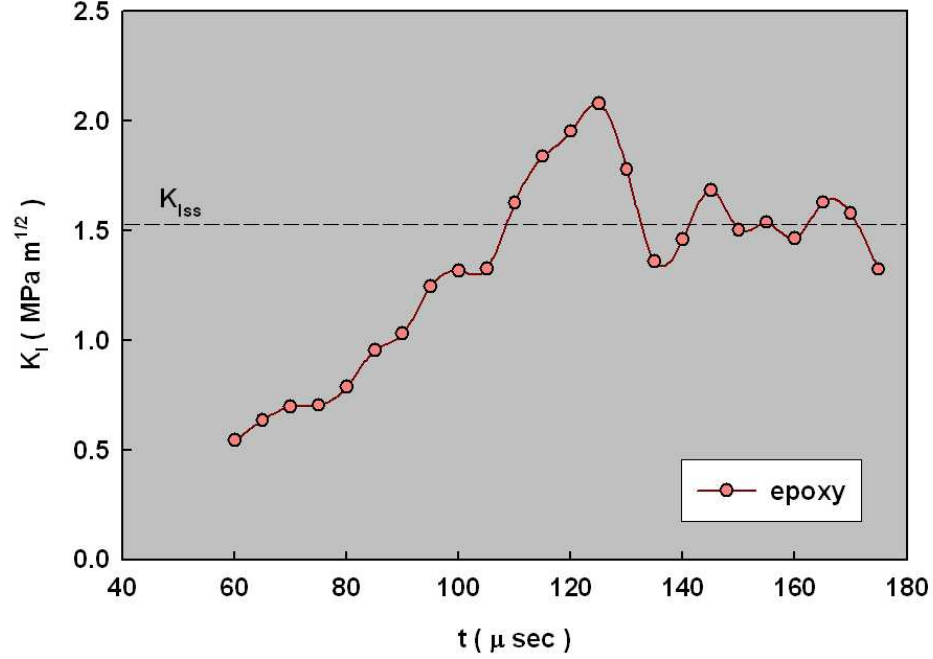


Figure 4.6: Stress intensity factor history for neat epoxy.

Stress intensity factor histories for specimens with weakly bonded particles (same particle sizes as in Fig. 4.5(a), for consistency) of various particle sizes are shown in Fig. 4.5(b). For each particle size, stress intensity factors monotonically increase until crack initiation. The average rate of increase dK_I/dt in each case is $\sim 32 \pm 3 \text{ MPa}\sqrt{\text{m}}/\text{ms}$. The similarity of pre-initiation stress intensity factor histories suggest nearly same crack tip loading rate. This in turn can be attributed to similar macroscopic elastic wave characteristics (Table 3.3) irrespective of particle size and filler-matrix adhesion strength. The crack initiation time varies from $95 \mu\text{sec}$ to $115 \mu\text{sec}$ for different particle sizes considered. In each case, crack initiation is followed by a small drop in K_I value followed by

a sustained oscillatory behavior about an average. Notations K_{Ii} and K_{Iss} will henceforth be used for maximum and steady state fracture toughness values, respectively. The K_{Ii} and K_{Iss} values for all weakly bonded particles are also tabulated in Table 4.1. The steady state fracture toughness of unfilled epoxy ($\approx 1.5 \pm 0.1 MPa\sqrt{m}$) is considered as a reference for further comparisons (see Fig. 4.6² and Table 4.1). Specimens with $35 \mu m$ particles show the value of K_{Iss} to be the highest, which is approximately 65% higher when compared to the one for neat epoxy. With a decrease or an increase in particle sizes relative to $35 \mu m$ size, K_{Iss} shows decreasing trend. Specimens with $11 \mu m$ particles show 40% and $7 \mu m$ particles show 34% higher fracture toughness, respectively, compared to the neat epoxy. From Table 4.1 it can be noticed that both $11 \mu m$ and $7 \mu m$ show similar stress intensity factor behaviors, with a relatively small difference in K_{Iss} suggesting possible saturation of fracture toughness as particle size decreases. Similar effects have been noticed when particle size is increased beyond $35 \mu m$. Specimens with $71 \mu m$ and $203 \mu m$ particles show approximately 37% and 18% increase in fracture toughness compared to the neat epoxy, which is successively lower compared to the ones with $35 \mu m$ particles. Figure 4.7 summarizes particle size effect on K_{Iss} in case of weakly bonded filler at 10% volume fraction. Evidently, there is a discernible optimum particle size at which fracture toughness is maximum for the selected volume fraction. As the particle size increases or decreases relative to this optimum value, steady state fracture toughness decreases. Quite interestingly, the optimum particle size for maximum steady state fracture toughness also corresponds to the minimum steady state velocity. With

²Stress intensity factor history for neat epoxy is shown in Fig. 4.6 for completeness. The overall features here are similar to the ones shown for glass-filled specimens. That is, a monotonic increase ($dK_I/dt \sim 25 MPa\sqrt{m}/ms$) in K_I up to initiation is followed by a drop and a steady state value at around $\sim 1.5 MPa\sqrt{m}$ can be seen.

a decrease or an increase in particle size relative to this optimum value, monotonic reduction in fracture toughness is accompanied by a monotonic increase in steady state velocity occurs. That is, an inverse relationship between steady state velocity and fracture toughness seems to exist as shown in Fig. 4.8. From Table 4.1 it can also be noticed that K_{Ii} trends are similar to that of $K_{I_{ss}}$. The trends again show optimum particle size to be $35 \mu m$. Further, K_{Ii} value is higher by 35%, 56%, 77%, 61% and 41% for $203 \mu m$, $71 \mu m$, $35 \mu m$, $11 \mu m$ and $7 \mu m$, respectively, when compared to the neat epoxy. This is similar to the decreasing trend in fracture toughness for particle sizes below $35 \mu m$ reported by Nakamura *et al.*[16, 17], who have studied the particle size effect in silica filled epoxy in $2 \mu m$ to $42 \mu m$ particle range.

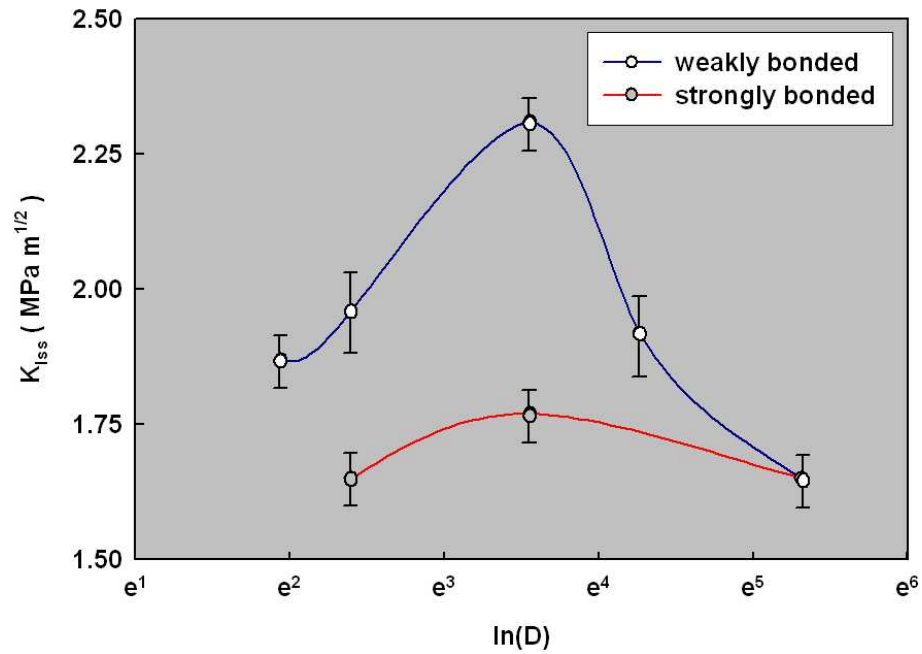


Figure 4.7: Particle size effect on steady state fracture toughness of glass-filled epoxy.

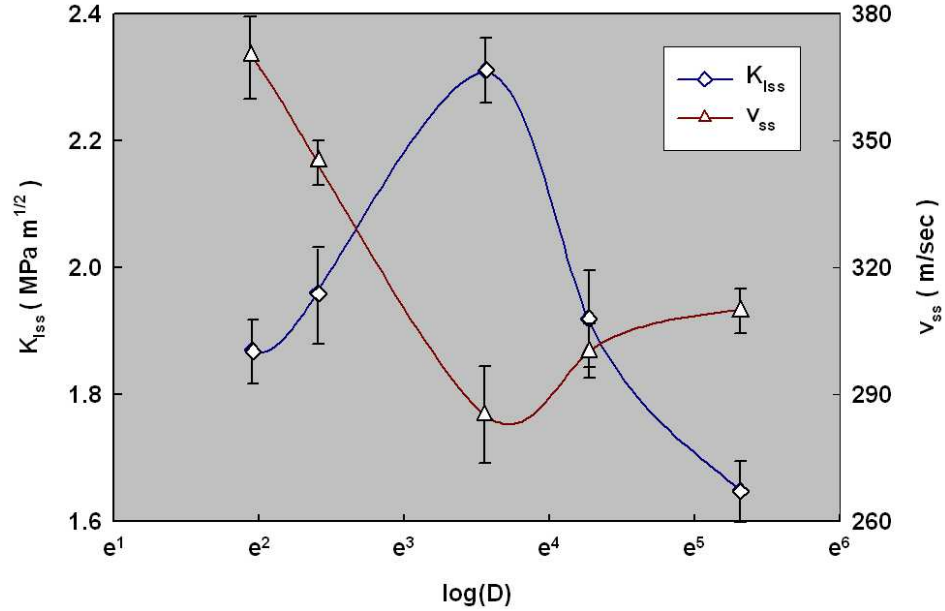


Figure 4.8: Variation in steady state velocity and fracture toughness with particle size in glass-filled epoxy with weakly bonded fillers.

4.3.2 Strongly bonded (silane treated) particles

To study the particle size effect on fracture behavior in case of silane treated fillers, experiments have been performed on three particle sizes, $203 \mu m$, $35 \mu m$ and $11 \mu m$. The selection of particle sizes here is limited due to the commercial availability. Figures 4.9(a) and (b) show crack velocity and stress intensity factor histories. For each particle size, crack velocity variations show rapid increase at initiation, with an estimated acceleration of the order of $\sim 10^7 m/sec^2$, for all three particle sizes. As in case of uncoated particles, maximum velocity (v_{max}) is followed by a noticeable drop and a steady but oscillatory behavior with an average value denoted by v_{ss} . From Table 4.2 it can be noticed that both v_{max} and v_{ss} increase as particle size decreases. The duration of steady state crack

Particle diameter D (μm)	Crack initiation time t_i (μsec)	Maximum crack velocity v_{max} (m/sec)	Steady state crack velocity v_{ss} (m/sec)	Steady state duration t_{ss} (μsec)	Crack initiation toughness K_{Ii} ($MPa\sqrt{m}$)	Steady state fracture toughness K_{Iss} ($MPa\sqrt{m}$)
203	95-100	366	312	35	1.79	1.65
35	105-110	428	320	30	1.93	1.77
11	105-110	536	375	15	1.73	1.65
epoxy	125-130	350	325	45	2.28	1.5

Table 4.2: Crack growth parameters for glass-filled epoxy with strongly bonded filler ($V_f=0.1$)

growth t_{ss} decreases with increase in steady state velocity and hence with decrease in particle size. Further, the steady state crack growth region is followed by a monotonic drop in crack velocity until complete fracture.

Similar to weakly bonded particles, stress intensity factor histories in Fig. 4.9(b) show monotonic increase in K_I until crack initiation for all particle sizes, with an average crack tip loading rate dK_I/dt of $30 \pm 3 MPa\sqrt{m}/ms$. As before, crack initiation is followed by a small drop in K_I and a steadily oscillatory value identified by mean K_{Iss} value. Unlike weakly bonded particles, strongly bonded particles do not show significant variation in K_{Iss} as particle size is varied. From stress intensity factor histories in Fig. 4.9(b) and Table 4.2 it is quite clear that steady state fracture toughness values for various particle sizes are rather close to each other (within the margin of measurement error), suggesting only a marginal effect of particle size on fracture toughness in case of strongly bonded particles. Specimens with $35 \mu m$ particles again show slightly higher fracture toughness when compared to the other two particle sizes. Since silane treatment increased the filler-matrix interface strength, one can hypothesize that for ideal

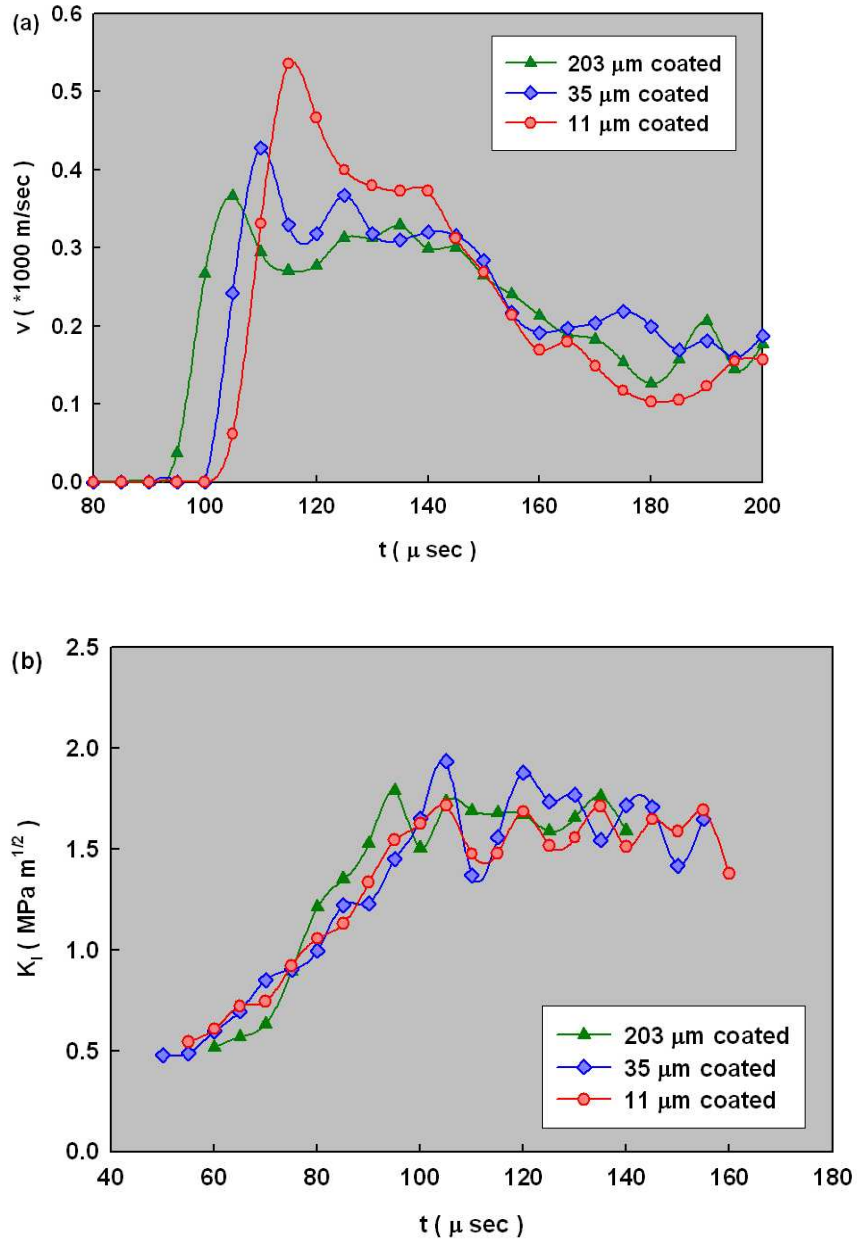


Figure 4.9: Crack velocity histories (a), and stress intensity factor histories (b) for different glass-filled epoxy specimens with strongly bonded (silane treated) particles.

filler-matrix interface strength, particle size effect on dynamic fracture toughness would potentially vanish.

4.4 Filler-matrix adhesion strength effect

From Tables 4.1 and 4.2 and Figs. 4.5(a) and 4.9(a) it can be concluded that increasing the filler-matrix interface strength increases the maximum as well as steady state crack velocities. Specimens with strongly bonded particles show 12-15% (8 – 10%) higher maximum (steady-state) velocities when compared to the ones with weakly bonded particles for similar particle sizes. As noted earlier for weakly bonded particles, steady state velocity shows an inverse trend with the duration of steady state velocity t_{ss} . For strongly bonded particles steady state velocities are marginally higher and hence have a smaller steady state duration compared to the case of weakly bonded particles. No discernible filler-matrix adhesion effect can be noticed regarding crack initiation time by comparing t_i for weakly and strongly bonded particles in Tables 4.1 and 4.2 for the same particle sizes.

The effect of filler-matrix adhesion on fracture toughness can be quantified from Table 4.1 and 4.2 and Figs. 4.5(b) and 4.9(b). Unlike weakly bonded particles, particle size does not affect fracture toughness significantly in case of strongly bonded filler. This suggests that increasing the filler-matrix adhesion affects the fracture toughness somewhat negatively under dynamic loading conditions, contrary to the conventional wisdom that increasing the filler-matrix bonding strength is generally beneficial. Some evidence of such a negative filler-matrix adhesion strength effect on fracture toughness

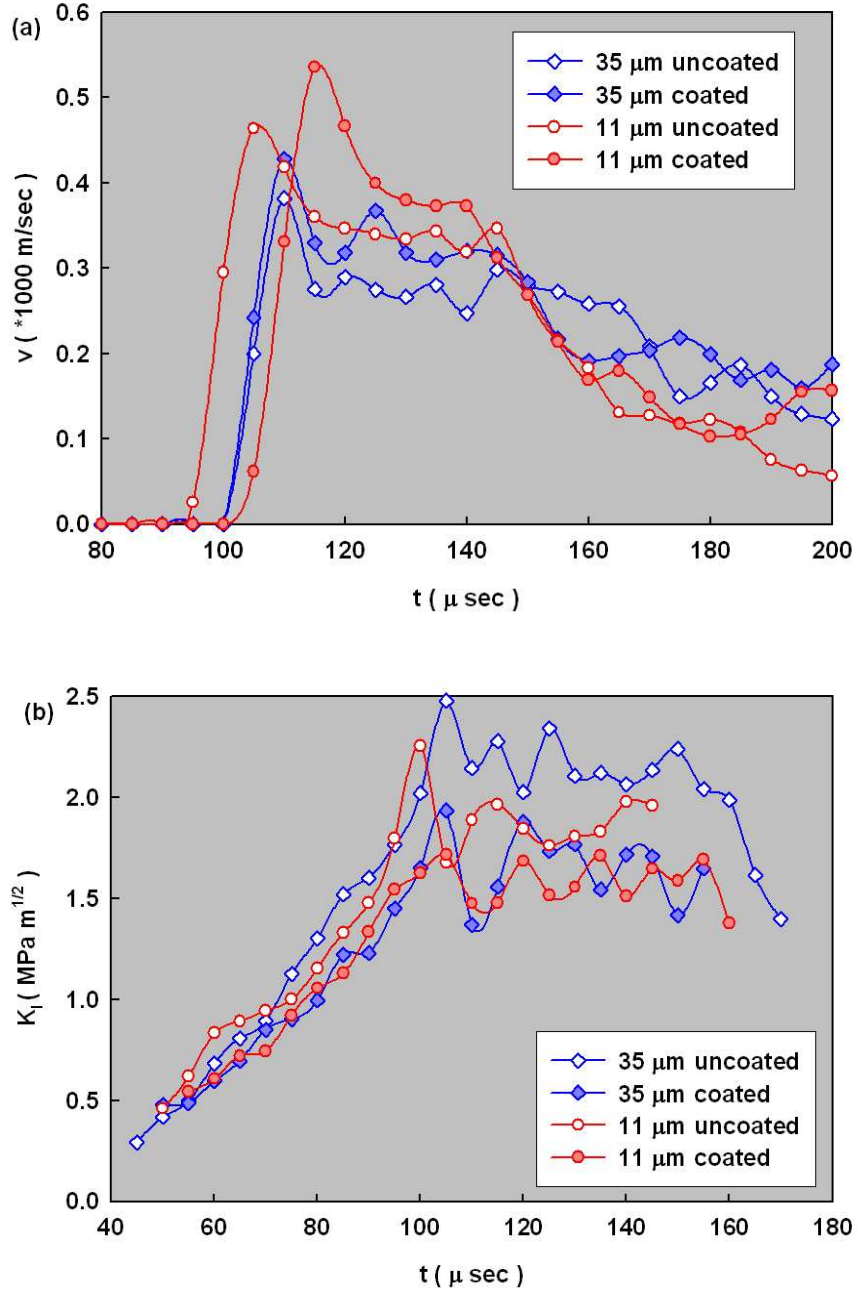


Figure 4.10: Filler-matrix adhesion effect on fracture behavior; Crack velocity history (a), and stress intensity factor histories (b) for 35 μm and 11 μm (coated and uncoated) particles filled epoxy, $V_f = 0.1$.

has also been seen by Moloney *et al.*[15] who have studied 40% silica filled epoxy in $60\ \mu\text{m}$ to $300\ \mu\text{m}$ range.

Figure 4.7 summarizes the particle size and filler-matrix adhesion effects. Error bars in the figure are based on multiple experiments. Figure shows the variation of $K_{I_{ss}}$ for strongly bonded fillers to be between 1.6 and $1.8\ \text{MPa}\sqrt{\text{m}}$. This suggests a relatively small particle size effect in the case of silane treated fillers. Also $K_{I_{ss}}$ values are consistently higher for uncoated particles even after considering the error bars. This negative filler-matrix adhesion effect decreases as the particle size departs more and more from the optimum value.

From Tables 4.1 and 4.2 it can be noticed that maximum increase in fracture toughness for weakly bonded filler is for $35\ \mu\text{m}$ particles, which is $\sim 30\%$ higher compared to strongly bonded $35\ \mu\text{m}$ particles. Weakly bonded $11\ \mu\text{m}$ particles show $\sim 18\%$ increase in $K_{I_{ss}}$ values relative to strongly bonded $11\ \mu\text{m}$ particles. Material with $203\ \mu\text{m}$ particles shows negligible effect of filler-matrix adhesion on fracture toughness. Similar trends can be noticed in regards to K_{I_i} , which are 5%, 30% and 30% higher for $203\ \mu\text{m}$, $35\ \mu\text{m}$ and $11\ \mu\text{m}$ weakly bonded particles as compared to strongly bonded ones.

4.5 Particle size (bimodality) distribution effect

Figure 4.11(a) shows the comparison of velocity history for mixed fillers of $35\ \mu\text{m}$ and $203\ \mu\text{m}$ sizes in diameter along with the ones for individual particle sizes. Similar to the case of single size filler particles, mixed fillers also show a rapid increase in velocity at initiation until it reaches a maximum value followed by a drop and a subsequent oscillatory behavior about an average. The steady state velocity is similar to those for

Average particle diameter D (μm)	Crack initiation time t_i (μsec)	Maximum crack velocity v_{max} (m/sec)	Steady state crack velocity v_{ss} (m/sec)	Steady state duration t_{ss} (μsec)	Crack initiation toughness K_{Ii} ($MPa\sqrt{m}$)	Steady state fracture toughness K_{Iss} ($MPa\sqrt{m}$)
35	105-110	382	285	45	2.5 ± 0.05	2.3 ± 0.05
35+203	105-110	394	295	50	2.3 ± 0.10	2.0 ± 0.10
203	95-100	325	310	55	1.9 ± 0.05	1.7 ± 0.04
11+203	100-105	408	335	40	2.2 ± 0.08	1.8 ± 0.05
11	100-105	464	345	35	2.3 ± 0.10	2.0 ± 0.08

Table 4.3: Crack growth parameters for glass-filled epoxy with single size filler particles and bimaterial mixtures with diffuse interface ($V_f=0.1$)

35 μm and 203 μm particle sizes and approximately bounded by those obtained in the monolithic configuration.

Figure 4.11(b) shows a comparison of stress intensity factor histories for mixed fillers (35 $\mu m + 203 \mu m$) with those for individual particle sizes. All show a monotonic increase in stress intensity factor until crack initiation. The average rate of increase in mixed fillers is $\sim 3.4 \times 10^4 MPa\sqrt{m}/s$, which is close to the ones with 35 μm and 203 μm filler particles. Similar crack tip loading rate in each case can again be attributed to similar macroscopic elastic properties (see Table 3.3). The crack initiates between 105 μsec and 110 μsec for the mixed particles. Both t_i and K_{Ii} for this case are very close to the respective values for 35 μm particles. Similar to 35 μm and 203 μm fillers crack growth in mixed filler specimen shows a drop in stress intensity factor at initiation followed by an oscillatory behavior. Some of the observations about velocity and stress intensity factor are quantified in Table 4.3. The steady state fracture toughness value for the the case of mixed filler particles ($\sim 2.0 MPa\sqrt{m}$) is between the respective values for

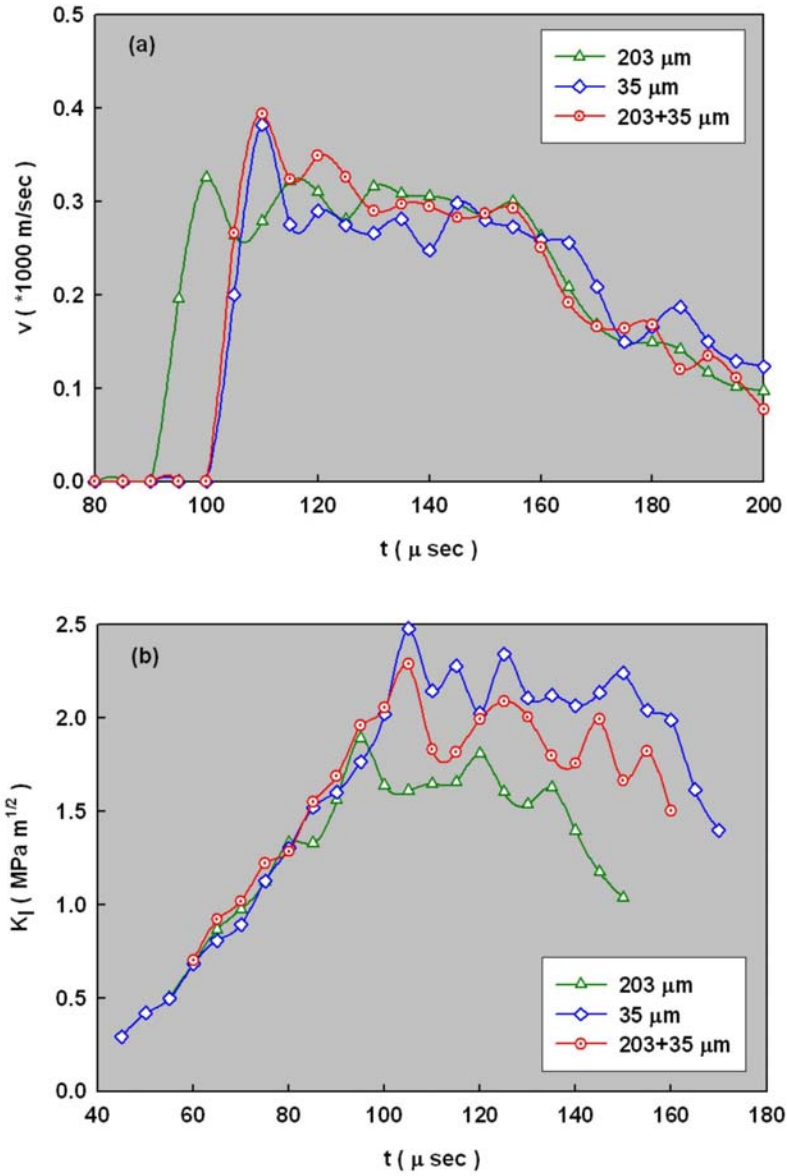


Figure 4.11: Crack velocity history (a), and stress intensity factor histories (b) in specimen with 35 + 203 μm mixed fillers (total $V_f = 10\%$). For comparison corresponding histories in specimens with single particle size are also shown.

samples with only $35\ \mu m$ and $203\ \mu m$ particles. Further, $K_{I_{ss}}$ for mixed filler is about 33% higher than that of the unfilled epoxy.

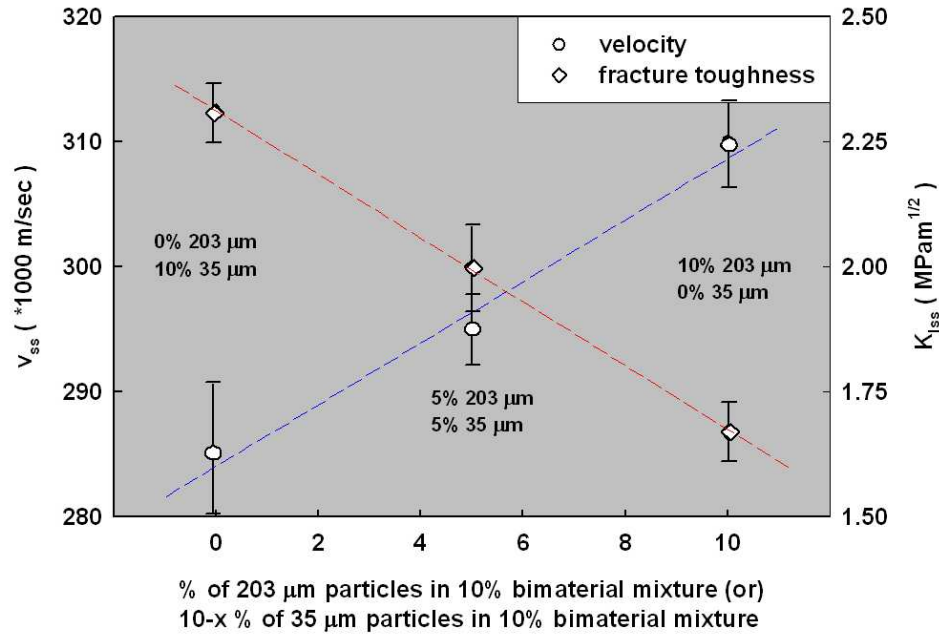


Figure 4.12: Steady-state fracture toughness and steady-state velocity variation with constituent filler percentage in 10% glass-filled epoxy specimens.

Figure 4.12 summarizes the effect of mixed particles on steady state fracture toughness and steady state crack velocity. Horizontal axis represents the volume fraction of $203\ \mu m$ particles in the mixture. The two vertical axes represent steady-state fracture toughness and velocity, respectively. The plot shows a nearly linear variation of $K_{I_{ss}}$ with V_f of the constituent particle sizes. Variation in v_{ss} with constituent particle volume fraction is not so discernible as $K_{I_{ss}}$ due to a relatively small velocity range. However, a monotonic variation of v_{ss} with constituent particle V_f is observable. Furthermore,

considering only the average of velocities, both v_{ss} and $K_{I_{ss}}$ plots show nearly linear variations with V_f of the constituent particle sizes but with opposite slopes, respectively. This is consistent with the inverse relationship between steady-state velocity and fracture toughness seen (Fig. 4.8) previously while studying particle size effect.

To further confirm the influence of particle sizes in the case of mixed fillers on crack velocity and fracture toughness, experiments were also performed on another specimen consisting of 203 and 11 μm particles at 5% V_f each. Table 4.3 shows the resultant steady state velocity and stress intensity factors. Similar to 203 + 35 μm filler mixture results, v_{ss} and $K_{I_{ss}}$ values for 203 + 11 μm particles mix specimen fall in between the respective values for those with only the respective reinforcement sizes. Both velocity and fracture toughness values vary monotonically with constituent volume fractions with opposite slopes (see Table 4.3). Steady state velocity and fracture toughness relationship is also monotonic with a negative slope as shown in case of 203 μm +35 μm mixture.

4.6 Comparison between static and dynamic fracture toughness

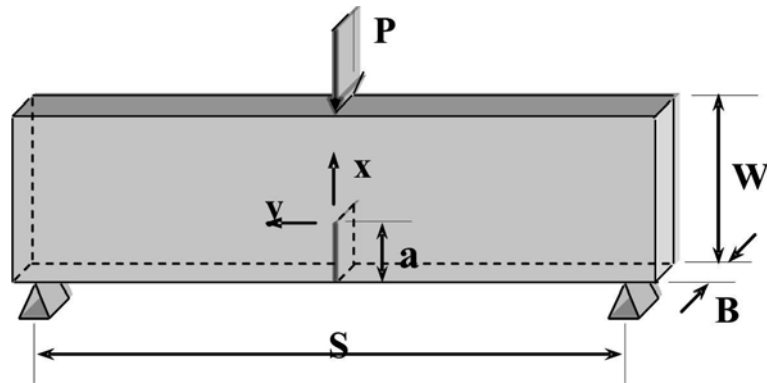


Figure 4.13: Quasi-statically loaded Single edge notch bend specimen ($S = 90\text{ mm}$, $W = 30\text{ mm}$, $B = 8\text{ mm}$).

Average particle dia. D (μm)	Static crack initiation toughness K_{Ic} ($MPa\sqrt{m}$)	Dynamic crack initiation toughness K_{Ii} ($MPa\sqrt{m}$)	Dynamic steady state fracture toughness K_{Iss} ($MPa\sqrt{m}$)
203	1.28 ± 0.15	1.9 ± 0.05	1.7 ± 0.04
85	1.65 ± 0.10	—	—
71	1.98 ± 0.05	2.2 ± 0.08	1.9 ± 0.08
35	3.36 ± 0.25	2.5 ± 0.05	2.3 ± 0.05
20	2.37 ± 0.10	—	—
11	1.69 ± 0.00	2.3 ± 0.10	2.0 ± 0.08
7	1.55 ± 0.05	2.0 ± 0.15	1.9 ± 0.05
epoxy	1.09 ± 0.05	2.3 ± 0.15	1.5 ± 0.10

Table 4.4: Crack growth parameters for uncoated (weakly bonded) glass-filled epoxy ($V_f=0.1$) showing loading rate dependence as well as particle size effect on fracture parameters

The investigation of particle size, filler-matrix adhesion strength and particle size distribution effect on dynamic fracture toughness for glass-filled epoxy composites with 10% filler volume fraction is described above. The results show nonmonotonic variation of K_{Iss} (see, Fig. 4.7) and K_{Ii} (see, Table 4.1 and 4.2) with particle size under dynamic loading conditions. Experiments also suggest an optimum particle size (35 μm in this study) for maximum fracture toughness with higher fracture toughness values for weakly bonded particles when compared to strongly bonded ones. An obvious question that arises from this result is, is the particle size effect on fracture behavior loading rate dependent? This necessitated experiments under quasi-static loading conditions and retrieve fracture parameters for different particle sizes to investigate the role of loading rate on fracture behavior.

Glass-filled epoxy (10% V_f) sheets were first prepared as described in Section 2.1. An edge notch of 5 mm nominal length was cut into the machined samples of the dimensions 90 mm x 30 mm x 8 mm. Next, a sharp crack of length 8 – 12 mm was grown in

Average particle dia. D (μm)	Static crack initiation toughness K_{Ic} ($MPa\sqrt{m}$)	Dynamic crack initiation toughness K_{Ii} ($MPa\sqrt{m}$)	Dynamic steady state fracture toughness K_{Iss} ($MPa\sqrt{m}$)
203	1.21 ± 0.01	1.79 ± 0.05	1.65 ± 0.05
85	1.26 ± 0.02	—	—
71	1.42 ± 0.08	—	—
35	2.25 ± 0.20	1.93 ± 0.20	1.77 ± 0.05
20	1.82 ± 0.01	—	—
11	1.86 ± 0.03	1.73 ± 0.30	1.65 ± 0.10
epoxy	1.09 ± 0.05	2.3 ± 0.15	1.5 ± 0.10

Table 4.5: Crack growth parameters for strongly bonded (silane treated) glass-filled epoxy ($V_f=0.1$) showing loading rate dependence as well as particle size effect on fracture parameters

the sample by forcing a wedge into the pre-cut notch until it ‘pops’ and arrests. These single edge notched bend, SENB (see 4.13), specimens were loaded in displacement control mode ($4.2 \times 10^{-6} m/sec$) in a symmetric three point bending configuration using INSTRON 4465 testing machine. The load at crack initiation was recorded and the crack initiation toughness, K_{Ic} , was calculated using the measured fracture load and the specimen geometry by[108],

$$K_I = \frac{3 \frac{PS}{BW^2} \sqrt{a}}{2 \left(1 + 2 \frac{a}{W}\right) \left(1 - \frac{a}{W}\right)^{3/2}} \left[1.99 - \frac{a}{W} \left(1 - \frac{a}{W}\right) \left\{ 2.15 - 3.93 \frac{a}{W} + 2.7 \left(\frac{a}{W}\right)^2 \right\} \right]. \quad (4.1)$$

The experiments involved 3 to 5 samples for each filler particle size. The static crack initiation toughness (K_{Ic}) values for various particle sizes are tabulated in Tables 4.4 and 4.5. For comparison purposes the dynamic fracture parameters (K_{Ii} and K_{Iss}) for respective particle sizes are also presented. Figure 4.14(a) shows variation of K_{Ic} with particle size for weakly and strongly bonded particles. From the plots it can be seen that, similar to K_{Iss} variation, the variation of K_{Ic} is nonmonotonic with the particle

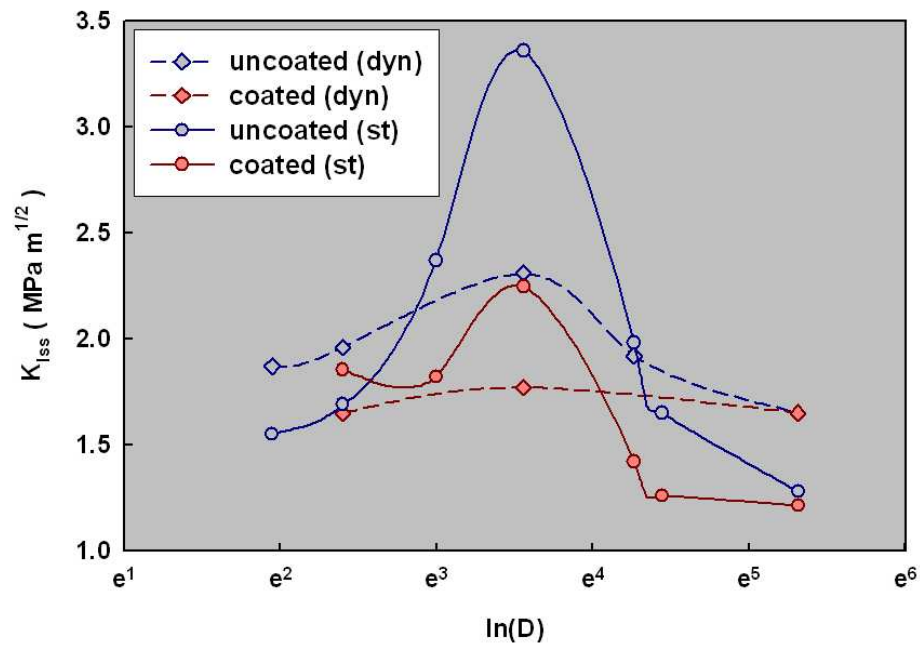
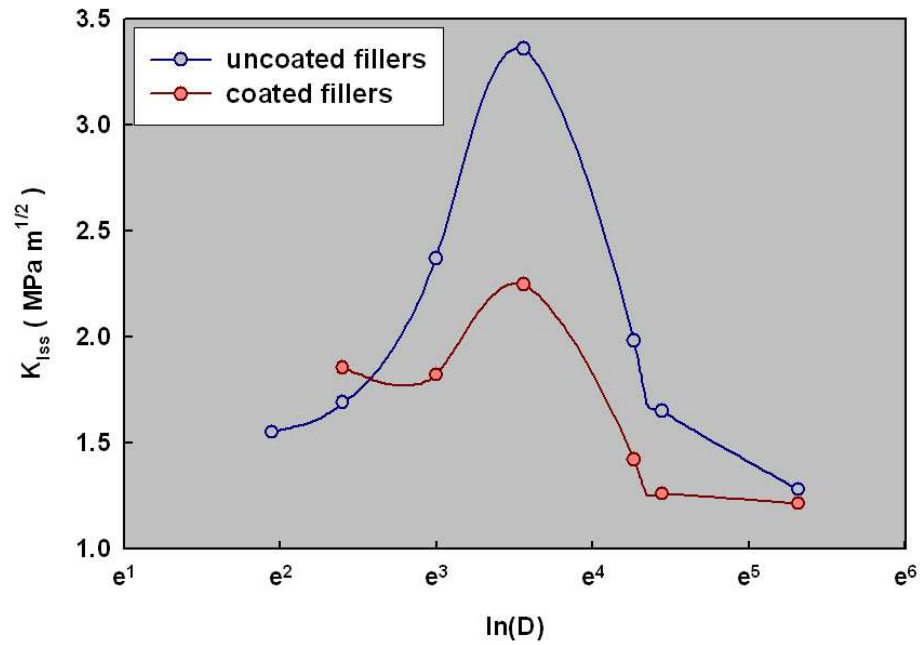


Figure 4.14: Particle size effect on fracture toughness; (a) Variation in quasi-static crack initiation toughness with particle size, (b) Effect of loading rate (quasi-static and dynamic) on fracture toughness.

size. The quasi-static fracture toughness values for weakly bonded particles are higher than strongly bonded ones of the respective particle size. The optimum particle size among the several others considered for maximum fracture toughness again turns out to be $35 \mu m$. With a decrease or an increase in particle size relative to this optimum size at this V_f , fracture toughness decreases. Also, the static fracture toughness values appear to be saturating as particle size is increased/decreased relative to the optimum particle size, similar to the dynamic case. Similar trends in fracture toughness variation for both quasi-static and dynamic loading cases suggest that fracture toughness variation with particle size is independent of the loading conditions.

Figure 4.14(b) shows the variation of K_{Ic} and K_{Iss} with filler particle size for both weakly and strongly bonded glass-filled composites. From the plots it can be noticed that the fracture toughness values between static and dynamic cases differ from each other for their respective particle sizes (coated and uncoated). The difference is quite significant for $35 \mu m$ particles, where the fracture toughness value for static case is $\sim 40\%$ for weakly bonded particles and $\sim 25\%$ for strongly bonded particles higher when compared to the dynamic case. The static fracture toughness values are higher when compared to the dynamic case when filler particles are of sizes close to the optimum particle size. Particle sizes $20 \mu m$, $35 \mu m$ and $85 \mu m$ show higher static fracture toughness for $10\% V_f$, when weakly bonded to the matrix material. For strongly bonded particle filled composite $11 \mu m$, $20 \mu m$ and $35 \mu m$ show higher fracture toughness for quasi-static loading. The bell shaped variation in fracture toughness with particle size is significant when weakly bonded particles are used (for both quasi-static and dynamic loading). When the particles are strongly bonded, the variation is obvious only for quasi-static

loading. For dynamic loading fracture toughness appears to be nearly unaffected by particle size.

4.7 Potential difference in toughening mechanisms

The above conclusions about particle size and filler-matrix adhesion effects on fracture behavior in the composite material of identical elastic properties can be attributed potentially to the differences in toughening mechanisms. In the literature review a few of these toughening mechanisms were mentioned. For silane treated particles having relatively strong filler-matrix interface, crack deflection mechanism can be presumed to increase the fracture toughness. On the contrary, in uncoated particles the filler-matrix interface is weak. This gives rise to blunting when the crack front lodges into the filler-matrix interface and results in an increase in fracture toughness seen in case of weakly bonded particles. The same can also be deduced by comparing crack velocities between weakly and strongly bonded particles. It can be noticed from Tables 4.1 and 4.2 that both steady state and maximum velocities are consistently higher for strongly bonded particles compared to weakly bonded ones of similar particle size. The crack growth is retarded when crack front encounters weaker filler-matrix interface. This gives rise to lower average velocity in weakly bonded particles compared to strongly bonded ones in which crack predominantly travels through the matrix material deflecting around obstacles. Crack blunting is also conjectured to cause microcrack formation. When crack is retarded momentarily in this manner, additional energy is needed for acceleration and/or re-initiation. Further, release of energy at re-initiation gives rise to microcracking. Thus, the total dissipated energy during fracture is consumed in crack propagation

as well as in the formation of localized microcracks. This diversion of energy is reflected in the higher fracture toughness in Tables 4.1 and 4.2. That is, fracture toughness for weakly bonded particles are consistently higher when compared to strongly bonded ones of similar particle size.

It can be justified that for a constant filler volume fraction, a decrease in particle size increases the blunting effect due to more number of fillers in the crack path. This suggests that fracture toughness should increase with decrease in particle size for weakly bonded particles. But this trend is not reflected in the measured fracture toughness values. It can be observed from Table 4.1 that in spite of the lowest steady state crack velocity, $35\ \mu\text{m}$ weakly bonded particles show maximum steady state fracture toughness. Also, Fig. 4.8 shows an inverse relationship between crack velocity (v_{ss}) and fracture toughness ($K_{I_{ss}}$). This is contrary to the observation that fracture toughness increases with increase in crack velocity seen among unfilled polymeric and metallic materials. Also the fracture toughness reduces further as particle size increases or decreases relative to $35\ \mu\text{m}$ particle size. This suggests that in the case of weakly bonded particles an additional mechanism is also affecting the fracture toughness. Although the data presented is limited to the case of strongly bonded fillers, $35\ \mu\text{m}$ particles show slightly higher fracture toughness compared to other particle sizes. With current macroscopic observations the reasons for optimum particle size for maximum fracture toughness could not be fully explained. A complementary microscopic investigation of the fracture surfaces is essential to provide a more comprehensive understanding. In Chapter 5, the effective mechanisms have been investigated in more detail by performing micro-measurements on the fracture surface.

CHAPTER 5

MICROMEASUREMENTS¹

In this chapter micromerements performed on fractured surfaces of glass-filled epoxy specimens are reported. Various surface features have been investigated both qualitatively and quantitatively to explain the role particle size, filler-matrix adhesion strength and particle size distribution play in the fracture process of particulate composites. Specifically, roughness parameters are correlated with the optical measurements reported in the previous chapter and a model linking fracture toughness to the surface roughness is developed. Unlike conventional homogeneous materials, correlating surface roughness features and macro fracture parameters is not straightforward in particulate composites due to the presence of secondary phases. Therefore, the contribution of particle size to surface roughness needs to be isolated prior to bridging micro-macro measurements.

5.1 Fracture surface micrographs: Qualitative observation

Scanning electron microscopy (SEM) is used for qualitative examination of fracture surface. Approximately 1.5 – 2 *mm* thin strip of fractured surface with cross sectional area 42 *mm* × 8 *mm* is stripped out from the fractured sample. Fracture surfaces are deposited with a thin layer of gold using a physical vapor deposition technique. Various locations are examined in the steady state crack growth region (see Fig. 5.1) using SEM.

¹ *Parts of this chapter appear in Ref. [106]*

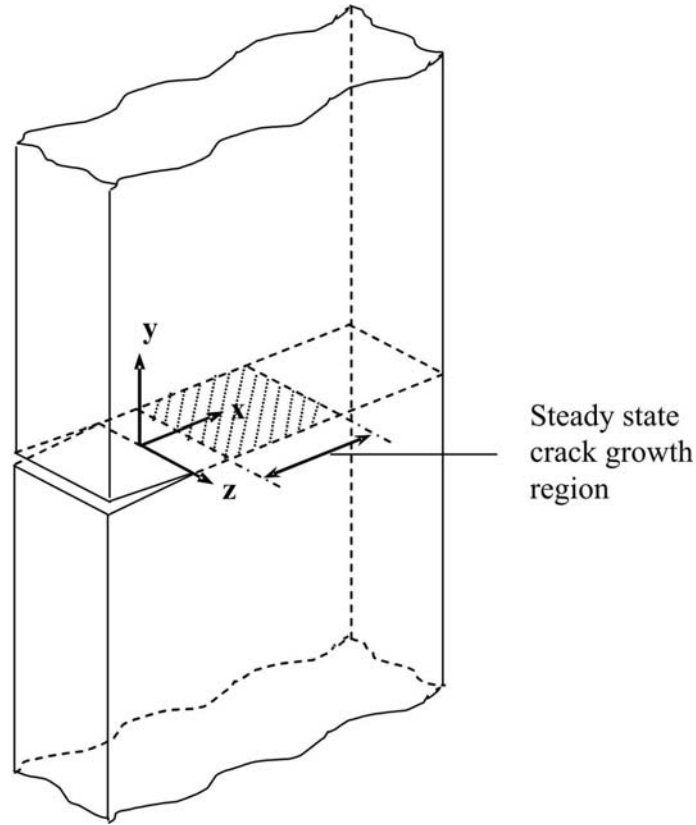


Figure 5.1: Schematic representing a growing crack in composite and steady-state region where micromasurements are performed.

Figure 5.2 shows micrographs of a few representative fractured surfaces. The images are for $203\ \mu\text{m}$ (Figs. 5.2(a), 5.2(b)), $35\ \mu\text{m}$ (Figs. 5.2(c), 5.2(d)) and $11\ \mu\text{m}$ (Figs. 5.2(e), 5.2(f)) weakly bonded and strongly bonded particles, respectively. It is evident from the micrographs that agglomeration effects are essentially nonexistent in these cases. The matrix wetting on filler particles in Figs. 5.2(b), 5.2(d) and 5.2(f) suggests relatively strong filler-matrix adhesion in case of silane coated fillers. Contrary to this, for uncoated particles in Fig. 5.2(a), 5.2(c) and 5.2(e), no such affinity between fillers and the matrix can be seen due to weaker filler-matrix interface. In the case of weakly bonded

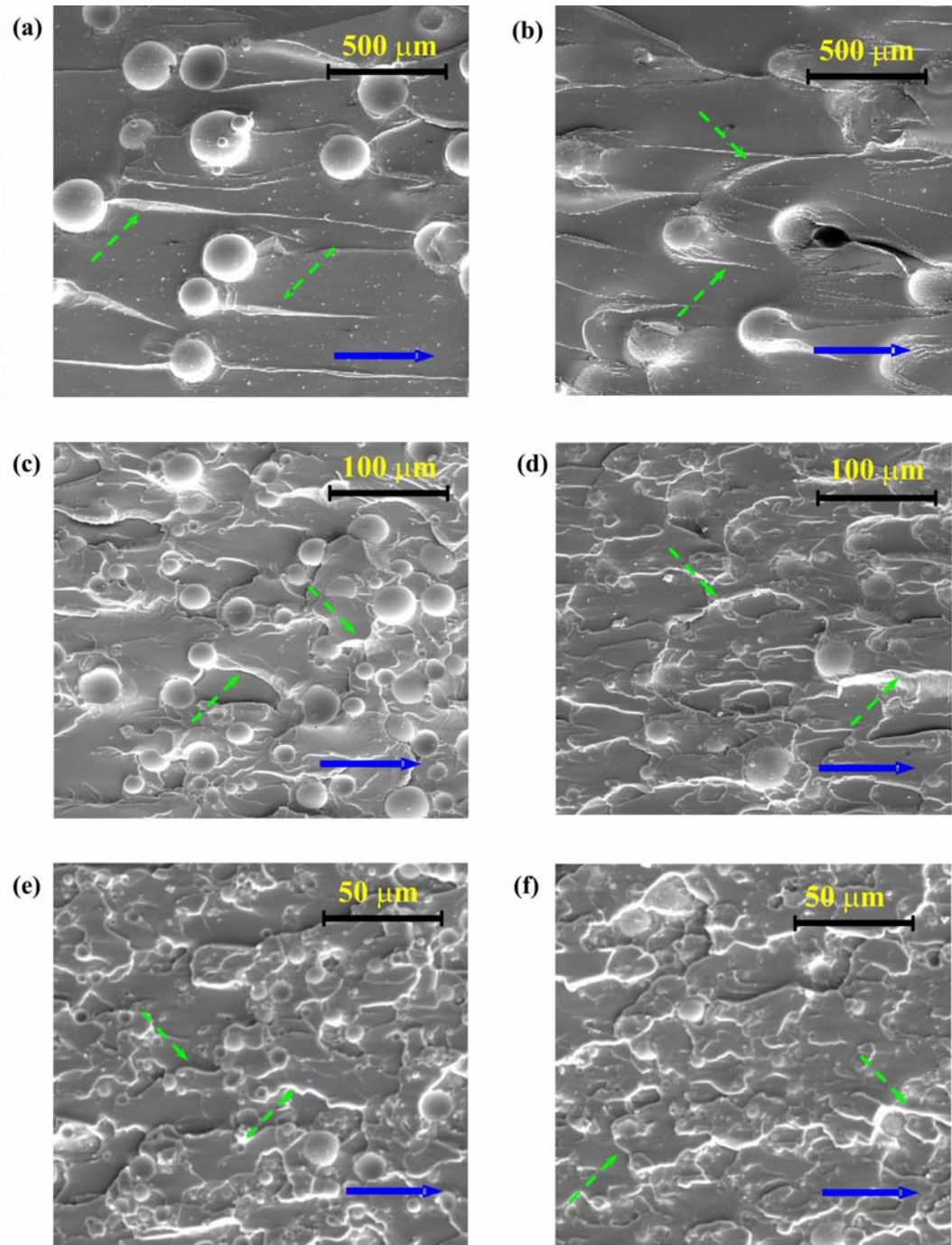


Figure 5.2: SEM micrographs: (a) 203 μm uncoated particles, (b) 203 μm coated particles, (c) 35 μm uncoated particles, (d) 35 μm coated particles, (e) 11 μm uncoated particles, (f) 203 μm coated particles. Solid arrow shows crack propagation direction and broken arrow shows “Tail lines”.

particles, inter-particle cleavage fracture can be noticed, with either particle or particle foot-prints left behind on the fracture surface. Higher surface waviness can be seen in strongly bonded particles as the crack appears to have mostly avoided the particles and has propagated through the matrix material. Due to this, fewer particles are exposed on the fracture surface. The situation can be imagined as if the particles are hidden just below/above a layer of matrix material adjacent to the fracture surface. On the contrary, larger number of particles and particle foot-prints in weakly bonded filler case suggests that there is only a weak resistance to filler-matrix interfacial separation. A highly textured surface in smaller particles suggests higher energy dissipation and hence higher fracture toughness compared to $203\ \mu\text{m}$ particles.

Next, to provide supplementary explanation for the observed particle size distribution effect on fracture behavior, fracture surface of mixed filler specimen is scanned. Figure 5.3(a) shows micrograph for $35 + 203\ \mu\text{m}$ filler mixture. It should be noted that both $35\ \mu\text{m}$ and $203\ \mu\text{m}$ particles were mixed with epoxy in equal volume fraction (5% each). A homogeneous distribution of larger as well as smaller particle/particle foot-prints are obvious from the micrographs. For comparison fractured surface of larger and smaller particle filled monolithic specimens are also shown (see Fig.5.3(b) and (c)). It can be noted that mixed filler specimen has higher roughness when compared to the homogeneous specimen with $203\ \mu\text{m}$ diameter particles (Fig.5.3(b)), while it shows lower roughness relative to the one with $35\ \mu\text{m}$ particles (Fig.5.3(c)). This commensurates well with the optical measurements namely, the steady state fracture toughness for interface crack is bounded by those for $203\ \mu\text{m}$ and $35\ \mu\text{m}$ particle sizes. Tail lines indicating

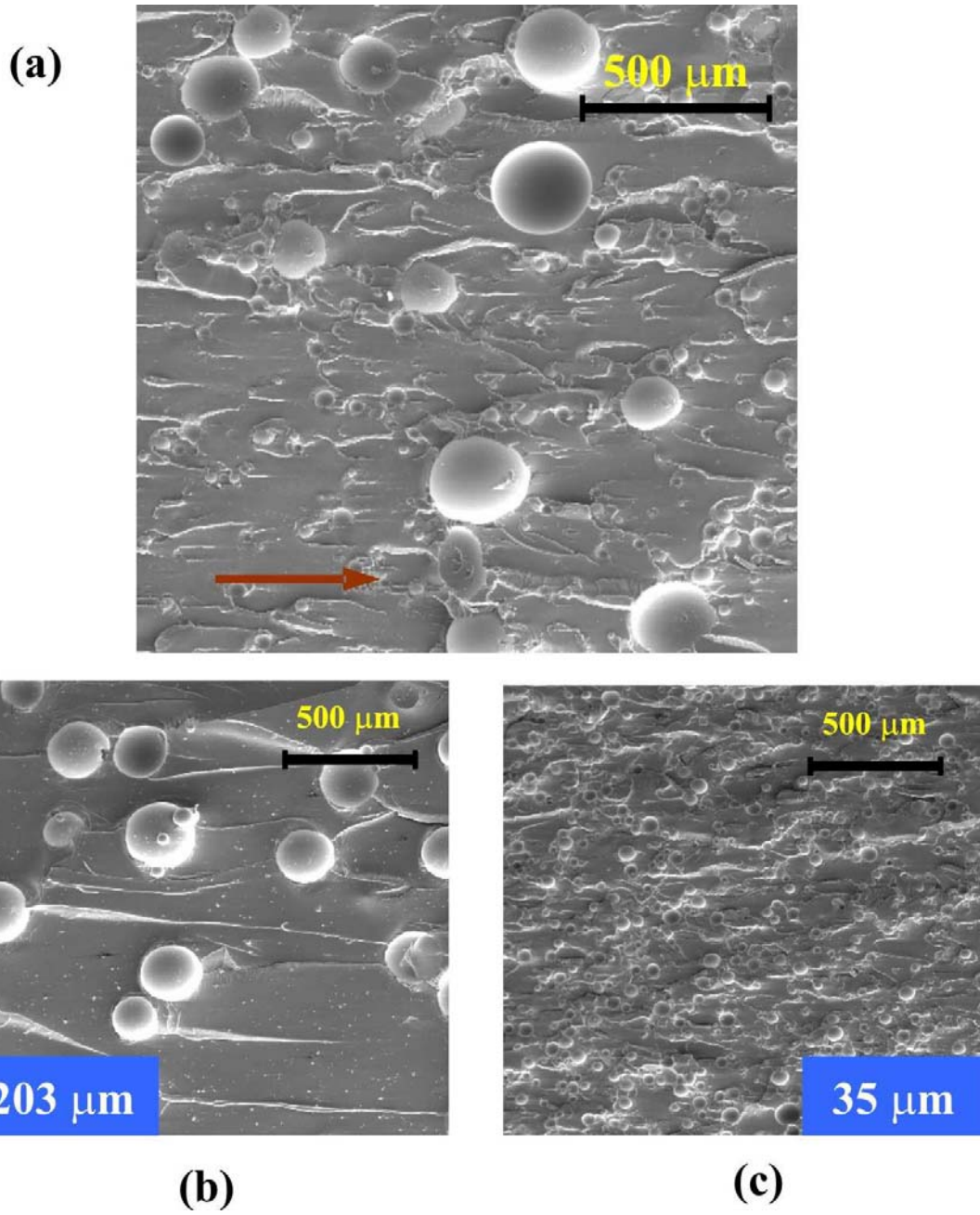


Figure 5.3: SEM micrographs of fractured surfaces, (a) shows $35 + 203\ \mu\text{m}$ diffuse interface, (b) and (c) show fractured surfaces of $203\ \mu\text{m}$ and $35\ \mu\text{m}$ monolithic materials, respectively.

crack propagation direction can be seen in both single filler size and mixed filler size specimens.

5.2 Quantitative investigation of fractured surfaces

Subsequent to qualitative investigations described above, quantitative micro measurements of fracture surfaces are performed using a Tencor P-1 long scan profiler with a stylus of $5\ \mu\text{m}$ root radius. Digitized surface profiles are measured in a region that corresponds to steady state crack growth. It can be noticed from velocity histories in the specimens (See Fig. 4.5 and 4.9 in chapter 4) that steady state region falls in the mid one-third along the specimen width. That is, $x = 4 - 18\ \text{mm}$ ahead of the initial crack tip depending upon the filler particle size. The data was recorded at 4 to 5 different locations within the steady state region.

Digitized data from the surface profiler is processed to get average surface roughness Ra using,

$$Ra = \lim_{L \rightarrow \infty} \frac{1}{L} \int_{-L/2}^{+L/2} |y(x) - \bar{y}| dx, \quad (5.1)$$

where,

$$\bar{y} = \lim_{L \rightarrow \infty} \frac{1}{L} \int_{-L/2}^{+L/2} y(x) dx. \quad (5.2)$$

Here, L is the scan length, and (x, y) are defined as shown in Fig. 5.1.

Figure 5.4 shows a few representative surface profiles for weakly and strongly bonded fillers of different particle sizes in the matrix. The profiles shown are for $11\ \mu\text{m}$, $35\ \mu\text{m}$ and $203\ \mu\text{m}$ filler particles. Each surface profile is qualitatively distinct from the others. In Fig. 5.4(a) the effect of particle size on surface profiles are compared for weakly

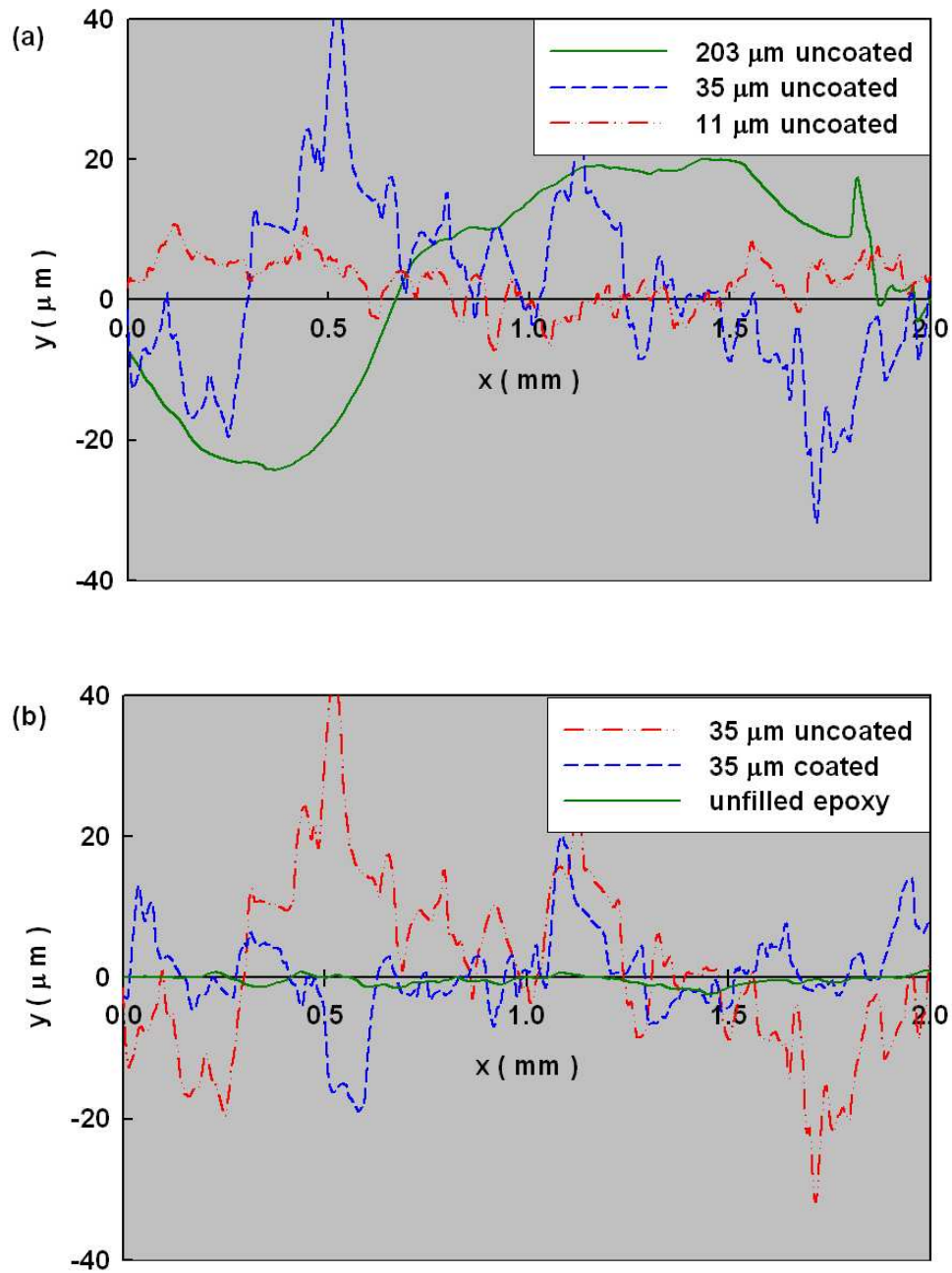


Figure 5.4: Representative fracture surface profiles for different glass-filled epoxy specimens. (a) particle size effect and (b) filler-matrix adhesion effect.

bonded case. The largest particle surface profile shows larger amplitudes and longer wavelengths with a relatively small higher frequency content when compared to other particle sizes. The specimen with $11\ \mu\text{m}$ particles, on the other hand, shows substantially higher frequency content with a surface profile generally much closer to the mean surface. That is, amplitudes are smaller compared to other particle sizes shown in the plot. Weakly bonded $35\ \mu\text{m}$ particles, which has shown the highest macroscopic fracture toughness among all the cases considered (see Fig. 4.7 in chapter 4), shows a frequency content similar to that of $11\ \mu\text{m}$ particles while the amplitude is larger, similar to that of $203\ \mu\text{m}$ particles. Next, the surface profiles of coated and uncoated $35\ \mu\text{m}$ are compared in Fig. 5.4(b). Evidently, the profile for the coated case has smaller amplitude when compared to the uncoated case. In Fig. 5.4(b), surface profile of unfilled epoxy is also shown for comparison. It can be seen that profile for epoxy is quite close to the mean surface with a relatively small surface amplitude. This suggests a lower surface roughness in case of unfilled epoxy compared to the filled ones. The effect of these difference in surface profiles can be clearly seen on average surface measurements to be described next. It should be noted that roughness of fractured surfaces has been evaluated for each sample in a region where steady state crack growth is observed. Surface roughness profiles in both the x -direction and the z -direction are recorded at 4 to 5 locations. Surface roughness is calculated using Eq. (5.1) and the resulting average values are tabulated in Table 5.1 as longitudinal roughness Ra_x and transverse roughness Ra_z , respectively.

Particle diameter D (μm)	longitudinal roughness Ra_x (μm)	transverse roughness Ra_z (μm)	average roughness Ra (μm)	Particle related roughness Ra_p (μm)	Fracture induced roughness Ra_f (μm)	Ra_f/\sqrt{D} ($\sqrt{\mu\text{m}}$)
203	16.50	18.80	17.61	11.17	6.44	0.45
71	9.85	9.95	9.90	3.91	5.99	0.71
35	9.63	11.09	10.33	1.93	8.40	1.42
11	3.48	3.57	3.52	0.61	2.91	0.88
7	2.31	2.41	2.36	0.39	1.97	0.75
epoxy	0.75	0.80	0.77	–	–	–
203*	16.34	17.78	17.04	11.17	5.87	0.41
35*	5.71	6.30	6.00	1.93	4.07	0.69
11*	2.36	2.49	2.42	0.61	1.81	0.55

Table 5.1: Roughness parameters for weakly and strongly bonded glass fillers in epoxy matrix, $V_f = 0.1$. * denotes strongly bonded particles.

5.2.1 Particle size and filler-matrix adhesion effect

In Table 5.1 both Ra_x and Ra_z show an increasing trend as particle size increases when uncoated (weakly bonded) particles are used to reinforce the matrix. Average roughness Ra has been calculated by geometrically averaging Ra_x and Ra_z . It can be seen from the table that average surface roughness increases with particle size. Also, roughness values are slightly but consistently higher in the transverse direction in all cases. It should be pointed out that average roughness values Ra do not provide a consistent explanation for the fracture toughness variation of the filled material as a function of particle size. This can be seen when micro- and macro-measurements listed in Table 5.2 are compared. That is, unlike fracture toughness, overall roughness is highest for the largest particle size and monotonically decreases as particle size decreases. In Table 5.2 steady state crack velocity v_{ss} and steady state fracture toughness $K_{I_{ss}}$ have been included from the previous chapter. Also, overall surface roughness values are

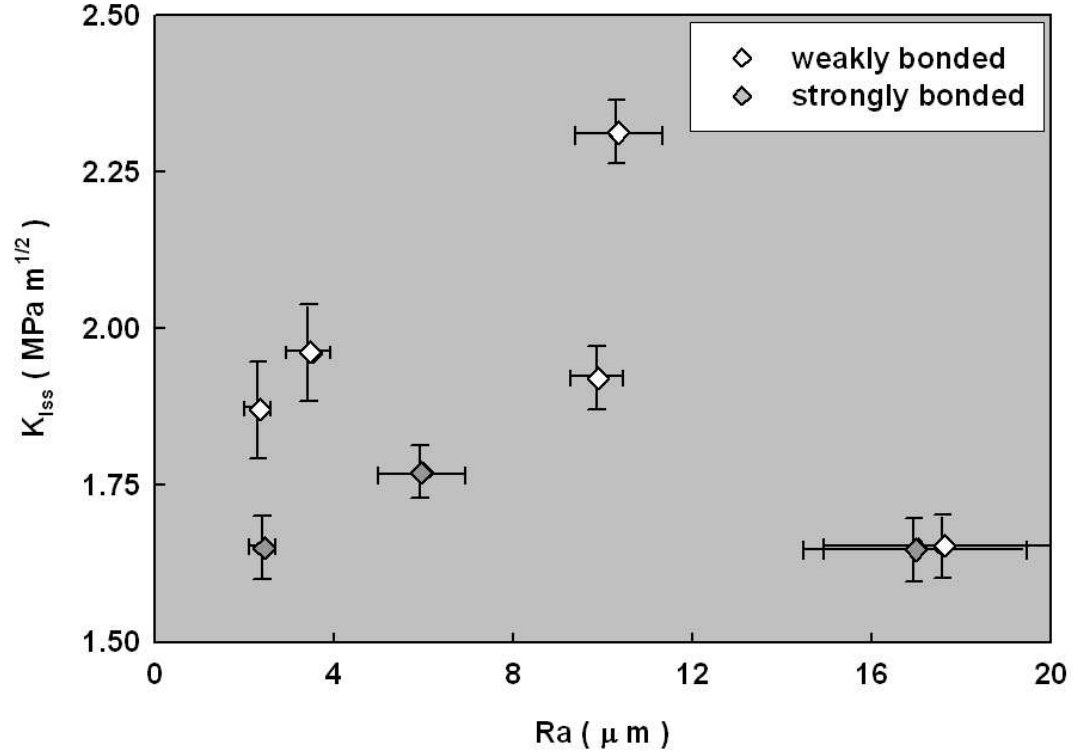


Figure 5.5: Steady-state fracture toughness variation as a function of overall surface roughness for different particle sizes.

plotted against fracture toughness values in Fig. 5.5. These do not show any obvious correlation between the quantities in question. Such a lack of correlation between Ra and $K_{I_{SS}}$ is due to the dominant contribution of particles and/or particle foot-prints present on the fractured surface to the overall roughness. Hence, an alternative parameter is essential for providing a consistent explanation.

Table 5.1 also shows experimentally measured roughness parameters, Ra_x , Ra_z and average roughness Ra for strongly bonded particles. Again, the roughness values are slightly but consistently higher in the transverse direction compared to the longitudinal

Average particle size μm	weakly bonded particles				strongly bonded particles			
	Crack velocity v_{ss}^* m/sec	Fracture toughness $K_{I_{ss}}^*$ $MPa\sqrt{m}$	Avg Roughness Ra μm	$\frac{Ra_f}{\sqrt{D}}$	Crack velocity v_{ss}^* m/sec	Fracture toughness $K_{I_{ss}}^*$ $MPa\sqrt{m}$	Avg Roughness Ra μm	$\frac{Ra_f}{\sqrt{D}}$
203	310	1.67	17.61	0.45	312	1.65	17.04	0.41
71	300	1.92	9.90	0.71	–	–	–	–
35	290	2.31	10.33	1.42	320	1.77	6.00	0.69
11	345	1.96	3.52	0.88	375	1.65	2.42	0.55
7	370	1.87	1.97	0.75	–	–	–	–

Table 5.2: Fracture and Roughness parameters for different particle sizes and filler-matrix strengths at $V_f = 0.1$. (subscript *ss* denotes “steady state”), * denotes data from Ref.[1]

direction. More importantly, as in case of weakly bonded particles, longitudinal, transverse, and overall roughness parameters increase with particle size. From Fig. 5.5 it can be seen again that Ra does not provide a unique correlation with $K_{I_{ss}}$ even for strongly bonded particles. The usefulness of overall surface roughness hence requires that contribution of particle size to the surface roughness be duly accounted for prior to correlating macromessurements with micromessurements.

Comparing Ra_x , Ra_z and Ra in Table 5.1 for respective particle sizes, it can be noted that roughness values are consistently higher for each case of weakly bonded particles when compared to the silane treated ones. A maximum increase in roughness values, are for the case of 35 μm particles, with weakly bonded particles showing in excess of 70% increase in average roughness compared to the one for strongly bonded particles. Similar comparison between weakly and strongly bonded fillers of 11 μm and 203 μm sizes show $\sim 45\%$ and negligible increase in Ra , respectively.

5.2.2 Potential toughening mechanisms and surface roughness

It can be seen from the micrographs that filler particles are unbroken in all composites and the crack front always travels through the matrix material. When the crack front encounters filler particles during crack propagation, it interacts with the filler phase in one of the following two ways depending upon filler-matrix interfacial strength. If the filler-matrix interface is strong, the crack tends to deviate from its path and bow around or tilt between rigid filler particles. Bowing around particles or crack tilting gives rise to mixed mode (mode-I and -II) fracture, while the crack twisting between particles results in mixed mode-I and -III[32, 33] condition. On the contrary, if the filler-matrix interface is weak, cleavage fracture can be noticed in the interparticle region with particle foot-prints left behind by the propagating crack (see Fig. 5.2). Clearly the matrix surrounding the filler particles is separated as the crack front encounters weaker filler-matrix interface. In this process the propagating crack front bows out wherever it meets the filler phase while being blunted at discrete locations along the front. Such a crack would experience lower stress intensification and needs additional energy to re-initiate and propagate further. This intermittent stalling, due to the crack front front lodging into a cavity gives rise to lower average crack speed. The same can be readily noticed by comparing the steady state crack velocities in Table 5.2, where crack velocities are always higher for strongly bonded particles compared to weakly bonded particles of similar sizes. The weaker filler-matrix interface could also act as a distribution of crack attractors for a propagating crack front. Hence the crack tends to meet-up with the nearest possible filler-matrix interface in its neighborhood during propagation, which

again gives rise to zig-zag crack propagation instead of relatively straight/smooth fracture path. These are schematically shown in Fig. 5.6. The above mentioned phenomena vary the microscopic surface features, giving rise to higher surface roughness and hence the macroscopic fracture toughness. This can be noticed by comparing roughness and fracture toughness values in Table 5.2 between weakly and strongly bonded particles. The values are consistently higher for the weakly bonded case of similar particles sizes.

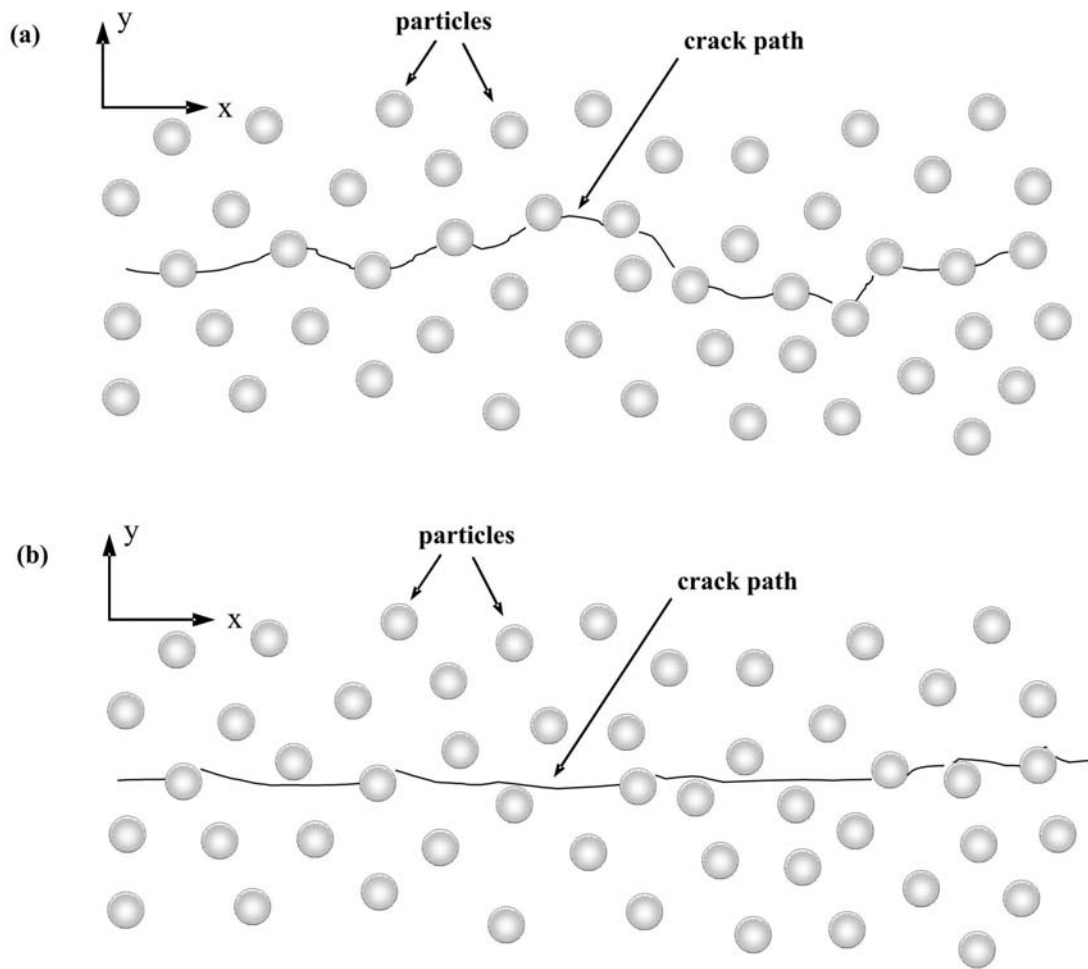


Figure 5.6: Schematic showing potential crack growth pattern: (a) weakly bonded particles and (b) strongly bonded particles.

From the above analysis it is clear that different mechanisms affect fracture toughness and surface roughness based on filler-matrix interface strength. In the micrographs “tail lines” emerging from the particles/cavities or within matrix material indicates the direction of crack propagation. These lines are also indicative of the magnitude of surface tortuosity and crack twisting during fracture. The formation of tail lines can be explained with the help of schematics shown in Fig.5.7. In case of strongly bonded particles tail lines appear more often in the inter particle region (see Fig. 5.2(b,d,f)). From the schematic in Fig. 5.7(a) it can be seen that when angle of twist ϕ of a crack front reaches its maximum value ϕ_{max} (Fig. 5.7(a.iii)), it starts to propagate at different elevations (different values of y on $x - z$ plane). This results in tail lines in the form of extra surface in the matrix material between the particles (Fig. 5.7(a.iv)). Unlike strongly bonded fillers (Fig. 5.7(b)), the weakly bonded particle tail lines appear to have been generated at the particles or particle foot-prints (see Fig. 5.2(a,c,e)) by a slightly different mechanism. As discussed previously, weaker filler-matrix interface acts as crack attractor, hence crack front goes through the particle or particle foot-print as shown in Fig. 5.7(b.i). When the angle of twist reaches its maximum value (Fig. 5.7(b.iii)), tail lines emerge from two neighboring particle sites (Fig. 5.7(b.iv)). It is clear that tail lines create extra surface dissipating additional energy. Also the surface features are affected and surface roughness increases. It can be further noticed in the micrographs that tail lines are more prominent in weakly bonded particles when compared to the strongly bonded ones. This suggests that crack twisting has occurred more often in weakly bonded particles giving rise to higher surface roughness. This can be

verified by comparing average roughness values in Table 5.1 for respective particle sizes.

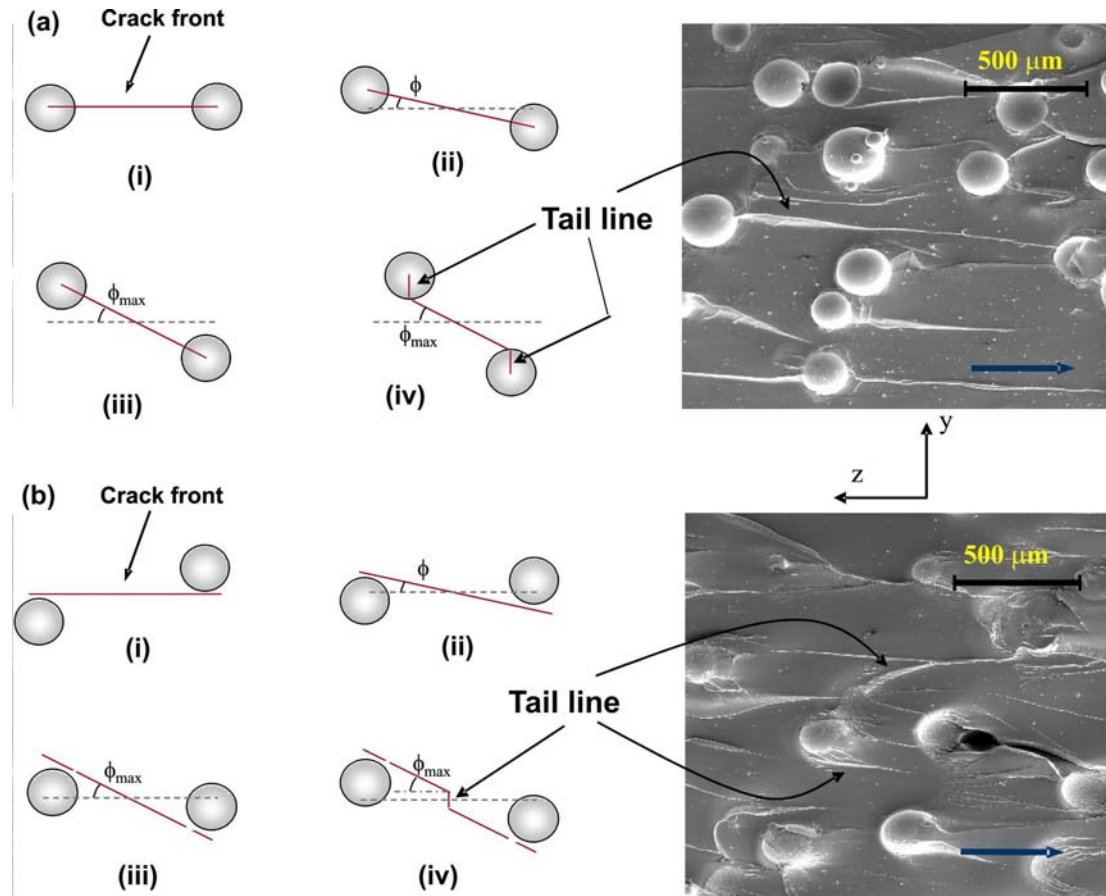


Figure 5.7: Schematic showing different crack front twisting mechanisms in case of: (a) weakly bonded particles and (b) strongly bonded particles. Formation of tail-lines from weakly bonded particles and particle foot-prints (a) and from the matrix in the vicinity of strongly bonded particles (b) are shown in micrographs of $203 \mu m$ particles filled epoxy.

As noted from results, $35 \mu m$ particles show maximum fracture toughness and fracture induced roughness values. Further increase or decrease in particle size decrease both of these parameters. This behavior can be noticed both in weakly and strongly bonded particles, suggesting that the same phenomena is responsible for an optimum

particle size. Previously described tail lines and crack twisting in strongly and weakly bonded cases explain this. Figure 5.7 shows crack twisting and formation of tail lines when the angle of twist ϕ reaches its maximum value ϕ_{max} . The random distribution of particles for 10% volume fraction is optimum for $35 \mu m$ particles, which gives an average ϕ nearly equal to maximum possible ϕ_{max} . Further increase in particle size increases the inter-particle separation l for constant volume fraction V_f (see Eq.(5.4)) increasing the probability of crack traveling through the matrix material. Hence average ϕ decreases as the particle size increases relative to the optimum value. On the other hand, when particle size decreases relative to the optimum size, inter-particle separation distance l decreases. More number of randomly distributed smaller particles per unit volume decrease the difference in elevations (in the y -direction) between neighboring particles (see Fig. 5.7), suggesting lower angle-of-twist. Also the smaller particle diameter gives rise to a smaller angle-of-twist if neighboring particles are at the same elevation. All these decrease the average ϕ . Hence it can be said that the optimum particle size seen in the experiments is primarily due to crack twisting. It should be pointed out, however, that the inter-particle separation distance l also depends on volume fraction of filler particles. This suggests that it is quite possible to see the deviation in optimum particle size from $35 \mu m$ to others for different volume fractions. This needs to be investigated by a study involving various particle sizes as well as different volume fractions, and has not been attempted in this research.

5.3 Linking macro- and micro-measurements

In the presence of filler material, surface profiles could be modeled as shown in Fig. 5.8. That is, the surface profile can be viewed as a combination of roughnesses due to particles/cavities and surface roughness due to the fracture process itself. Or, one can consider this to be a sum of *particle related roughness* and *fracture induced roughness*. The *particle related roughness*, Ra_p , is the average surface roughness in the presence of embedded particles without considering disturbances to the surface profile generated by the fracture process. The *fracture induced roughness*, Ra_f , on the other hand can be viewed as the average roughness of fractured surface generated due to energy dissipation without considering the filler phase but inclusive of all its manifestations during fracture. Thus, the average surface roughness measured by the profiler can be approximated to be a combination of Ra_p and Ra_f . Since various mechanisms affecting the fracture toughness of the material are reflected in the *fracture induced surface roughness* component, it is appropriate to examine Ra_f to investigate the effect of particle size and filler-matrix adhesion on macro-scale fracture parameters in particulate composites. The fracture induced roughness is thus obtained as,

$$Ra_f = Ra - Ra_p . \quad (5.3)$$

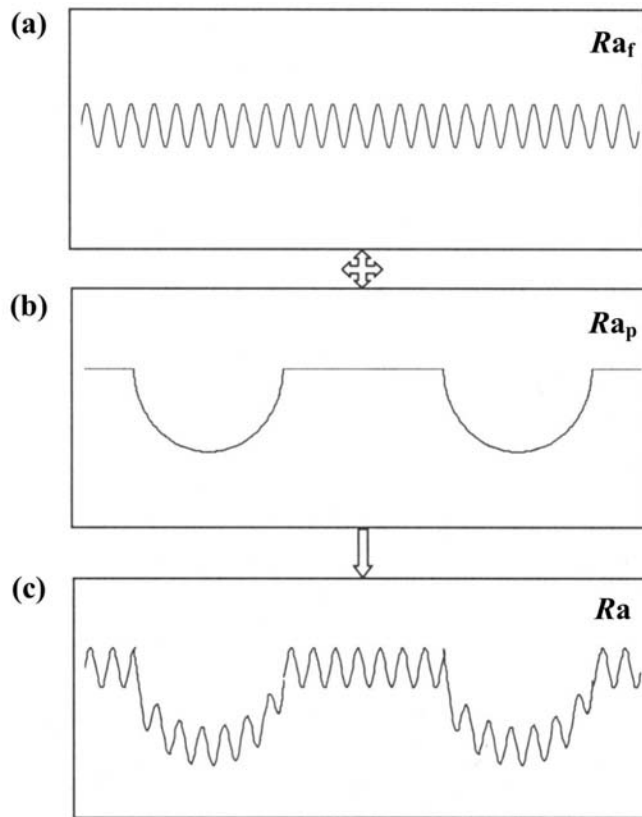


Figure 5.8: Schematic representation of the effect of embedded particle/particle foot-prints on fracture surface morphology: (a) fracture surface profile excluding embedded particles/particle foot-prints, (b) isolated surface profile due to embedded particles/particle foot-prints and (c) fracture surface profile in the presence of embedded particles/particle foot-prints.

5.3.1 Particle related roughness

Let us assume an ideal case of particles being uniformly distributed in the matrix and crack interacts with particles exactly at the equatorial sections of particles while propagating through the matrix. Two extreme possibilities of material separation are shown schematically in Fig. 5.9. The first possibility is shown in Figs. 5.9(a) and (b). Figure 5.9(a) corresponds to when all the particles have exited the matrix material

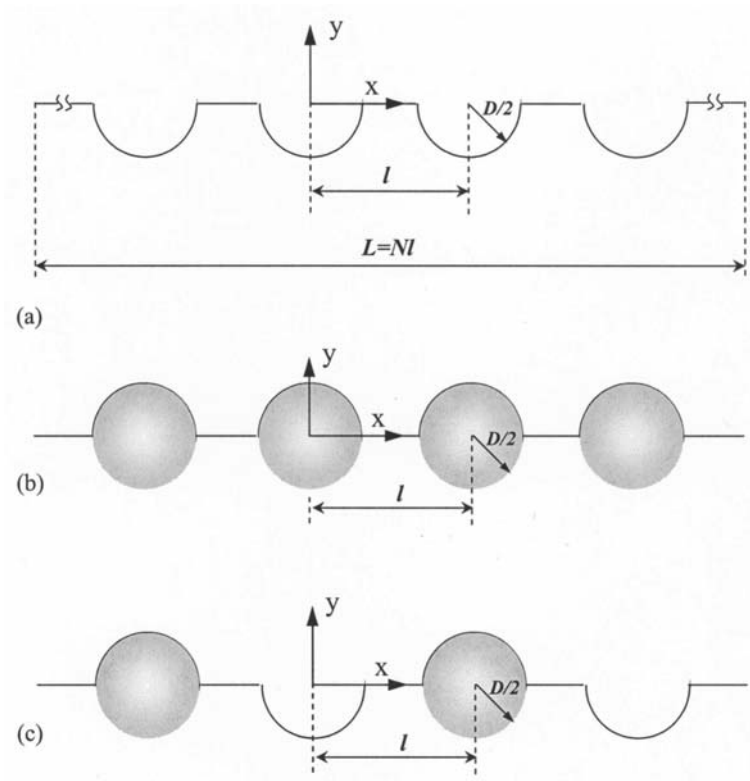


Figure 5.9: Schematic representation of fracture surface: (a) in the presence of particle foot-prints, (b) in the presence of particles, (c) in the presence of particles and particle foot-prints.

during fracture forming cavities while Fig. 5.9(b) is when all the particles exist on one of the fracture surfaces. The second possibility in Fig. 5.9(c) shows that equal numbers of particles are pulled out or left behind in the matrix during fracture. Clearly, these two are limiting cases for particles/cavities on the fracture surface. Average inter-particle separation l for a given volume fraction V_f and an average particle diameter D is given by [103, 104],

$$l = \frac{2D(1 - V_f)}{3V_f}. \quad (5.4)$$

Let us first consider the case corresponding to Fig. 5.9(a). Surface profile $y(x)$ due to particles/cavities on fracture surface can be simply represented as,

$$y(x) = -\sqrt{(D/2)^2 - x^2}. \quad (5.5)$$

Hence the average surface profile \bar{y} from Eq.(5.2),

$$\bar{y} = \frac{1}{Nl} \int_{-Nl/2}^{Nl/2} y(x) dx, \quad (5.6)$$

where scan length L is replaced by Nl , N being the number of particles within L and l is inter-particle separation as defined earlier. From the schematic it can be seen that $\bar{y} = 0$ between particle foot-prints, hence average surface profile can further be simplified to

$$\bar{y} = \frac{N}{Nl} \int_{-D/2}^{D/2} y(x) dx. \quad (5.7)$$

Considering the profile symmetry about the y -axis leads to,

$$\bar{y} = \frac{2}{l} \int_0^{D/2} y(x) dx = -\frac{\pi}{2l} (D/2)^2. \quad (5.8)$$

From Eq.(5.4) let,

$$\frac{D/2}{l} = \frac{3V_f}{4(1 - V_f)} = C, \quad (5.9)$$

where C is the ratio of particle radius to inter-particle distance and is a function of volume fraction only. Thus from Eq.(5.8) and (5.9),

$$\bar{y} = -\frac{\pi C D}{4}. \quad (5.10)$$

Now from Eq.(5.5),

$$x|_{y=\frac{\pi C D}{4}} = \frac{D}{2} \sqrt{1 - \left(\frac{\pi C}{2}\right)^2} = \frac{D}{2} \delta, \quad (5.11)$$

where $\delta = \sqrt{1 - \left(\frac{\pi C}{2}\right)^2}$.

Then from Eq.(5.1) the *particle related roughness* is,

$$Ra_p = \frac{2}{l} \int_0^{D/2} |y(x) - \bar{y}| dx = \frac{2}{l} \left\{ \int_0^{D\delta/2} (\bar{y} - y(x)) dx + \int_{-D\delta/2}^{D/2} (y(x) - \bar{y}) dx \right\}, \quad (5.12)$$

where $L = Nl$ has been utilized again. Upon integration, we get,

$$Ra_p = \frac{D}{2} C \left\{ \frac{\pi}{2} (1 + 2C - 4C\delta) - 2 \cos^{-1} \delta + \sin(2 \cos^{-1} \delta) \right\}. \quad (5.13)$$

For $V_f = 10\%$, $C = 0.0833$ and $\delta = 0.9914$, particle induced roughness from Eq.(5.13) is,

$$Ra_p = 0.0505D. \quad (5.14)$$

It should be noted that the result in Eq.(5.14) remains unaltered if Fig. 5.9(b) were considered. Similarly for the case corresponding to Fig. 5.9(c), $\bar{y} = 0$ and $Ra_p = \pi C D/4$.

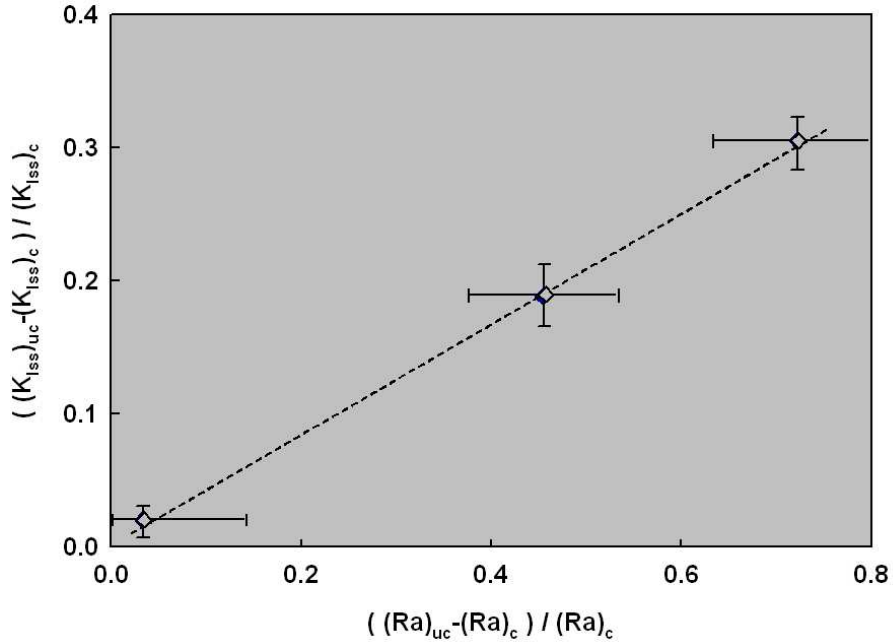
Hence for 10% volume fraction it can be shown that,

$$Ra_p = 0.0655D. \quad (5.15)$$

The two cases above are the limiting values of Ra_p . The actual values will be bounded by these two, depending upon particles/cavity distribution on the fracture surface. The value of $Ra_p = 0.0655D$ has been considered for further analysis in this paper. However, the results and conclusions remain unaffected if Eq.(5.14) is considered instead.

5.3.2 Fracture toughness - Surface roughness relation excluding particle-size effect

Attempts to relate optically measured fracture toughness to surface roughness parameters are described next. As noted earlier, experimentally measured overall roughness values do not reflect a true linkage of fracture toughness to roughness parameters since roughness values are skewed by filler phase. Therefore the component of roughness due to particle size needs to be isolated from the one due to the actual fracture process. This can be accomplished by nondimensionalizing the overall roughness values appropriately. An obvious question that arises is, what parameter/value should be used for nondimensionalizing? Using fracture toughness and surface roughness parameters of matrix material to nondimensionalize is inappropriate since the elastic properties of unfilled epoxy are different from the filled ones (see, Table 1 in chapter 4). Thus, one needs to nondimensionalize using the ones of same elastic characteristics, thereby avoiding the influence of extraneous parameters. It should be noted here that very little effect of



subscript: ss, steady-state; uc, uncoated particles; c, coated particles.

Figure 5.10: Fracture toughness-surface roughness dependence excluding particle size effect.

particle size is noticed on measured fracture toughness in case of strongly bonded filler. Based on this, it can be safely assumed that fracture toughness differences are negligible when particle-matrix interfaces are ideally bonded. Hence properties/parameters for the case of strongly bonded particles can be used to nondimensionalize the respective fracture and roughness parameters of various weakly bonded particle sizes. This would eliminate the particle size effect altogether and isolate the particle-matrix strength effects only. Figure 5.10 shows *percentage* increase in average roughness as a function of *percentage* increase in fracture toughness, respectively, for weakly bonded particles relative to strongly bonded particles for each particle size. Interestingly the plot shows a simple linear variation for all three particle sizes considered in this study. Thus a linear

dependence of surface roughness on dynamic fracture toughness of glass-filled epoxy is demonstrated when particle size effect is “excluded”.

5.3.3 Fracture toughness - Surface roughness correlation

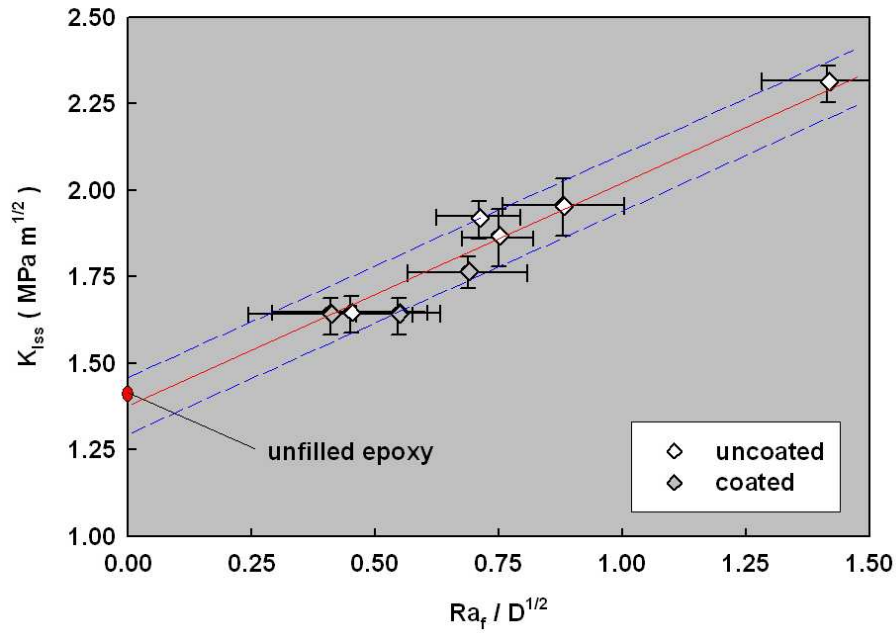


Figure 5.11: Steady-state fracture toughness variation with fracture induced roughness and particle size of glass-filled epoxy composite.

Next task is to correlate fracture toughness and surface roughness in the presence of different particle sizes and different filler-matrix adhesion strengths. As a first step, fracture toughness of the composite is expressed as,

$$K_I = K_{Im} + \Delta K_I, \quad (5.16)$$

where K_I is overall fracture toughness of the composite, K_{Im} is the fracture toughness of unfilled matrix and ΔK_I is the change in fracture toughness due to the reinforcement. The total energy dissipation during the fracture process can be related to various parameters such as filler particle size, filler-matrix adhesion strength, surface morphology, critical strength of matrix material and so on, by considering various processes - breaking matrix constraints due to filler particles, driving the crack forward, creating the new surfaces, etc,- in which energy is consumed.

Let us first consider the energy used for overcoming the matrix constraints due to filler particles. It can be seen from the micrographs that crack invariably travels through the matrix material and particles are not fractured in these composites. When the crack propagates through the matrix material surrounded by filler particles, the matrix is relatively shielded from far-field stresses and experiences a reduced stress intensification at the crack tip. As a result, the critical value of far-field stresses for fracture increases in the presence of filler particles. Let σ_c^m and σ_c^f be critical far-field stresses required for fracture in the absence and presence of filler particles, respectively. Then, the additional energy required to overcome the effect of filler particles can be assumed to be some function of $\Delta\sigma_c = \sigma_c^f - \sigma_c^m$. Clearly $\Delta\sigma_c$ depends on particle volume fraction. In the absence of particle agglomeration, higher the filler volume fraction greater will be the matrix constraint and crack tip shielding, and hence higher $\Delta\sigma_c$. Another important parameter which affects the constraint is inter-particle separation distance l . Without much difficulty one can presume that smaller the inter-particle l , larger will be the matrix constraint and crack tip shielding. Combining both factors, the increase in energy dissipation due to these and hence ΔK is proportional to $(\Delta\sigma_c)^p/l^q$ where p and q are

real constants. As per Eq.(5.4), two aspects namely particle size and volume fraction of the filler particles affect inter particle distance. Hence using Eq.(5.4), for constant volume fraction, ΔK can be written as,

$$\Delta K \propto (\Delta\sigma_c)^p/D^q, \quad (5.17)$$

where D is the particle size.

Now considering the energy component used for creating new surfaces and thus reflecting its effect on fracture surface roughness. As noticed earlier, glass-filled epoxy, with both weakly and strongly bonded particles show increasing average roughness with particle size. This increasing trend, however, is not reflected in optically measured fracture toughness. From the roughness analysis in Section 5.1, it is quite evident that average roughness is a cumulative effect of roughness due to energy dissipation during fracture and the roughness due to the presence of particles on the fracture surface. Clearly the effect of *particle related roughness* Ra_p increases with particle size. Based on a simple model, Ra_p has been calculated to be a function of particle size and volume fraction (see, sub-section-5.3.1). Roughness induced by the fracture process or, *fracture induced roughness* Ra_f , can be filtered out from total roughness Ra by subtracting Ra_p from Ra . Hence ΔK can be considered as some function of Ra_f . Assuming,

$$\Delta K \propto (Ra_f)^r, \quad (5.18)$$

where r is another positive real constant. Here it should be noted that the effects of filler-matrix adhesion will be reflected in the surface roughness. Hence an extrinsic parameter

to represent filler-matrix adhesion strength in the model is not necessary. That is, Ra_f incorporates all the details pertaining to crack tilting, twisting and blunting.

Combining Eq.(5.17) and Eq.(5.18) and using proportionality constant β , one can express ΔK as,

$$\Delta K = \beta \frac{(\Delta\sigma_c)^p}{D^q} Ra_f^r. \quad (5.19)$$

Further ΔK can be replaced in Eq.(5.16) by using Eq.(5.19) to get

$$K_I = K_{Im} + \beta \frac{(\Delta\sigma_c)^p}{D^q} Ra_f^r. \quad (5.20)$$

In section 5.3.3, it has been demonstrated that increase in average surface roughness linearly varies with fracture toughness, which suggests that exponent r should be unity. On substituting for $r = 1$, and assuming that β and $\Delta\sigma_c$ are constants, Eq.(5.20) has been attempted for various values of exponent q . Among several possibilities, $q = 1/2$ gives the best fit to the experimental data, which results in,

$$K_I = K_{Im} + \beta \frac{(\Delta\sigma_c)^p}{\sqrt{D}} Ra_f. \quad (5.21)$$

Figure 5.11 shows variation of dynamic fracture toughness $K_{I_{ss}}$ with Ra_f/\sqrt{D} for both weakly and strongly bonded particles of various particle sizes. The linear variation between $K_{I_{ss}}$ and Ra_f/\sqrt{D} clearly justifies a simple two parameters relationship given in Eq.(5.21). Quite interestingly the linear fit of the experimental data gives $K_{Im} \approx 1.4 MPa\sqrt{m}$. This value is close to the fracture toughness of unfilled epoxy extracted from the experiments, which is in the range of $1.4-1.6 MPa\sqrt{m}$ (see Fig. 4.6 in Chapter 4). On the other hand, in case of unfilled epoxy, setting $\Delta\sigma_c = 0$ reduces Eq.(5.21) to

$K_I = K_{Im}$, further justifying the chosen form of the model. The model can be further refined by performing dimensional analysis on Eq.(5.21). The slope of a linear fit of data in Fig.10 of constant slope shows $\beta(\Delta\sigma_c)^p = \text{constant}$. If β is chosen to be non-dimensional constant, p should have a value of unity, which in turn also justifies our prior assumption of $\Delta\sigma_c = \text{constant}$, for a constant V_f . Hence the model can be reshaped in its final form as,

$$K_I = K_{Im} + \beta \frac{\Delta\sigma_c}{\sqrt{D}} Ra_f. \quad (5.22)$$

CHAPTER 6

EXPERIMENTAL INVESTIGATION OF CRACK-PARTICLE INTERACTIONS

In previous chapters role of microstructure on dynamic fracture behavior was described. Particle size, filler-matrix adhesion and particle size bimodality were shown to greatly influence the fracture toughness of particulate composites. Based on fracture surface observations different toughening mechanisms were hypothesized. A detailed study of a growing crack interacting with a second phase inclusion is needed to fully quantify associated failure mechanisms. Various numerical studies can be found in the literature on this topic and experimental investigations are essentially non-existent. In this chapter preliminary dynamic fracture investigation of crack-particle interactions is performed using CGS and high-speed photography as a first step towards meeting this goal. Two types of inclusions, strongly and weakly bonded to the matrix, are considered at different eccentricities with respect to the initial crack plane. An attempt to quantify fracture parameters during the initial encounter are used to address possible failure mechanisms seen in the composite.

6.1 Material preparation and specimen geometry

Material preparation is similar to the one described for particle filled composite specimens in Chapter 3 except that neat epoxy is used instead of glass-epoxy mixture. First resin and hardener are thoroughly mixed in the ratio of 100 : 36. Prior to transferring the mixture to the mold, a cylindrical glass inclusion of diameter $d = 4 \text{ mm}$ and length equal to the specimen thickness (8 mm) is located and held at the center of the

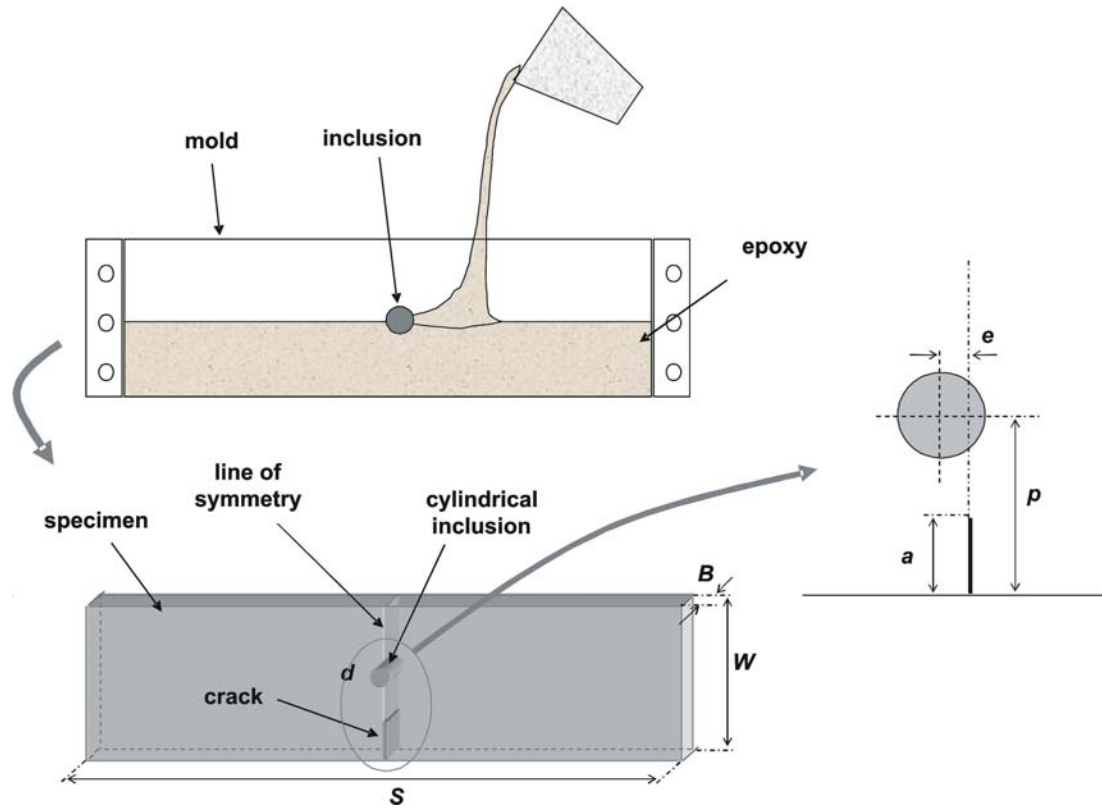


Figure 6.1: Epoxy specimen preparation with cylindrical glass inclusion located in front of initial crack-tip. Inclusion location is defined by p , the initial distance of the inclusion center from the specimen edge which contains the crack and the eccentricity e , the distance between the inclusion center and the line-of-symmetry. $p = 20 \text{ mm}$, $d = 4 \text{ mm}$, $S = 140 \text{ mm}$, $W = 42 \text{ mm}$, $B = 8 \text{ mm}$, $a = 5 \text{ mm}$.

mold, as shown in Fig. 6.1. The material is cured at room temperature for about three days. To create a weak inclusion-matrix interface an uncoated inclusion is used. Silane (Γ -aminopropyltrimethoxysilane) treated inclusion is used when strong interface is to be simulated.

Cured sheets are machined into test specimens of dimensions $152 \text{ mm} \times 42 \text{ mm} \times 8 \text{ mm}$ as shown in Fig. 6.1. The specimen surface is polished with 150 grit sand paper

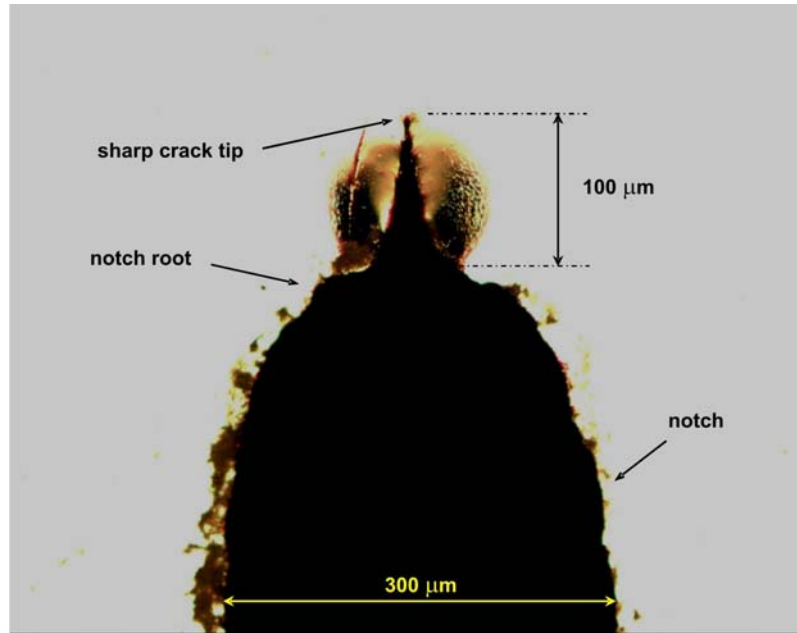


Figure 6.2: Sharp crack tip created by forcing a razor blade into the notch root.

prior to transferring a thin Aluminum film to create optically specular surface as described in Chapter 3. An edge notch of $150\ \mu\text{m}$ root radius and $5\ \text{mm}$ nominal length is cut into the specimen. Further, a sharp crack-tip is created by pressing a sharp razor blade into the notch root. A microscopic image of the sharp crack-tip is shown in Fig. 6.2. A relatively dark region around the initial notch tip indicates permanent deformation due to compressive stresses generated when razor blade is pressed into the notch root. It should also be noted that a shorter initial crack length ($5\ \text{mm}$) is used in these investigations unlike the ones described in Chapter 4. This allows a stable crack growth (steady-state) to occur over a longer distance prior to crack-inclusion interaction. A virtual line joining the initial crack and the loading direction, which bisects the specimen into two equal halves, is referred to as the *line-of-symmetry*. The location of inclusion in the specimen is identified by two parameters, p and e (see Fig. 6.1). The distance

of the inclusion center from the specimen edge which contains the crack is defined as p . The inclusion eccentricity, e , is defined as the distance between the inclusion center and the line-of-symmetry. In the current investigations two different eccentricities, $e = 0$ and $d/2$ are considered, and $p = 20 \text{ mm}$ is maintained constant in all experiments. Thus prepared specimens are impact loaded at a velocity of $\sim 5.3 \text{ m/sec}$. CGS interferometry and high-speed imaging are employed to record crack-tip deformation fields, as described in Chapter 2. As in earlier experiments, a framing rate of 200,000 fps ($5 \mu\text{s}$ repetition rate, 40 ns exposure) is used. The qualitative analysis of interference fringes is given in the following section.

6.2 Fringe analysis

6.2.1 Weakly bonded inclusion ($e = 0$)

Optical interference fringes shown in Fig. 6.3 are obtained for an epoxy specimen with a symmetrically located ($e = 0$) weakly bonded inclusion. The designated time at the top-left corner of each image is the time instant after impact. The first image at $70 \mu\text{sec}$ corresponds to the one from the pre-initiation period. Interference fringes at the impact point and the crack-tip, similar to the ones seen in glass-filled epoxy (Figs. 4.1, 4.2 and 4.3 in Chapter 4) can be seen. Two lobes of fringes on the top and bottom around the inclusion can also be noticed due to material discontinuity at inclusion-matrix interface. Next image at $100 \mu\text{sec}$ is from just before crack-initiation. Both impact point and crack-tip fringes can be seen to have evolved in size when compared to the previous image.

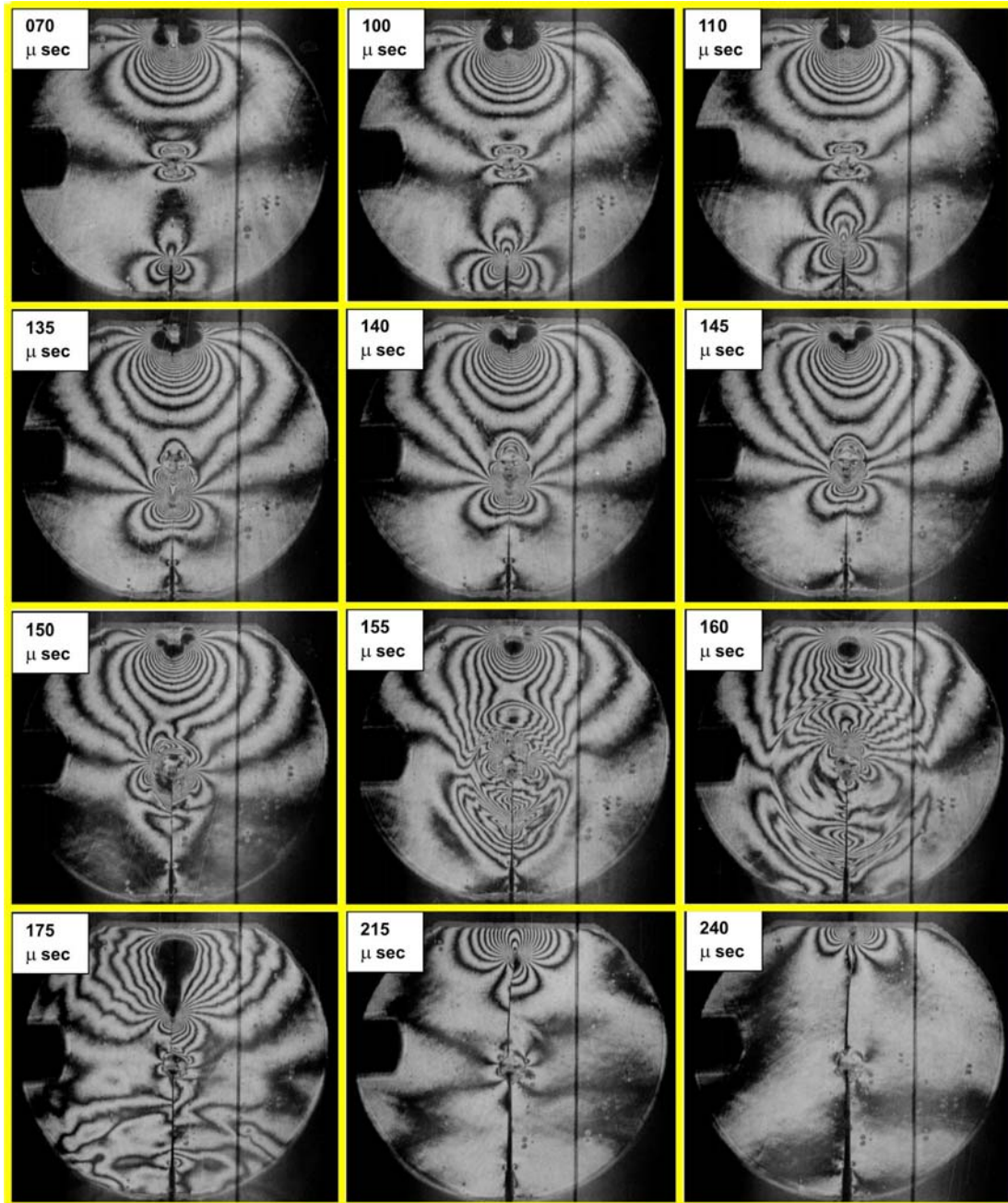


Figure 6.3: Selected fringe pattern representing surface slope contours ($\delta w / \delta x$) for epoxy specimen with weakly bonded inclusion located symmetrically ($e = 0$) with respect to the initial crack-tip. (Distance between the crack and the vertical line is 10 mm.)

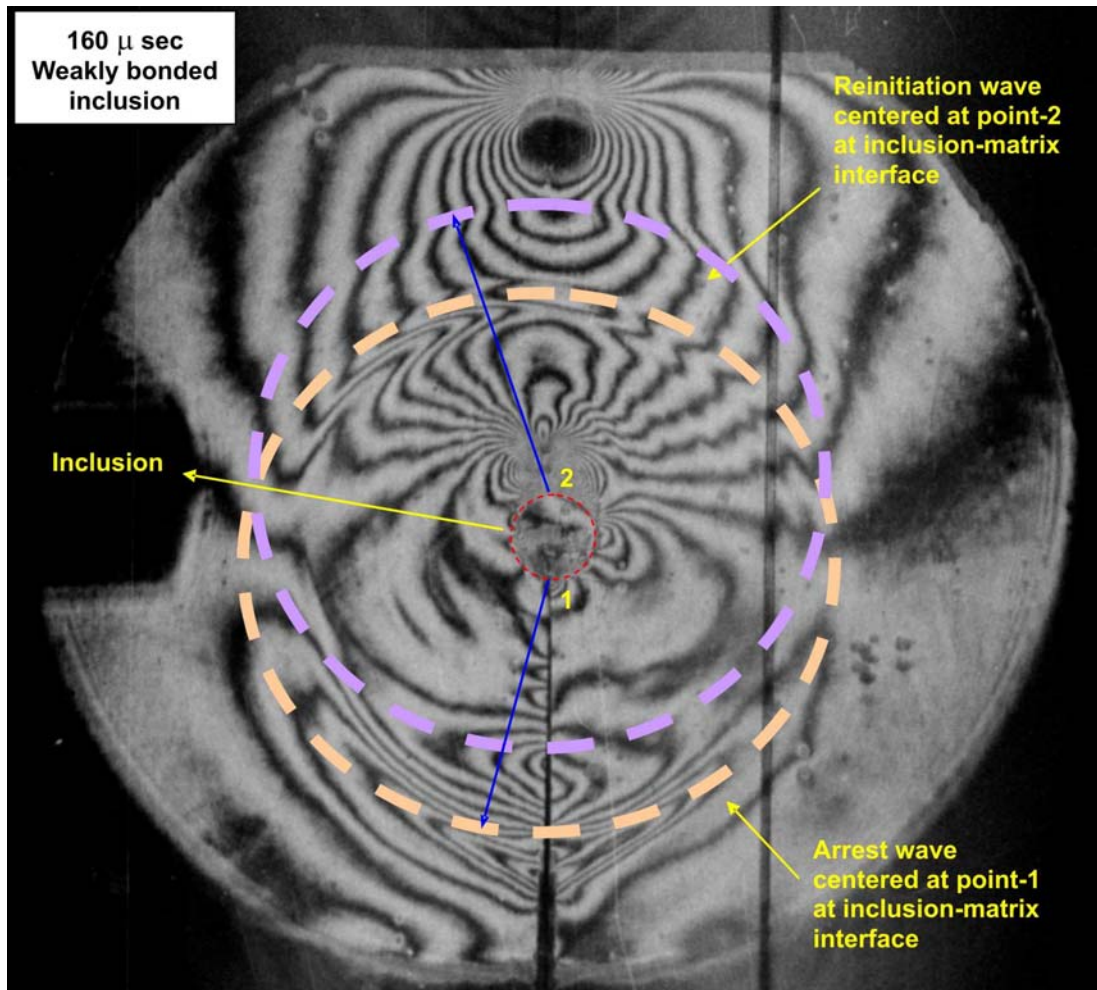


Figure 6.4: Stress waves due to crack-inclusion interaction when the inclusion is weakly bonded. Trace of kinks in fringes suggest arrest and reinitiation waves.

In this experiment, crack initiation occurs at $105 \mu\text{sec}$ (not shown). The image at $110 \mu\text{sec}$ shown in Fig. 6.3 is one frame immediately after crack initiation. A sharp crack-tip used in the experiment results in a relatively gradual crack initiation event without perturbing crack-tip fringes visibly. This is unlike a highly transient initiation often seen when a blunt notch of $150 \mu\text{m}$ root radius is used; see, Figs. 4.1-4.3 in Chapter 4. Such a gradual initiation is important to the current investigation because crack initiation dynamics are less important when compared to the ones due to crack-inclusion interaction. Next three images at 135 , 140 and $145 \mu\text{sec}$ time instants show the crack propagating towards the inclusion. Symmetry of interference fringes relative to the crack plane suggests mode-I fracture event. As the crack approaches the inclusion, front lobes of the symmetric tri-lobed CGS pattern interact with the inclusion and merge into the inclusion-matrix interface. No perturbation could be noticed in the rear lobes during this time. This is clearly evident when the crack first encounters inclusion-matrix interface at $145 \mu\text{sec}$. At this time instant, size of fringe lobes behind the crack-tip is visibly reduced, indicative of lower stress intensity factor. Between $145 \mu\text{sec}$ to $150 \mu\text{sec}$, propagating crack appears to have nearly stalled. Crack interaction with the inclusion at instants 150 , 155 and $160 \mu\text{sec}$ show a large disturbance in crack-tip fringes. Some perturbation in fringes can be noticed near inclusion-matrix interface at $150 \mu\text{sec}$, which has evolved in the form of an arrest wave. The reinitiation wave also can be seen in the next two images at $155 \mu\text{sec}$ and $160 \mu\text{sec}$ time instants. From the images it appears that as crack approaches the inclusion, weak inclusion-matrix interface fails and the inclusion debonds from the matrix material almost instantaneously.

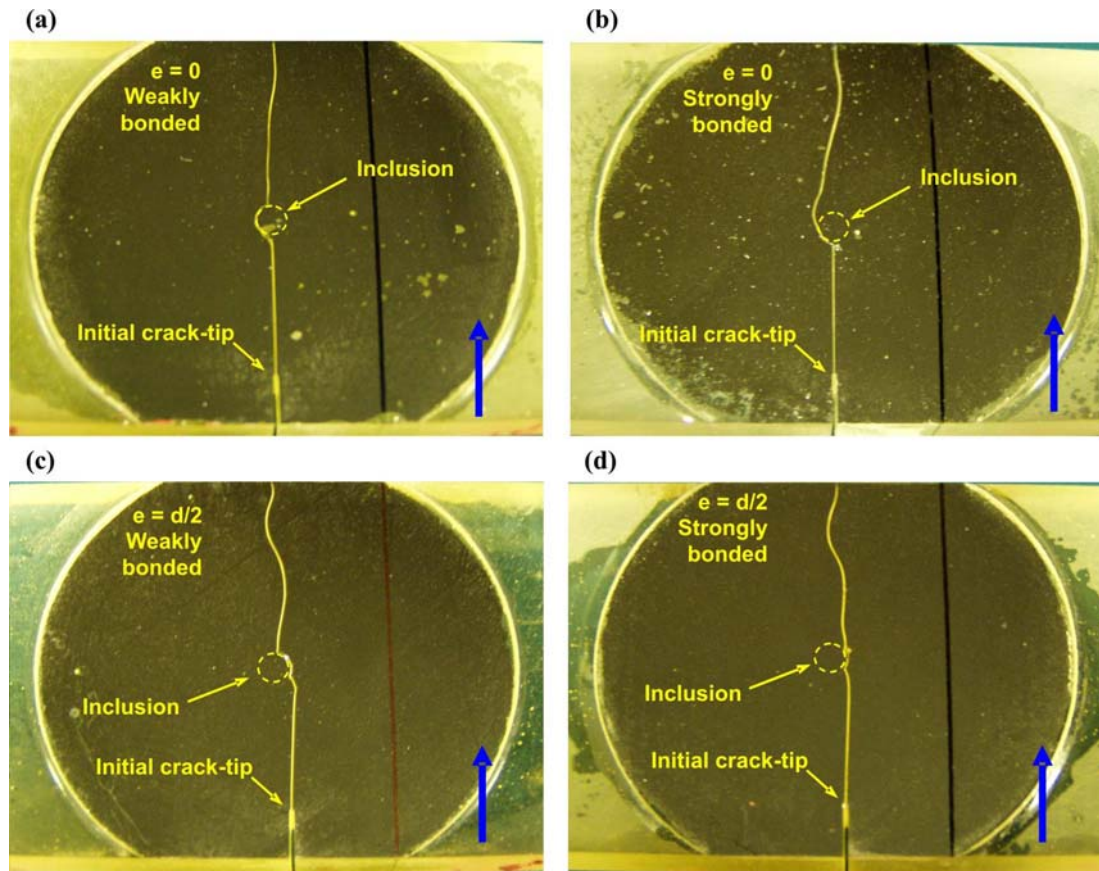


Figure 6.5: Images of fractured specimens showing differences in crack-inclusion interaction: (a) symmetrically located ($e = 0$) weakly bonded inclusion, (b) symmetrically located ($e = 0$) strongly bonded inclusion, (c) tangentially located ($e = d/2$) weakly bonded inclusion, (d) tangentially located ($e = d/2$) strongly bonded inclusion. (Arrow indicates crack growth direction.)

The arrest and reinitiation waves are better visible in the enlarged interferogram at $160 \mu\text{sec}$ time instant shown in Fig. 6.4. It should be noted that during crack arrest and reinitiation events multiple waves emerge from the inclusion-matrix interface. Collectively, these waves are represented by the dotted lines as shown in the figure. Broadly, two different waves can be identified. First, an arrest wave, centered at the point where the crack first meets the inclusion and the second, a reinitiation wave, centered at the point on the inclusion-matrix interface from where the crack reinitiates. Nearly the same size (radii) of the arrest and the reinitiation waves, with latter being slightly smaller, suggests that due to weak inclusion-matrix interface the reinitiation takes place almost instantaneously after the crack first encounters the inclusion. From time lapse calculations, both arrest and reinitiation waves are traveling at a velocity $\sim 950 \text{ m/sec}$ which is close to the value of the Rayleigh wave speed for epoxy. The temporal resolution used in this work ($5 \mu\text{sec}$ interframe time) may be insufficient to capture the details of the debonding dynamics and is deferred to a later investigation.

The crack velocity drops and crack nearly stalls when it reaches inclusion-matrix interface. The crack reinitiates from the inclusion-matrix interface at a different location. At $175, 215$ and $240 \mu\text{sec}$ in Fig. 6.3 both the debonded inclusion and the reinitiated crack are clearly visible. A photograph of the fractured specimen from this experiment is shown in Figure 6.5(a). The vertical arrow indicates the direction of crack propagation whereas a dotted circle shows the inclusion embedded in the specimen. Inclusion debonding and location of crack reinitiation is clearly visible from the image. The crack has reinitiated nearly in mode-I from the delaminated inclusion-matrix interface and with zero offset relative to the initial crack path.

6.2.2 Strongly bonded inclusion ($e = 0$)

A set of fringes shown in Fig. 6.6 is from a specimen with a symmetrically located ($e = 0$) inclusion bonded strongly to the matrix. First two images at $65 \mu\text{sec}$ and $105 \mu\text{sec}$ are from pre-initiation period with the latter for the instant just before crack initiation. Similar to weakly bonded inclusion, a gradual crack initiation is noticed at $115 \mu\text{sec}$. Next three images at 140, 145 and $150 \mu\text{sec}$ time instants show interaction of frontal lobes of crack-tip fringes as the crack approaches the inclusion. The perturbation in crack-tip fringes at $155 \mu\text{sec}$ can be noticed as the crack meets up with inclusion-matrix interface. This originates an arrest and a reinitiation wave from inclusion-matrix interface. The waves are clearly visible in the next two images at 160 and $165 \mu\text{sec}$.

In Fig. 6.7 an enlarged interferogram at $165 \mu\text{sec}$ time instant shows multiple stress waves due to crack-inclusion interaction. A distinct difference in emanating stress waves can be noticed when Figs. 6.4 and 6.7 are compared for weakly and strongly bonded inclusions, respectively. Unlike in weakly bonded inclusion, it is difficult to distinguish the arrest wave from the reinitiation wave in case of strongly bonded inclusion because both waves have nearly the same center of origin at a point where the crack first meets the inclusion. Also, disturbance in fringes is relatively spread out over a relatively large band.

The interferograms at time instants from 165 to $215 \mu\text{sec}$ in Fig. 6.6 show the crack propagating away from the inclusion following interaction. In all these images shrinking size of crack-tip fringes suggests lower stress intensity as the crack approaches the impact point. The images also show that the crack has circumvented the inclusion in this case. The crack deflection and propagation around a strongly bonded inclusion

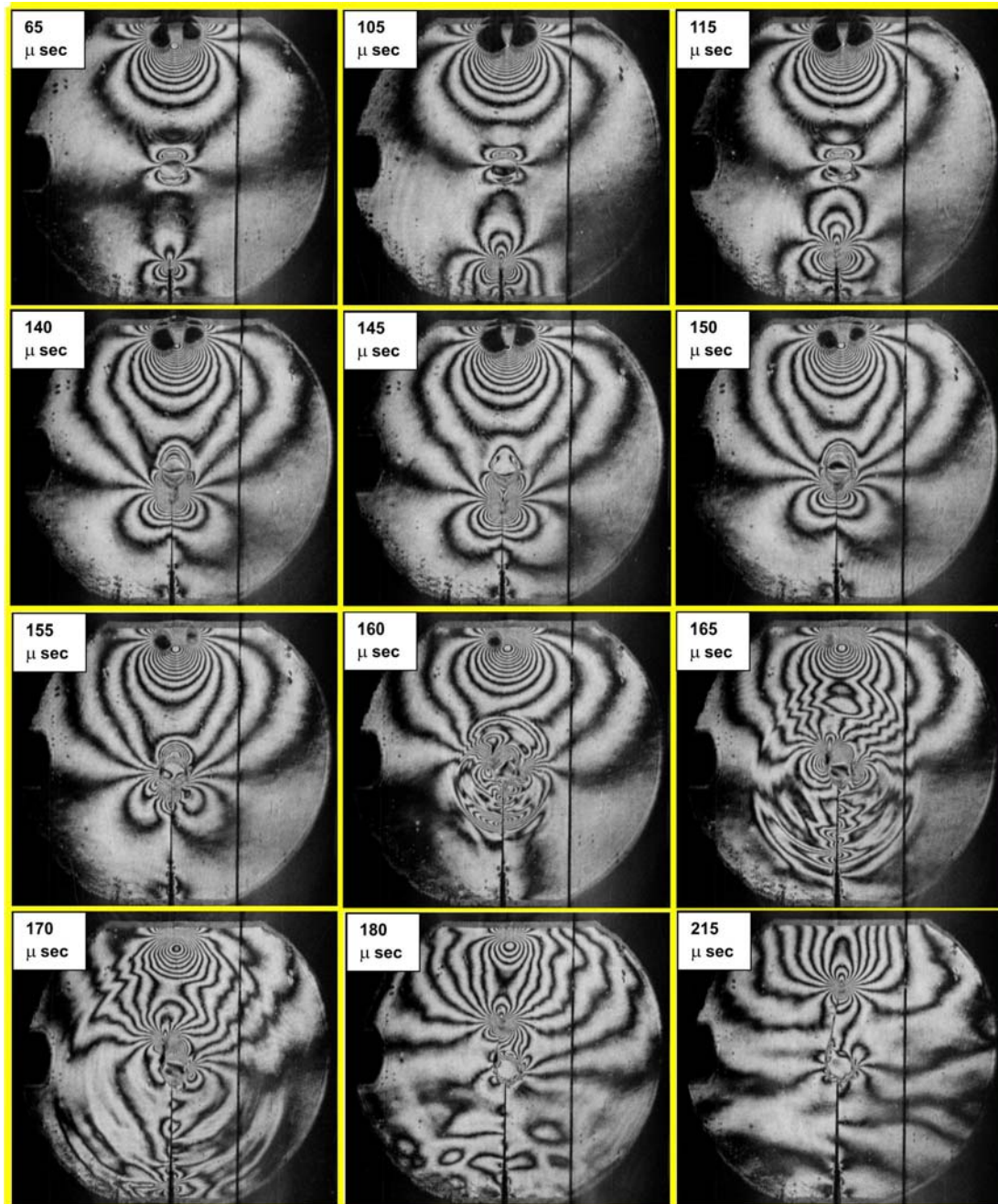


Figure 6.6: Selected fringe pattern representing surface slope contours ($\delta w / \delta x$) for specimen with strongly bonded inclusion located symmetrically ($e = 0$) with respect to the initial crack-tip. (Vertical line is at 10 mm from the crack line.)

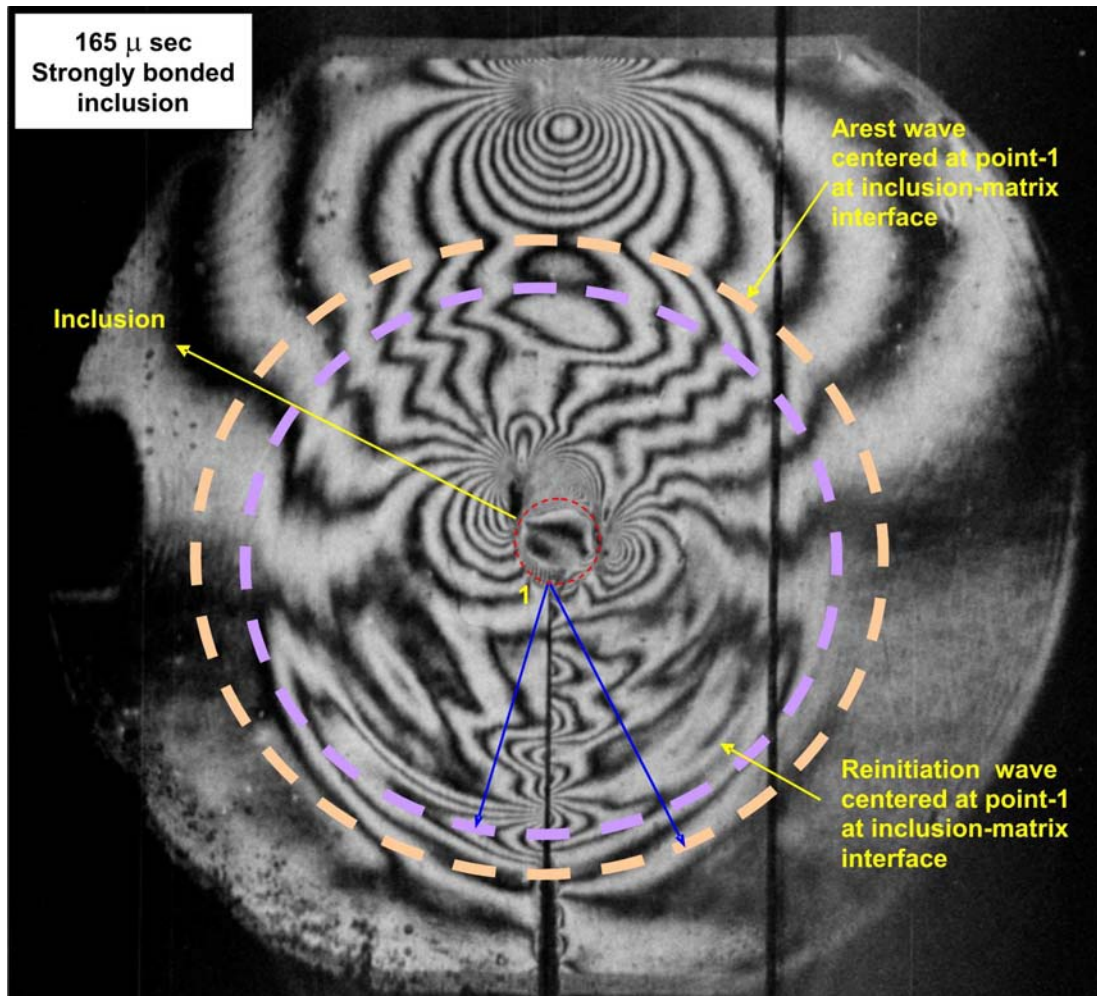


Figure 6.7: Stress waves due to crack-inclusion interaction when the inclusion is strongly bonded. Trace of kinks in fringes suggest arrest and reinitiation waves.

is shown in photograph in Fig. 6.5(b). This is unlike weakly bonded case where the inclusion-matrix interface completely delaminates and the crack lodges into interfacial cavity before reinitiation.

6.2.3 Weakly and strongly bonded inclusions ($e = d/2$)

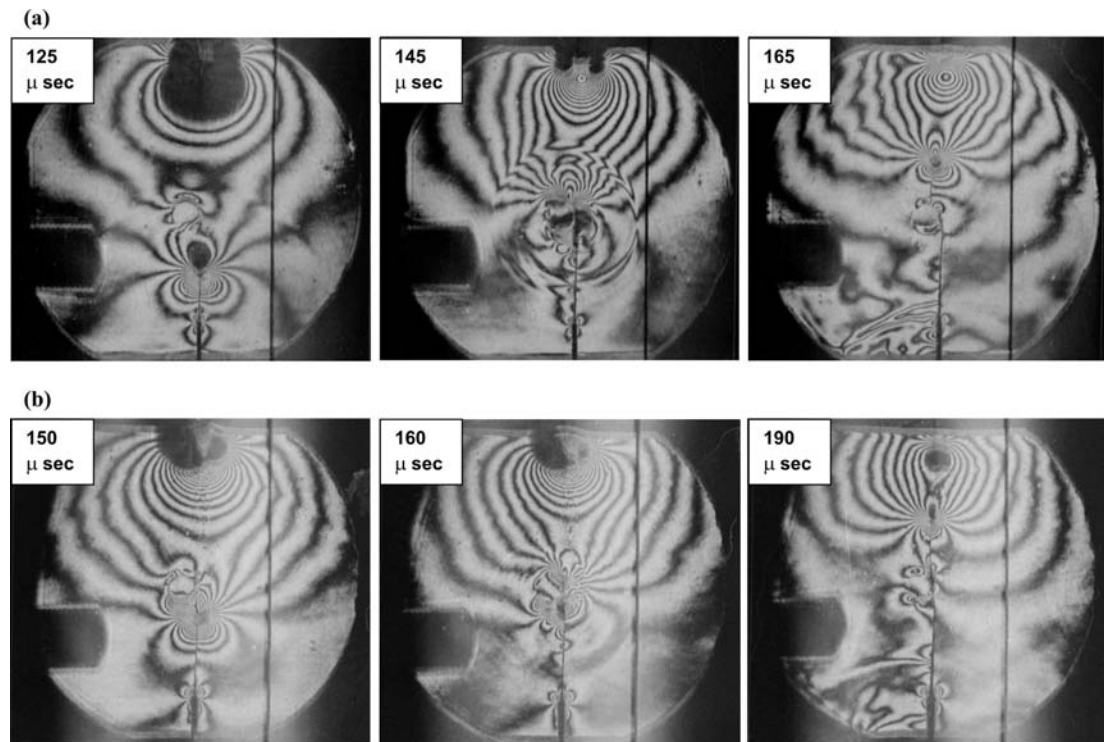


Figure 6.8: Selected fringe pattern representing surface slope contours of $\delta w / \delta x$ for specimen with tangentially located inclusion with respect to initial crack orientation ($e = d/2$). Images show crack-inclusion interaction for the specimen with, (a) Weakly and (b) Strongly bonded inclusion.

Experiments are also performed for the case when the inclusion is initially located with an offset distance relative to the initial crack ($e = d/2$). That is, the crack is initially oriented tangentially to the inclusion boundary. Figure 6.8 shows selected crack-inclusion interaction interferograms for weakly and strongly bonded inclusion cases. For brevity

only three interferograms from each experiment (all from post-crack initiation regime) are shown. The first image at $125 \mu\text{sec}$ time instant in Fig. 6.8(a) for the specimen with weakly bonded inclusion shows crack propagating towards inclusion. Frontal lobes of crack-tip fringes interacting with the inclusion can be seen. Next image at $145 \mu\text{sec}$ shows a reinitiated crack at the inclusion-matrix interface and centered at a point shifted to the left of its original track. This interferogram also shows evidence of an arrest wave seen as a circular perturbation of otherwise smooth fringes in the field. The path of the perturbed crack in the region past the inclusion is evident in the third image at $165 \mu\text{sec}$. The shifted crack paths are more clear in this frame. The corresponding fractured specimen photograph is shown in Fig. 6.5(c).

Figure 6.8(b) shows interferograms for a specimen with strongly bonded inclusion. The first image at $150 \mu\text{sec}$ shows the crack-tip fringes interacting with the inclusion when the crack is about to reach the inclusion. A relatively mild stress wave emerging from the inclusion-matrix interface can be noticed from the next image at $160 \mu\text{sec}$ as the crack just grazes past the inclusion while propagating tangentially to it. This is visible in the third image at $190 \mu\text{sec}$, where the crack has sufficiently propagated past the inclusion. The corresponding fractured specimen photograph is shown in Fig. 6.5(d).

6.3 Effect of crack-inclusion interaction on crack velocity

The interferograms recorded were digitized to determine crack growth and hence crack speed histories. First, the effect of inclusion eccentricity is described for both weakly and strongly bonded inclusions.

6.3.1 Effect of inclusion eccentricity

Crack velocity histories in specimens with weakly and strongly bonded inclusions are shown in Figs. 6.9(a) and (b), respectively. Two different eccentricities, $e = 0$ and $d/2$, are considered. Crack velocity plots in 6.9(a) for weakly bonded inclusions show rapid acceleration (of the order of 10^7 *m/sec*), reaching a velocity of ~ 275 *m/sec*. Subsequently, a small but gradual increase in velocity is noticed as the crack approaches the inclusion. Interestingly, this value of velocity, ~ 325 *m/sec*, just before the crack meets the weakly bonded inclusion is equal to the steady-state velocity seen in case of neat epoxy (see, Fig. 4.6 in Chapter 4). As the crack encounters inclusion-matrix interface, both specimens with $e = 0$ and $d/2$ show a rapid acceleration due to reinitiation from weak/weakened interface. An extremely high crack speed ~ 850 *m/sec*, which is nearly 85% of the Rayleigh wave speed in neat epoxy, close to reinitiation is noticed¹. This is due to the high-speed interfacial crack growth as well as reinitiation from a highly ‘blunted’ tip when the crack lodges into inclusion-matrix interface. Prior to attaining this peak velocity, a significant drop upto ~ 140 *m/sec* is seen when the inclusion is located symmetrically ($e = 0$). This is an indication of a rapid deceleration, possibly arrest at inclusion-matrix interface. The maximum crack velocity is followed by an instantaneous drop to ~ 300 *m/sec* and subsequently a monotonic reduction occurs prior to total fracture as the crack propagates away from the inclusion.

Figure 6.9(b) shows velocity histories for specimens with strongly bonded inclusion at $e = 0$ and $d/2$ eccentricities. Similar to the case of weakly bonded inclusion, a

¹It should be noted that uncertainty in crack speed is rather high during this period due to several transient events, namely a mode-I crack becoming an interfacial crack before returning to being a mode-I crack again. The temporal resolution is clearly insufficient to resolve all the details.

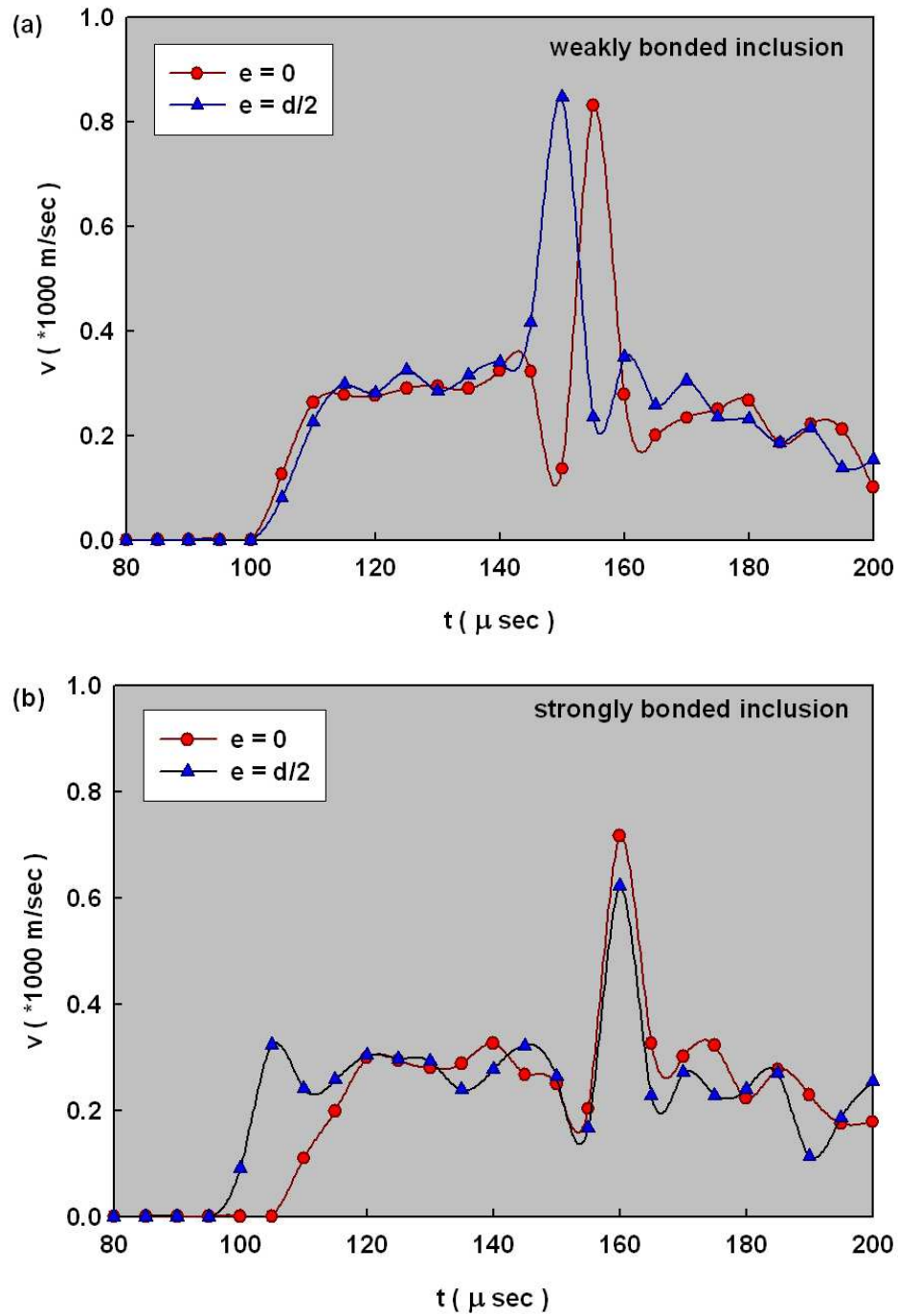


Figure 6.9: Crack velocity histories in specimens embedded with (a) weakly bonded and (b) strongly bonded cylindrical inclusions.

rapid acceleration of the order of $\sim 10^7$ *m/sec* at initiation is seen. As the crack approaches the inclusion, crack velocity is ~ 325 *m/sec* (equal to the steady-state velocity seen in neat epoxy) before dropping to ~ 200 *m/sec*. This deceleration as the crack approaches inclusion-matrix interface is unlike the case of weakly bonded inclusion where the crack speed increases monotonically until crack reaches inclusion-matrix interface. Subsequently, the crack grows around the inclusion at speeds reaching ~ 700 *m/sec* and ~ 600 *m/sec* for $e = 0$ and $d/2$ eccentricities, respectively. An instantaneous drop in velocity to ~ 300 *m/sec* in case of weakly bonded inclusions. Subsequently, specimen fractures as crack propagates away from the inclusion with a monotonically decreasing velocity.

6.3.2 Effect of inclusion-matrix adhesion strength

Next, the effect of inclusion-matrix adhesion strength on crack velocities is described. As discussed previously, inclusion is coated with silane to create a stronger inclusion-matrix interface. In Figs. 6.10(a) and (b) velocity histories in weakly and strongly bonded inclusions are compared for $e = 0$ and $d/2$ inclusion eccentricities, respectively. Figure 6.10(a) is for the case of symmetrically located inclusion. The velocity profiles of weakly and strongly bonded inclusions nearly follow each-other until the propagating crack approaches the inclusion. Before reaching the inclusion-matrix interface, the velocity profile for weakly bonded inclusion deviates from the one for strongly bonded case. In the former the crack velocity shows a sudden drop to ~ 140 *m/sec* (within $5 \mu\text{sec}$) as the crack reaches weak/delaminated inclusion-matrix interface whereas the latter shows a gradual drop in velocity from ~ 300 *m/sec* to ~ 200 *m/sec* in about $15 \mu\text{sec}$, as the

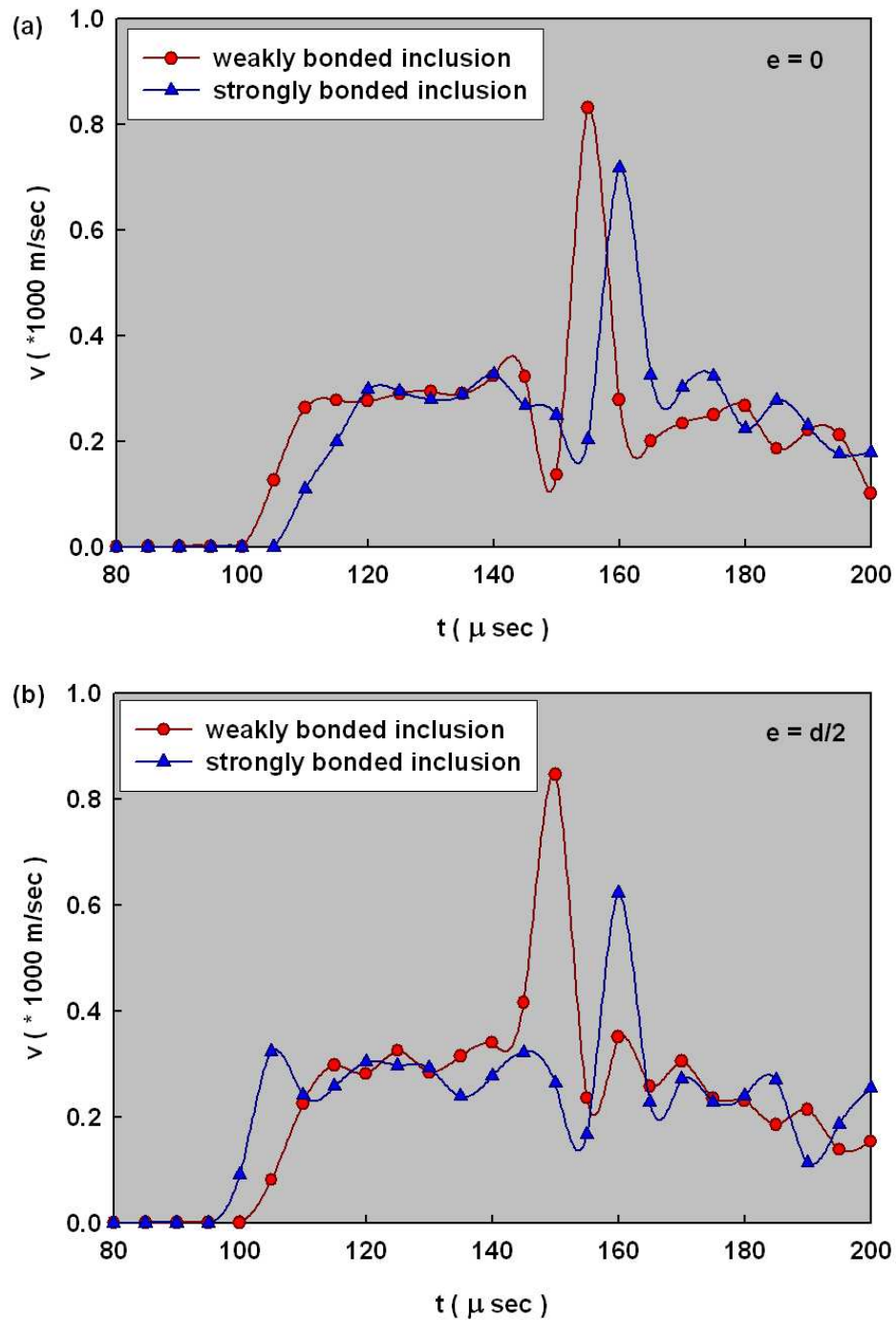


Figure 6.10: Crack velocity histories in epoxy specimen embedded with inclusions, (a) symmetrically located ($e = 0$) in front of crack-tip, (b) tangentially located ($e = d/2$) to initial crack orientation.

crack propagates and reaches inclusion-matrix interface. Subsequently, reinitiation velocity from delaminated interface in weakly bonded inclusion reaches an extremely high value of $\sim 850 \text{ m/sec}$ within one interframe period ($5 \mu\text{sec}$), which is $\sim 260\%$ of steady-state velocity seen in neat epoxy. On the other hand, the deflected crack propagates around the rigid inclusion in strongly bonded case attaining a velocity of $\sim 700 \text{ m/sec}$. These maximum crack velocities are further followed by a rapid drop to 200 m/sec and 300 m/sec in weakly and strongly bonded inclusions, respectively, followed by a monotonic reduction until specimens fracture completely.

Figure 6.10(b) shows velocity histories of weakly and strongly bonded cases when the inclusion is located tangentially ($e = d/2$) to the initial crack orientation direction. The features here are similar to the other until the inclusion is close to the crack tip during the initial approach. As the crack approaches the inclusion, velocity in the strongly bonded case shows a gradual drop to about 160 m/sec . This is followed by a sudden rise in crack velocity to $\sim 600 \text{ m/sec}$ as the crack propagates nearly in the same direction after passing the inclusion tangentially. On the contrary, the crack achieves a maximum crack velocity of $\sim 850 \text{ m/sec}$ when it reinitiates from a delaminated inclusion-matrix interface in weakly bonded inclusion case. It should be noted that in this case that the propagating crack has turned towards the inclusion-matrix interface and reinitiated at an off-set distance relative to its initial path from the top of the inclusion-matrix interface. Subsequent growth characteristics are similar to the case of the strongly bonded inclusion.

6.4 Effect of crack-inclusion interaction on SIF histories

Interferograms are also used to extract fracture parameters. Optical informations are retrieved by digitizing crack-tip fringes to tabulate fringe locations and fringe order. The Eq. (2.15), used to extract mode-I stress intensity factor[66], is extended for mixed-mode (mode-I and mode-II) situation as,

$$\frac{\partial w}{\partial x} = -\frac{\nu B}{2E} f(v) \sum_{n=1}^{\infty} \left[\left(\frac{n}{2} - 1 \right) r_l^{\left(\frac{n}{2} - 2 \right)} \left\{ A_n \cos \left(\frac{n}{2} - 2 \right) \theta_l + B_n \sin \left(\frac{n}{2} - 2 \right) \theta_l \right\} \right] = \frac{Np}{2\Delta}, \quad (6.1)$$

where $f(v)$, θ_l and r_l are as given by Eq. (2.16) and A_n and B_n are constants of the asymptotic series. The digitized data are used in above equation in conjunction with overdeterministic least-squares analysis to evaluate mode-I and mode-II stress intensity factors ($K_I = A_1 \sqrt{\frac{\pi}{2}}$, $K_{II} = B_1 \sqrt{\frac{\pi}{2}}$). Further, K_I and K_{II} are used to calculate effective stress intensity factor, K_e is given by,

$$K_e = \sqrt{K_I^2 + K_{II}^2}, \quad (6.2)$$

and phase angle ψ given by,

$$\psi = \tan^{-1} \left(\frac{K_{II}}{K_I} \right). \quad (6.3)$$

As the crack encounters the inclusion, crack tip fringes are greatly disturbed due to arrest/reinitiation waves. Also, interaction of crack tip fringes with rigid inclusion affect the shape and size of fringes immensely making it difficult to accurately identify fringe orders. Moreover, when the crack-tip is close to the inclusion, the crack tip singularity is affected and is different than the one in a homogeneous material (see, Zak and Williams,

1958). Therefore, fringe analysis becomes difficult once the crack-tip has reached the inclusion-matrix interface and is not attempted in this work.

In the following section, effects of inclusion eccentricity and inclusion-matrix adhesion strength on K_e histories are described. Crack tip fringes are analyzed before the crack tip reaches the inclusion-matrix interface. The fracture behavior of neat epoxy (see, Fig. 4.6 in Chapter 4) is considered as a reference for comparison².

6.4.1 Effect of inclusion eccentricity

Stress intensity factor histories for specimens with weakly and strongly bonded inclusions are shown in Fig. 6.11(a) and (b), respectively. Both symmetrically ($e = 0$) and tangentially ($e = d/2$) located weakly bonded inclusions in Fig. 6.11(a) show monotonic increase in K_e until crack initiation from the original tip. The average crack tip loading rate, dK_e/dt , before crack initiation is nearly the same $\sim 23 \pm 2 \text{ MPa}\sqrt{\text{m}}/\text{ms}$ as that of neat epoxy. Similar pre-initiation K_e history and the same crack tip loading rate when the inclusion is sufficiently away from the crack tip, suggests that the inclusion eccentricity does not play any significant role on pre-crack initiation behavior. In each case, crack initiation is followed by a drop in K_e value before attaining a steady-state value. The K_e at crack initiation for symmetrically located inclusion ($\sim 1.5 \text{ MPa}\sqrt{\text{m}}$) is slightly lower when compared to the case of tangentially located inclusion ($1.6 \text{ MPa}\sqrt{\text{m}}$). As the crack approaches an inclusion, the K_e histories for the two specimens show differences. For the case of $e = 0$, post initiation K_e history shows oscillations about an average value ($\sim 1.3 \text{ MPa}\sqrt{\text{m}}$) somewhat lower than the steady-state fracture toughness

²The neat epoxy specimen shows an average pre-initiation crack tip loading rate $dK_e/dt \approx 25 \text{ MPa}\sqrt{\text{m}}/\text{ms}$ and the steady state fracture toughness $K_{I,ss} \approx 1.5 \text{ MPa}\sqrt{\text{m}}$.

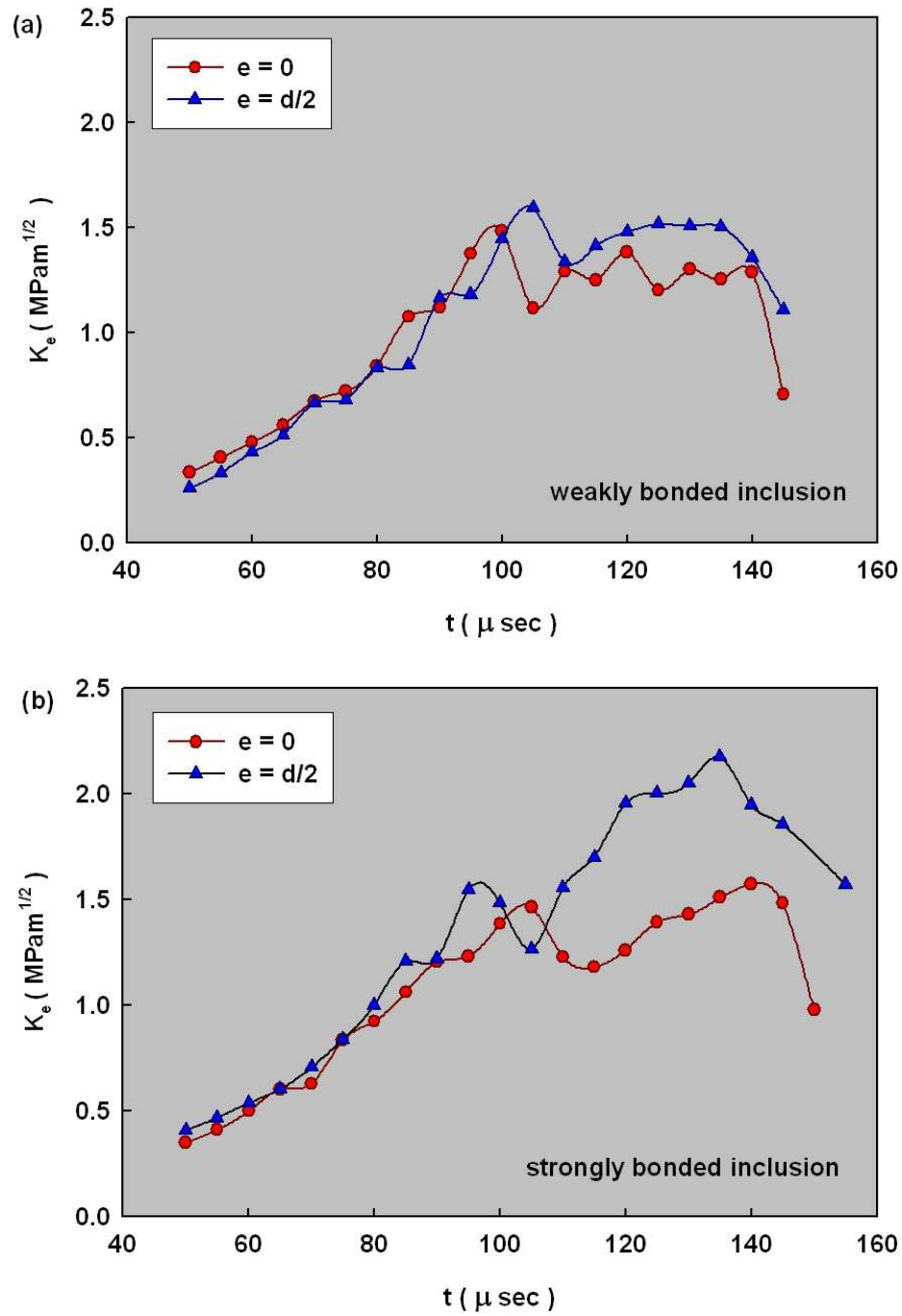


Figure 6.11: Stress intensity factor histories in specimen embedded with (a) weakly bonded and (b) strongly bonded cylindrical inclusions.

value for neat epoxy ($\sim 1.5 MPa\sqrt{m}$). On the contrary, in case of $e = d/2$ a monotonic increase in K_e can be noticed until it stabilizes at $\sim 1.5 MPa\sqrt{m}$, the value equal to K_{Iss} for neat epoxy. As the crack tip reaches the proximity of the inclusion, both $e = 0$ and $d/2$ specimens show a decrease in K_e value. This drop in K_e is relatively abrupt in the former case.

Figure 6.11(b) shows K_e histories for two different eccentricities of silane treated (strongly bonded) inclusions. The specimens show an average rate of increase in effective SIF $\sim 24 \pm 2 MPa\sqrt{m}/ms$, which is nearly the same as that of the weakly bonded case. Similar to weakly bonded inclusion, K_e at crack initiation is slightly higher for $e = d/2$. Both eccentricities show a small drop in K_e value at initiation followed by a monotonic increase as the crack approaches an inclusion. The rate of increase in K_e is higher for the case when the inclusion is tangentially situated in front of the initial crack tip. As the crack propagates towards the inclusion, dK_e/dt for $e = 0$ and $e = d/2$ are $\sim 15 MPa\sqrt{m}/ms$ and $\sim 30 MPa\sqrt{m}/ms$, respectively. When the crack is very near the inclusion a steep drop in K_e is seen until it meets inclusion-matrix interface.

6.4.2 Effect of inclusion-matrix adhesion strength

Next, the effect of bonding strength between an inclusion and the matrix on SIF is discussed. Figure 6.12 shows K_e histories of weakly and strongly bonded inclusions at $e = 0$ eccentricity. Both show nearly same pre- initiation behaviors ($dK_e/dt \sim 25 MPa\sqrt{m}/ms$). Also, the inclusion-matrix adhesion strength does not affect K_e values at initiation ($\sim 1.5 MPa\sqrt{m}$). A small drop in K_e following crack initiation is evident in each case. As the crack propagates towards an inclusion, K_e values oscillate about an

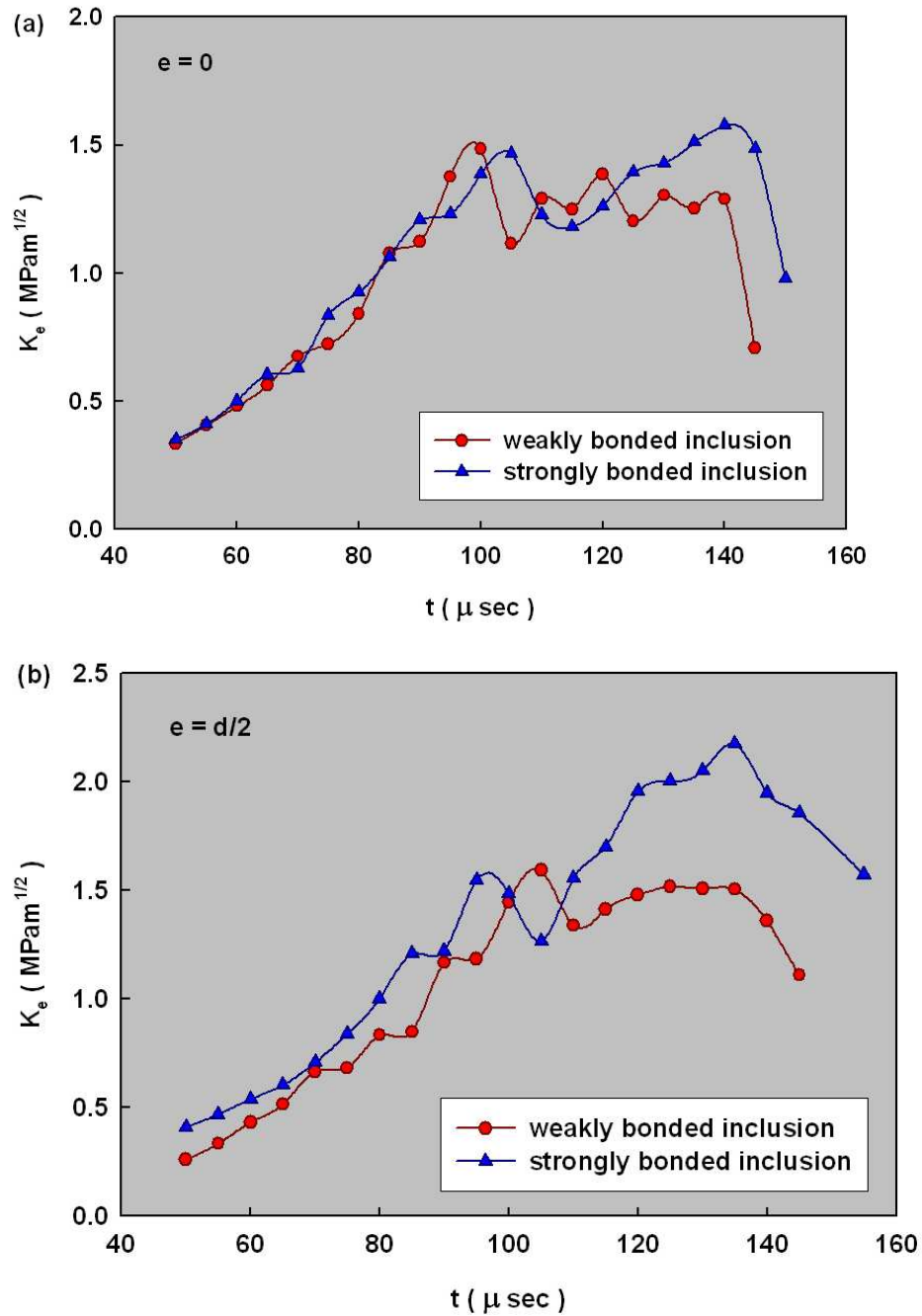


Figure 6.12: Stress intensity factor histories in specimen embedded with cylindrical inclusions, (a) symmetrically located ($e = 0$) in front of the crack-tip, (b) tangentially located ($e = d/2$) to initial crack orientation.

average of $\sim 1.3MPa\sqrt{m}$ in case of weakly bonded inclusion. On the other hand, strongly bonded inclusion shows monotonic increase in K_e from $\sim 1.3MPa\sqrt{m}$ to $\sim 1.6MPa\sqrt{m}$ as the crack propagates towards the inclusion. In the proximity of inclusion both weakly and strongly bonded inclusion specimens show noticeable drop in K_e with nearly the same dK_e/dt .

Figure 6.12(b) shows the effect of inclusion-matrix adhesion strength when the inclusion is located tangentially ($e = d/2$) with respect to the initial crack. Again, similar pre- initiation behavior with nearly the same crack tip loading rate is noticed for both weakly and strongly bonded inclusions. Crack initiated at $K_e \approx 1.6MPa\sqrt{m}$ followed by a small drop in K_e value. Similar to $e = 0$, weakly bonded specimen case shows a crack growth stabilizing at a K_e value of $\sim 1.5MPa\sqrt{m}$ while propagating towards the inclusion whereas in case of strongly bonded counterpart, crack grows with a monotonically increasing K_e value. Among all the cases considered, strongly bonded and $e = d/2$ inclusion shows largest increase in K_e from $1.3MPa\sqrt{m}$ to $2.2MPa\sqrt{m}$ with $dK_e/dt \sim 30MPa\sqrt{m}/ms$ as the crack propagates towards the inclusion.

CHAPTER 7

CRACK-PARTICLE INTERACTION STUDY USING BEM¹

In previous chapters an experimental study of the effects of microstructure on fracture behavior of particulate polymer composites was presented. To explain potential toughening mechanisms, limited crack-inclusion interaction studies on epoxy specimens embedded with a cylindrical glass inclusion were carried out experimentally. In this chapter a numerical tool, SGBEM, is used to provide additional insight into crack-inclusion interaction when the inclusion is weakly or strongly bonded to the matrix material. The computations are limited to quasi-static conditions and are used to complement experimental observations when appropriate. First, the difference in crack growth behavior is discussed for two different inclusion-matrix interface strengths. The effect of delamination on energy release rate and mode mixity is parametrically studied next. And finally, interaction of a crack with a particle-cluster is studied with emphasis on orientation and volume fraction of the cluster on fracture behavior when investigated for strongly bonded inclusions are involved.

7.1 Model geometry

A plane stress situation involving a cracked sheet of dimensions $140 \text{ mm} \times 40 \text{ mm} \times 8 \text{ mm}$ is considered to investigate the effects of inclusion orientation and inclusion-matrix interfacial strength on crack inclusion interaction. The material properties of the matrix and inclusions are matched with those for epoxy and glass, respectively, with an elastic

¹*Parts of this chapter appear in Ref. [107]*

modulus (E_m) 3.2 GPa and Poisson's ratio (ν_m) 0.3 for epoxy and $E_g = 70$ GPa, $\nu_g = 0.3$ for glass. Two different loading configurations are considered in the simulations. To investigate the effect of a weakly bonded inclusion on crack growth, simulations are performed on a single edge notched tensile specimen loaded in uniform tension. To perform parametric study on specimens with strongly bonded inclusion, 3-point bending of an edge cracked beam is considered. A crack is located at the edge of the sheet opposite to the loading point and along the loading axis. The line joining the initial crack tip and loading point is referred to as line-of-symmetry throughout this study.

7.2 Benchmarking and mesh convergence

To ensure a high degree of accuracy of SIFs calculated by BE simulations, first a single edge notched geometry (see inset in Fig. 7.1(a)) of neat matrix material without any inclusions is carried out. The geometry is a symmetrically loaded 3-point bend configuration. The initial crack length is chosen such that $a/W = 0.25$ where W is the total width of the chosen geometry. In the simulations, equal length boundary elements are used to represent specimen edges including the initial crack. This length is determined first by performing a convergence study. The SIF results for different element lengths varying from $W/10$ to $W/40$ as a function of crack length are determined for a symmetrically loaded 3-point bend configuration using Eq. (4.1). Nondimensional SIF ($=K_I \frac{B\sqrt{W}}{P}$) values from SGBEM are compared with analytical results in Fig. 7.1(a) for different a/W ratios. With a decrease in element length accuracy of SIF calculations increase. Good agreement between calculated K_I values using SGBEM and analytical results are evident when an element length of $W/40$ is used. For this choice, a high

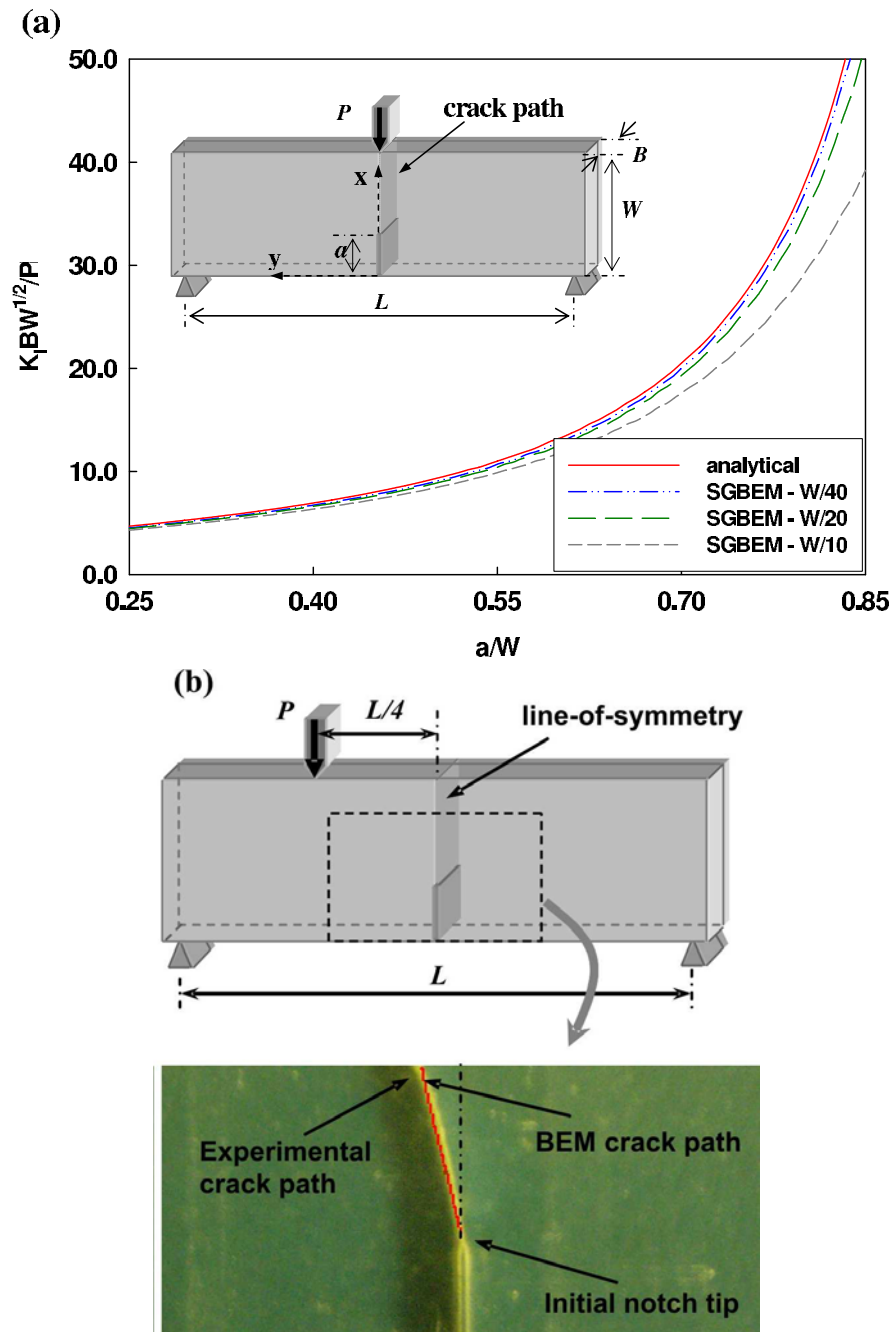


Figure 7.1: (a) Comparison between analytical results and SGBEM results for various boundary element lengths, (b) Crack propagation for mixed-mode loading; crack trajectory from BEM is superimposed on experimentally obtained crack path for an eccentrically applied load at the distance $L/4$ from the line-of-symmetry.

degree of accuracy can be expected up to $a/W = 0.75$ with an error less than 2.5%. Beyond $a/W = 0.75$, however, the accuracy reduces due to the dominance of loading point stresses on the crack tip stress field.

Next, the crack tip increment length in the direction of propagation is determined separately to match experimentally determined crack paths in a mixed-mode loading situation. The crack geometry used in the simulations is same as the one shown earlier for the mode-I case (Fig. 7.1(a)), except for the location of the applied load. The loading point is at a distance of $L/4$ from the line-of-symmetry, where L is the span. Various crack tip increments are used before choosing $\Delta a/W = 6.25 \times 10^{-3}$ in the simulations. The loading configuration, specimen geometry and the fractured epoxy specimen from an experiment are shown in Fig. 7.1(b). The crack trajectory from BE analysis is superimposed on experimentally obtained crack path. Excellent agreement between crack paths shows the accuracy of SGBEM in capturing mode-mixity using the chosen crack tip increment.

The accuracy of energy release rate (ERR) calculations are validated next against the results reported in Ref. [41]. The geometry and loading configuration (See Figs. 3 and 7 in [41]) is shown in Fig. 7.2(a). The inclusion radius r is considered as $L/20$, where L is the length of the planar body with an edge crack. The ratio of the elastic moduli E_p/E_m is varied from 2 to 8, where the subscripts p and m correspond to the inclusion and the matrix, respectively. The Poisson's ratio for the inclusion and matrix are considered as 0.33 and 0.17, respectively. In Fig. 7.2(b) nondimensional ERR, G/G_0 , is plotted with varying nondimensionalized crack lengths, where G_0 is the ERR for the case without inclusion. The crack tip shielding increases (i.e., G/G_0 decreases) with

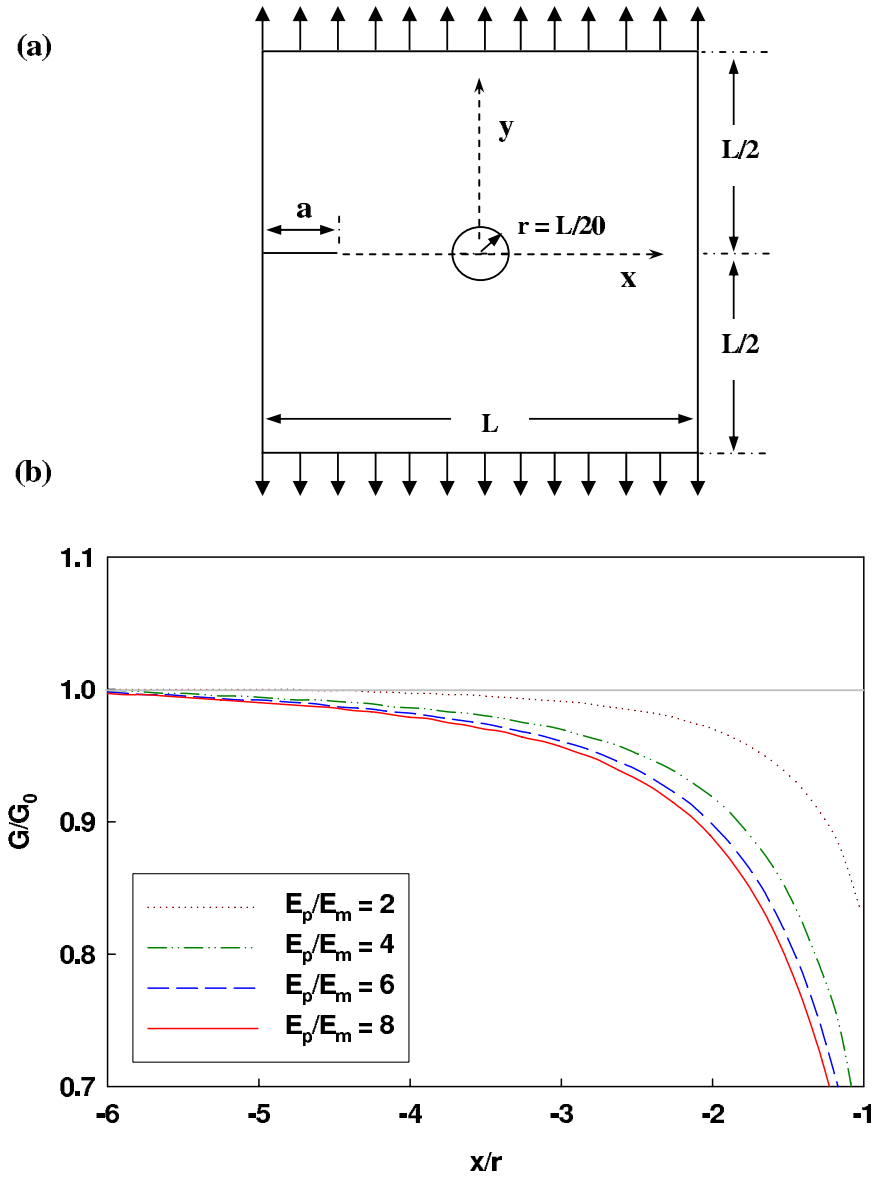


Figure 7.2: Validation of ERR calculation from SGBEM in the presence of secondary phase filler, (a) Problem geometry and loading configuration, (b) Variation of nondimensional ERR for various E_p/E_m , $\nu_p = 0.17$, $\nu_m = 0.33$.

increasing E_p/E_m . The crack senses the rigid particle in front of it at least from a distance of ≈ 5 radii. The observed G/G_0 variations for various E_p/E_m are same as the ones reported by Bush[41]) and hence suggests the accuracy of ERR calculations from SGBEM in the presence of secondary phases. Minor differences in ERR value, when the crack reaches the particle can be attributed to the different methods of ERR calculation (DCT method in current study).

7.3 Effect of inclusion-matrix adhesion on crack growth

Crack-inclusion interaction is investigated in this section, when an inclusion is weakly and strongly bonded to the matrix material. As described earlier an edge cracked geometry of dimensions $140 \text{ mm} \times 40 \text{ mm} \times 8 \text{ mm}$ with material properties, $E_m = 3.2 \text{ GPa}$, $\nu_m = 0.3$, $E_g = 70 \text{ GPa}$, $\nu_g = 0.3$, is used in the simulation. The inclusion is located tangentially to the initial crack orientation direction as shown in Fig. 7.3(a). A uniform tension is applied to specimen as shown in figure. An ideal inclusion-matrix interface is considered to represent a strong interface. A weak interface is modeled by considering a delaminated inclusion. That is, it is assumed that the inclusion is delaminated prior to crack growth. In the simulation the right half of the inclusion-matrix interface is considered to have free boundary condition, which is represented by delamination angle $\alpha = 180^\circ$ (see, Figure 7.3(b)). The outer specimen boundary is meshed with quadratic elements of size $W/40$, whereas, the circular inclusion edge is modeled as a 12 edged polygon.

Figure 7.3(c) shows crack paths when the inclusion is weakly and strongly bonded to the matrix material. For both interface strengths initial crack propagation are in mode-I.

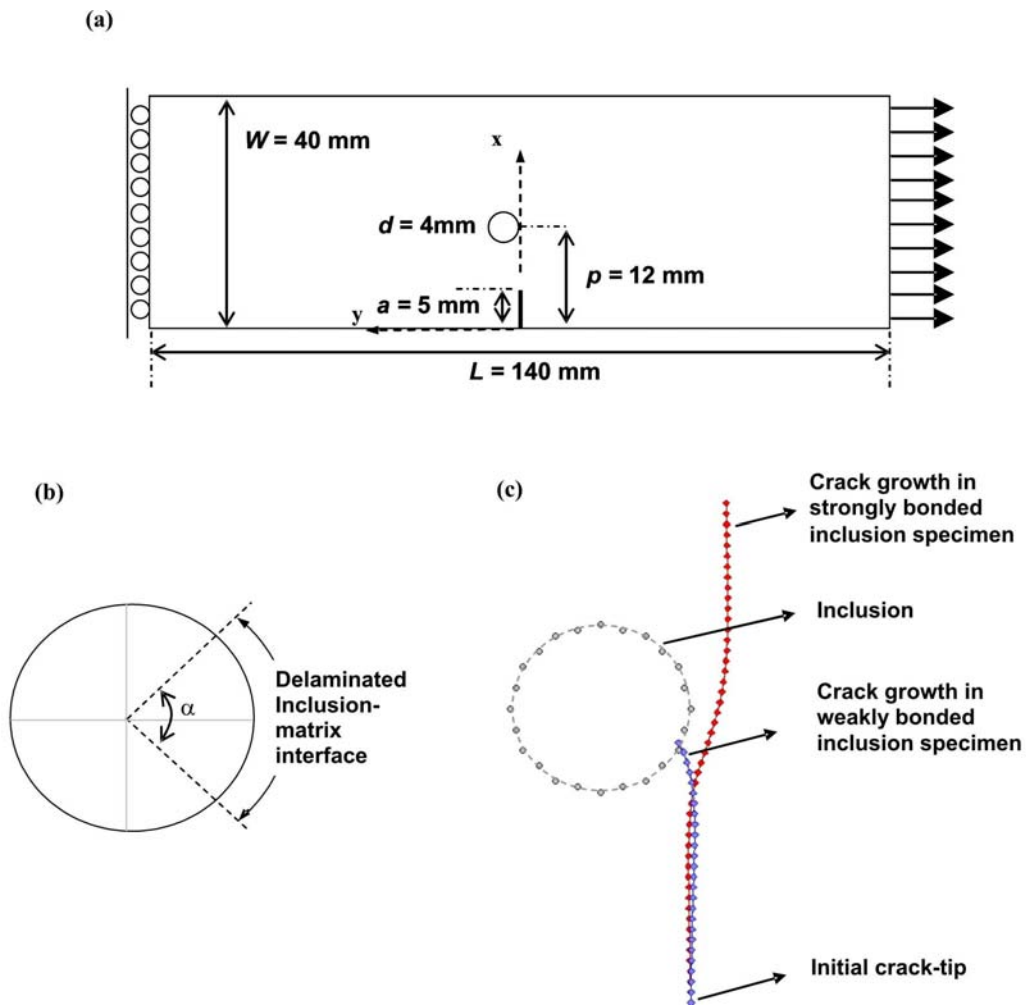


Figure 7.3: Modeling role of interfacial strength on Crack-particle interaction, (a) Specimen configuration, (b) The angle, α , represents the part of inclusion delaminated from matrix, (c) Crack paths for weakly and strongly bonded inclusions: Crack attracted towards delaminated inclusion-matrix interface ($\alpha = 180^\circ$), and deflected away from inclusion when it is strongly bonded to matrix.

As the crack approaches the inclusion, mixed-mode propagation occurs. A delaminated interface attracts the crack towards it, whereas an ideal inclusion-matrix interface repels the crack away. These results are consistent with the experimental results discussed in Chapter 6. The experiments showed a propagating crack lodging itself into a weak inclusion-matrix interface before reinitiation, whereas, a crack invariably propagated around the rigid inclusion when the interface is strong. The effect of inclusion-matrix interface strength on mode-mixity is parametrically studied in the following section. It is shown that mode-mixity in case of delaminated inclusion is significantly higher when compared to the strongly bonded case. This suggests that more energy is needed for crack propagation when the inclusion is weakly bonded to the matrix material. This is again consistent with the results discussed in Chapter 3, where weakly bonded filled material shows higher fracture toughness when compared to the strongly bonded ones.

7.4 Effect of delamination on fracture parameters

Effects of delamination on ERR and mode-mixity are investigated next. The delamination angle α , as shown in Fig. 7.3, is varied from 0° to 180° . It should be noted that 0° corresponds to the ideally bonded inclusion-matrix interface. Simulations in delaminated inclusion are performed until crack meets inclusion-matrix interface. Figure 7.4(a) shows the variation of nondimensional ERR, G/G_0 with a/W . In the case of strongly bonded inclusion, crack-tip shielding and amplification is evident as the crack propagates towards and away from the inclusion, respectively. In the case of delaminated inclusion (e.g. $\alpha = 30^\circ$) first amplification and then shielding is noticed as the delaminated interface attracts the propagating crack. The shielding appears to be greater than

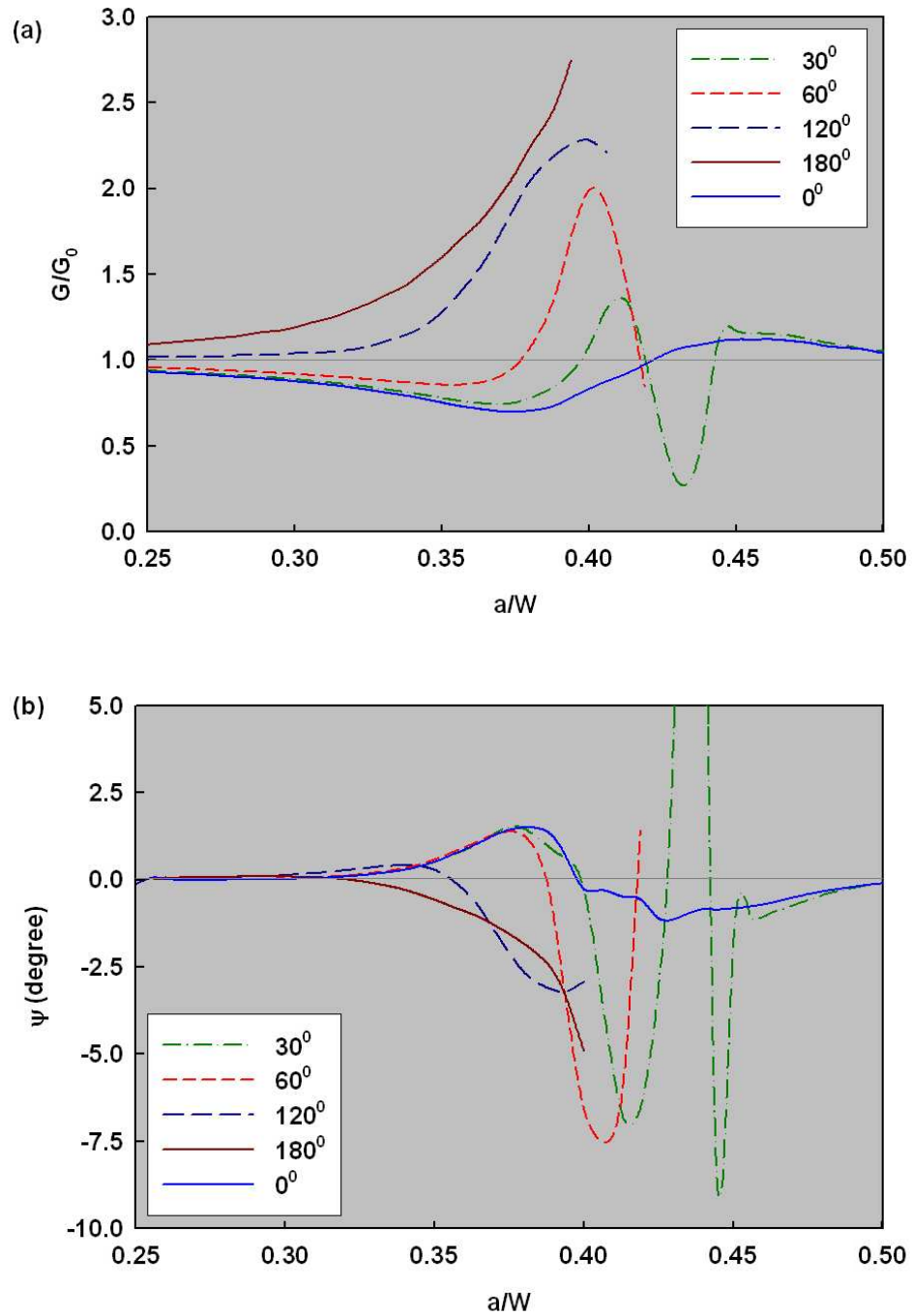


Figure 7.4: Effects of inclusion-matrix delamination on (a) Energy release rate (b) Mode-mixity.

amplification from G/G_0 record. It can be seen that the effect of delamination on amplification/shielding increases with increase in delamination angle (highest for $\alpha = 180^\circ$).

Figure 7.4(b) shows the variation of mode-mixity (phase angle ψ), for various a/W . The variation in ψ is relatively smooth for 0° delamination angle when compared to others. This suggests that if the inclusion is delaminated, crack propagates with a relatively higher mode-mixity which resists crack propagation. It can also be noticed from the plot that mode-mixity increases with increase in delamination angle.

7.5 Parametric study of strongly bonded inclusion and inclusion clusters

Next, crack growth through particle cluster is simulated to investigate the cluster orientation and volume fraction effects on ERR. Ideal inclusion-matrix interface is assumed in all simulations. When inclusions are perfectly bonded to the matrix material, crack deflection is a prominent toughening mechanism. The crack deflection depends on inclusion size, inclusion eccentricity with respect to the crack orientation, the number of inclusions surrounding the crack tip, etc. As mentioned earlier, a rigid inclusion in a relatively compliant matrix shields the crack tip as it is approached. However, shielding depends on the location of the inclusion with respect to the initial crack orientation. Also, the particle size, particle eccentricity, the number of particles and arrangement of particles around the crack tip are some of the other parameters which affect the degree of shielding. Therefore, a parametric study is conducted on crack interaction with single particle, prior to simulating propagation through a particle-cluster.

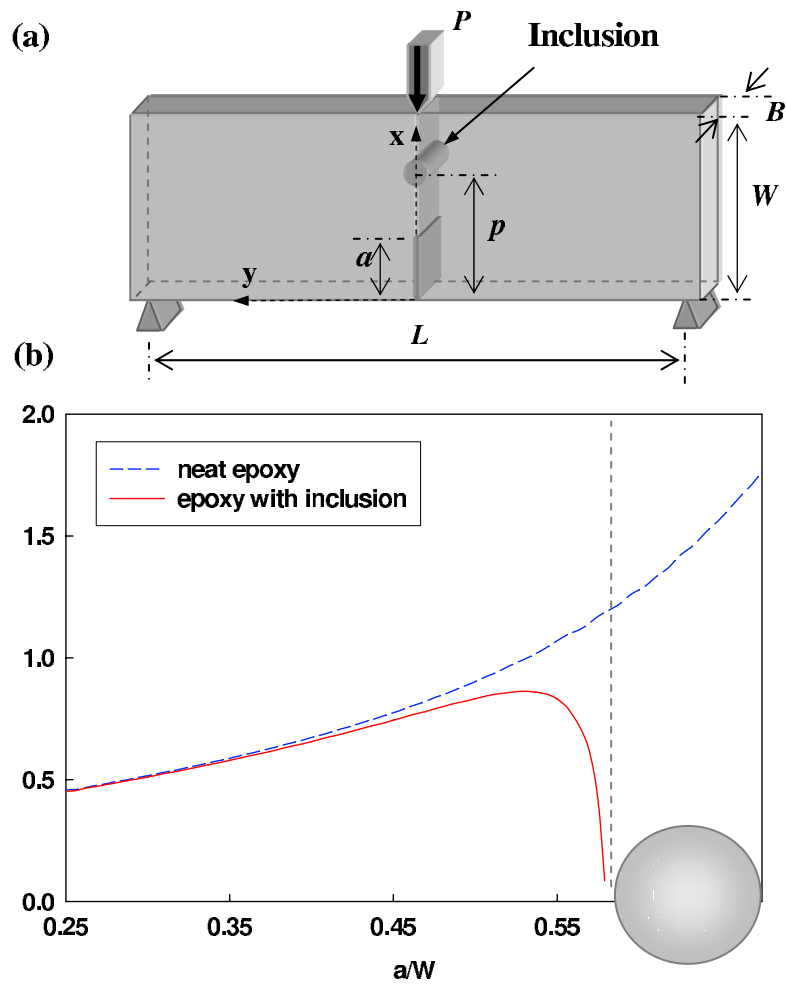


Figure 7.5: Crack tip shielding by a rigid inclusion in front of a mode-I crack, (a) Loading configuration, (b) Comparison between SIF variations in the presence and absence of inclusion.

7.5.1 Crack tip shielding

First, a case when a cylindrical inclusion of diameter $d = W/10$ symmetrically located in front of a crack tip is considered. Here, the inclusion is located in front of the initial crack tip at $p/W = 0.65$, where p is the distance of the center of the inclusion in the \mathbf{x} -direction (see Fig. 7.5(a)). The plot in Fig. 7.5(b) shows the variation of nondimensional K_I with crack length a/W . For comparison the K_I variation for the case of the neat matrix is also shown. A sharp decrease in SIF can be noticed from the plot as the crack approaches the inclusion. The inclusion in front of the crack shows negligible effect on K_I until the crack reaches a length of approximately $a/W = 0.45$. This suggests that the presence of rigid inclusion in front of the crack is felt only when the tip is at the distance of $\approx 1d$ from the inclusion. When the crack is $d/4$ away from the inclusion, K_I decreases substantially. The K_I approaches zero as the crack propagates further and reaches the inclusion.

The crack tip shielding and amplification effects are further explored by simulating a mode-I problem with a pair of inclusions ahead of a propagating crack. A *symmetrically* located pair of inclusions with respect to the crack orientation, as shown in Fig. 7.6, leads to crack growth under mode-I conditions. Here the inclusions are located at $p/W = 0.5$ or, $W/4$ away in the \mathbf{x} -direction from the initial crack tip. The separation distance ‘ s ’ between inclusions is varied from $d/8$ to $2d$, where $d = W/10$. Figure 7.6 shows the variation of G/G_0 with a/W .

Denoting the inclusion location (the orientation of the center of the inclusion(s)) in the \mathbf{x} -direction as p/W , it is evident that as the crack length approaches p/W , crack tip shielding effects begin to manifest as decreasing ERR ($G/G_0 < 1$) values with a/W . It

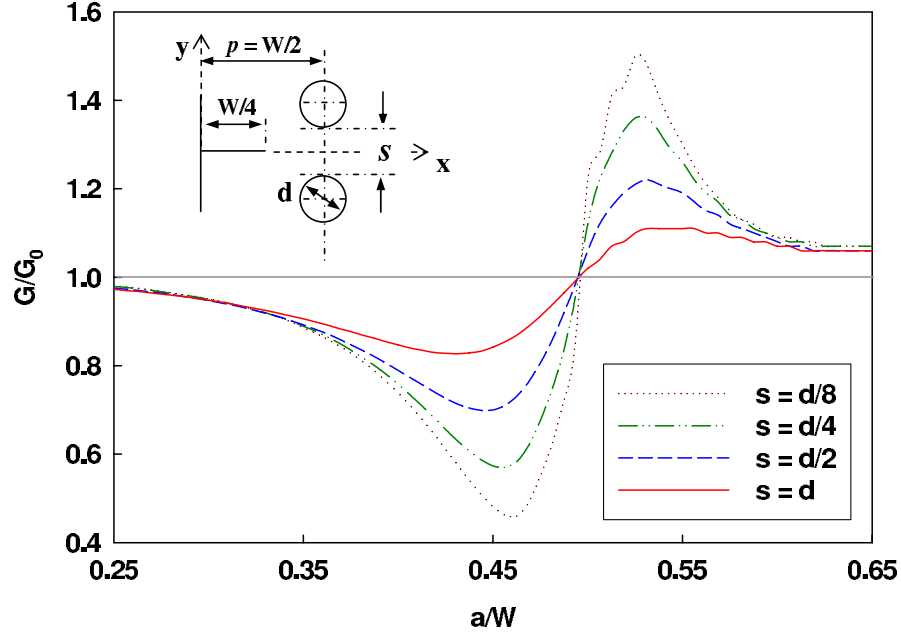


Figure 7.6: Crack tip shielding and amplification effects due to a pair of symmetrically situated inclusions in the crack path.

can be noticed that maximum shielding occurs when the crack tip is approximately $d/2$ in front of the center of the inclusion. Further crack propagation decreases shielding. That is, the nondimensional ERR reaches a value of unity when the propagating crack length a/W reaches p/W . As the crack propagates beyond p/W , an amplification of ERR ($G/G_0 > 1$) can be seen. The maximum amplification is seen when the crack tip is at a distance of $d/2$ away from the center of the inclusion. The amplification begins to vanish as the crack propagates away from this location. The above crack shielding/amplification effects are similar to the ones reported in Refs. [40] and [41].

From the plots in Fig. 7.6 it can also be seen that the shielding/amplification effect increases as the inclusion separation distance decreases. The effects are quite evident even

when the inclusions are $2d$ apart. Interestingly, the magnitude of maximum shielding is always greater than the magnitude of maximum amplification for a given value of s . If one were to associate the decrease in inclusion separation as a measure of increase in filler volume fraction, these results suggest that even at low volume fractions shielding effects are significant and the effect increases as the filler volume fraction increases.

7.5.2 Particle eccentricity effect

Next, interaction between a crack and an isolated inclusion located eccentrically to the initial crack is investigated. Of particular interest is the role inclusion eccentricity plays on crack deflection and the resulting ERR variation during crack growth. As shown in Fig. 7.7(a), the center of the inclusion is located $W/4$ away from the initial crack tip in the x -direction. The inclusion eccentricity ‘ e ’ (the distance between the center of the inclusion and the line-of-symmetry) is varied from $d/4$ to $2d$ while the load is applied symmetrically in a 3-point bend configuration as before. The crack paths around inclusions for different values of eccentricity are shown in Fig. 7.7(a). In these simulations, the crack propagates nearly in a mode-I fashion until the tip reaches $a/W \approx 0.45$ or $\approx 1d$ in front of the center of the inclusion. As the crack propagates further, the angle of deflection² increases. A sharp increase in the angle of deflection can be noticed from $a/W \approx 0.45$ onwards, when the crack is $d/2$ behind the the center of the inclusion. The angle of deflection attains a maximum value at $a/W \approx 0.475$. This is followed by a decrease in the angle of deflection with the crack still propagating away from the line-of-symmetry. When the crack travels $\approx d/2$ away from the particle location p/W ,

²Angle of deflection is the absolute angle between the *line-of-symmetry* (initial crack orientation) and the tangent to the crack path at any instant.

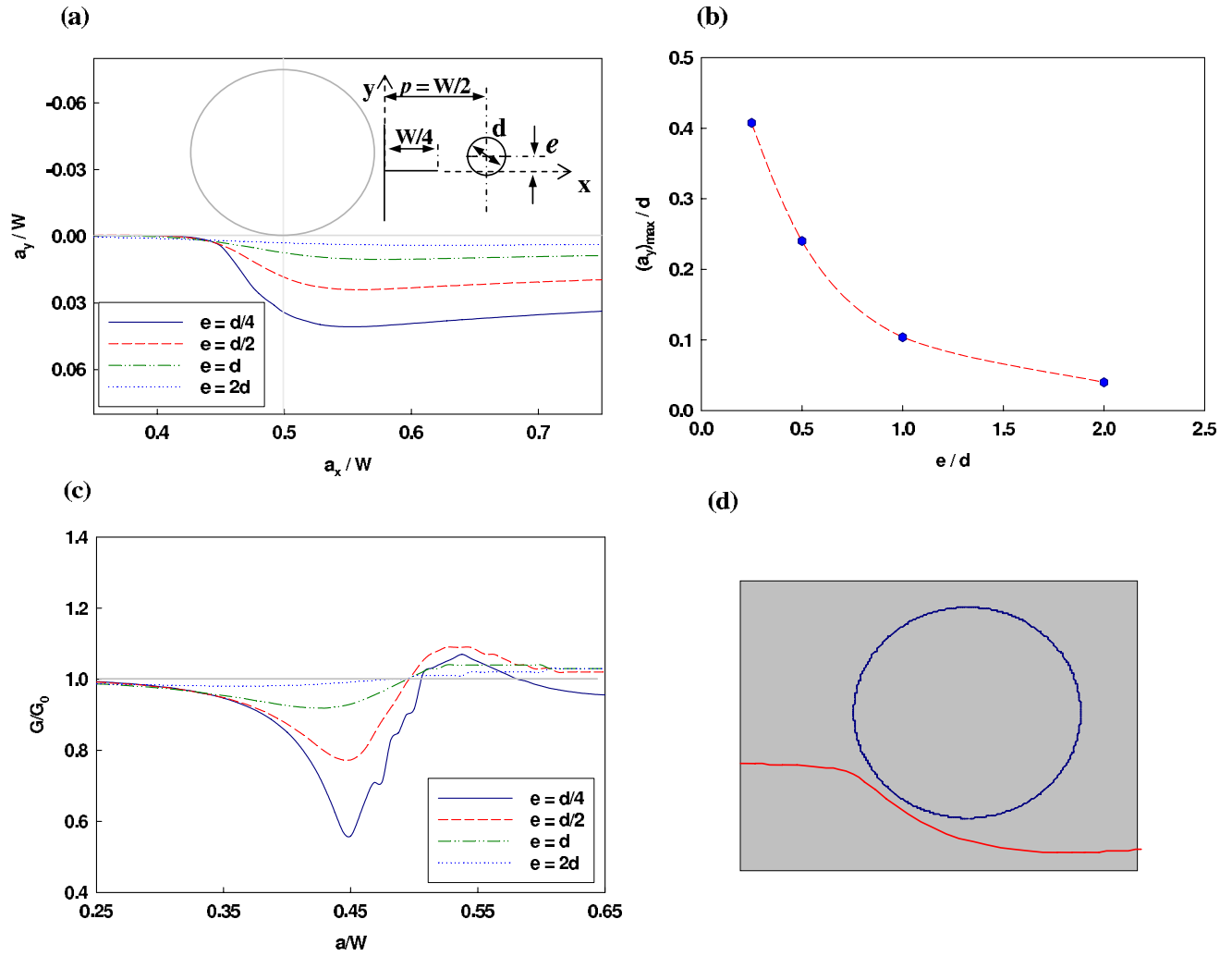


Figure 7.7: The effect of eccentrically situated rigid inclusions relative to the initial crack on crack deflection and energy release rate (ERR), (a) Crack deflection with varying inclusion eccentricity; the inclusion location is shown with respect to initial crack orientation, (b) Variation of maximum crack deflection from the line-of-symmetry with inclusion eccentricity for inclusion diameter $d = W/10$, (c) Variation in nondimensional ERR with a/W , (d) Crack propagation around a rigid inclusion from SGBEM simulation.

the crack begins to propagate towards the line-of-symmetry with a relatively small angle of deflection. These plots suggest that the crack deflection increases as the eccentricity decreases. A symmetrically oriented inclusion ($e = 0$) can be viewed as a limiting case when the crack gets stalled at the inclusion-matrix interface (see Fig. 7.5(b)). The variation of maximum crack deflection with inclusion eccentricity is shown in Fig. 7.7(b). From the plot it appears that the maximum crack deflection increases exponentially with decreasing eccentricity.

The effect of inclusion eccentricity on ERR is presented in Fig. 7.7(c). The figure shows the variation of nondimensional ERR, G/G_0 , with a/W . It can be seen from the plots that ERR decreases as the crack approaches the inclusion. The minimum value of ERR occurs when $a/W \approx 0.45$ or when the crack tip is located $\approx d/2$ behind the the center of the inclusion. With further crack propagation, ERR values increase and approach unity as a/W reaches p/W . An amplification in SIF and hence ERR can be noticed as the crack starts propagating away (recede) from the inclusion. This relatively small increase in ERR continues until the crack propagates a distance of approximately $d/2$ away from the inclusion. With further crack propagation, G/G_0 decreases and asymptotically approaches unity. Similar to the effects of eccentricity on crack deflection, G/G_0 increases as the inclusion eccentricity e decreases. The maximum effect can be seen for zero eccentricity (also shown in Fig.7.5(b)).

It should be emphasized here that the crack growth and ERR calculations are based on propagation occurring in the matrix material at all times. If the crack were to enter the matrix-inclusion interfacial region, crack tip fields corresponding to dissimilar material interfaces will have to be used[109]. Simulations reported here correspond to

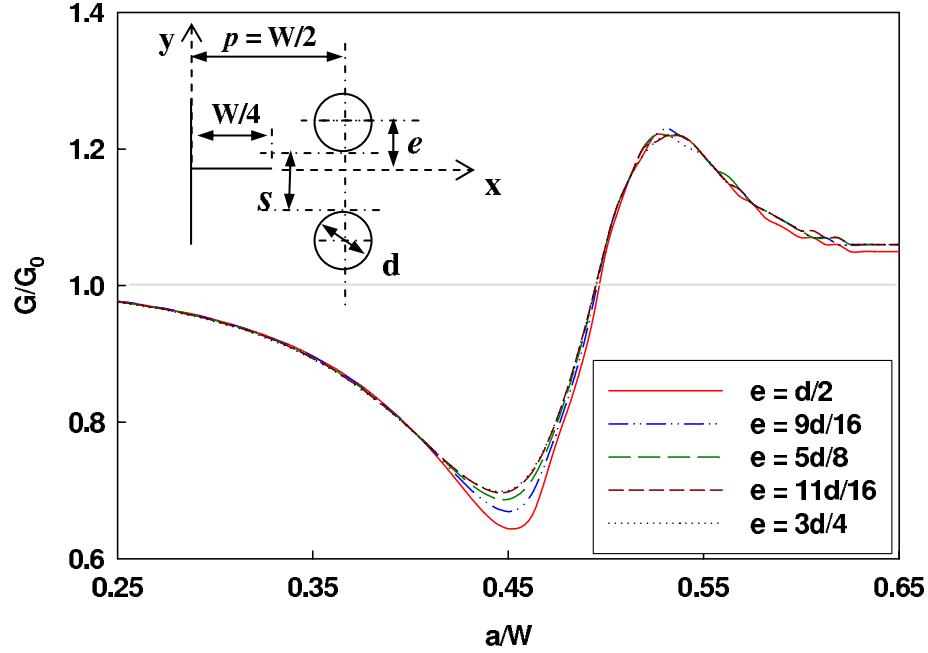


Figure 7.8: Variation of G/G_0 with a/W in the presence of eccentrically located pair of inclusions showing the combined effect of shielding and inclusion eccentricity (Note: Eccentricity of the inclusion-pair is defined for the nearest inclusion center relative to the crack).

the crack growth occurring close to an interface yet in the matrix only as a sub-interfacial crack. An example of the same for the case of $e = d/4$ is shown in Fig. 7.7(d).

For the sake of completeness, the combined effects of shielding and eccentricity are studied next using a pair of inclusions located eccentrically with respect to the line-of-symmetry (See Fig.7.8). The separation distance ‘ s ’ between the inclusions is kept constant ($s = d/2$) while the *eccentricity of the inclusion nearest to the line-of-symmetry* is varied from $d/2$ to $3d/4$. The variation of crack path for various eccentricities are not shown here for brevity which showed similar eccentricity effect as for the case of single inclusion (Fig. 7.7(a)) with an exception of relatively small crack deflections.

The variation of G/G_0 with a/W is plotted in Fig. 7.8. Plots overlap on each other in most part except when the crack propagates between $a/W \approx 0.4$ and 0.5 (i.e., from a distance $\approx 1d$ in front of the particle center) for various eccentricities. Small but monotonic variation in minimum value of G/G_0 can be noticed with increasing inclusion eccentricity. The lowest magnitude of G/G_0 (at $a/W \approx 0.45$) decreases with decrease in eccentricity, the minimum being for the case of symmetrically located pair of particles. Interestingly the eccentricity of a pair of particles is noticed to be playing negligible role on amplification.

7.5.3 Particle size effect

In this part the effect of inclusion size on crack deflection and ERR is investigated. An inclusion is located at a distance $W/4$ away from the initial crack tip with an eccentricity of $d/2$ (see Fig. 7.9(a)). The inclusion diameter is varied from $W/40$ to $W/5$. The crack paths for various sizes of inclusions at $p/W = 0.5$ is shown in Fig.7.9(a). Again, the load is applied symmetrically in a 3-point bend configuration. Evidently, the crack propagates in a mode-I fashion until the inclusion is $\approx 1d$ in front of the crack tip. As the distance between the inclusion and the crack tip decreases, crack deflection increases. The angle of deflection attains a maximum value when the crack tip is at a distance of $\approx d/4$ from the particle center. Interestingly, the crack deflection keeps increasing even after the crack tip grows past the particle centerline. Maximum crack deflection occurs when the crack travels across the inclusion and propagates $d/2$ away from the inclusion center. With further crack propagation a slight reversal of angle of deflection can be seen and the crack travels towards the line-of-symmetry with a relatively small angle.

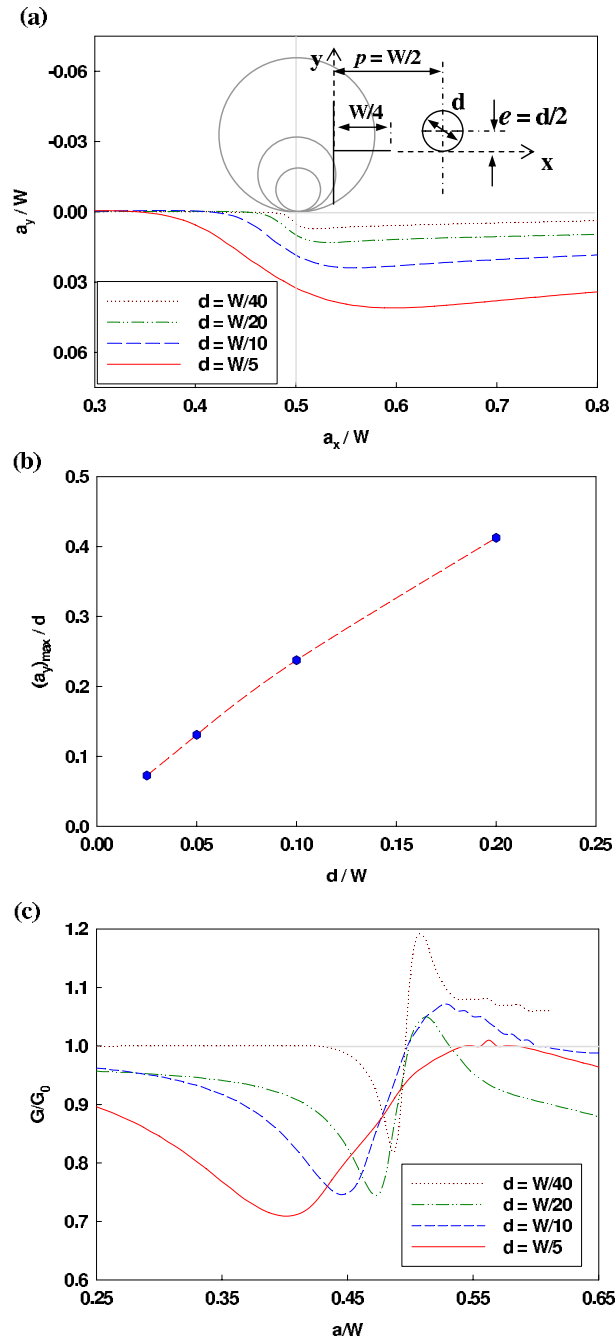


Figure 7.9: Role of particle size on crack deflection and ERR: (a) Crack deflection in the presence of inclusions of various diameters for a fixed eccentricity $e = d/2$, (b) Variation of maximum crack deflection from the line-of-symmetry with inclusion diameter, (c) Variation in nondimensional ERR with a/W .

Also it can be noticed that the presence of a larger inclusion is felt earlier by the crack tip. The amount of crack deflection increases with the increase in inclusion size. Figure 7.9(b) shows the variation of maximum deflection from the line-of-symmetry with inclusion diameter. For an eccentricity of $d/2$, plot suggests that the maximum deflection varies monotonically (with slight non-linearity) with inclusion size.

The inclusion size effect on ERR is shown in Fig. 7.9(c). This plot shows the variation of G/G_0 with a/W for various inclusion sizes. The size effect in terms of decreasing ERR is evident for all inclusion sizes. As one would expect, the effect can be noticed much earlier as the particle size increases. The largest, among the chosen inclusions, shows the lowest nondimensional ERR, while in the case of smallest inclusion the crack propagates with $G/G_0 \approx 1$ until a length of $a/W \approx 0.40$. For all inclusion sizes G/G_0 decreases when the crack propagates towards the inclusion, which attains a minimum when the crack tip is at a distance of $d/2$ from the inclusion centerline. This is similar to the results obtained in the case of crack-tip shielding and inclusion eccentricity effects. With further crack propagation G/G_0 increases and reaches a maximum just before it travels $d/2$ across the center of the inclusion. This is followed by a monotonic but gradual decrease in G/G_0 . Similar to the previous results, for all inclusion sizes greater shielding occurs while the crack is traveling towards the inclusion compared to the amplification effect while receding from the inclusion. Also from the plots it can be noticed that these effects increase with an increase in inclusion size.

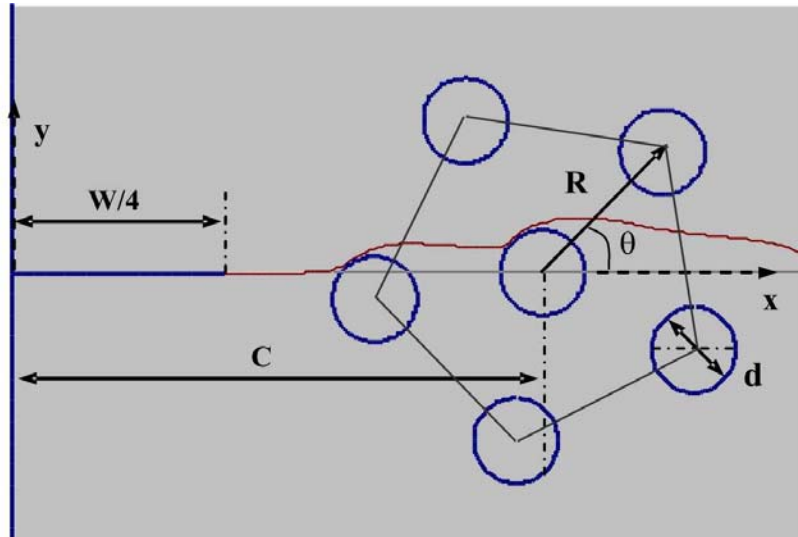


Figure 7.10: Interaction between a crack and a particle cluster with a pentagonal arrangement. Cluster orientation is defined in terms of θ . Crack path in the presence of particle cluster is shown.

7.5.4 Crack propagation through particle clusters

Next, simulations of crack growth through idealized clusters of particles in a brittle and compliant matrix is undertaken. In a typical particulate composite secondary phase is randomly distributed in a matrix at a known volume fraction. In the present work, this situation is approximated using a particle-cluster. Particle distribution, particle size, inter particle distance (cluster radius), and cluster orientation relative to the initial crack orientation, are some of the parameters which can be used to characterize a cluster. In this study, a six-particle-cluster (see, Fig. 7.10 with a centrally located particle surrounded by five others at the corners of a uniform pentagon) is used. Unlike square, hexagonal or octagonal arrangements of particles, this pattern captures randomness of fillers in a matrix to a greater degree while being characterized by a few simple parameters. In the current study, a single cluster is positioned ahead of a crack tip in

the loading geometry used earlier. The cluster geometry for a chosen particle diameter d is defined in terms of (i) distance between particles on the periphery and the center one (cluster radius R) and (ii) the smallest angle (θ) of the surrounding particles from the line-of-symmetry, as shown in the figure. Clearly, the crack particle cluster interaction and its effects on crack path and ERR depend on the cluster orientation θ and a measure of volume fraction, which are investigated next.

Effect of cluster orientation

As the propagating crack negotiates various members of a particle-cluster, the crack path become tortuous causing greater energy dissipation and higher overall fracture toughness compared to a neat matrix. In this context, it is interesting to address the effect of particle arrangement such as cluster orientation relative to the initial crack impingement. Accordingly, the role of angular parameter θ (see, Fig. 7.10) on crack growth behavior through a particle cluster is studied next. In these simulations, the center of the cluster is considered to be located at a distance of $C/W \approx 0.4$ where C is the distance of the center of the inclusion from the initial crack tip. The cluster radius is considered as $2d$, d being the inclusion diameter. The angle θ is varied from 21° to 33° for the pentagonal arrangement used here. Figure 7.11(a) shows the crack propagation for various cluster orientation angles. Evidently, significant crack path deflections within the cluster can be noticed from the figure. The crack deflection from the first particle influences the subsequent growth towards the second and so on. The crack, already deflected away from the line-of-symmetry of the cluster at the first interaction, undergoes further deflection due to the central particle of the cluster. As the crack propagates

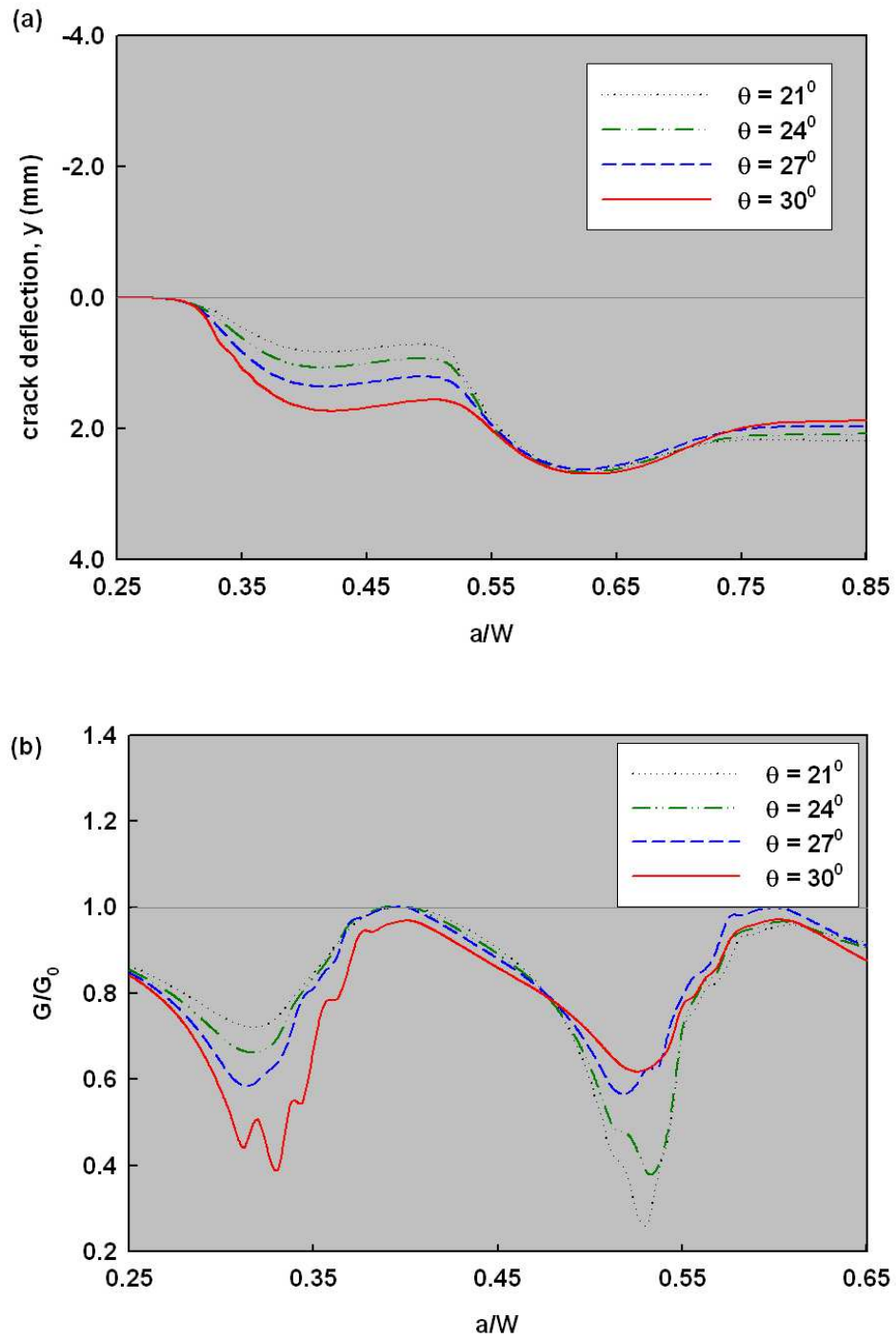


Figure 7.11: Crack growth through a particle cluster is, (a) Crack deflection in the presence of particle cluster of various orientations, (b) Variation of ERR with a/W showing the effect of cluster orientation. 167

further and away from the central particle, the effect of next neighboring particles can be noticed. The differences in crack paths are greatest when the crack interacts with the first particle of the cluster. That is, crack deflection increases monotonically with increasing angular parameter θ . The opposite trend is evident when the crack reaches the central particle - the crack deflection at the central particle of the cluster decreases with θ . Once the crack recedes from the central particle, all crack paths essentially coincide as the crack leaves the cluster. These observations suggest that, the net effect of the angular parameter θ on cumulative crack deflection is small even though crack paths within the cluster are significantly different.

The above observations can be further quantified in terms of ERR for each crack path corresponding to different values of θ . The effect of the change in θ on ERR is shown in Fig. 7.11(b). Nondimensional ERR is plotted against a/W for various cluster orientations. Plots show significant variation in G/G_0 as the crack propagates and interacts with surrounding particles. Interestingly, ERR values for all cluster orientations are lower when compared to the case of unfilled (neat) matrix material. This suggests lowering of crack tip stress intensification as various elements of the cluster are encountered by the crack resulting in an overall increase in fracture toughness of the material. The cluster orientation affects crack propagation and hence G/G_0 differently. As can be seen from the plots that for 30° orientation, the first particle interaction gives lowest G/G_0 , while for the case of 21° orientation the center particle in the cluster affects G/G_0 the most. For other orientations, the values of G/G_0 are bounded by the values for these two cases. In order to estimate which cluster orientation dissipates the most energy, average value of nondimensional ERR (ERR_a) for each case is determined. Here, ERR_a

is defined as,

$$ERR_a = \frac{1}{(a/W)} \int \frac{G}{G_0} d \left(\frac{a}{W} \right). \quad (7.1)$$

The ERR_a for the crack propagation between $a/W = 0.25$ and 0.70 has been evaluated. For the chosen cluster orientations 21° , 24° , 27° and 30° , the ERR_a values are 0.83 , 0.83 , 0.84 and 0.80 , respectively. Thus, it can be again be concluded that the effect of cluster orientation has negligible effect on energy dissipation.

Effect of cluster volume fraction

The effect of particle volume fraction on crack growth is considered next. This can be done by changing either the cluster radius (R) and keeping the particle size (d) constant or by changing the particle size and keeping the cluster radius constant. To avoid particle size effects, an investigation is performed for various cluster radii with a fixed particle size³. It has already been shown in the previous section that cluster orientation has only a small effect on ERR. Therefore the cluster orientation is chosen such that the central particle of the cluster is located symmetrically at $C/W \approx 0.4$ relative to the initial crack tip and the particle nearest to the initial crack tip has $d/3$ eccentricity (e) as shown in Fig. 7.10. Defining a control volume to find volume fraction is not straight forward for the chosen pentagonal cluster arrangement because it can not be replicated symmetrically in all directions. Therefore instead of volume fraction, a parameter ‘area ratio’ is defined for quantification purpose. The area ratio, AR , is

³ $\frac{C}{W} = \frac{3}{40}$ in this case. A different particle diameter is chosen compared to the previous computations so that simulations can still be performed for lower volume fractions without the cluster geometry interfering with the initial crack tip.

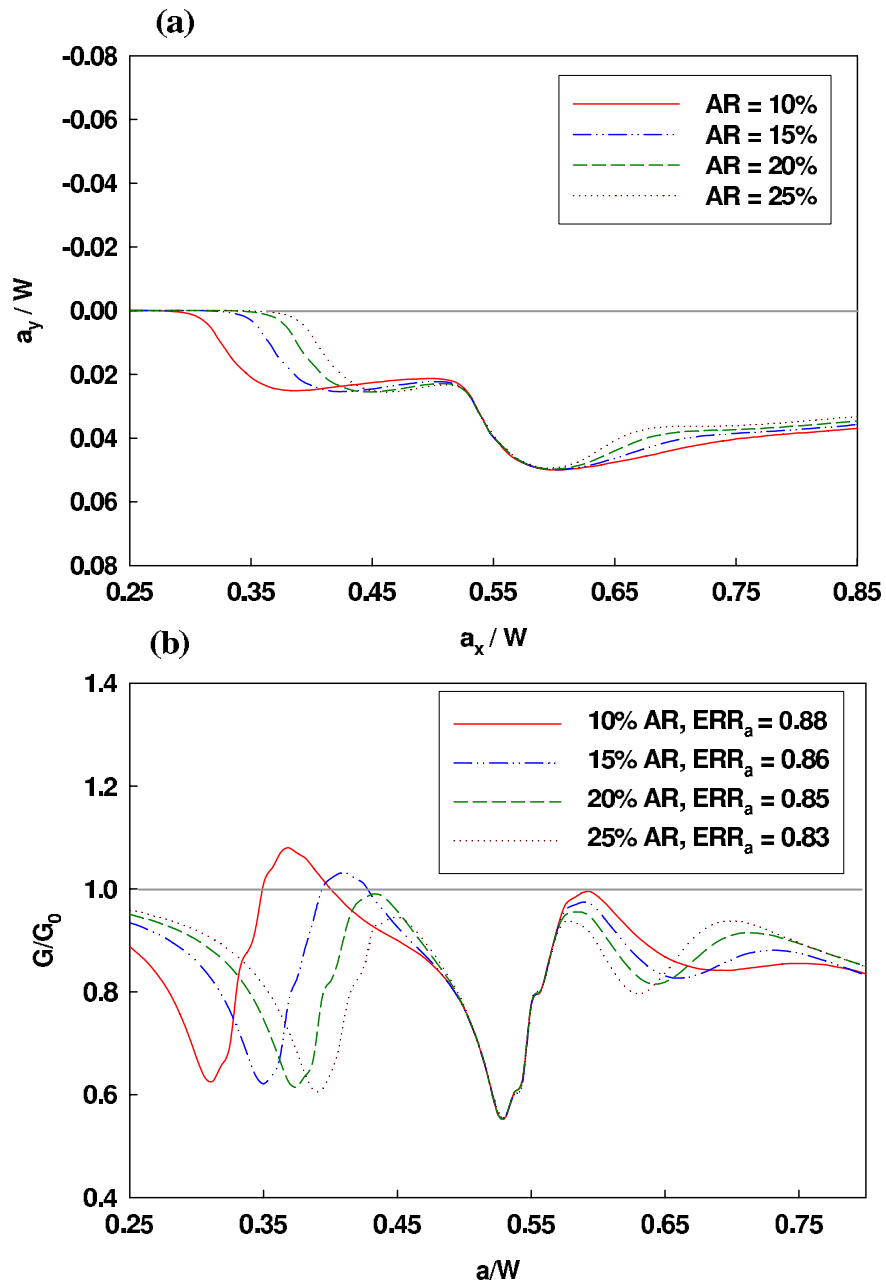


Figure 7.12: Interaction of a crack with a particle cluster to study the effect of volume fraction, (a) Crack deflection for various volume ratios; volume ratio is changed by expanding the cluster radius R shown in Fig. 7.10, (b) Variation of energy release rate with crack growth.

defined as the ratio of the total area occupied by the particles inside the pentagon to the total area of the pentagon itself.

Figure 7.12(a) shows crack deflections in the presence of particle cluster for 10% to 25% area ratios. Similar but distinct crack paths can be seen for various values of AR . As with the cluster orientation study, crack paths show dependency on the value of AR . Earlier crack deflection can be noticed for the case of 10% AR due the presence of a particle much closer to the initial crack tip when compared to other AR values. With an increase in AR , the crack deflections occur at different a/W values sequentially. The first interaction is the only dominant distinguishing feature among the different crack paths. The paths tend to merge while propagating around the central inclusion. That is, the crack trajectory is essentially same between $a/W \approx 0.54$ and 0.60 in the figure. With further crack propagation the paths show variation with AR . The distinct crack paths beyond $a/W \approx 0.60$ are due to the difference in surrounding inclusion locations. Interestingly, when compared to the crack deflection in the presence of a single particle (Fig. 7.7(a) and 7.9(a)), prominent and higher crack deflection can be noticed for the cluster for all values of AR .

Figure 7.12(b) shows the variation of nondimensional ERR with a/W for various area ratios. A combined effect of crack tip shielding and amplification, particle size effect and particle eccentricity with respect to propagating crack can be seen in terms of distinct G/G_0 variation for different AR s. For lower AR values the decrease in ERR can be noticed earlier due to the proximity of initial crack tip to the nearest particle. But this also gives rise to an early amplification as the crack propagates away from the particle. The amplification effect is more prominent for lower AR values due to its larger

inter-particle separation distance. In case of higher AR s, however, the amplification effect is relatively suppressed due to the proximity of next neighboring particle. When a crack negotiates the first peripheral particle of the cluster, the lowest G/G_0 occurs at different a/W values depending upon the particle location with respect to the initial crack tip. Even though the plots show distinct variations of G/G_0 for various AR s when a crack propagates around its first encounter, they all tend to follow the same path as the central particle is approached. For all values of AR , nearly the same G/G_0 variation between $a/W = 0.5$ to 0.58 is evident. Further crack propagation shows the effect of next neighboring particle effect on G/G_0 , where again lowest G/G_0 occurs at different a/W depending upon the particle location. This is followed by some increase in G/G_0 similar to the amplification effect, and then a monotonic but gradual decrease in G/G_0 .

Here again the area ratio effect is quantified using average ERR, ERR_a , defined earlier in eq. (7.1). A crack propagates different distances within the particle cluster due to different cluster radius for each AR . Hence, the same crack propagation length can not be used to evaluate ERR_a . Subsequently, a crack propagation length of $2R$ within the particle cluster is considered for comparison. For 10%, 15%, 20% and 25% AR values, the ERR_a values have been calculated as 0.88, 0.86, 0.85 and 0.83 respectively. A monotonic decrease in ERR_a with increase in AR can be noticed. This in turn suggests that the material becomes relatively more resistant to crack propagation with increase in volume fraction of secondary phase rigid fillers.

CHAPTER 8

CONCLUSIONS

The role of microstructure on fracture behavior of particle reinforced polymer composites is investigated experimentally and numerically. The study focuses on the effects of filler particle size, filler-matrix adhesion strength and particle size bimodality on effective fracture toughness under impact loading conditions. Optical interferometry and high-speed photography are used for characterizing fracture behaviors at continuum scales. Based on qualitative observation of fractured surfaces, the key toughening mechanisms responsible for different fracture behaviors due to microstructural variations are identified. The effects of toughening mechanisms are quantified by performing micro-measurements on fractured surfaces. Subsequently, surface features are linked to optically measured fracture toughness. To provide additional insight into the observed toughening mechanisms, a limited study of crack-inclusion interaction under dynamic loading conditions is also carried out. Numerical investigations using boundary element method are used to supplement experimental studies.

To study particle size and filler-matrix adhesion strength effects on fracture behavior, crack-tip field measurements are performed in glass-filled epoxy composites under dynamic loading conditions. Uncoated (weakly bonded) and silane coated (strongly bonded) fillers from $7\ \mu\text{m}$ to $203\ \mu\text{m}$ in mean dia. are used to prepare macroscopically homogeneous test specimens at 10% filler volume fraction (V_f) in epoxy matrix. To investigate particle size bimodality effects on fracture behavior, two different particle sizes, each of 5% V_f are used in epoxy binder to prepare fracture specimens. Uniaxial tension

tests and ultrasonic pulse-echo measurements show that neither particle size nor filler-matrix adhesion strength influence elastic properties in a discernible fashion. Reflection CGS and high-speed photography are used to measure crack-tip fields near dynamically growing cracks. Fracture parameters are evaluated using three-term asymptotic field description of interferograms. Both weakly and strongly bonded filler particles in the matrix show higher steady-state fracture toughness ($K_{I_{ss}}$) compared to neat epoxy. The experimental results show significant particle size effect on fracture toughness (both initiation K_{I_i} and steady-state $K_{I_{ss}}$ values) in weakly bonded particles. There is a distinct optimum particle size ($35 \mu\text{m}$ at $10\% V_f$) at which fracture toughness is maximum. Fracture toughness decreases as particle size increases or decreases relative to this particular size and shows saturation at relatively large particle size. On the other hand, particle size shows little or no effect on fracture toughness parameters (K_{I_i} and $K_{I_{ss}}$) in strongly bonded filler particles, which suggests that increasing filler-matrix adhesion strength affects dynamic fracture toughness negatively under high-strain rate loading conditions. Also, the increase in fracture toughness ($K_{I_{ss}}$) of weakly bonded particles with respect to the strongly bonded ones is maximum for the optimum particle size and tends to vanish as particle size is either increased or decreased. In case of mixed particles ($35 \mu\text{m} + 203 \mu\text{m}$ weakly bonded and at a total $10\% V_f$ fracture toughness ($K_{I_{ss}}$) value is bounded by the respective values of particulate composites containing a single particle size of the same V_f and seems to vary linearly with constituent particle volume fraction.

Microstructure also affects crack growth behavior in particulate composites. Maximum crack velocity (v_{max}) increases as particle size decreases for weakly bonded particles

whereas steady-state velocity (v_{ss}) shows an inverse relationship with $K_{I_{ss}}$. The minimum v_{ss} corresponds to the optimum particle size of $35\ \mu m$ yielding maximum $K_{I_{ss}}$ at $10\% V_f$. In case of strongly bonded filler particles, v_{max} and v_{ss} increase as particle size decreases and are consistently higher when compared to the respective values for weakly bonded fillers. Similar to the $K_{I_{ss}}$ variation, the steady-state crack velocity for mixed particles ($35\ \mu m + 203\ \mu m$ weakly bonded) at $10\% V_f$ vary linearly with constituent particle volume fraction (but with opposite slopes relative to $K_{I_{ss}}$ variation) and is bounded by the respective values of the composites containing a single particle size.

Next, fractured surfaces of glass-filled epoxy specimens are analyzed qualitatively using scanning electron microscopy. The mechanisms affecting fracture and roughness parameters in the presence of various particle sizes and different filler-matrix adhesion strengths are studied. Micrographs show that a moving crack front deflects around stiff silane treated fillers due to strong filler-matrix interfacial strength while it readily intercepts untreated fillers due to relatively weak filler-matrix interface strength. Crack tilting and twisting are identified as dominant mechanisms in strongly bonded particles whereas crack front twisting and crack front blunting effects dominate weakly bonded counterparts. The tail lines, indicative of crack twisting during fracture, are more prominent in weakly bonded particles, resulting in higher roughness parameters when compared to strongly bonded ones. Weaker filler-matrix interfaces not only retards crack growth and lower steady-state crack velocity but also acts as distributed attractors of a the propagating crack giving rise to higher surface roughness.

The quantitative analysis of fracture surfaces are performed using a surface profilometer. Average surface roughness (Ra) is found to be consistently higher for weakly

bonded particles as compared to strongly bonded ones. That is, Ra increases as particles size increases. This, however, does not correlate with macroscopically measured steady-state fracture toughness for various particle sizes. Therefore, to isolate the particle size effect from surface roughness, Ra is modeled as a sum of particle related roughness, Ra_p , and fracture induced roughness, Ra_f , where Ra_p is a function of particle size and volume fraction and Ra_f reflecting the effects of the intrinsic fracture mechanisms involved. A method for calculating Ra_p and hence Ra_f is proposed. Based on this, a simple model is proposed for correlating fracture toughness, fracture induced roughness and particle size. The quantity Ra_f/\sqrt{D} , D being the average particle size, has been found to vary linearly with steady-state dynamic fracture toughness, $K_{I_{ss}}$.

To understand fundamental toughening mechanisms involved investigations on crack-particle interactions are initiated using CGS and high-speed photography. Test specimens using two types of inclusions, strongly and weakly bonded to the matrix located at two different eccentricities, symmetrically ($e = 0$) and tangentially ($e = d/2$) with respect to initial crack plane are studied. Measurable inclusion eccentricity and inclusion-matrix adhesion strength effects are seen on fracture parameters. For the cases of $e = 0$ and $d/2$, similar pre-initiation behaviors are noticed with nearly same crack-tip loading rate. For a crack propagating towards a weakly bonded inclusion, effective stress intensity factor ($K_e = \sqrt{K_I^2 + K_{II}^2}$) in post crack initiation region is seen to be slightly higher for the case of $e = d/2$ when compared to $e = 0$ case. On the other hand, the case of strongly bonded inclusion shows monotonically increasing K_e with dK_e/dt being higher for $e = d/2$.

To provide additional insight into crack-inclusion interaction a numerical tool namely symmetric Galerkin boundary element method, is used to simulate crack growth. The simulations are limited to quasi-static growth as a first step. Crack paths and SIFs under plane stress conditions are computed. The crack-growth prediction tool is first benchmarked and simulations are performed for the cases when inclusions are weakly and strongly bonded to the matrix. The parametric study shows that mode-mixity increases with increase in inclusion-matrix delamination (weakening) which in turn requires greater energy expenditure during crack propagation. This is consistent with the experimental results where composites with weakly bonded filler particles showed higher fracture toughness when compared to the strongly bonded ones.

Another set of parametric study using boundary element method is performed to investigate how a crack would interact with an isolated particle and a cluster of particles in a matrix. The study is limited to the case of static loading and strongly bonded inclusions of relatively large size. In case of isolated inclusions, the role of particle size and eccentricity are examined and in case of particle-clusters, cluster orientation and cluster size effects are studied. The numerical results show that as crack approaches a stiff, isolated inclusion, the energy release rate (ERR) is affected when the crack is a few inclusion diameters (d) away from it, whereas crack deflection is detectable only when the crack is $\leq 3d/2$ from the center of the inclusion. For both symmetric and eccentric (with respect to the initial crack orientation) inclusions, the energy release rate is minimum when the crack tip is at a distance of $\approx d/2$ from the center of the inclusion. As eccentricity increases, the crack deflection decreases but the energy release rate

increases. Crack tip shielding and amplification increase with decrease in inter particle separation distance in a particle-pair arranged symmetrically relative to the crack. For an eccentrically arranged particle-pair, on the other hand, the crack tip shielding is greater when compared to the symmetric case. However, eccentricity has negligible effect on amplification. In general, shielding effects are greater than amplification effects when a crack propagates around a particle. Crack deflection increases and the energy release rate decreases with increase in particle size. A propagating crack is influenced by a larger particle in front much earlier than the smaller ones. A crack propagating through a particle cluster shows distinct crack trajectories for different cluster orientations. The cluster orientation, however, has negligible effect on overall energy dissipation. The crack path depends upon the cluster area ratio, AR . The total energy dissipation decreases with increase in cluster AR . This suggests that the material becomes more resistant to the crack propagation for higher area ratios.

Future Directions

To study the effects of microstructural variation on fracture behavior of particulate composites spherical glass particles at a constant volume fraction are considered. Additional investigations of volume fraction and particle shape effects on failure behavior could provide clarification on unresolved issues in current dissertation (e.g. why fracture toughness varies nonmonotonically with particle size) and add to the overall understanding of fracture mechanisms involved.

In current dissertation micro- size filler particles are used to prepare test specimens because they are readily available in various sizes and in both coated and uncoated forms.

Fracture behavior of nano composites can be significantly different when compared to micro-fillers due to very high surface to volume ratios. Therefore, a relatively large particle-matrix interface area can play considerably different role in toughening mechanisms. The effect of nano particles on fracture behavior is yet to be well understood, and could be investigated in future.

The experimental investigation of crack-inclusion interaction is performed using high speed photography with temporal resolution of $5 \mu\text{sec}/\text{frame}$. From the interferograms it is noticed that this framing rate is insufficient to resolve all details of crack-inclusion interaction due to very high crack velocity and significant transient events. The framing rate, which is one of the constraints in the current set-up can be increased in next phase.

The current boundary element code is limited to crack propagation through a single material, even though the heterogeneous material can be modeled. This restricts a crack growth through bimaterial interfaces, a key requirement to model weak inclusion-matrix interface. This constraint can be removed by modifying the code for interfacial crack propagation.

Currently used BEM code simulates fracture behavior in a heterogeneous media under quasi-static loading conditions. If interfacial loading is accounted for in the BE-code, dynamic crack growth events can be studied. The inclusion of inertial effects will also assist in simulating currently performed experiments to a greater accuracy.

A brittle polymer matrix is used to prepare particulate composites in the current study. The use of linear elastic fracture mechanics is quite appropriate while investigating failure behavior at high strain rate loading conditions due to linear stress-strain relationship. The situation will be different in the presence of inelastic matrix, filler or

both. Modeling fracture behavior in a nonlinear material system can be considered in the future investigations.

BIBLIOGRAPHY

- [1] Frear D. R., Materials issues in Area-Array Microelectronic packaging, *J. Metals* 1999, **51(3)**, 22-27.
- [2] Yazici R., Karuv B., Garrow J., Kalyon D. M., Particulate based conductive composites exploiting percolation-range microstructure, *Soc. Plastics Engineers Annual Technical Conference, Technical papers*, 1999, **45**, 1551-1555.
- [3] Norman S. A., Michele E., Amaya A., Gonzalo S., Christopher M. L., Verran J., Stratton J., McIntyre R. B., Degradation and stabilisation of polymers and coatings: nano versus pigmentary titania particles, *Polymer Degradation and Stability*, 2004, **85**, 927-946.
- [4] Seamark M. J., Use of syntactic foams for subsea buoyancy, *Cellular Polymers*, 1991, **10(4)**, 308-321.
- [5] Thomas C. R., Invited Review: Syntactic carbon foam, *Mater. Sci. Eng.* 1973, **12(5-6)**, 219-233.
- [6] Hiel C., Dittman D., Ishai O., Composite sandwich construction with syntactic foam core: a practical assessment of post-impact damage and residual strength, *Composites* 1993, **24(5)**, 447-450.
- [7] Gdoutos E. E., Pilakoutas K., Rodopoulos C. A., Failure analysis of industrial composite materials, *McGraw-Hill*, 2000, 533-540.
- [8] Kessler M. R., Sottos N. R., White S. R., Self-healing structural composite materials, *Composites-Part A* 2003, **34**, 743-753.
- [9] Brown E. N., Sottos N. R., White S. R., Fracture testing of a self-healing polymer composite, *Exp. Mech.* 2002, **42(4)**, 372-379.
- [10] Butcher R. J., Rousseau C. E., Tippur H. V., A functionally graded particulate composite: Preparation, measurements and failure analysis, *Acta Mater.* 1999, **47(1)**, 259-268.
- [11] Marur P. R., Tippur H. V., Dynamic response of bimaterial and graded interface cracks under impact loading, *Int. J. Fract.* 2000, **103**, 95-109.
- [12] Kirugulige M. S., Kitey R., Tippur H. V., Dynamic fracture behavior of model sandwich structures with functionally graded core: a feasibility study, *Composites Sci. Tech.* 2005, **34**, 1052-1068.

- [13] Spanoudakis J. and Young R. J., Crack propagation in a glass particle-filled epoxy resin, Part 1 Effect of particle volume fraction and size, *J. Mater. Sci.* 1984, **19**, 473-486.
- [14] Spanoudakis J. and Young R. J., Crack propagation in a glass particle-filled epoxy resin, Part 2 Effect of particle-matrix adhesion, *J. Mater. Sci.* 1984, **19**, 487-496.
- [15] Moloney A. C., Kausch H. H., Kaiser T. and Beer H. R., Review - Parameters determining the strength and toughness of particulate filled epoxide resins, *J. Mater. Sci.* 1987, **22**, 381-393.
- [16] Nakamura Y., Okabe S. and Iida T., Effects of particle shape, size and interfacial adhesion on the fracture strength of silica-filled epoxy resin, *Polym. Polym. Compos.* 1999, **7(3)**, 177-186 .
- [17] Nakamura Y. and Yamaguchi M., Effects of particle size on the fracture toughness of epoxy resin filled with spherical silica *Polymer* 1992, **33(16)**, 3415-3426.
- [18] Hutchinson J. W., Mear M. E., Rice J. R., Crack paralleling an interface between dissimilar materials, *Trans. ASME* 1987, **54**, 828-831.
- [19] Williams M. L., The stresses around a fault or crack in dissimilar media, *Bul. Seismol. Soc. Amer.* 1959, **49(2)**, 199-203.
- [20] Erdogan F., Fracture mechanics of functionally graded materials, *Composites Eng.* 1995, **5(7)**, 753-770.
- [21] Khor K. A., Dong Z., L., Gu Y., W., Plasma sprayed functionally graded thermal barrier coatings, *Mater. Letters* 1999, **38**, 437-444.
- [22] Jung Y. G., Paik U., Choi C., Influence of the particle size and phase type of zirconia on the fabrication and residual stress of zirconia/stainless-steel 304 functionally graded material, *J. Mater. Sci.* 1999, **34**, 5407-5416.
- [23] Fukui Y., Takashima K., Ponton C. B., Measurement of Young's modulus and internal friction of an in situ Al-Al₃Ni functionally gradient material, *J. Mater. Sci.* 1994, **29**, 2281-2288.
- [24] Tandon S. and Faber K. T., Effects of loading rate on the fracture of cementitious materials, *Cem. Concr. Res.* 1999, **29**, 397-406.
- [25] Issa A. Mo., Issa A. Ma., Islam M. S. and Chudnovsky A., Fractal dimension-a measure of fracture roughness and toughness of concrete, *Eng. Fract. Mech.* 2003, **70**, 125-137.
- [26] Abell A. B. and Lange D. A., Fracture mechanics modeling using images of fracture surfaces, *Int. J. Solids Struct.* 1998, **35**, 4025-4033.

- [27] Cotterell B., Fracture propagation in organic glass, *Int. J. Fract. Mech.* 1968, **4**, 209-217.
- [28] Ravi-chandar K. and Knauss W. G., Experimental investigation into dynamic fracture: II. Microstructural aspects, *Int. J. Fract.* 1984, **26(1)**, 65-80.
- [29] Arakawa K. and Takahashi K., Relationships between fracture parameters and fracture surface roughness of brittle polymers, *Int. J. Fract.* 1991, **48**, 103-114.
- [30] Takahashi K., Kido M. and Arakawa K., Fracture roughness evolution during mode I dynamic crack propagation in brittle materials, *Int. J. Fract.* 1998, **90**, 119-131.
- [31] Sharon E., Gross S. P. and Fineberg J., Energy dissipation in dynamic fracture, *Phys. Rev. Lett.* 1996, **76(12)**, 2117-2120.
- [32] Faber K. T. and Evans A. G., Crack deflection process-I Theory, *Acta Metall.* 1983, **31(4)**, 565-576.
- [33] Faber K. T. and Evans A. G., Crack deflection process-II Experiment, *Acta Metall.* 1983, **31(4)**, 577-584.
- [34] Davidson D. L., Fracture surface roughness as a gauge of fracture toughness: aluminium- particulate SiC composites *J. Mater. Sci.* 1989, **24**, 681-687.
- [35] Lange F. F., The interaction of a crack front with a second-phase dispersion, *Phil. Mag.* 1970, **22**, 983-992.
- [36] Evans A. G., The strength of brittle materials containing second phase dispersions, *Phil. Mag.* 1972, **26**, 1327-1344.
- [37] ATKINSON, C., 1972, "The interaction between a crack and an inclusion", International Journal of Engineering Science, **10**, pp. 127-136.
- [38] ERDOGAN, C., GUPTA, G. D., RATWANI, M., 1974, "Interaction between a circular inclusion and an arbitrary oriented crack", Journal of Applied Mechanics (Transaction of the ASME), **Dec**, pp. 1007-1013.
- [39] FABER, K.T., AND EVANS, A.G., 1983, "Crack deflection process - I Theory," Acta Materiala, **31**, pp. 565-576.
- [40] LI, R., AND CHUDNOVSKY, A., 1993, "Variation of the energy release rate as a crack approaches and passes through an elastic inclusion," International Journal of Fracture, **59**, pp. R69-R74.
- [41] BUSH, M.B., 1997, "The interaction between a crack and a particle cluster," International Journal of Fracture, **88**, pp. 215-232.

- [42] KNIGHT, M.G., WROBEL, L.C., HENSHALL, J.L., AND DE LACERDA, L.A., 2002, "A study of the interaction between a propagating crack and an uncoated/coated elastic inclusion using the BE technique," *International Journal of Fracture*, **114**, pp. 47–61.
- [43] TAMATE, O., 1968, "The effect of a circular inclusion on the stresses around a line crack in a sheet under tension," *International Journal of Fracture*, **4**, pp. 257–265.
- [44] SENDECKYJ, G.P., 1974, "Interaction of cracks with rigid inclusions in longitudinal shear deformation," *International Journal of Fracture*, **10**, pp. 45–52.
- [45] HWU, C., LIANG, Y.K., AND YEN W.J., 1995, "Interactions between inclusions and various types of cracks," *International Journal of Fracture*, **73**, pp. 301–323.
- [46] LI, R., AND CHUDNOVSKY, A., 1993, "Energy analysis of crack interaction with an elastic inclusion," *International Journal of Fracture*, **63**, pp. 247–261.
- [47] LIPETZKY, P., AND SCHMAUDER, S., 1994, "Crack-particle interaction in two-phase composites part I: Particle shape effects," *International Journal of Fracture*, **65**, pp. 345–358.
- [48] LIPETZKY, P., AND KNESL, Z., 1995, "Crack-particle interaction in two-phase composites part II: Crack deflection," *International Journal of Fracture*, **73**, pp. 81–92.
- [49] HADDI, A., AND WEICHERT, D., 1998, "Three-dimensional interaction between a crack front and particles," *International Journal for Numerical Methods in Engineering*, **42**, pp. 1463–1476.
- [50] WANG, C., LIBARDI, W., AND BALDO, J.B., 1998, "Analysis of crack extension paths and toughening in a two phase brittle particulate composite by the boundary element method," *International Journal of Fracture*, **94**, pp. 177–188.
- [51] LEI, J., WANG, Y.-S., AND GROSS, D., 2005, "Analysis of dynamic interaction between an inclusion and a nearby moving crack by BEM," *Engineering Analysis with Boundary Elements*, **29**, pp. 802–813.
- [52] Kitey R., Tippur H. V., Role of particle size and filler-matrix adhesion on dynamic fracture of glass-filled epoxy. I. Macromechanisms, *Acta Mater.* 2005, **53**, 1153–1165.
- [53] Frocht M. M., Photoelasticity, John Wiley and Sons, Inc., New York, **1**, 1941, **2**, 1948.
- [54] Durelli A. J., Riley W. F., Introduction to photomechanics, Prentice-Hall, Englewood Cliffs, N.J., 1965.

- [55] Kuske A., Robertson G., Photoelastic stress analysis, John Wiley and Sons, Inc., New York, 1974.
- [56] Tolansky S., Introduction to Interferometry, Halsted Press, second edition, New York, 1973.
- [57] Theocaris, P. S., Elastic plastic strain and stress distribution in notched plate under plane stress, *J. Mech. Phys. Solids* 1998, **11(6)**, 411-416.
- [58] Theocaris, P. S., Koutsabe S., Slope measurement by means of Moire fringes, *J. Scientific Instruments* 1965, **42(8)**, 607.
- [59] Tippur H. V., Interpretation of fringes obtained with coherent gradient sensing, *App. Opt.* 1994, **33(19)**, 4167-4170.
- [60] Coherent gradient sensing: A Fourier optics analysis and application to fracture, Tippur H. V., *App. Opt.* 1992, **31(22)**, 4428-4439.
- [61] Dally, J. W., Riley W. F., Experimental Stress Analysis, McGraw Hill (1991).
- [62] Smith H. M., Principals of Holography, Second Edition, John Wiley and Sons, Inc., New York, 1975.
- [63] John R., Wykes C., Holographic and Speckle Interferometry, Second Edition, Cambridge University Press, New York, 1989.
- [64] Ransom W. F., Sutton M. A., Peters W. H., Handbook on Experimental Mechanics (Holographic and Laser Speckle Interferometry), Prentics-Hall, Englewood Cliffs, N.J., 1993.
- [65] Tippur H. V., Krishnaswamy S. and Rosakis A. J., Optical mapping of crack tip deformations using the methods of transmission and reflection coherent gradient sensing: a study of crack tip K -dominance, *Int. J. Fract.* 1991, **52**, 91-117.
- [66] Krishnaswamy S., Tippur H. V. and Rosakis A. J., Measurement of transient crack-tip deformation fields using the method of coherent gradient sensing, K -dominance, *J. Mech. Phys. Solids* 1992, **40(2)**, 339-372.
- [67] Tippur H. V., Simultaneous and real-time measurement of slope and curvature fringes in thin structures using shearing interferometry, *Opt. Eng.* 2004, **43(12)**, 1-7.
- [68] Needleman A., A continuum model for void nucleation by inclusion debonding, *J. App. Mech.* 1987, **54**, 525-531.
- [69] Xu X. -P., Needleman A., Numerical simulations of fast crack growth in brittle solids, *J. Mech. Phys. Solids* 1994, **42(9)**, 1397-1434.

- [70] Rashid M. M., The arbitrary local mesh refinement method: an alternative to remeshing for crack propagation analysis, *Computer Methods App. Mech. Eng.* 1998, **154**, 133-150.
- [71] Swenson D., Ingraffea A., Modeling mixed-mode dynamic crack propagation using finite elements: theory and applications, *Comp. Mech.* 1988, **3**, 381-397.
- [72] Belytscho T., Black T., Elastic crack growth in finite elements with minimal remeshing, *Int. J. Num. Methods Eng.* 1999, **45(5)**, 601-620.
- [73] Moes N., Dolbow J., Belytscho T., A finite element method for crack growth without remeshing, *Int. J. Num. Methods Eng.* 1999, **46**, 131-150.
- [74] Belytscho T., Lu Y. Y., Gu L., Element-free Galerkin methods, *Int. J. Num. Methods Eng.* 1994, **37**, 229-314.
- [75] Belytscho T., Krongauz Y., Organ D., Fleming M., Krysl P., Meshless Methods: an overview and recent developments, *Computer Methods App. Mech. Eng.* 1996, **139**, 3-47.
- [76] Aliabadi M. H., Boundary element formulations in fracture mechanics, *App. Mech. Rev.* 1997, **50(2)**, 83-97.
- [77] Mukhopadhyay N. K., Maiti S. K., Kakodkar A., A review of SIF evaluation and modelling of singularities in BEM, *Comp. Mech.* 2000, **25**, 358-375.
- [78] Rizzo F. J., An integral equation approach to boundary value problems of classical elastostatics, *Quart. App. Math.* 1967, **25(1)**, 83-95.
- [79] Cruse T. A., Numerical solutions in three dimensional elastostatics, *Int. J. Solids Struct.* 1969, **5**, 1259-1274.
- [80] Cruse T. A., Van Buren W., Three dimensional elastic stress analysis of a fracture specimen with an edge crack, *Int. J. Fract. Mech.* 1971, **7**, 1-15.
- [81] Blandford G. E., Ingraffea A. R., Liggett G. A., Two-dimensional stress intensity factor computations using the boundary element method, *Int. J. Num. Methods Eng.* 1981, **17**, 387-404.
- [82] Watson J. O., Singular boundary elements for the analysis of cracks in plane strain, *Int. J. Num. Methods Eng.* 1995, **38**, 2389-2411.
- [83] Portela A., Aliabadi M. H., Rooke D. P., Dual boundary element method: Efficient implementation for crack problems, *Int. J. Num. Methods Eng.* 1992, **33**, 1269-1287.
- [84] Richardson D., Cruse T. A., Nonsingular BEM for fracture modeling, *Comp. Struct.* 1998, **66**, 695-703.

- [85] Snyder M. D., Cruse T. A., Boundary-integral analysis of anisotropic cracked plates, *Int. J. Fract. Mech.* 1975, **11**, 315-328.
- [86] BONNET, M., 1995, *Boundary Integral Equation Methods for Solids and Fluids*, John Wiley & Sons, England.
- [87] BONNET, M., MAIER, G., AND POLIZZOTTO, C., 1998, "Symmetric Galerkin boundary element method," ASME Applied Mechanics Reviews, **51**, pp. 669-704.
- [88] GRAY, L.J., 1991, "Evaluation of hypersingular integrals in the boundary element method," Mathematical and Computer Modeling, **15**, pp. 165-174.
- [89] MARTIN, P.A., AND RIZZO, F.J., 1996, "Hypersingular integrals: how smooth must the density be?," International Journal for Numerical Methods in Engineering, **39**, pp. 687-704.
- [90] HENSHELL, R.D., AND SHAW, K.G., 1975, "Crack tip finite elements are unnecessary," International Journal for Numerical Methods in Engineering, **9**, pp. 495-507.
- [91] BARSOUM, R.S., 1976, "On the use of isoparametric finite elements in linear fracture mechanics," International Journal for Numerical Methods in Engineering, **10**, pp. 25-37.
- [92] BLANDFORD, G.E., INGRAFFEA, A.R., AND LIGGETT, J.A., 1981, "Two-dimensional stress intensity factor computations using the boundary element method," Int. J. Num. Meth. Engng, **17**, pp. 387-404.
- [93] BANKS-SILLS, L., 1991, "Application of the finite element method to linear elastic fracture mechanics," Appl. Mech. Rev., **44**, pp. 447-461.
- [94] GRAY, L.J., AND PAULINO, G.H., 1998, "Crack tip interpolation, revisited," SIAM J. Applied Mathematics, **58**, pp. 428-455.
- [95] GRAY, L.J., PHAN, A.-V., PAULINO, G.H., AND KAPLAN, T., 2003, "Improved quarter-point crack tip element," Engineering Fracture Mechanics, **70**, pp. 269-283.
- [96] ERDOGAN, F., AND SIH. G.C., 1963, "On the crack extension in plates under plane loading and transverse shear," Journal of Basic Engineering, **86**, pp. 519-527.
- [97] Gao X. W., Davies T. G., Boundary element programming in mechanics, 1960.
- [98] Trevelyan J., Boundary element for engineers: theory and applications, 1994.
- [99] MARTIN, P.A., 1991, "End-point behavior of solutions to hypersingular equations," Proc. R. Soc. Lond., A, **432**, pp. 301-320.
- [100] SIH. G.C., 1974, "Strain energy density factor applied to mixed mode crack problems," International Journal of Fracture, **10**, pp. 305-321.

- [101] Gifkins R. C., Optical microscopy of metals, American Elsevier Publishing Company Inc., N.Y., 1970, 168-195.
- [102] Richardson J. H., Optical microscopy for the materials sciences, Marcel Dekker Inc., N.Y., 1971, 592-628.
- [103] Fullman R. L., Measurement of particle sizes in opaque bodies, *Trans. AIME J. Metals* 1953, **March**, 447-452.
- [104] Lange F. F. and Radford K. C., Fracture energy of an epoxy composite system, *J. Mater. Sci.* 1971, **6**, 1197-1203.
- [105] Kitey R., Tippur H. V., Dynamic crack growth in particulate bimaternal having discrete and diffuse interfaces: Role of microstructure, *Eng. Fract. Mech.* 2005, **72**, 2721-2743.
- [106] Kitey R., Tippur H. V., Role of particle size and filler-matrix adhesion on dynamic fracture of glass-filled epoxy. II. Linkage between macro- and micro-measurements, *Acta Mater.* 2005, **53**, 1167-1178.
- [107] Kitey R., Tippur H. V., Modeling of crack growth through particulate clusters in brittle matrix by Symmetric-Galerkin Boundary Element Method, *Int. J. Fract.* 2005, Accepted for publication.
- [108] Anderson T. L., Fracture Mechanics, Fundamentals and Applications (Second Edition), CRC Press, 1995, 603-605.
- [109] He M. Y., Hutchinson J. W., Crack deflection at an interface between dissimilar elastic material, *Int. J. Solids Struct.* 1989. **25(9)**, pp. 1053-1067.

APPENDIX A

LEAST-SQUARES ANALYSIS OF OPTICAL DATA

Consider the governing equation of CGS (see, Eq. (2.15)) for linear elastic asymptotic stress field in the vicinity of a steadily propagating mode-I crack and neglecting the effect of crack velocity to get,

$$\frac{\partial w}{\partial x} = -\frac{\nu B}{2E} f(v) \sum_{n=1}^{\infty} \left[A_n \left(\frac{n}{2} - 1 \right) r^{\left(\frac{n}{2} - 2 \right)} \cos \left(\frac{n}{2} - 2 \right) \theta \right] = \frac{Np}{2\Delta} , \quad (\text{A.1})$$

The above equation can be expanded as,

$$\begin{aligned} \frac{\partial w}{\partial x} &= -\frac{\nu B}{2E} \left[A_1 \left(-\frac{1}{2} r^{-3/2} \cos \frac{3\theta}{2} \right) + A_3 \left(\frac{1}{2} r^{-1/2} \cos \frac{\theta}{2} \right) + A_4 \left(-\frac{1}{2} r^0 \cos 0 \right) + \dots \right] \\ &= \frac{Np}{2\Delta} . \end{aligned} \quad (\text{A.2})$$

Consider $f_n(r, \theta) = \left(\frac{n}{2} - 1 \right) r^{\left(\frac{n}{2} - 2 \right)} \cos \left(\frac{n}{2} - 2 \right) \theta$. Also, for simplicity consider only four terms of Eq. (A.1) to get,.

$$\frac{\partial w}{\partial x} = -\frac{\nu B}{2E} [A_1 f_1 + A_3 f_3 + A_4 f_4] = \frac{Np}{2\Delta} . \quad (\text{A.3})$$

Substitute $\frac{\nu B}{2E} = D$ and $\frac{p}{2\Delta} = C$ in the above to get,

$$D [A_1 f_1 + A_3 f_3 + A_4 f_4] + CN = 0 . \quad (\text{A.4})$$

Square the above equation and sum up for all digitized data around the crack tip to get,

$$\sum_{i=1}^k [D (A_1 f_1 + A_3 f_3 + A_4 f_4) + CN]^2 = 0, \quad (\text{A.5})$$

where k is the number of data points.

Differentiate above equation with respect to A_1 to get,

$$2D \sum_{i=1}^k [\{D (A_1 f_1 + A_3 f_3 + A_4 f_4) + CN\} f_1] = 0, \quad (\text{A.6})$$

or,

$$A_1 \sum_{i=1}^k f_1 f_1 + A_3 \sum_{i=1}^k f_3 f_1 + A_4 \sum_{i=1}^k f_4 f_1 = -\frac{C}{D} \sum_{i=1}^k N f_1 \quad (\text{A.7})$$

Similarly, differentiating Eq. A.5 with respect to A_3 and A_4 and writing resultant set of simultaneous equations in matrix form as,

$$\begin{bmatrix} \sum_{i=1}^k f_1 f_1 & \sum_{i=1}^k f_3 f_1 & \sum_{i=1}^k f_4 f_1 \\ \sum_{i=1}^k f_1 f_3 & \sum_{i=1}^k f_3 f_3 & \sum_{i=1}^k f_4 f_3 \\ \sum_{i=1}^k f_1 f_4 & \sum_{i=1}^k f_3 f_4 & \sum_{i=1}^k f_4 f_4 \end{bmatrix} \begin{Bmatrix} A_1 \\ A_3 \\ A_4 \end{Bmatrix} = -\frac{C}{D} \begin{Bmatrix} \sum_{i=1}^k N f_1 \\ \sum_{i=1}^k N f_3 \\ \sum_{i=1}^k N f_4 \end{Bmatrix} \quad (\text{A.8})$$

Above set of linear equations can now be solved for A_i , $i = 1, 3, 4$ where mode-I stress intensity factor, K_I , is given by $K_I = A_1 \sqrt{\frac{\pi}{2}}$. Similar analysis can be performed for a crack propagating in mixed-mode (mode-I and mode-II) condition. A code (attached ahead) using programming language ‘C’ is developed to apply least-square-analysis on digitized data to solve the governing equation of CGS and to extract mode-I and mode-II stress intensity factors.

```

/*=====
Designed and Developed by Rajesh Kitey.

Code to solve governing equation of CGS and to extract mode-I and mode-II SIF
from digitized data. Co-ordinate system is located at the crack tip with the
direction of crack orientation as positive x axis. Number of terms in
asymptotic series can be chosen while executing the code. Data within 3-D zone
is discarded (r/B <= 0.5).
=====*/

#include <stdio.h>
#include <math.h>

#define SINGULAR_ERROR -1001
#define PI ( 4 * atan ( 1.0 ) )

void read_input ( char *input_file, int *num_data_points, double **x_cord,
                 double **y_cord, double **fringe_order );

void get_polar ( double crack_length, int num_data_points, double *x_cord,
                double *y_cord, double **r_cord, double **phi );

void construct_matrix ( FILE *fp_w, int num_asmp_terms, double grating_pitch,
                       double grating_distance, double elastic_modulus,
                       double poissons_ratio, double plate_thickness,
                       int num_data_points, double *r_cord, double *phi,
                       double *fringe_order, double ***K_mat, double **F_vec );

int gauss_elimination ( int mat_size, double ***a_mat, double **b_mat );

int back_substitution ( int mat_size, double **a_mat, double *b_mat,
                       double **x_mat );

main ( int argc, char *argv[] )
{
    int inx = 0;
    FILE *fp_w;
    int num_data_points = 0, num_asmp_terms = 0;
    double crack_length = 0.0, grating_pitch = 0.0, grating_distance = 0.0,
           elastic_modulus = 0.0, poissons_ratio = 0.0, plate_thickness = 0.0;
    double *x_cord = NULL, *y_cord = NULL, *r_cord = NULL, *phi = NULL,
           **K_mat = NULL, *F_vec = NULL, *Williams_const = NULL,
           fracture_toughness = 0.0, *fringe_order = NULL ;
    char *out_file = ( char * ) malloc ( ( strlen ( argv[1] ) + 5 )
                                         * sizeof ( char ) );

    strcpy ( out_file, argv[1] );
    strcat ( out_file, ".out" );
    fp_w = fopen ( out_file, "w" );

    read_input ( argv[1], &num_data_points, &x_cord, &y_cord, &fringe_order );
    printf ( "read_input pass\n" );

    num_asmp_terms = atoi ( argv[2] );
    grating_pitch = atof ( argv[3] );
    grating_distance = atof ( argv[4] );
    elastic_modulus = atof ( argv[5] );
    poissons_ratio = atof ( argv[6] );
    plate_thickness = atof ( argv[7] );
    crack_length = atof ( argv[8] );

    if ( num_asmp_terms == 1 )
        num_asmp_terms = 2;

    fprintf ( fp_w, "num_asmp_terms = %d\ngrating_pitch = %lf\n",
              num_asmp_terms, grating_pitch );
    fprintf ( fp_w, "grating_distance = %lf\nelastic_modulus = %lf\n",
              grating_distance, elastic_modulus );
    fprintf ( fp_w, "poissons_ratio = %lf\nplate_thickness = %lf\n",
              poissons_ratio, plate_thickness );

    get_polar ( crack_length, num_data_points,
                x_cord, y_cord, &r_cord, &phi );
    printf ( "get_polar pass\n" );
}

```

```

construct_matrix ( fp_w, num_asmp_terms, grating_pitch, grating_distance,
                  elastic_modulus, poissons_ratio, plate_thickness,
                  num_data_points, r_cord, phi, fringe_order, &K_mat, &F_vec );
printf ( "construct_matrix pass\n" );

gauss_elimination ( 2*(num_asmp_terms-1), &K_mat, &F_vec );
printf ( "gauss_elimination pass\n" );

back_substitution ( 2*(num_asmp_terms-1), K_mat, F_vec, &Williams_const );
printf ( "back_substitution pass\n" );

fprintf ( fp_w, "\n\nWilliam's Constants : " );
for ( inx = 0 ; inx < num_asmp_terms-1 ; inx++ )
{
    if ( inx == 0 )
        fprintf ( fp_w, "\n\nA(%d) = %lf\n", inx+1, Williams_const[inx] );
    else
        fprintf ( fp_w, "A(%d) = %lf\n", inx+2, Williams_const[inx] );
}
for ( inx = 0 ; inx < num_asmp_terms-1 ; inx++ )
{
    if ( inx == 0 )
        fprintf ( fp_w, "\n\nB(%d) = %lf\n",
                  inx+1, Williams_const[inx+num_asmp_terms-1] );
    else
        fprintf ( fp_w, "B(%d) = %lf\n",
                  inx+2, Williams_const[inx+num_asmp_terms-1] );
}

fracture_toughness = *Williams_const * pow ( ( 2.0 * PI ), 0.5 ) / 2.0 ;
fprintf ( fp_w, "\nfracture toughness K(I) = %lf Pascal root meter\n\n",
          fracture_toughness );
printf ( "\nfracture toughness K(I) = %lf Pascal root meter\n\n",
         fracture_toughness );

fracture_toughness = Williams_const[num_asmp_terms-1]
                    * pow ( ( 2.0 * PI ), 0.5 ) / 2.0 ;
fprintf ( fp_w, "fracture toughness K(II) = %lf Pascal root meter\n\n",
          fracture_toughness );
printf ( "fracture toughness K(II) = %lf Pascal root meter\n\n",
         fracture_toughness );

fclose ( fp_w );
}

void read_input /* Function to read data from input_file */
( char *input_file, int *num_data_points, double **x_cord,
  double **y_cord, double **fringe_order )
{
    int inx = 0, jnx = 0, data_index = 0;
    char temp ;
    FILE *fp_r;

    fp_r = fopen ( input_file, "r" );

    *x_cord = ( double * ) malloc ( 1 * sizeof ( double ) );
    *y_cord = ( double * ) malloc ( 1 * sizeof ( double ) );
    *fringe_order = ( double * ) malloc ( 1 * sizeof ( double ) );

    while ( 1 )
    {
        fscanf ( fp_r, "%lf", &((*x_cord)[data_index]) );

        if ( feof (fp_r) )
            break;
        else
        {
            *x_cord = ( double * ) realloc ( (void *)(*x_cord),
                                             ( data_index+2 ) * sizeof ( double ) );
            *y_cord = ( double * ) realloc ( (void *)(*y_cord),
                                             ( data_index+2 ) * sizeof ( double ) );
            *fringe_order = ( double * ) realloc ( (void*)(*fringe_order),
                                                  ( data_index+2 ) * sizeof ( double ) );
        }
    }
}

```

```

        fscanf ( fp_r, "%lf", &((*y_cord)[data_index]) );
        fscanf ( fp_r, "%lf", &((*fringe_order)[data_index]) );

        data_index++;
    }
    *num_data_points = data_index;

    fclose ( fp_r );
}

void get_polar /* Converting digitized data into polar co-ordinates */
( double crack_length, int num_data_points, double *x_cord,
  double *y_cord, double **r_cord, double **phi )
{
    int inx = 0;
    double x_new = 0.0, y_new = 0.0, abs_phi = 0.0;

    *r_cord = ( double * ) malloc ( num_data_points * sizeof ( double ) );
    *phi = ( double * ) malloc ( num_data_points * sizeof ( double ) );

    for ( inx = 0; inx < num_data_points; inx++ )
    {
        x_new = y_cord[inx] ;
        y_new = - x_cord[inx] ;

        (*r_cord)[inx] = pow( ( pow( x_new, 2.0 ) + pow( y_new, 2.0 ) ), 0.5 );
        (*r_cord)[inx] *= 0.001;
        abs_phi = atan ( fabs ( y_new / x_new ) ) ;

        if ( x_new >= 0.0 )
        {
            if ( y_new >= 0.0 )
                (*phi)[inx] = abs_phi ;
            else
                (*phi)[inx] = - abs_phi ;
        }
        else
        {
            if ( y_new >= 0.0 )
                (*phi)[inx] = PI - abs_phi ;
            else
                (*phi)[inx] = - ( PI - abs_phi ) ;
        }
    }
}

void construct_matrix /* Constructing Coefficient matrix and known vector */
( FILE *fp_w, int num_asmp_terms, double grating_pitch,
  double grating_distance, double elastic_modulus, double poissons_ratio,
  double plate_thickness, int num_data_points, double *r_cord,
  double *phi, double *fringe_order, double ***K_mat, double **F_vec )
{
    int inx = 0, jnx = 0, knx = 0;
    double fvec_const = 0.0, gvec_const = 0.0,
        *fnx_rphi = NULL, *gnx_rphi = NULL;

    if ( num_asmp_terms == 1 )
        num_asmp_terms = 2;

    fnx_rphi = ( double * ) malloc ( (num_asmp_terms-1) * sizeof ( double ) );
    gnx_rphi = ( double * ) malloc ( (num_asmp_terms-1) * sizeof ( double ) );
    *K_mat = ( double ** ) malloc ( 2 * (num_asmp_terms-1) * sizeof (double * ) );
    *F_vec = ( double * ) malloc ( 2 * (num_asmp_terms-1) * sizeof ( double ) );

    for ( inx = 0; inx < 2 * (num_asmp_terms-1) ; inx++ )
    {
        (*K_mat)[inx] =
            ( double * ) malloc ( 2 * (num_asmp_terms-1) * sizeof ( double ) );
        for ( jnx = 0; jnx < 2 * (num_asmp_terms-1) ; jnx++ )
            (*K_mat)[inx][jnx] = 0.0;
        (*F_vec)[inx] = 0.0;
    }
    fvec_const = gvec_const = ( elastic_modulus * grating_pitch )
        / ( grating_distance * poissons_ratio * plate_thickness );
}

```

```

for ( inx = 0; inx < num_data_points; inx++ )
{
    fprintf ( fp_w, "\n\npoint(%d) : r = %lf, phi = %lf\n",
             inx+1, r_cord[inx], phi[inx] );

    if ( r_cord[inx] / plate_thickness <= 0.5 )
    {
        fprintf ( fp_w, "3-D zone, point discarded !!!\n" );
        continue;
    }

    for ( jnx = 0; jnx < num_asmp_terms; jnx++ )
    {
        if ( jnx == 0 )
            knx = 0;
        else if ( jnx == 1 )
            continue;
        else
            knx = jnx - 1;

        fnx_rphi[knx] = -1.0 * ((double)(jnx-1)/2.0)
            * pow ( r_cord[inx], ((double)(jnx-3)/2.0) )
            * cos ( ((double)(jnx-3)/2.0) * phi[inx] );
        gnx_rphi[knx] = -1.0 * ((double)(jnx-1)/2.0)
            * pow ( r_cord[inx], ((double)(jnx-3)/2.0) )
            * sin ( ((double)(jnx-3)/2.0) * phi[inx] );
        fprintf ( fp_w, "f(%d) = %lf\tg(%d) = %lf\t",
                 jnx+1, fnx_rphi[knx], jnx+1, gnx_rphi[knx] );
    }

    for ( jnx = 0; jnx < num_asmp_terms-1 ; jnx++ )
    {
        for ( knx = 0; knx < num_asmp_terms-1 ; knx++ )
        {
            (*K_mat)[jnx][knx] += ( fnx_rphi[jnx] * fnx_rphi[knx] );
            (*K_mat)[jnx][knx+num_asmp_terms-1]
                += ( fnx_rphi[jnx] * gnx_rphi[knx] );
            (*K_mat)[jnx+num_asmp_terms-1][knx]
                += ( gnx_rphi[jnx] * fnx_rphi[knx] );
            (*K_mat)[jnx+num_asmp_terms-1][knx+num_asmp_terms-1]
                += ( gnx_rphi[jnx] * gnx_rphi[knx] );
        }
        (*F_vec)[jnx] += ( fvec_const * fnx_rphi[jnx] * fringe_order[inx] );
        (*F_vec)[jnx+num_asmp_terms-1]
            += ( gvec_const * gnx_rphi[jnx] * fringe_order[inx] );
    }
}

fprintf ( fp_w, "\n\nK Mat :\n" );
for ( jnx = 0; jnx < 2 * (num_asmp_terms-1) ; jnx++ )
{
    for ( knx = 0; knx < 2 * (num_asmp_terms-1) ; knx++ )
        fprintf ( fp_w, "%lf(%d%d)\t", (*K_mat)[jnx][knx], jnx+1, knx+1 );
    fprintf ( fp_w, "\n" );
}
fprintf ( fp_w, "\nF Vec :\n" );
for ( jnx = 0; jnx < 2 * (num_asmp_terms-1) ; jnx++ )
    fprintf ( fp_w, "F(%d) = %lf\n", jnx+1, (*F_vec)[jnx] );
}

int gauss_elimination /* Solving system of equations by Gauss elimination */
( int mat_size, double ***a_mat, double **b_mat )
{
    int inx = 0, jnx = 0, knx = 0;

    for ( inx = 0 ; inx < mat_size-1 ; inx++ )
    {
        if ( fabs ( (*a_mat)[inx][inx] ) < 1e-06 )
        {
            int swp_row = 0;

            for ( jnx = inx+1 ; jnx < mat_size ; jnx++ )
            {

```

```

        if ( fabs ( (*a_mat)[jnx][inx] ) >= 1e-06 )
        {
            swp_row = jnx;
            break;
        }
    }

    if ( swp_row )
    {
        double temp_element = 0.0;

        for ( jnx = 0 ; jnx < mat_size ; jnx++ )
        {
            temp_element = (*a_mat)[inx][jnx];
            (*a_mat)[inx][jnx] = (*a_mat)[swp_row][jnx];
            (*a_mat)[swp_row][jnx] = temp_element;
        }

        temp_element = (*b_mat)[inx];
        (*b_mat)[inx] = (*b_mat)[swp_row];
        (*b_mat)[swp_row] = temp_element;
    }

    for ( jnx = inx+1 ; jnx < mat_size ; jnx++ )
    {
        (*a_mat)[jnx][inx] = (*a_mat)[jnx][inx]/(*a_mat)[inx][inx];

        for ( knx = inx+1 ; knx < mat_size ; knx++ )
            (*a_mat)[jnx][knx] = (*a_mat)[jnx][knx]
                - (*a_mat)[jnx][inx] * (*a_mat)[inx][knx];

        (*b_mat)[jnx] = (*b_mat)[jnx]
            - (*a_mat)[jnx][inx] * (*b_mat)[inx];
    }
}

int back_substitution /* Back substitution part of Gauss elimination */
( int mat_size, double **a_mat, double *b_mat, double **x_mat )
{
    int inx = 0, jnx = 0;
    double sum = 0.0;

    *x_mat = ( double * ) malloc ( mat_size * sizeof ( double ) );
    (*x_mat)[mat_size-1] = b_mat[mat_size-1]/a_mat[mat_size-1][mat_size-1];

    for ( inx = mat_size-2 ; inx >= 0 ; inx-- )
    {
        sum = 0.0;
        for ( jnx = inx+1 ; jnx < mat_size ; jnx++ )
            sum += a_mat[inx][jnx] * (*x_mat)[jnx];
        (*x_mat)[inx] = ( b_mat[inx] - sum ) / a_mat[inx][inx];
    }
}

/*-----
executing the code :
a.out in_file.dat 3 0.000025 0.0475 3e+09 -0.33 0.0053 0.012
argv 1 :      executable
argv 2 :      input file name ( data be in mm: x, y, N )
argv 3 :      number of asymptotic terms
argv 4 :      grating pitch ( meters )
argv 5 :      grating distance ( meters )
argv 6 :      elastic modulus ( Pascal )
argv 7 :      poisson's ratio
argv 8 :      plate thickness ( meters )
argv 9 :      crack length ( meters )
-----*/

```

APPENDIX B

SGBEM INPUT DATA FILE: DETAILS

SGBEM is a symmetric-Galerkin boundary element code to simulate quasi-static crack growth in a two-dimensional isotropic linear elastic domain. FORTRAN 77 in conjunction with C is used to implement boundary element formulation. The program incorporates quadratic elements to approximate the domain boundaries. The crack-tip is modeled using a quarter-point element. The stress intensity factor is computed using crack opening displacement at the mid-node of the quarter-point element. Maximum tangential stress theory is applied to identify the direction of crack propagation. Crack-initiation is based on the criteria $K_I = K_{Ic}$.

The code can be compiled on UNIX/LINUX platform either by running a Makefile or by compiling all fortran files together (f77 *.f). The generated executable (SGBEM/a.out) can be run to perform simulations in command prompt (<Executable> <Input file> <Output file>).

The input file should be written in the following format:

NUM-MAX-STEP

STEP-SIZE

NUM-ZONES

NUM-NODES

NDX_i NDY_i NDXBV_i NDYBV_i NDXBC_i NDYBC_i

NUM-EDGE-CRACKS

LEGND_j LEGND-TOP_j LEGND-BOTTOM_j

NUM-ELEMS_k
 E_k ν _k K_{Ic} -k
 ELND1_p_k ELND2_p_k ELND2_p_k
 NUM-BODY-FORCES_k
 NUM-CRACK-TIPS_k
 CRTIP-ND_k CRTIP-ELE_k CRTIP-ID_k

In the above data file maximum number of crack increments in crack growth simulation is defined by NUM-MAX-STEP. The STEP-SIZE defines the size/length of crack increment. NUM-ZONES suggests the number of zones in the domain. Total number of nodes is given by NUM-NODES. Nodal coordinates for the i^{th} node is given by NDX_i and NDY_i. The values of boundary conditions in the x - and the y - directions for the i^{th} node are followed next (NDXBV_i and NDYBV_i). The displacement/traction boundary condition is identified for the given boundary values by NDXBC_i and NDYBC_i, in x and y directions, respectively. The 0 flag represents displacement boundary condition whereas 1 suggests that traction boundary condition is prescribed on the node. The nodes on interface edges are identified with a flag 2. The total number of edge cracks is defined further by NUM-EDGE-CRACKS. For the j^{th} edge crack three nodes LEGND_j, LEGND-TOP_j and LEGND-BOTTOM_j at the crack leg are defined where LEGND is the node from the crack edge element. The next two nodes, LEGND-TOP and LEGND-BOTTOM, are the end nodes of the boundary edges which merge at the crack leg as shown in Fig. B.1. The LEGND-TOP and LEGND-BOTTOM are defined such that the $u(\text{LEGND-TOP}) - u(\text{LEGND-BOTTOM})$ gives positive crack opening displacement, where u is the nodal displacement. Similarly, next edge crack information can be given.

Number of elements in k^{th} zone is given by NUM-ELEMS_k. The nodal connectivity for p^{th} element in the k^{th} zone is defined by ELND1_p_k ELND2_p_k ELND2_p_k where the node numbers are given in anti-clockwise fashion. The number of body forces in k^{th} zone NUM-BODY-FORCES_k is not used in the current code, hence always given as 0. The NUM-CRACK-TIPS_k gives the number of crack-tips in k^{th} zone. This is followed by crack tip node CRTIP-ND_k, crack tip element CRTIP-ELE_k and a crack tip id CRTIP-ID_k in k^{th} zone. Crack tip id is 0 if the crack tip node number is smaller than the node number of quarter-point node, or else the crack tip id is defined as -1. Similar element information can be given for next zone and so on. In the above data file domain corners are defined by double nodes.

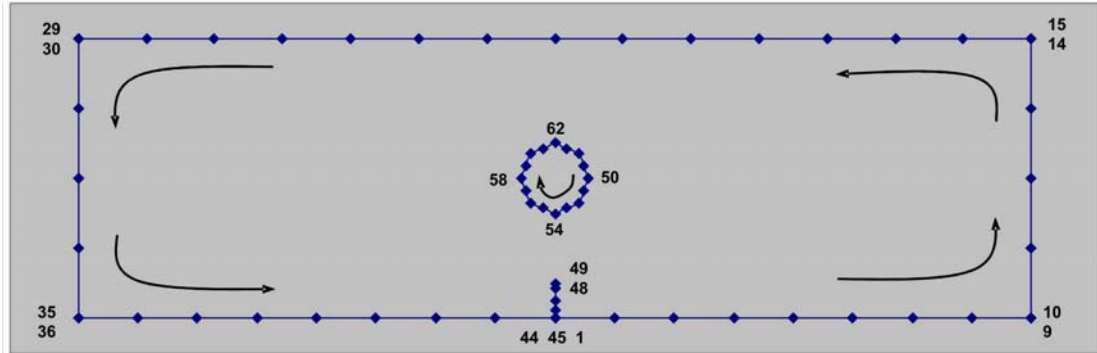


Figure B.1: A cracked geometry with an inclusion. Node numbers are assigned to run the crack growth simulation using SGBEM. Outer boundary is meshed counter-clockwise whereas the meshing on inclusion-matrix interface is clockwise. Quarter point element is defined at the crack-tip. Crack leg is modeled with triple node. Specimen corners contain double nodes.

An input data file is added next for a cracked specimen geometry with an inclusion as shown in Fig. B.1. A uniaxial tension is applied on the edge with nodes 10 to 14. The edge with nodes 30 to 35 is modeled as an edge with uniform roller supports.

100

2.500000e-04

2

65

0.000000e+00	-1.000000e-02	0.000000e+00	0.000000e+00	1	1	1
8.750000e-03	-1.000000e-02	0.000000e+00	0.000000e+00	1	1	2
1.750000e-02	-1.000000e-02	0.000000e+00	0.000000e+00	1	1	3
2.625000e-02	-1.000000e-02	0.000000e+00	0.000000e+00	1	1	4
3.500000e-02	-1.000000e-02	0.000000e+00	0.000000e+00	1	1	5
4.375000e-02	-1.000000e-02	0.000000e+00	0.000000e+00	1	1	6
5.250000e-02	-1.000000e-02	0.000000e+00	0.000000e+00	1	1	7
6.125000e-02	-1.000000e-02	0.000000e+00	0.000000e+00	1	1	8
7.000000e-02	-1.000000e-02	0.000000e+00	0.000000e+00	1	1	9
7.000000e-02	-1.000000e-02	1.000000e-01	0.000000e+00	1	1	10
7.000000e-02	0.000000e+00	1.000000e-01	0.000000e+00	1	1	11
7.000000e-02	1.000000e-02	1.000000e-01	0.000000e+00	1	1	12
7.000000e-02	2.000000e-02	1.000000e-01	0.000000e+00	1	1	13
7.000000e-02	3.000000e-02	1.000000e-01	0.000000e+00	1	1	14
7.000000e-02	3.000000e-02	0.000000e+00	0.000000e+00	1	1	15
6.000000e-02	3.000000e-02	0.000000e+00	0.000000e+00	1	1	16
5.000000e-02	3.000000e-02	0.000000e+00	0.000000e+00	1	1	17
4.000000e-02	3.000000e-02	0.000000e+00	0.000000e+00	1	1	18
3.000000e-02	3.000000e-02	0.000000e+00	0.000000e+00	1	1	19
2.000000e-02	3.000000e-02	0.000000e+00	0.000000e+00	1	1	20
1.000000e-02	3.000000e-02	0.000000e+00	0.000000e+00	1	1	21
0.000000e+00	3.000000e-02	0.000000e+00	0.000000e+00	1	1	22
-1.000000e-02	3.000000e-02	0.000000e+00	0.000000e+00	1	1	23
-2.000000e-02	3.000000e-02	0.000000e+00	0.000000e+00	1	1	24
-3.000000e-02	3.000000e-02	0.000000e+00	0.000000e+00	1	1	25
-4.000000e-02	3.000000e-02	0.000000e+00	0.000000e+00	1	1	26
-5.000000e-02	3.000000e-02	0.000000e+00	0.000000e+00	1	1	27
-6.000000e-02	3.000000e-02	0.000000e+00	0.000000e+00	1	1	28
-7.000000e-02	3.000000e-02	0.000000e+00	0.000000e+00	1	1	29
-7.000000e-02	3.000000e-02	0.000000e+00	0.000000e+00	0	1	30
-7.000000e-02	2.000000e-02	0.000000e+00	0.000000e+00	0	1	31
-7.000000e-02	1.000000e-02	0.000000e+00	0.000000e+00	0	1	32
-7.000000e-02	1.000000e-02	0.000000e+00	0.000000e+00	0	0	33
-7.000000e-02	0.000000e+00	0.000000e+00	0.000000e+00	0	0	34
-7.000000e-02	-1.000000e-02	0.000000e+00	0.000000e+00	0	0	35
-7.000000e-02	-1.000000e-02	0.000000e+00	0.000000e+00	1	1	36
-6.125000e-02	-1.000000e-02	0.000000e+00	0.000000e+00	1	1	37
-5.250000e-02	-1.000000e-02	0.000000e+00	0.000000e+00	1	1	38
-4.375000e-02	-1.000000e-02	0.000000e+00	0.000000e+00	1	1	39
-3.500000e-02	-1.000000e-02	0.000000e+00	0.000000e+00	1	1	40
-2.625000e-02	-1.000000e-02	0.000000e+00	0.000000e+00	1	1	41
-1.750000e-02	-1.000000e-02	0.000000e+00	0.000000e+00	1	1	42
-8.750000e-03	-1.000000e-02	0.000000e+00	0.000000e+00	1	1	43
0.000000e+00	-1.000000e-02	0.000000e+00	0.000000e+00	1	1	44
0.000000e+00	-1.000000e-02	0.000000e+00	0.000000e+00	1	1	45
0.000000e+00	-8.750000e-03	0.000000e+00	0.000000e+00	1	1	46
0.000000e+00	-7.500000e-03	0.000000e+00	0.000000e+00	1	1	47
0.000000e+00	-5.625000e-03	0.000000e+00	0.000000e+00	1	1	48
0.000000e+00	-5.000000e-03	0.000000e+00	0.000000e+00	1	1	49
5.000000e-03	1.000000e-02	0.000000e+00	0.000000e+00	2	2	50
4.267767e-03	8.232233e-03	0.000000e+00	0.000000e+00	2	2	51
3.535534e-03	6.464466e-03	0.000000e+00	0.000000e+00	2	2	52
1.767767e-03	5.732233e-03	0.000000e+00	0.000000e+00	2	2	53
-9.184851e-19	5.000000e-03	0.000000e+00	0.000000e+00	2	2	54
-1.767767e-03	5.732233e-03	0.000000e+00	0.000000e+00	2	2	55
-3.535534e-03	6.464466e-03	0.000000e+00	0.000000e+00	2	2	56
-4.267767e-03	8.232233e-03	0.000000e+00	0.000000e+00	2	2	57

-5.000000e-03	1.000000e-02	0.000000e+00	0.000000e+00	2	2	58
-4.267767e-03	1.176777e-02	0.000000e+00	0.000000e+00	2	2	59
-3.535534e-03	1.353553e-02	0.000000e+00	0.000000e+00	2	2	60
-1.767767e-03	1.426777e-02	0.000000e+00	0.000000e+00	2	2	61
3.061617e-19	1.500000e-02	0.000000e+00	0.000000e+00	2	2	62
1.767767e-03	1.426777e-02	0.000000e+00	0.000000e+00	2	2	63
3.535534e-03	1.353553e-02	0.000000e+00	0.000000e+00	2	2	64
4.267767e-03	1.176777e-02	0.000000e+00	0.000000e+00	2	2	65

1

45 44 1

29

3.200000e+03

3.000000e-01

0.000000e+00

1	2	3	1
3	4	5	2
5	6	7	3
7	8	9	4
10	11	12	5
12	13	14	6
15	16	17	7
17	18	19	8
19	20	21	9
21	22	23	10
23	24	25	11
25	26	27	12
27	28	29	13
30	31	32	14
33	34	35	15
36	37	38	16
38	39	40	17
40	41	42	18
42	43	44	19
45	46	47	20
47	48	49	21
50	51	52	22
52	53	54	23
54	55	56	24
56	57	58	25
58	59	60	26
60	61	62	27
62	63	64	28
64	65	50	29

0

1

49 21 -1

8

7.000000e+04

3.000000e-01

0.000000e+00

50	65	64	30
64	63	62	31
62	61	60	32
60	59	58	33
58	57	56	34
56	55	54	35
54	53	52	36
52	51	50	37

0

0